DISS. ETH NO. 22231

Experimental and numerical study of electrically-driven MHD flow

A dissertation submitted to attain the degree of

DOCTOR OF SCIENCES of ETH ZURICH
(Dr. sc. ETH Zurich)

presented by
ZACHARIAS STELZER

Dipl.-Geophys., Karlsruhe Institute of Technology, Germany
born on 28.07.1984
citizen of Germany

accepted on the recommendation of

Andrew Jackson
Jérôme Noir
David Cébron
Thierry Alboussière

2014

> Πάντα ῥεῖ.
>
> attributed to Heraclitus

Abstract

Flows of electrically conducting fluids interact with magnetic fields in various ways. On the one hand, they are influenced by an imposed magnetic field as exploited in engineering applications, e.g. pumping and flow control in metallurgy. On the other hand, flows of electrically conducting fluids create their own magnetic field which may modify or even generate the main field as in the case of geo- and astrophysical dynamos. These interactions of flow and magnetic fields are studied in the area of magnetohydrodynamics (MHD).

This dissertation is concerned with two topics from the different areas of MHD mentioned above. The first topic is the flow of liquid metal in a modified cylindrical annulus which is driven by the Lorentz force arising from an applied radial electrical current within an imposed axial magnetic field. The feedback of the flow on the magnetic field is negligible. Our ZUCCHINI (ZUrich Cylindrical CHannel INstability Investigation) setup is characterized by an inner electrode that protrudes from the inner cylinder and gives rise to a free Shercliff layer parallel to the magnetic field. We study the flow in a laboratory experiment, as well as by finite element simulations which allow for complementary information. The liquid GaInSn flow in the experiment is probed by ultrasound Doppler velocimetry and potential difference probes. In this way, we gain insight into the dynamics of different flow regimes, namely the steady base flow (Chapter 3), the instability of the free Shercliff layer in the form of traveling vortices which become container-filling at larger forcing, and finally the transition to turbulence in Hartmann layers at walls perpendicular to the magnetic field (Chapter 4). The 2D3C numerical simulations of the base flow and the linear stability analysis largely recover the dynamics observed in the experiment.

The second topic deals with numerical geodynamo simulations. Despite huge differences in the parameter regime, these simulations are able to produce magnetic fields that are largely similar to the one of the Earth. Hence they are used to infer properties and dynamics of the outer core. This inference relies on two assumptions: firstly the relevant dynamical processes have to be the same in the models and the core, and secondly we need to extract scaling laws which contain the relevant parameters. The latter in essence is a model selection problem which we tackle by using the statistical method of cross-validation (Chapter 5). It turns out that more parameters should be regarded in scaling laws than previously suggested. Especially the non-negligibility of diffusivities has important consequences for the application to Earth's core.

Zusammenfassung

Strömungen von elektrisch leitfähigen Flüssigkeiten wechselwirken mit Magnetfeldern auf verschiedene Weise. Einerseits werden sie von externen Magnetfeldern beeinflusst, was in industriellen Anwendungen wie beim Pumpen und der Strömungskontrolle in der Metallverarbeitung genutzt wird. Andererseits rufen Strömungen von elektrisch leitfähigen Flüssigkeiten ihrerseits ein Magnetfeld hervor, welches das externe Feld ändern oder wie im Fall von geo- und astrophysikalischen Dynamoprozessen gar erzeugen kann. Die Wechselwirkung von Strömung und Magnetfeld wird im Forschungsgebiet der Magnetohydrodynamik (MHD) untersucht.

Diese Dissertation befasst sich mit zwei Themen aus den verschiedenen genannten Gebieten der MHD. Das erste ist die Strömung von Flüssigmetall in einem modifizierten zylindrischen Ring, welche durch die Lorentzkraft angetrieben wird, die von einem radialen elektrischen Strom in einem axialen Magnetfeld hervorgerufen wird. Die Rückwirkung der Strömung auf das Magnetfeld ist vernachlässigbar. Unser Aufbau von ZUCCHINI (ZUrich Cylindrical CHannel INstability Investigation) ist dadurch gekennzeichnet, dass die innere Elektrode aus dem inneren Zylinder hervorragt, was zu einer freien Shercliffschicht parallel zum Magnetfeld führt. Wir untersuchen die Strömung sowohl in einem Laborexperiment als auch mit Finite-Elemente-Simulationen, die komplementäre Informationen liefern. Die Strömung von flüssigem GaInSn im Experiment wird durch Ultraschall-Doppler-Verfahren und Potentialdifferenz-Messungen aufgezeichnet. Auf diese Weise erkunden wir die Dynamik in den verschiedenen Parameterbereichen, im Einzelnen die stationäre Grundströmung (Kapitel 3), die Instabilität der freien Shercliffschicht in Form von wandernden Wirbeln, die bei höherem Strom das gesamte Behältnis ausfüllen, und schliesslich der Übergang zur Turbulenz in den Hartmannschichten an Wänden senkrecht zum Magnetfeld (Kapitel 4). Die 2D3C-Simulationen der Grundströmung und die lineare Stabilitätsanalyse bestätigen die im Experiment beobachtete Dynamik weitgehend.

Das zweite Thema dreht sich um numerische Simulationen des Geodynamo. Trotz riesiger Unterschiede im Parameterbereich sind diese Simulationen in der Lage, Magnetfelder zu erzeugen, die in vielen Punkten mit dem der Erde übereinstimmen. Daher werden sie dazu benutzt, Eigenschaften und Dynamik des äusseren Erdkerns zu erschliessen. Diese Methode beruht auf zwei Annahmen: Erstens müssen die relevanten Prozesse in den Modellen und im Kern übereinstimmen, zweitens müssen wir Skalierungsgesetze extrahieren, welche die relevanten Parameter enthalten. Letzteres ist im Wesentlichen ein

Modellauswahl-Problem, das wir mit dem Verfahren der Kreuzvalidierung lösen (Kapitel 5). Es stellt sich heraus, dass in Skalierungsgesetzen mehr Parameter berücksichtigt werden müssen als bisher gedacht. Besonders die Notwendigkeit von Diffusivitäten hat wichtige Auswirkungen für die Anwendung auf den Erdkern.

Acknowledgements

A multifaceted time of work and study at ETH draws to a close, and at the same time a very nice period of my life indeed. At this stage, I would like to thank all the people that contributed to this work, supported me in various ways and made my time so joyful.

In particular I am grateful to Andy who took me under his wing. I very much appreciate his guidance as well as the opportunity to learn about different interesting topics, to attend various conferences and to work and think independently. His love for science is fascinating, as is his ability to always know when his advice is needed.

Further I am deeply indebted to my scientific advisers Stijn, David, Sophie and Jérôme. I came to Zürich as a novice in fluid dynamics. A good portion of the knowledge I acquired in this area over time originates from numerous discussions with them. Stijn never tired in supporting me with his huge knowledge of liquid metal MHD flows. David introduced me to simulations with a ‘famous’ finite element software package. Jérôme and Sophie were there for me when it came to experimental planning, flow measurements and data interpretation.

As you gather from this thesis, a better part of my work took place in the lab. In this respect, a special thanks goes to our engineering team Peter, Thomas, Roland and Federico. They accompanied ZUCCHINI from the beginning of the design phase, built the experiment and advised me with their technical experience whenever needed.

I want to thank my office mates who made for a relaxed and enjoyable but also concentrated working atmosphere over the last roughly three and a half years. Furthermore I would like to extend this thanks to all members of our EPM group. I enjoyed the great team spirit, numerous coffee and lunch break discussions, and especially our amazing team activities.

I was fortunate enough to find friends for all sorts of fascinating activities be it mountaineering, ski touring or running, organizing events or music. I am very grateful to all of you, and look forward to new challenges together with you in the future.

Finally I want to thank my family as well as my wife Teresa for their perpetual love and support.

Zacharias Stelzer
September 2014

Contents

Abstract iii

Zusammenfassung v

Acknowledgements vii

List of Figures xiii

List of Tables xvii

1 Introduction 1
- 1.1 Motivation . . . 1
- 1.2 Navier, Stokes and Maxwell in a nutshell . . . 3
  - 1.2.1 Fundamentals of fluid dynamics . . . 3
  - 1.2.2 Fundamentals of electromagnetism . . . 4
  - 1.2.3 The governing equations of magnetohydrodynamics . . . 6
  - 1.2.4 Dynamics at large *Rm*: the geodynamo . . . 7
  - 1.2.5 Dynamics at low *Rm*: liquid metal MHD applications . . . 9
- 1.3 Liquid metal MHD experiments . . . 10
  - 1.3.1 Advent of liquid metal MHD . . . 11
  - 1.3.2 Early studies of MHD flow in straight ducts . . . 12
  - 1.3.3 Theoretical results on flow in cylindrical ducts . . . 13
  - 1.3.4 Early cylindrical duct experiments . . . 15
  - 1.3.5 The MATUR experiment . . . 17
  - 1.3.6 Instability of the Hartmann layer . . . 20
  - 1.3.7 Numerical picture of MHD duct flow . . . 22
  - 1.3.8 Recent cylindrical duct experiments . . . 22
  - 1.3.9 Related MRI experiments . . . 23
- 1.4 Composition of the thesis . . . 24
- References . . . 24

2 Experiments and simulations 29
- 2.1 Experimental setup and tests . . . 29
  - 2.1.1 The ZUCCHINI tank . . . 29
  - 2.1.2 Magnetic coil systems . . . 33
    - 2.1.2.1 Caylar coils . . . 34
    - 2.1.2.2 Cryomagnet . . . 36

2.1.3 Current supply . . . 39
2.1.3.1 Caylar setup . . . 40
2.1.3.2 Effects of non-axisymmetric current distribution . . . 41
2.1.3.3 Cryo setup . . . 43
2.1.4 GaInSn and the argon system . . . 43
2.1.5 Measurement techniques . . . 47
2.1.5.1 Ultrasonic Doppler velocimetry . . . 47
2.1.5.2 Potential difference probes . . . 48
2.1.5.3 Further measurements . . . 49
2.2 Numerical techniques in complex geometries . . . 50
2.2.1 Finite elements . . . 50
2.2.2 Weak formulation and solution . . . 52
2.2.3 Specific options in COMSOL . . . 54
2.2.4 Concluding remarks on the FEM . . . 55
References . . . 55

3 The base flow in ZUCCHINI **57**
Manuscript: ZUCCHINI (1) Base flow . . . 57
Summary . . . 57
3.1 Introduction . . . 58
3.2 Model description . . . 62
3.3 Numerical simulation . . . 63
3.3.1 Numerical model . . . 63
3.3.2 Parameter study . . . 64
3.3.2.1 Flow structure . . . 65
3.3.2.2 Scaling of azimuthal velocity . . . 66
3.3.2.3 Scaling of radial and axial velocities . . . 68
3.3.2.4 Boundary and shear layer scaling . . . 70
3.4 Experiment . . . 72
3.4.1 Setup . . . 72
3.4.2 Methods . . . 74
3.4.2.1 Measurements . . . 74
3.4.2.2 Processing . . . 75
3.4.2.3 Data example . . . 76
3.4.3 Results . . . 77
3.4.3.1 Mean azimuthal flow . . . 79
3.4.3.2 Radial and axial recirculation . . . 81
3.4.4 Experiment versus numerics . . . 83
3.4.4.1 General comparison . . . 83
3.4.4.2 Numerical recovery of the jet . . . 86
3.5 Conclusions . . . 87
Appendix . . . 88
3.A Governing equations in cylindrical coordinates . . . 88
3.B Electrical boundary conditions . . . 89
3.C Convergence study . . . 89
3.D Comparison mean versus rms azimuthal velocity . . . 91
3.E Argument for the velocity scaling at high M . . . 91

3.F Details of the experimental setup . . . 93
3.G The magnetic setups ‘Caylar’ and ‘Cryo’ . . . 93
3.H Power supplies . . . 96
Acknowledgements . . . 96
References . . . 96

4 Characterization of the instabilities 99

Manuscript: ZUCCHINI (2) Instabilities . . . 99
Summary . . . 99
4.1 Introduction . . . 100
4.2 Model description . . . 102
4.3 Numerical simulation . . . 104
  4.3.1 First-order perturbation equations . . . 104
  4.3.2 Numerical model . . . 104
  4.3.3 Parameter study . . . 105
    4.3.3.1 Parameters and processing . . . 105
    4.3.3.2 Growth rates and frequencies . . . 107
    4.3.3.3 Stability diagram . . . 109
    4.3.3.4 Structure of the modes . . . 109
4.4 Experiment . . . 111
  4.4.1 Setup . . . 111
  4.4.2 Methodology . . . 114
    4.4.2.1 Measurements . . . 114
    4.4.2.2 Processing and data examples . . . 116
  4.4.3 Results . . . 117
    4.4.3.1 Mean azimuthal flow . . . 117
    4.4.3.2 Free Shercliff layer thickness . . . 120
    4.4.3.3 Radial and axial flow structure . . . 120
    4.4.3.4 PDP measurements . . . 126
    4.4.3.5 Oscillations . . . 126
    4.4.3.6 Friction factor . . . 131
    4.4.3.7 Stability diagram . . . 133
  4.4.4 Comparison with numerics . . . 134
4.5 Conclusions . . . 135
Appendix . . . 137
4.A Validation of the base flow . . . 137
4.B PDP data example . . . 137
4.C First-order perturbation equations in cylindrical coordinates . . . 138
Acknowledgements . . . 139
References . . . 139

5 Extracting scaling laws from numerical dynamo models 143

Summary . . . 143
5.1 Introduction . . . 144
5.2 Dynamo dataset . . . 145
  5.2.1 Numerical dynamo simulations . . . 145
  5.2.2 Scaling laws and model setup . . . 147

5.2.3 Errors in the dependent variable 148
5.2.4 Parameter range 148
5.2.5 Dynamical regime 149
5.3 Cross-validation 151
5.3.1 Model selection 151
5.3.2 Leave-one-out cross-validation 152
5.3.3 Example: Curve fitting 153
5.4 Diffusivity-free scalings 154
5.4.1 Heat transport 155
5.4.2 Flow velocity 158
5.4.3 Magnetic field strength 160
5.4.4 Discussion 160
5.5 Scaling with traditional parameters 161
5.6 Magnetic dissipation in Earth's core 162
5.6.1 Magnetic dissipation time 162
5.6.2 LOOCV analysis for τ_{diss} 163
5.6.3 Application to Earth's core 165
5.6.4 Implications 166
5.7 Conclusions 167
Acknowledgements 168
Appendix 168
5.A Equal errors in the original variable 169
5.B Reduced dataset: Earth-like dynamo models 169
Recent developments 170
References 172

6 Conclusions and perspectives **175**
6.1 ZUCCHINI 175
6.2 Perspectives for future experiments 176
6.3 Scaling laws from numerical dynamos 177
References 178

List of Figures

1.1 Sketch of the ZUCCHINI experiment. 10
1.2 Portrait of Julius Hartmann, taken from Moreau and Molokov [2007]. . . . 12
1.3 Original sketch of the cylindrical annulus of Baylis and Hunt [1971]. . . . 13
1.4 Bottom plate of MATUR taken from Messadek and Moreau [2002]. 18
1.5 Original sketch of the experiment for the study of the instability in the Hartmann layer by Moresco and Alboussiere [2004]. 21
1.6 Original plot of friction factor F vs. $R = Re/M$ from Moresco and Alboussiere [2004]. 21

2.1 Vertical cross-section of the ZUCCHINI container. 30
2.2 Top view of the container with orientation of UDV probes 1 (radial) and 2 (chordwise). 31
2.3 Components of the ZUCCHINI tank. 32
2.4 Sketch and photo of ZUCCHINI in the Caylar magnetic coil setup. 34
2.5 Rotatable lever for magnetic measurements in the Caylar setup. 35
2.6 PVC cuboid with three mutually perpendicular Hall probes glued onto it. 36
2.7 Measurements of the three components B_z, B_r and B_ϕ of the magnetic field at different positions in the Caylar setup as well the angle of deviation of the field from the axial direction. 37
2.8 Impressions of transferring ZUCCHINI to the Cryo configuration. 38
2.9 Line measurements of B_z (a-b) and B_r (c) in the single-coil cryomagnetic setup. 39
2.10 Map of magnetic field strength of a single loop approximating the field of the ‘Cryo’ setup at 1 T. 40
2.11 Photo of the copper busbars distributing the forcing current from the power supplies to the cables (not mounted). 41
2.12 Effects of non-axisymmetric current distribution on radial velocity measurements. 42
2.13 Photo of the argon overpressure system to prevent the GaInSn from oxidation. 44
2.14 Photos of the filter system to remove sludge from the GaInSn. 44
2.15 Scheme of the pneumatic board controlling the argon overpressure system used for filling and emptying the ZUCCHINI tank. 46
2.16 Ultrasonic Doppler velocimetry probes. 47
2.17 Potential difference probes. 49
2.18 Finite element mesh used for our 2D axisymmetric parameter study. . . . 51

3.1 Sketch of the modified cylindrical annulus ZUCCHINI. 60

3.2 Nondimensional velocity $\mathbf{u}$ in the numerical simulation at $Re_i = 10$ and varying M. 65

3.3 Nondimensional electrical current density in the numerical simulation at $M = 200$, $Re_i = 10$. 66

3.4 Nondimensional azimuthal rms velocity $u_{\phi,rms}$ as function of the Hartmann number M. 66

3.5 Dimensional azimuthal velocity $u^*_{\phi,rms}$ as function of the forcing current I. 67

3.6 Nondimensional radial velocities u_r and axial velocities u_z normalized by the input Reynolds number Re_i as function of the Hartmann number M. . 69

3.7 Scaling of the Hartmann and Shercliff layers in the numerical models. . . . 71

3.8 Top view of tank with orientation of UDV probes 1 (radial) and 2 (chordwise). 76

3.9 UDV data example of steady flow recorded at $B = 875$ mT, $I = 7$ A ($M = 1770$, $Re = 9570$). 78

3.10 Profiles of $\overline{u_\phi}(r)$ measured at 1 A and varying B (M). 80

3.11 Normalized jet amplitude A_{jet} observed in steady flow for $M \gtrsim 250$. . . . 81

3.12 Radial mean of (temporal) mean azimuthal velocity $\langle\overline{u_\phi}\rangle$ depending on forcing current and magnetic field strength. 81

3.13 Profiles of mean radial velocity $\overline{u_r}(r)$ at $M = 253$ and 2022. 82

3.14 Radial rms values $\langle\cdot\rangle_{rms}$ of the mean radial velocity $\overline{u_r}(r)$ versus the forcing current. 82

3.15 Profiles of mean axial velocity $\overline{u_z}(z)$ for stable flow at $M = 35$ and 169 (a), as well as 2022 (b). 84

3.16 Axial rms values $\langle\cdot\rangle_{rms}$ of the mean axial velocity $\overline{u_z}(z)$ versus the forcing current. 85

3.17 Comparison of azimuthal velocity profiles $\overline{u_\phi}(r)$ at 1 A in experiment, numerics and large-M theory. 85

3.18 Nondimensional azimuthal velocity normalized by M from numerical simulations with a more realistic magnetic field of a single current loop at a forcing current of 1 A. 86

3.19 Convergence of global and local quantities. 90

3.20 Components of ZUCCHINI. 93

3.21 Characterization of magnetic field in 'Caylar' setup. 94

3.22 Map of magnetic field strength of a single loop approximating the field of the 'Cryo' setup at 1 T. 95

4.1 Sketch of the modified cylindrical annulus ZUCCHINI. 100

4.2 Temporal evolution of kinetic energies of perturbation $E'_{kin,i}$ where $i \in \{r, \phi, z\}$. 106

4.3 Growth rates σ versus azimuthal wave number m for ($M = 100, Re_i = 30$ and 50) as well as ($M = 20, Re_i = 500$). 107

4.4 Frequencies of the oscillations of the azimuthal velocity u'_ϕ in the linear stability study. 108

4.5 Diagrams of linear stability in terms of (a) nondimensional parameters M and Re_i and (b) dimensional quantities B and I. 110

4.6 Curves of neutral stability ($\sigma = 0$) for different azimuthal wave numbers m in dimensional parameter space (B, I). 111

4.7 Temporal evolution of the perturbation velocities u'_i with $i \in \{r, \phi, z\}$ over one period for the slightly supercritical case ($M = 20, Re_i = 200, m = 4$). . 112
4.8 Shear rate γ of the axisymmetric base flow for the slightly supercritical case ($M = 20, Re_i = 200, m = 4$). 113
4.9 Top view of tank with orientation of UDV probes 1 (radial) and 2 (chordwise) in red and the location of the PDP A and B in yellow. 114
4.10 UDV example data: u_r measured at 875 mT and 150 A ($M = 1769$, $Re = 1.10 \cdot 10^5$). 116
4.11 Mean azimuthal velocity profiles $\overline{u_\phi}(r)$ at different magnetic fields. 118
4.12 Radial mean of (temporal) mean azimuthal velocity $\langle\overline{u_\phi}\rangle$ vs. (a) the current I and (b) the forcing IB. 119
4.13 Free Shercliff layer thickness δ_S versus (a) Re/M and (b) $Re/M^{1.2}$. 121
4.14 Mean radial velocity profiles $\overline{u_r}(r)$ at different magnetic fields. 122
4.15 Mean axial velocity profiles $\overline{u_z}(z)$ at different magnetic fields. 123
4.16 Rms values along the UDV profiles of (a) mean radial, (b) axial velocity and (c) their ratio. 124
4.17 Mean of PDP measurements corresponding to azimuthal velocities. 125
4.18 UDV measurements of u_r at 875 mT ($M = 1769$). 127
4.19 Frequencies f_1 (filled) and f_2 (open) of significant spectral peaks from UDV measurements of u_r (black squares) and PDP recordings of 'Aazi1' (red diamonds). 128
4.20 Amplitudes A_1 and A_2 of the dominant spectral peaks in UDV recordings of u_r compared with the renormalized standard deviation $\sqrt{2}\sigma_{u_r}$ of the signal. 129
4.21 Threshold of the first instability as observed experimentally in UDV measurements of u_r. 130
4.22 Plot of dominant frequencies f_1 (filled) and f_2 (open) in u_r versus the mean value of mean azimuthal velocity $\langle\overline{u_\phi}\rangle$. 131
4.23 Friction factor F (Eq. 4.16) versus $R = Re/M$ which is the Reynolds number based on the Hartmann layer thickness. 132
4.24 Stability diagram of the ZUCCHINI flow. 133
4.25 PDP example data. 138

5.1 Histograms of the values of the non-dimensional parameters in the 116 simulations used in the scaling law analysis. 150
5.2 Plot of Nu vs. Ra for all 185 dynamo models of the database. 150
5.3 Earth-likeness of the 116 dynamo models used in this study according to the criteria of Christensen et al. [2010]. 151
5.4 Curve fitting, synthetic example. 154
5.5 Heat transport scaling, preferred scaling law by LOOCV. 157
5.6 Flow velocity, favoured scaling law. 158
5.7 Flow velocity scaling only with Ra_Q^* (not preferred by LOOCV). 159
5.8 Residuals between *Ro*-data and model predictions from fig. 5.7 plotted vs. Pm. 159
5.9 Magnetic field strength, favoured scaling law. 161
5.10 Magnetic dissipation time. Favoured scaling law. 164
5.11 Magnetic dissipation time. Simple *Rm*-law with unresolved further dependencies. 164

List of Tables

1.1 Parameter values of experimental studies. 16
1.2 Key timescales (in s) in the MATUR experiment of Messadek and Moreau [2002]. 19

2.1 Physical properties of GaInSn from Morley et al. [2008]. 45
2.2 Operation sequence of the pneumatic system for filling, emptying and flushing the ZUCCHINI tank with argon. 45

3.1 Parameter values of experimental studies. 61
3.2 Scaling of nondimensional velocities in the limit of large M. 70
3.3 Overview of the measurements taken in the two setups ‘Caylar’ and ‘Cryo’. 73
3.4 Physical properties of GaInSn from Morley et al. [2008]. 73
3.5 Comparison of the mean azimuthal velocity $\overline{u_\phi}$ with the rms azimuthal velocity $u_{\phi,rms}$ for the most extreme models in our data set. 91

4.1 Physical properties of GaInSn from Morley et al. [2008] who provide data for various composition ratios. 113
4.2 Overview of the measurements taken in the two setups ‘Caylar’ and ‘Cryo’.113
4.3 Comparison of kinetic energies in simulations of the base flow from the dedicated parameter study (superscript ^{o}, cf. Paper 1) with the ones from this study which have less degrees of freedom. 137

5.1 Non-dimensional parameters, their estimated values for Earth’s core, following Olson [2007] and values in the models studied here. 146
5.2 Curve fitting, synthetic example. True polynomial coefficients β_{true} used in the synthetic example, and their multiple linear regression estimates $\hat{\beta}$. 154
5.3 Curve fitting, synthetic example. Values of mean quadratic misfit χ^2 and LOOCV estimate of prediction error P_{CV} for polynomials of degrees m from 0 to 8 and 48 to 50. 155
5.4 Cross-validation estimates of prediction error P_{CV} for the best-fitting scaling laws for heat transport, flow velocity and magnetic field strength for all possible parameter combinations. 156
5.5 Overview of the scaling laws preferred by LOOCV for the diffusivity-free parameters. 158
5.6 Overview of the scaling laws preferred by LOOCV for the traditional parameters. 162
5.7 Overview of the scaling laws preferred by LOOCV assuming equal errors in y. 169

5.8 Earth-like dynamo models: Overview of the scaling laws preferred by LOOCV for the diffusivity-free parameters assuming equal errors in $\zeta = \log(y)$. 169

Chapter 1

Introduction

1.1 Motivation

The scope of this dissertation is the interaction between electrically conducting fluids and magnetic fields. This area of research is called magnetohydrodynamics (MHD). Interest in different flavours of MHD arises from diverse topics ranging from geo- and astrophysics to engineering applications.

A topic which is in various ways central to the Earth and mankind is the geodynamo. The geomagnetic field is generated by a feedback process between induction processes and the motions of liquid iron in the Earth's outer core. For a recent overview, see Olson [2007]. Not only does the magnetic field facilitate navigation, but it also acts as an effective shield against high-energy particles from the solar wind, and it supplies heat at the core-mantle boundary partially constraining mantle convection. In the field of astrophysics, MHD effects profoundly influence the dynamics, e.g. by possibly making an accretion disk turbulent via the magnetorotational instability [Velikhov, 1959, Balbus and Hawley, 1991].

In engineering applications and laboratory settings, the interaction between fluid motion and magnetic field often reduces to a one-way effect of the magnetic field on the flow when the induced magnetic field is negligible compared with the imposed one. This regime is called quasi-static. It governs the applications in nonintrusive electromagnetic control in metallurgy and material processing, liquid metal blankets of fusion reactors as well as electromagnetic flow meters and pumps. Recent reviews of MHD in materials processing, flow control and fusion blankets are given by Davidson [1999], Weier et al. [2007] and Bühler [2007].

This dissertation treats two topics from the above-mentioned areas, one coming from the field of numerical geodynamo modeling, the other from the area of liquid metal MHD flow in the laboratory. Our experimental and numerical work on liquid metal flow in ZUCCHINI (ZUrich Cylindrical CHannel INstability Investigation) was first motivated by the proposed experimental study of electrically-driven liquid sodium flow in a rapidly-rotating spherical shell [Hollerbach et al., 2013] which is currently under construction in our laboratory under the acronym SpiNaCH (Spinning Natrium in the Confoederatio Helvetica). SpiNaCH will be used to study the magnetostrophic regime, i.e. a dominant balance between the Lorentz force on moving electrically charged particles and the Coriolis force due to global rotation, which is believed to be relevant in Earth's core. ZUCCHINI serves as a prelude and point of comparison for SpiNaCH. For instance it helped us to gain experience in liquid metal treatment, current injection and flow diagnostics which had not been used before in our laboratory. In contrast to the future experiment, the ZUCCHINI setup is a non-rotating modified cylindrical annulus filled with the liquid metal alloy GaInSn. In both cases, the flow is driven by the Lorentz force generated through an applied electrical current under an imposed magnetic field. Besides the characterization of the base flow in this device (Chapter 3), our main focus lies on the instabilities of the flow (Chapter 4). In this respect, ZUCCHINI joins a series of laboratory experiments on the fundamental properties of liquid metal MHD flow in ducts and channels addressing topics like instability criteria and mechanisms (cf. Section 1.3). A very recent review on experimental and numerical activities in this area is Zikanov et al. [2014]. The design, assembly and operation of the ZUCCHINI experiment as well as the processing and interpretation of the data, which was complemented by a numerical study, has been my main occupation during the PhD time.

The second topic of this dissertation (Chapter 5) comes from geophysics as well. Numerical simulations of the geodynamo produce an important contribution to our knowledge about the dynamics of the Earth's core, see e.g. the recent review by Christensen and Wicht [2007]. Through the numerical solution of the governing equations of an incompressible, electrically conducting fluid flow driven by convection in a spherical shell (cf. Eqs. 5.1-5.5), several features of the observed geomagnetic field can be reproduced. This agreement gives rise to the hypothesis that we can apply the numerical results to the core. However, there is a major discrepancy between the numerical models and the Earth's core in terms of the parameter regime. This gap can not be bridged easily due to the enormous computational power required to resolve all relevant time and length scales. A way to overcome this problem lies in scaling laws which can be used to extrapolate quantities calculated in the numerical simulations to the parameter regime of the core. In order to be geophysically applicable, the numerical models have to live in the same dynamical regime as Earth's core, and scaling laws have to include the relevant parameters. The latter results in a problem of model selection which we tackle with a statistical technique termed *leave-one-out cross-validation.* With our work, we contribute to the extraction of appropriate scaling laws from numerical dynamo models, especially the role of diffusivities for the flow velocity and magnetic field scalings, and their applicability to Earth's core.

1.2 Navier, Stokes and Maxwell in a nutshell

The subject of MHD is concerned with the interaction of electrically conducting fluids and electromagnetic fields. Hence MHD relies on the fundamental equations of both fluid dynamics and electromagnetism. We will introduce these equations separately starting from the conservation of mass and momentum for hydrodynamic flow and specifying the mutual interactions of flow and electromagnetic field afterwards. Depending on the system of interest, different assumptions are appropriate, leading to different systems of governing equations for the geodynamo and standard liquid metal MHD. In our derivation, we follow the concise introductions of Vantieghem [2011] and Davidson [2001].

1.2.1 Fundamentals of fluid dynamics

Since we are interested in macroscopic phenomena in this work, we will employ the continuum hypothesis, meaning that the flow can be modeled by continuous functions of the spatial coordinates $\mathbf{x}$ and time t, like the mass density $\rho(\mathbf{x}, t)$ and the velocity $\mathbf{u}(\mathbf{x}, t)$.

For an arbitrary fluid parcel with volume Ω moving through space and time, mass conservation is fulfilled when

$$\frac{\mathrm{d}}{\mathrm{d}t}\int_\Omega \rho(\mathbf{x}, t)\,\mathrm{d}V = \int_\Omega \left(\frac{\mathrm{d}}{\mathrm{d}t}\rho(\mathbf{x}, t) + \rho\nabla\cdot\mathbf{u}\right)\mathrm{d}V = 0. \tag{1.1}$$

The second term takes explicitly into account that the fluid parcel may change its shape or size over time. The total time derivative is decomposed using the chain rule

$$\frac{\mathrm{d}}{\mathrm{d}t}\rho(\mathrm{x}, t) = \frac{\partial\rho}{\partial t} + \mathbf{u}\cdot\nabla\rho. \tag{1.2}$$

Since the equation above has to hold for any volume Ω, the integral formulation can be transformed into a local constraint as

$$\frac{\partial\rho}{\partial t} + \nabla\cdot(\rho\mathbf{u}) = 0. \tag{1.3}$$

The equation of mass conservation is also called the continuity equation. It can be further simplified when considering incompressible fluids, $\partial\rho/\partial t = 0$, leading to

$$\nabla\cdot\mathbf{u} = 0, \qquad \text{the incompressible continuity equation.} \tag{1.4}$$

The incompressible continuity equation holds when flow velocities are small compared to the sound speed in the medium which is always the case in this work.

The second conserved quantity is momentum as expressed by Newton's second law,

$$\frac{\mathrm{d}}{\mathrm{d}t}\int_{\Omega}\rho\mathbf{u}\,\mathrm{d}V = \mathbf{F}. \tag{1.5}$$

The net force $\mathbf{F}$ on the fluid parcel can be written as a volume integral of a body force density $\mathbf{f}_b$ (like gravity, buoyancy or electromagnetic forces) and a surface force density $\mathbf{f}_s$ (like friction), which in turn can be expressed by a surface integral of the stress tensor $\boldsymbol{\tau}$,

$$\mathbf{F} = \int_{\Omega}(\mathbf{f}_b + \mathbf{f}_s)\,\mathrm{d}V = \int_{\Omega}\mathbf{f}_b\,\mathrm{d}V + \oint_{\partial\Omega}\boldsymbol{\tau}\cdot\mathrm{d}\mathbf{S}. \tag{1.6}$$

Reformulation of the total time derivative in Newton's second law (Eq. 1.5) and using Gauss' divergence theorem on the surface integral (Eq. 1.6), yields

$$\rho\left(\frac{\partial\mathbf{u}}{\partial t} + \mathbf{u}\cdot\nabla\mathbf{u}\right) = \nabla\cdot\boldsymbol{\tau} + \mathbf{f}_b. \tag{1.7}$$

Angular momentum conservation requires that the stress tensor $\boldsymbol{\tau}$ is symmetric. Throughout this work, we assume Newtonian fluids meaning that the stress tensor is an isotropic and linear function of the velocity gradient tensor (also called the strain tensor). For an incompressible Newtonian fluid, it can be shown that the proportionality constant is given by the dynamic viscosity μ as

$$\boldsymbol{\tau} = -p\mathbf{1} + \mu\left(\nabla\mathbf{u} + (\nabla\mathbf{u})^T\right), \tag{1.8}$$

where p is the pressure and $\mathbf{1}$ the unit tensor. Using the kinematic viscosity $\nu = \mu/\rho$, we rewrite the momentum equation as

$$\rho\left(\frac{\partial\mathbf{u}}{\partial t} + \mathbf{u}\cdot\nabla\mathbf{u}\right) = -\nabla p + \rho\nu\nabla^2\mathbf{u} + \mathbf{f}_b, \qquad \text{the Navier-Stokes equation.} \tag{1.9}$$

Together with the continuity equation (Eq. 1.4), it governs incompressible flow. Besides the body forces $\mathbf{f}_b$ which we will specify later, the system of equations requires boundary and initial conditions. Throughout this work, we adopt no-slip mechanical boundary conditions, $\mathbf{u} = \mathbf{0}$ at all boundaries.

1.2.2 Fundamentals of electromagnetism

An important pillar of classical electromagnetism are Maxwell's equation which allow to determine electric and magnetic fields, $\mathbf{E}$ and $\mathbf{B}$, from distributions of electric charge and current densities, ρ_e and $\mathbf{j}$ respectively. For fluids which are neither dielectric nor diamagnetic, Maxwell's equation read

$$\nabla \cdot \mathbf{E} = \frac{\rho_e}{\epsilon_0}, \qquad \text{Gauss' law,} \tag{1.10}$$

$$\nabla \cdot \mathbf{B} = 0, \qquad \text{Solenoidal nature of } \mathbf{B}, \tag{1.11}$$

$$\nabla \times \mathbf{E} = -\frac{\partial \mathbf{B}}{\partial t}, \qquad \text{Faraday's law,} \tag{1.12}$$

$$\nabla \times \mathbf{B} = \mu_0 \left(\mathbf{j} + \epsilon_0 \frac{\partial \mathbf{E}}{\partial t} \right), \qquad \text{Ampère-Maxwell equation.} \tag{1.13}$$

where ϵ_0 and μ_0 are the permittivity and the permeability of free space respectively. Maxwell's equations imply charge conservation

$$\frac{\partial \rho_e}{\partial t} + \nabla \cdot \mathbf{j} = 0. \tag{1.14}$$

Similar to the case of mass conservation, this law can be simplified when quasi-neutrality assumption yielding

$$\nabla \cdot \mathbf{j} = 0, \qquad \text{charge conservation.} \tag{1.15}$$

The underlying assumption that the charge relaxation time is much shorter than the flow phenomena we are interested in, is always fulfilled in this work. A similar reasoning leads to the reduction of the Ampère-Maxwell law to its pre-Maxwell form

$$\nabla \times \mathbf{B} = \mu_0 \mathbf{j}, \qquad \text{Ampère's law.} \tag{1.16}$$

In order to close the system of Maxwell's equations, we need an expression for the current density. For moving isotropic conductors, this is given by

$$\mathbf{j} = \sigma_e (\mathbf{E} + \mathbf{u} \times \mathbf{B}), \qquad \text{Ohm's law,} \tag{1.17}$$

with the electrical conductivity σ_e. Ohm's law embodies the effect of the flow $\mathbf{u}$ on the electromagnetic variables. The last ingredient required before we can move on to MHD, is a description of the effect of electromagnetic fields on the flow. This is provided by the Lorentz force density on a charged continua,

$$\mathbf{f}_L = \rho_e \mathbf{E} + \mathbf{j} \times \mathbf{B}. \tag{1.18}$$

Again applying the quasi-neutrality assumption leads to neglecting the electric term, and hence

$$\mathbf{f}_L = \mathbf{j} \times \mathbf{B} \tag{1.19}$$

will be the expression of the Lorentz force for use as a body force in the Navier-Stokes equation.

1.2.3 The governing equations of magnetohydrodynamics

We are now at a stage where we can derive an equation relating the magnetic field **B** to the flow velocity **u**. Substituting Ohm's law (Eq. 1.17) into Faraday's law (Eq. 1.12) eliminates the induced electric field,

$$\frac{\partial \mathbf{B}}{\partial t} = \nabla \times (\mathbf{u} \times \mathbf{B}) - \nabla \times \frac{\mathbf{j}}{\sigma_e}. \tag{1.20}$$

Further inserting Ampère's law in its pre-Maxwell form (Eq. 1.16), eliminates the current density,

$$\frac{\partial \mathbf{B}}{\partial t} = \nabla \times (\mathbf{u} \times \mathbf{B}) - \frac{1}{\mu_0 \sigma_e} \nabla \times (\nabla \times \mathbf{B}), \tag{1.21}$$

which is valid for uniform σ_e. Applying an identity of vector calculus as well as the solenoidal nature of the magnetic field yields

$$\frac{\partial \mathbf{B}}{\partial t} = \nabla \times (\mathbf{u} \times \mathbf{B}) + \eta \nabla^2 \mathbf{B}, \qquad \text{the induction equation,} \tag{1.22}$$

where $\eta = (\mu_0 \sigma_e)^{-1}$ is the magnetic diffusivity. Together with the Navier-Stokes equation (Eq. 1.9), the continuity equation (Eq. 1.4) and the solenoidal nature of the magnetic field (Eq. 1.11), it constitutes the complete description of MHD flow. We state the complete system of governing equations,

$$\rho \left(\frac{\partial \mathbf{u}}{\partial t} + \mathbf{u} \cdot \nabla \mathbf{u} \right) = -\nabla p + \rho \nu \nabla^2 \mathbf{u} + \mathbf{j} \times \mathbf{B} + \mathbf{f} \tag{1.23}$$

$$\nabla \cdot \mathbf{u} = 0 \tag{1.24}$$

$$\frac{\partial \mathbf{B}}{\partial t} = \nabla \times (\mathbf{u} \times \mathbf{B}) + \eta \nabla^2 \mathbf{B} \tag{1.25}$$

$$\nabla \cdot \mathbf{B} = 0. \tag{1.26}$$

This system of governing equations can be written in nondimensional form by choosing scales L_0 for length, U_0 for velocity and B_0 for the magnetic field. With the substitutions $\mathbf{u} \to U_0\, \mathbf{u}$, $\mathbf{B} \to B_0\, \mathbf{B}$, $\nabla \to L_0^{-1}\, \nabla$, $t \to L_0 U_0^{-1}\, t$, $\mathbf{j} \to \sigma_e U_0 B_0\, \mathbf{j}$, $p \to \rho U_0^2\, p$, we obtain

$$\frac{Re}{M^2} \left(\frac{\partial \mathbf{u}}{\partial t} + \mathbf{u} \cdot \nabla \mathbf{u} \right) = -\nabla p + \frac{1}{M^2} \nabla^2 \mathbf{u} + \mathbf{j} \times \mathbf{B} + \mathbf{f} \tag{1.27}$$

$$\nabla \cdot \mathbf{u} = 0 \tag{1.28}$$

$$\frac{\partial \mathbf{B}}{\partial t} = \nabla \times (\mathbf{u} \times \mathbf{B}) + \frac{1}{Rm} \nabla^2 \mathbf{B} \tag{1.29}$$

$$\nabla \cdot \mathbf{B} = 0 \tag{1.30}$$

where **f** is kept as a variable to introduce further body force densities like buoyancy in the next section.

As the three control parameters, we have introduced

$$Re = \frac{U_0 a}{\nu}, \qquad \text{the (hydrodynamic) Reynolds number,} \tag{1.31}$$

$$Rm = \frac{U_0 a}{\eta}, \qquad \text{the magnetic Reynolds number,} \tag{1.32}$$

$$M = aB_0\sqrt{\frac{\sigma_e}{\rho\nu}}, \qquad \text{the Hartmann number.} \tag{1.33}$$

Alternatively, it is possible to use

$$N = \frac{\sigma_e B_0^2 L_0}{\rho U_0} = \frac{M^2}{Re}, \qquad \text{the interaction parameter,} \tag{1.34}$$

also called the Stuart number, instead of either Re or M. The control parameters can physically be interpreted as ratios of different terms in the Navier-Stokes equation. The Reynolds number Re gives the ratio of the advective (inertial) to the viscous term. At low Re, the flow is laminar, and small-scale fluctuations are damped by the action of the viscous term. At large Re, small-scale fluctuations can grow due to the action of the nonlinear advective term. In the purely hydrodynamic case, this almost inevitably leads to turbulence, a state which is characterized by the presence of a large range of spatial and temporal scales. Note that the presence of a strong magnetic field or rotation can relaminarize the flow even at high Re.

In a similar way, the magnetic Reynolds number Rm gives the ratio of the advective and diffusive terms in the induction equation. In fact the value of Rm determines largely the relevant processes and features of a given MHD flow. We postpone a closer inspection of the large-Rm and the low-Rm regimes to the following Sections 1.2.4 and 1.2.5. The square of the Hartmann number M^2 gives the ratio of Lorentz to viscous forces. The interaction parameter N is a measure of the strength of the Lorentz force versus inertia.

1.2.4 Dynamics at large Rm: the geodynamo

For large Rm which are characteristic for geo- and astrophysical objects, e.g. Earth's outer core with $Rm = \mathcal{O}(10^4)$, the right-hand side of the induction equation (Eq. 1.29) is dominated by the advective first term. The magnetic field can be regarded as 'frozen into' the fluid and advected with the flow. Given an appropriate driving mechanism for the flow, this can lead to self-sustained magnetic fields. This so-called dynamo process is supposed to be responsible for the Earth's magnetic field. In the numerical dynamo models of Chapter 5, we are concerned with the large-Rm regime.

In our standard model, the material in the outer core consists of roughly 90% liquid iron, 5% nickel and debatable amounts of light elements such as silicon, oxygen, sulphur, carbon or phosphor [McDonough, 2004]. The driving mechanism for the flow is mostly assumed to be thermal and compositional convection. Thermal convection is supposed to be driven by the rising of hotter and hence less dense material from the inner-core boundary (ICB) and the cooling at the core-mantle boundary (CMB). In the case of compositional convection, dense material crystallizes at the ICB in the process of cooling, and the remaining lighter part is again subject to a buoyancy force. Apart from buoyancy, the energy for the dynamo could also be provided by tidal forcing.

The numerical dynamo models of Christensen and co-workers studied in Chapter 5 employ thermal convection as the driving mechanism. Hence the governing MHD Equations 1.27-1.30 are amended with a buoyancy force density $\mathbf{f}_T = -\rho\alpha T\mathbf{g}$ where α is the coefficient of thermal expansion, T the temperature and $\mathbf{g} = -g_o\mathbf{r}$ gravitational acceleration. For the dynamics, also the global rotation of the system is of paramount importance. Transforming the governing equations to the rotating frame essentially adds a Coriolis force term $\mathbf{f}_C = 2\rho(\boldsymbol{\Omega}\times\mathbf{u})$ to the left-hand side of the Navier-Stokes equation. Furthermore the four governing equations of MHD have to be completed by an expression for the evolution of the temperature which is

$$\frac{\partial T}{\partial t} + (\mathbf{u}\cdot\nabla)T = \kappa\nabla^2 T \tag{1.35}$$

assuming no volumic heating with the thermal diffusivity $\kappa = k(\rho c_p)^{-1}$, k thermal conductivity and c_p specific heat capacity. The whole system of equations is given in Equations 5.1 - 5.5.

For the nondimensionalization of the resulting system of five equations governing rotating MHD convection, four control parameters are needed according to the Buckingham-Π theorem. Using as scales the thickness D of the outer core, the temperature difference ΔT between ICB and CMB and the inverse rotation rate Ω^{-1}, leads to

$$Ek = \frac{\nu}{\Omega D}, \qquad \text{the Ekman number,} \tag{1.36}$$

$$Ra = \frac{\alpha g_o \Delta T D^3}{\nu\kappa}, \qquad \text{the Rayleigh number,} \tag{1.37}$$

$$Pr = \frac{\nu}{\kappa}, \qquad \text{the Prandtl number,} \tag{1.38}$$

$$Pm = \frac{\nu}{\eta}, \qquad \text{the magnetic Prandtl number,} \tag{1.39}$$

as used in Chapter 5. Another often used parameter is

$$\Lambda = \frac{\sigma_e B_0^2}{\rho\Omega}, \qquad \text{the Elsasser number,} \tag{1.40}$$

which describes the relative balance of Lorentz to Coriolis forces, and is assumed to be of order unity for the Earth. This regime of $\Lambda = \mathcal{O}(1)$ is called the 'magnetostrophic regime'. The Ekman number Ek gives the ratio of viscous to Coriolis forces. The Rayleigh number compares buoyancy and viscous effects (times Pr). The two Prandtl numbers are material properties, Pr being the ratio of momentum to thermal diffusivity, and Pm being momentum over magnetic diffusivity. As detailed in Table 5.1, present numerical dynamo models are far from the Earth's core in terms of having too slow rotation (Ek too large), being less turbulent (Ra too small) and excessively viscous relative to their electrical conductivity (Pm too large). This will be the starting point for our study of scaling laws relating core properties to numerical dynamo models in Chapter 5.

1.2.5 Dynamics at low Rm: liquid metal MHD applications

On the other end of the parameter range of the magnetic Reynolds number is the regime of low Rm. For $Rm \ll 1$, magnetic field diffusion dominates over advection in the induction equation. In this case, magnetic fields $\mathbf{b}$ induced by the flow are negligible compared to imposed fields $\mathbf{B}$. It can be shown that $\mathcal{O}(\mathbf{b})/\mathcal{O}(\mathbf{B}) = Rm$. Hence this regime is called the quasi-static limit. The interaction between magnetic field and flow reduces to a one-way flow control by the magnetic field. This is the regime of most liquid metal MHD engineering applications and laboratory experiments. With our liquid metal experiment in Chapters 3 and 4, we work in this low-Rm limit.

In the quasi-static limit, it is advantageous to write the system of MHD equations as

$$\rho\left(\frac{\partial \mathbf{u}}{\partial t} + \mathbf{u}\cdot\nabla\mathbf{u}\right) = -\nabla p + \rho\nu\nabla^2\mathbf{u} + \mathbf{j}\times\mathbf{B} \tag{1.41}$$

$$\nabla\cdot\mathbf{u} = 0 \tag{1.42}$$

$$\mathbf{j} = \sigma_e\left(\mathbf{E} + \mathbf{u}\times\mathbf{B}\right) \tag{1.43}$$

$$\nabla\cdot\mathbf{j} = 0, \tag{1.44}$$

with Ohm's law instead of the induction equation. A step-by-step derivation proving the equivalence with Equations 1.27-1.30 for low Rm is given in Vantieghem [2011].

Writing the electric field as the gradient of a potential $\mathbf{E} = -\nabla\Phi$ and making use of charge conservation, the electric field $\mathbf{E}$ as well as the current density $\mathbf{j}$ are eliminated from the equations. In nondimensional form, the system now reads

$$\begin{aligned}\frac{Re}{M^2}&\left(\frac{\partial \mathbf{u}}{\partial t} + \mathbf{u}\cdot\nabla\mathbf{u}\right)\\ &= -\nabla p + \frac{1}{M^2}\nabla^2\mathbf{u} + \left(-\nabla\Phi + \mathbf{u}\times\mathbf{B}\right)\times\mathbf{B}\end{aligned} \tag{1.45}$$

$$\nabla\cdot\mathbf{u} = 0 \tag{1.46}$$

$$\nabla^2\Phi = \nabla\cdot\left(\mathbf{u}\times\mathbf{B}\right). \tag{1.47}$$

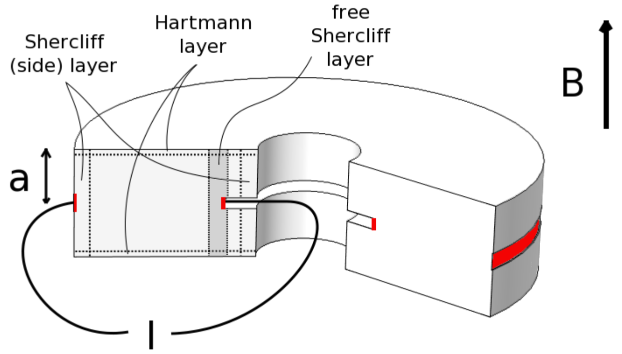

FIGURE 1.1: Sketch of the modified cylindrical annulus ZUCCHINI. Forcing an axisymmetric electrical current I through the liquid metal under an imposed magnetic field $\mathbf{B}$ gives rise to a Lorentz force which drives an azimuthal flow. The electrodes are coloured in red, the remaining walls are insulating. The half-height a is used as length scale.

In contrast to the full MHD Equations 1.27-1.30, we only require two control parameters in the quasi-static limit.

Before we continue with a digest of historical liquid metal MHD experiments, a word on the role of the imposed magnetic field seems in order. At large $M \gg 1$ (strong magnetic fields), the effect of the magnetic field is two-fold. Firstly it tends to smooth gradients of the quantities along its direction in the core of the flow, thus making the flow quasi-2D. Secondly so-called Hartmann layers of thickness $\delta_H \sim M^{-1}$ form at boundaries perpendicular to the magnetic field. They contain essentially the whole Joule dissipation (also called Ohmic dissipation) and damping of the quasi-2D flow. These will be essential features also observed in our own experimental study in Chapters 3 and 4.

1.3 Liquid metal MHD experiments

The flow in our ZUCCHINI experiment is driven by the Lorentz force generated by a forced radial current in an imposed axial field. A sketch is given in Figure 1.1. The setup will be detailed in later chapters.

In this section, we put our experiment in the historical context by giving an overview of previous liquid metal MHD experiments. Most, but not all, experiments operate in the quasi-static regime of small $Rm \ll 1$ where magnetic fields induced by the flow are negligible. Exceptions are mainly the dynamo experiments which require a large Rm in order to generate a self-sustained magnetic field, as well as their relatives intended for the study of geo- and astrophysical dynamics. In particular, the two first experiments showing a dynamo effect in Riga and Karlsruhe belong to this category [Gailitis et al., 2000, Stieglitz and Muller, 2001]. In these setups, a flow of molten sodium was forced on helical trajectories by the arrangement of tubes and baffles in order to create flows that had been shown theoretically to be dynamo-capable with the critical Rm_c for dynamo action being as low as 17.7 and 9 respectively [Gailitis et al., 2003, Rädler et al., 2002]. Other attempts and preliminary stages for laboratory dynamos are the Von-Karman-Sodium (VKS) experiment in Cadarache with Rm up to 90 [Monchaux et al., 2007], as well as the 3m-sodium sphere in Maryland [Zimmerman et al., 2011] and the liquid metal and plasma experiments in Madison [Spence et al., 2008]. The latter plasma dynamo is predicted to operate at $Rm = \mathcal{O}(10^3)$, and was studied in numerical simulations [Spence et al., 2009]. Another large-Rm experiment is the Perm torus filled with liquid sodium reaching $Rm = 30$. It was used to study turbulent viscosity and magnetic diffusivity [Noskov et al., 2012].

Conceptually the most similar to our SpiNaCH experiment under construction is the Grenoble experiment DTS (Derviche Tourneur Sodium) filled with liquid sodium. The inner sphere hosts a permanent magnet creating a dipolar field, and can co- or counter-rotate with the outer one leading to a spherical Couette flow. The DTS geometry and the possibility to operate partially in the magnetostrophic regime agree with SpiNaCH which, however, has an electrical driving of the flow like ZUCCHINI. Since it is relevant to the flow in ZUCCHINI, we mention here some findings from DTS. Nataf et al. [2008] studied the mean azimuthal flow in DTS, and found the transition between magnetostrophic flow near the inner sphere and geostrophic flow near the outer one to be controlled by the local Elsasser number. The flow exhibits a zone of high-velocity 'magnetic wind' near the inner sphere. Schmitt et al. [2008] studied the waves occurring in DTS. They observed several types of azimuthally traveling hydromagnetic waves that differ by their dispersion relation and selection of azimuthal wave numbers. The waves were identified as magneto-inertial waves due to the proximity of the magnetic and inertial characteristic time scales. The regime of magnetic Reynolds numbers Rm reached in DTS extends well above unity, and induced magnetic fields are clearly detected.

We now turn to the low-Rm regime in which our ZUCCHINI experiment operates, and describe the historical evolution of liquid metal MHD experiments in this area.

1.3.1 Advent of liquid metal MHD

There has been interest in the subject of electrically-driven liquid metal flows ever since the invention of the electromagnetic conduction pump by Julius Hartmann in Copenhagen around 1915 [Moreau and Molokov, 2007]. In 1937, Hartmann (portrait in Fig. 1.2) published two articles on 'Hg dynamics' studying the flow of mercury in pipes and ducts in the presence of a homogeneous transverse magnetic field. In the first one [Hartmann, 1937], he derived the governing equations and the velocity profile for laminar MHD channel flow. This includes the characteristic electromagnetic boundary layers, which are now called Hartmann layers, and the scaling of their width as $\delta_H \sim M^{-1}$. In the second article, Hartmann and Lazarus [1937] reported a variety of experimental measurements on

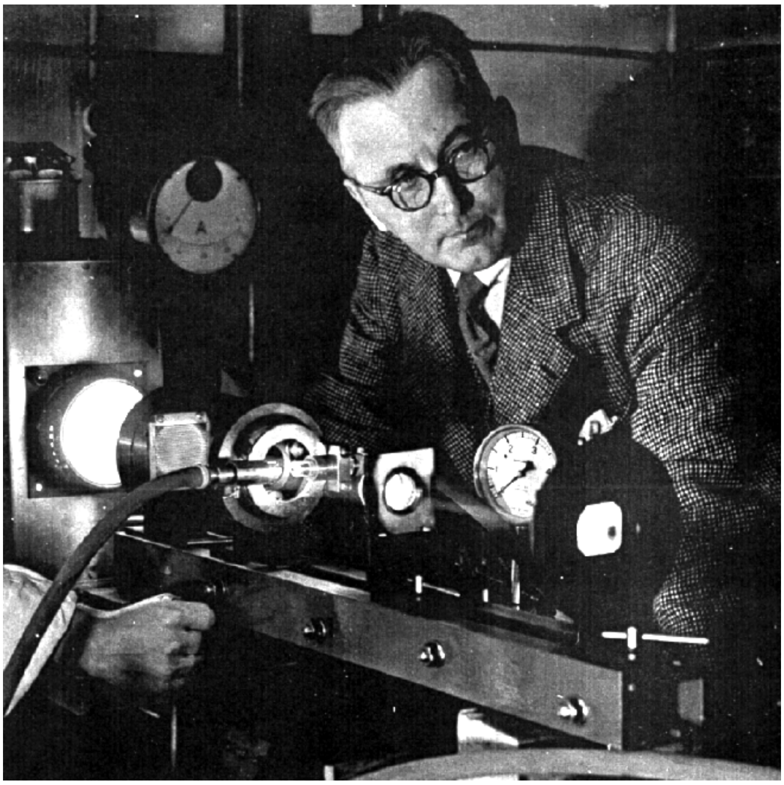

FIGURE 1.2: Portrait of Julius Hartmann, taken from Moreau and Molokov [2007].

flows of mercury in circular and rectangular ducts under the influence of a transverse magnetic field. These two papers are today considered as the starting point of liquid metal MHD.

1.3.2 Early studies of MHD flow in straight ducts

Since the times of Hartmann, a lot of studies considered the simple case of MHD flow in straight channels and ducts. Just to mention some of the original papers: Shercliff [1953] derived an exact solution for the equations governing steady incompressible flow in insulating rectangular ducts with transverse magnetic fields perpendicular to one side. He also found the scaling of the thickness of boundary layers parallel to the magnetic field, $\delta_S \sim M^{-1/2}$, which are now called Shercliff layers. The corresponding governing equations subject to various combinations of electrical boundary conditions were analyzed by among others, Hunt [1965], Hunt and Stewartson [1965] and Hunt and Williams [1968].

Hunt and Stewartson [1965] looked at the setup of walls perpendicular to the magnetic fields being electrically insulating and parallel walls conducting. They found expressions for the flow rate through the duct in the form of an expansion in descending powers of M in the limit of large M (so secondary flows can be neglected). In their boundary-layer technique, the flow is divided into different parts, namely the core flow and various boundary layer regions. The authors also studied the purely electrically-driven case of an MHD pump, which is exactly the driving mechanism in our ZUCCHINI experiment.

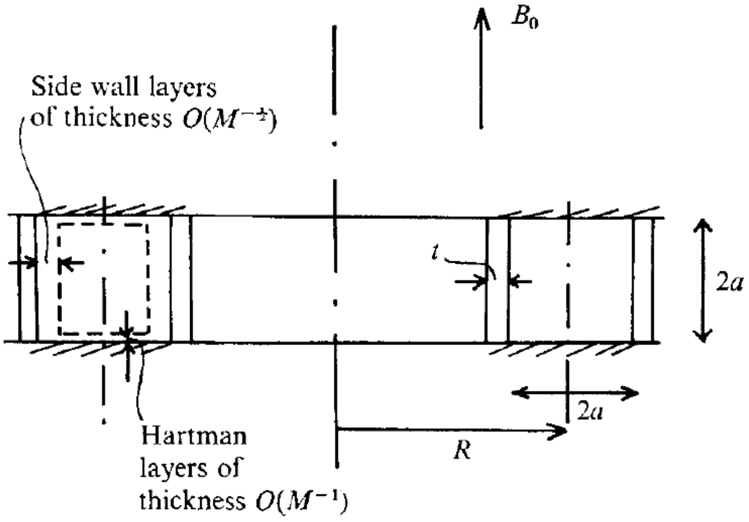

Figure 1.3: Original sketch of the cylindrical annulus of Baylis and Hunt [1971], 'showing the boundary layers which exist when $M \gg 1$'. Top and bottom walls were electrically insulating whereas side walls were conducting.

For experiments, flows in straight ducts pose the difficulty of avoiding the disturbances induced by the finite length of the duct (entrance effect). This problem is circumvented by the use of closed geometries like cylindrical ducts or spherical shells. In the following, we focus on electrically-driven MHD flow under an imposed magnetic field in cylindrical geometries. We report previous studies focussing on experiments that contribute to the understanding of the dynamics present in ZUCCHINI.

1.3.3 Theoretical results on flow in cylindrical ducts

In order to derive theories or even analytical solutions, a problem usually has to be simplified. In liquid metal MHD flow, it is usually assumed that the fluid is incompressible and has homogeneous electrical conductivity. Also the walls are supposed to have piecewise homogeneous conductivity. Moreover simple geometries are preferred. For the problem of electrically-driven MHD flow in a cylindrical duct, usually a rectangular annulus is considered which has conducting parallel walls and insulating perpendicular walls (cf. Fig. 1.3). Cylindrical coordinates (r, ϕ, z) are used. The flow is driven either by a pressure gradient or, as done in ZUCCHINI, by the Lorentz force resulting from the interaction of a radial electrical current with an axial magnetic field. The geometrical setup is different from ours in the sense that it does not give rise to a free Shercliff layer. However, it is the closest simple geometry and hence worth to take a look at.

Baylis and Hunt [1971] considered the flow in such a cylindrical annulus with rectangular cross section as sketched in Figure 1.3. Walls parallel to the magnetic field are electrically conducting, whereas perpendicular walls are insulating. Apart from the modified geometry, their study uses the same assumptions and techniques as Hunt and

Stewartson [1965] (cf. Section 1.3.2), particularly that M is large enough for secondary flow effects to be negligible. Hence Baylis and Hunt [1971] neglect radial and axial velocities. The condition for the inertial term to be actually negligible is

$$\frac{a^2}{R^2}\frac{Re^2}{M^4} \ll 1 \qquad \text{or} \qquad \left(\frac{K}{M^2}\right)^2 \lambda \ll 1. \tag{1.48}$$

The geometrical quantities a (half-height) and R (mean radius of the annular channel) are defined in Figure 1.3. $K = \lambda^{1/2} Re$ is termed the Dean number in honour of the seminal study of fluid motion in a curved channel by Dean [1928]. K measures curvature effects, $\lambda = a/R$ is the curvature ratio. For inertial effects to be negligible also in the side layers, a slightly stricter condition needs to be satisfied,

$$\left(\frac{K}{M^2}\right)^2 M^{1/2} \ll 1. \tag{1.49}$$

Under these conditions, Baylis and Hunt [1971] set up a balance between the Lorentz and the viscous force, and derive the azimuthal velocity in the core u_ϕ^c as

$$u_\phi^c(r) = \frac{I}{4\pi r\sqrt{\sigma_e \rho \nu}}. \tag{1.50}$$

The electrical current in the core vanishes, and is essentially contained in the Hartmann layers ($\delta_H \sim M^{-1}$). The $1/r$-scaling of the velocity comes from a geometrical spreading of the electric current and hence a decreasing Lorentz force with increasing radius. Additionally taking into account the side layers (also called Shercliff layers with thickness $\delta_S \sim M^{-1/2}$), Baylis and Hunt [1971] find the flow rate $Q = \int_{r_1}^{r_2}\int_{-a}^{a} u_\phi \,\mathrm{d}r\,\mathrm{d}z$ in the channel to be

$$Q = \frac{-aI\ln(r_2/r_1)}{2\pi\sqrt{\sigma_e\rho\nu}}\left[1 - \frac{0.956(1/r_2+1/r_1)a}{M^{1/2}\ln(r_2/r_1)} - \left\{\frac{1}{M} + \mathcal{O}\left(\frac{a^2(r_2^2-r_1^2)}{r_1^2 r_2^2}M^{-1}\right)\right\}\right]. \tag{1.51}$$

The corresponding drop in potential between the side walls of the channel is

$$\Delta\Phi = \frac{B_0 Q}{2a} - \frac{I\ln(r_2/r_1)}{4\pi a\sigma_e}. \tag{1.52}$$

Baylis and Hunt [1971] also present experimental data that test these predictions and hence the theory of Hunt and Stewartson [1965]. Within the experimental error bars and the accuracy of the asymptotic theory, the theory is confirmed.

A further theoretical study on laminar MHD flow in annular ducts with rectangular cross-section was undertaken by Tabeling and Chabrerie [1981]. Also using a boundary-layer technique, they focussed on secondary flows, that Baylis and Hunt [1971] had neglected, in the high-M regime. Tabeling and Chabrerie [1981] employed a perturbation method containing expansions in ascending powers of the curvature ratio $\lambda = a/R$. In their setup, the flow is driven by a constant pressure gradient $\partial p/\partial\phi$. They derive the velocities in the core and the Hartmann layers, and find that secondary flows in these regions are dominantly one-dimensional (suppression of u_z). For the Shercliff layers, secondary flows are far more intense. The secondary flow structure and the number of eddies in the Shercliff layer depends on the conductivities of the walls. In the case applying to ZUCCHINI (Hartmann walls insulating, side walls mostly insulating), the secondary flow in this region is predicted to consist of a single eddy.

The expansion in terms of ascending powers of λ in the perturbation method of Tabeling and Chabrerie [1981] converges, if

$$\frac{K}{M^{5/4}} \ll 1. \tag{1.53}$$

This is also a more stringent criterion for inertial effects to be negligible than equation 1.49 found by Baylis and Hunt [1971]. When $KM^{-5/4}$ becomes large, viscous forces compete with strong inertial forces in the Shercliff layer, which in turn becomes thinner ($\delta_S \sim K^{-1/2}$). This process relies on a purely hydrodynamic equilibrium. The value of $KM^{-5/4}$ being large enough for secondary flow effects to become important was found to be around 5 by Tabeling and Chabrerie [1981] examining their own experiments and the ones of Baylis [1971].

1.3.4 Early cylindrical duct experiments

One of the first experimental studies of electrically-driven MHD flow in the simple geometry of a cylindrical duct was conducted by Baylis [1964]. In this short letter to Nature, the author gives a description of a narrow-gap experiment (gap width $d = r_2 - r_1 = 1.2$ mm) dedicated to study the onset of instability in cylindrical MHD flow. The values of the relevant parameters are given in Table 1.1. Baylis [1964] finds that the voltage drop $\Delta\Phi$ between the side walls for fixed magnetic field B and electrical current I 'falls progressively below the value given by the [theoretical] expression above the critical point'. The theoretical value of critical $k = Re\sqrt{d/R}$ is confirmed within the error bars of the experiment.

Baylis [1971] performed a study of electrically-driven laminar flow in curved channels of square section. The width (and height) of the duct varied between roughly 0.4 and 3 cm (more details in Table 1.1). For the calculation of the friction factor F which is a measure of the dissipation in the system, the Reynolds number Re and the Dean number K, it is necessary to know the mean azimuthal velocity u_m in the core. Lacking direct velocity measurements, u_m was deduced from measurements of the voltage drop $\Delta\Phi$

Table 1.1: Parameter values of experimental studies. Height $h = 2a$, outer radius r_o and width d of duct, maximum magnetic field strength B_{max}, as well as resulting maximum Hartmann number M^*_{max} and liquid metal used. Note: The definition of the Hartmann number used in this table is based on the entire channel height h, which means it is double the Hartmann number M used throughout our manuscripts in Chapters 3 and 4. This is due to the fact that M^* was reported in the previous studies. Hg is mercury, PD(P) potential difference (probes).

	h in cm	r_o in cm	d in cm	B_{max} in T	M^*_{max}	I in A	fluid	measurements
Baylis [1964]	5	2.7	0.12	0.5	15	up to 30	Hg	global PD
Baylis [1971]	0.39-3.1	7	0.39-3.1	0.4	128	0.1-110	Hg	global PD
Moresco and Alboussiere [2004]	1	5	1	13	1690	650	Hg	global PD, pressure
Boisson et al. [2012]	12	4	1.2	0.15	460	50	GaInSn	UDV
Mikhailovich et al. [2012]	6.25	3.525	3.125	0.125	160	120	GaInSn	local PDP
Messadek and Moreau [2002]	1	11	5.6, 1.7 (11)	6	1800	10-70	Hg	local PDP
ZUCCHINI (this work)	10	20.5	13 (16)	1	4000	300	GaInSn	UDV, local PDP

between the inner and outer wall using Equation 1.52 and $Q = d^2 u_m$,

$$u_m = \frac{\Delta\Phi}{dB} - \frac{I}{2\pi\sigma_e d^2 B} \ln\left(\frac{2r+d}{2r-d}\right). \tag{1.54}$$

Baylis [1971] found three distinct flow regimes with changing K/M^2. For $K/M^2 < 4$, the flow is said to be similar to flow in a straight duct (‘Hartmann flow’). For higher K/M^2, there is a transition to the so-called ‘high secondary flow regime’, and for yet larger K/M^2, the author observes the transition to turbulence. However, Baylis [1971] was really interested only in the ‘high secondary flow regime’. There he found the ratio of friction factors (Eq. 1.59) for curved and straight ducts, F_c and F_s, to scale as $F_c/F_s = 0.107\,K^{1/2}$.

As mentioned in Section 1.3.3, Baylis and Hunt [1971] also presented experimental data. They pointed to two aspects that must be considered when comparing experimental data with the theory. The first one is the contact resistance between walls and fluid that cannot be avoided in experiments, but is neglected in theories. The second one concerns the conductance (inverse resistance, $G = R^{-1}$) of the side walls that has to be much higher than that of the liquid in order to resemble the theory. For ZUCCHINI this is the case with the copper electrodes having a roughly 20 times higher conductivity than the liquid GaInSn.

Baylis and Hunt [1971] analyzed experimental data from the ‘Hartmann flow’ regime of Baylis [1971] at low K/M^2. They found good agreement with the theoretical prediction of Equation 1.51 down to Hartmann numbers of $M = 16$, and hence confirmed the theory of Hunt and Stewartson [1965], valid for large M, for the side wall boundary layer.

1.3.5 The MATUR experiment

Alboussiere et al. [1999] carried out an experimental study of quasi-2D MHD turbulent shear layers. Their setup called MATUR (MAgnetohydrodynamic TURbulence) consisted of a cylinder with height 1 cm and radius 11 cm in an axial magnetic field (Fig. 1.4). The electric current was introduced at a ring of small electrodes at a radius of either 5.4 or 9.3 cm flowing radially outward to the outer wall. In this way, a shear layer was generated, similar to our experiment. The flow was either measured by potential probes or visualized at the free surface.

The free shear layer was observed to become unstable to 2D columnar eddies. Their wave length was growing with the forcing from 2 cm to the integral radial scale of the container through an inverse cascade. With the occurrence of the eddies, the thickness of the free shear layer increased by about one order of magnitude. Kinetic energy spectra plotted over the wave number k showed slopes of $k^{-5/3}$ and k^{-3} at low and high forcing currents, respectively, in agreement with other 2D turbulence results. The transition between both was established to depend on the time scale of energy transfer compared

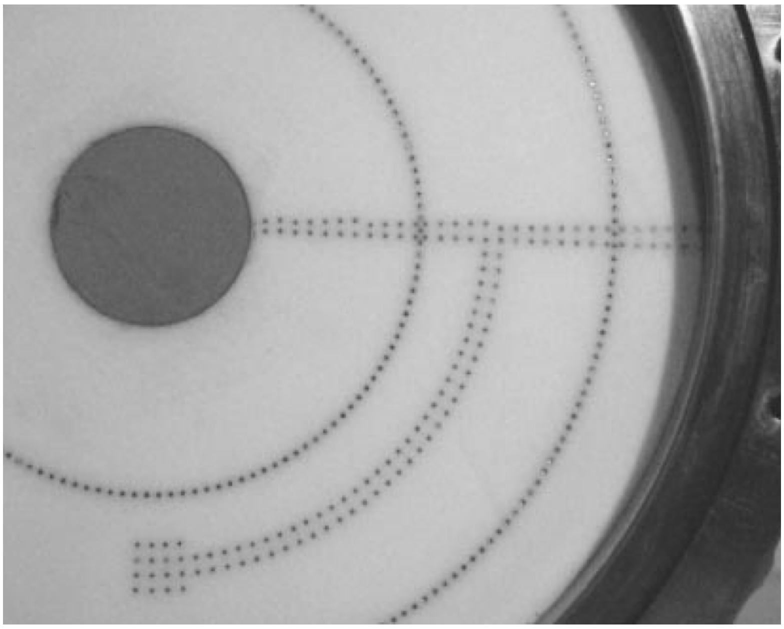

FIGURE 1.4: Bottom plate of MATUR taken from Messadek and Moreau [2002]. The dots are the two electrode rings and the potential probes.

to the one of dissipation in the Hartmann layer. By additional heating of the center and temperature measurements along the radius, the authors found that 2D MHD turbulence is not very efficient at transporting heat compared to momentum transport. Hence they suggested that the turbulent Prandtl number $Pr_t = \nu_t/\kappa_t$ would not tend to unity. Here ν_t and κ_t are the turbulent values of the viscous and thermal diffusivities which often are supposed to become equal since the turbulent transport of all quantities is thought to be equally efficient.

Messadek and Moreau [2002] performed another experimental study of quasi-2D turbulent shear flows in the MATUR setup described above. The authors report that the shear layer above the electrodes became unstable already for $I \leq 1$ A. Hence in their regime of interest, $I > 10$ A, the flow was turbulent. Measurements were mainly done by up to 140 potential differences, which were rechecked with a UDV signal.

Five phenomena were identified to be relevant in the experiment, each having its specific timescale, see Table 1.2. The numerical values in the table were calculated using values from ZUCCHINI for two locations in the parameter regime. Similar in both experiments, MATUR and ours, two-dimensionalization takes place almost instantly ($\tau_{2D} \ll \tau_{tu}$) and viscous effects are negligible ($\tau_{tu} \ll \tau_\nu$). Messadek and Moreau [2002] found that the only relevant phenomena are the ones related to τ_{tu} and τ_H. The parameter

$$\frac{\tau_{tu}}{\tau_H} = \frac{M}{Re}\left(\frac{l_\perp}{h}\right)^2 \tag{1.55}$$

with $l_\perp$ a transverse length scale, shows also that the ratio between Lorentz force and inertia in the turbulent core is of order M/Re (and not $N = M^2/Re$, the interaction parameter, which has been introduced as the ratio of Lorentz to inertial terms in Eq. 1.34). In the MATUR experiment, the ratio τ_{tu}/τ_H could be varied between small and order one. This suggested a change in the scaling of the energy spectrum from $k^{-5/3}$ to k^{-3}. In our experiment, however, τ_{tu} is always small compared with τ_H. We do not focus on energy spectra since preliminary plots of spectra from the potential difference probe did not show clear trends over more than a decade in k.

TABLE 1.2: Key timescales (in s) in the MATUR experiment of Messadek and Moreau [2002]. Numerical values are given for the MATUR experiment at $B = 5$ T, as well as for two regimes accessible in ZUCCHINI: (a) $B = 0.1$ T $(M = 200)$, $U = 0.1$ m/s, $l_\perp = 0.15$ m, $h = 0.1$ m; (b) $B = 1$ T $(M = 2000)$, $U = 1$ m/s.

			MATUR	(a)	(b)
Joule damping	τ_J	$\frac{\rho}{\sigma_e B^2}$	$\sim 10^{-4}$	$\sim 10^{-1}$	$\sim 10^{-3}$
Establishment of 2D	τ_{2D}	$\frac{\rho}{\sigma_e B^2}\frac{h^2}{l_\perp^2}$	$\sim 10^{-3}$	$\sim 10^{-1}$	$\sim 10^{-3}$
Energy transfer between transverse scales	τ_{tu}	$\frac{l_\perp}{U}$	~ 1	~ 1	$\sim 10^{-2}$
Hartmann dissipation	τ_H	$\frac{h}{B}\sqrt{\frac{\rho}{\sigma_e \nu}}$	~ 1	$\sim 10^2$	~ 10
Viscous effects	τ_ν	$\frac{l_\perp^2}{\nu}$	$\sim 10^3$	$\sim 10^5$	$\sim 10^5$

Looking at azimuthal velocities in the free shear layer, Messadek and Moreau [2002] were able to establish the temporal evolution from laminar acceleration to unsteady quasi-two-dimensional vortices, as well as the thickness of the shear layer. It was found that the non-dimensionalized turbulent shear layer thickness scales as

$$\frac{\delta_\parallel}{h} = C\left(\frac{M}{Re}\right)^{-n}, \tag{1.56}$$

where n is in the range $\frac{1}{2.3}$ to $\frac{1}{2.2}$ and $C \approx 1$; laminar theory would predict $\delta_\parallel \sim M^{-1/2}$. A simple model expressing the equilibrium between inertial effects and the Hartmann damping was proposed to explain this observed scaling. The authors also compared their experimentally found global angular momentum

$$L = \int_{r_1}^{r_2} r^2 u_\phi(r)\mathrm{d}r \tag{1.57}$$

with the theoretical case of steady inertialess flow,

$$L = \frac{I}{4\pi\sqrt{\sigma_e \rho \nu}}\left(r_2^2 - r_1^2\right), \tag{1.58}$$

and found reasonable agreement for high B, including L being independent of B. The slightly smaller slope (by 15%) is attributed to the Hartmann wall conductivity which introduces an extra dissipation. For $B < 2$ T, L is dependent on B, which was explained by the stronger secondary flows in this regime.

Using G.I. Taylor's hypothesis (i.e. turbulence is 'frozen into the flow' following Taylor [1938], and spatial velocity signals $u_\phi(x)$ can be obtained from temporal velocity information at one point, $u_\phi(t)$), Messadek and Moreau [2002] constructed power spectra. In a range of less than one decade in k, they observed the predicted power law scalings $k^{-5/3}$ for low B and I, as well as k^{-3} for high B and I.

Concerning the large-scale structures which are fed by the inverse energy transfer in quasi-two-dimensional flows, MATUR was not used to observe and characterize the first instability. However, it was possible to reconstruct the vorticity field of these structures in the supercritical regime by using an array of potential difference probes. Their transit velocity was slightly above $u_{\phi,max}/2$. The number N_s of large-scale structures appeared to scale with $(M/Re)^{1/2.5}$, again pointing to a competition between inertial effects and the damping in the Hartmann layers.

1.3.6 Instability of the Hartmann layer

Moresco and Alboussiere [2004] conducted a well-known experiment to study the stability of the Hartmann layer. It was the first study with insulating Hartmann walls dedicated to find the transition to turbulence in the Hartmann layer. Earlier linear stability analyses for the Hartmann layer had found critical $R = Re/M$ of approximately $5 \cdot 10^4$. Lingwood and Alboussière [1999] confirmed that this instability has a viscous origin, and the Lorentz force only plays an indirect role by generating the basic velocity profile. However, it was known that experimental MHD flows in similar geometries become unstable far below this threshold of linear stability.

The experimental setup of Moresco and Alboussiere [2004] is shown in Figure 1.5, the relevant numbers are given in Table 1.1. The side walls were electrically conducting, whereas the Hartmann walls were insulating and made exchangeable with two different roughnesses. The axial magnetic field **B** as well as the current I between the side walls were imposed. Measured quantities included the voltage $\Delta\Phi$ and the pressure drop Δp between the side walls, as well as the temperature T. Most of the analysis relies on the voltage measurements from which a mean velocity u_m is derived using Equation 1.54. This in turn is used to calculate the friction factor

$$F = \frac{IB}{u_m^2 \rho 2\pi r}. \tag{1.59}$$

Results are given as plots of F over $R = Re/M$ which is the Reynolds number based on the thickness of the Hartmann layer. Figure 1.6 shows the experimental data together with the laminar value from theory. There is a clear transition to higher values of the

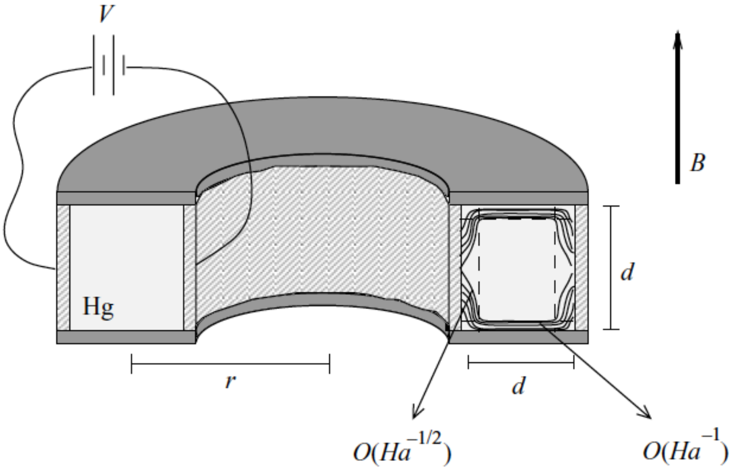

FIGURE 1.5: Original sketch of the experiment for the study of the instability in the Hartmann layer by Moresco and Alboussiere [2004]. The Hartmann number is $Ha = M$ in our notation.

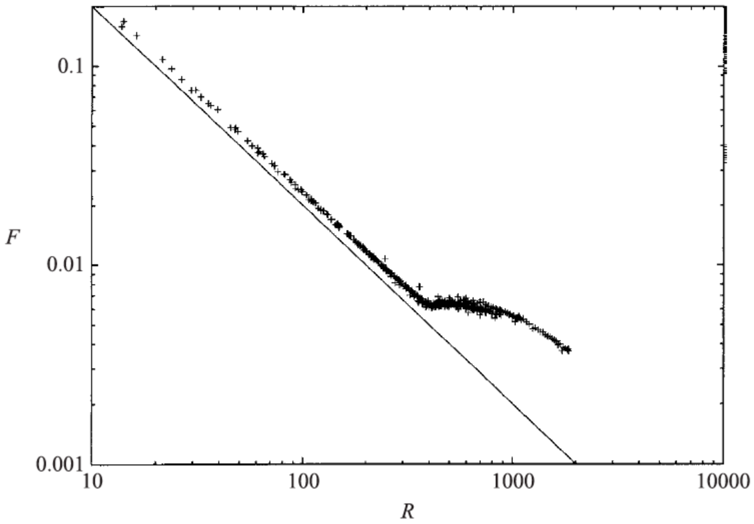

FIGURE 1.6: Original plot of friction factor F vs. $R = Re/M$ from Moresco and Alboussiere [2004]. Electrical currents range from 0 to 400 A, magnetic fields from 1 to 12 T. The straight line indicates F for laminar Hartmann layers.

friction factor around $R \approx 380$. The differences between the experimental values and the theoretical curve were attributed to either impurities in the mercury or uncertainties in the magnetic field strength. Note also that no hysteresis was observed, i.e. no different behaviour when approaching the transition from below or above.

In the experiment of Moresco and Alboussiere [2004], the laminar regime of the Hartmann layer was not approached until $B \approx 2$ T. This is due to the importance of rotational effects as was shown using Criteria 1.48. For high magnetic fields, $B > 6$ T, the critical R appears to be smaller than 380. This was attributed to the effect of the roughness becoming comparable in size (δ_r) with the thickness of the Hartmann layer (δ_H). Changing the roughness of the Hartmann walls, it was confirmed that the corresponding criterion is $\delta_r/\delta_H > 0.3$. For the laminar Hartmann layer, the roughness did not appear to change the friction factor even if δ_r was several times larger than δ_H.

In comparison with linear stability theory, the transitional value of $R \approx 380 \pm 10\%$ found by Moresco and Alboussiere [2004] is two orders of magnitude smaller. The instability of the Hartmann layer was concluded to be of finite-amplitude type, possibly triggered by disturbances originating in the side layers which have a lower threshold of instability. The limit of global stability was shown to be $R \approx 26$ in an energetic stability analysis by Lingwood and Alboussière [1999].

1.3.7 Numerical picture of MHD duct flow

Numerical simulations of the cylindrical duct experiment at low M by Krasnov et al. [2004] found the transition in the Hartmann layer between $R = 350$ and 400 in agreement with the experiment. The instability was identified to be of finite-amplitude type. This explains the range of critical R and makes the experimental flow sensitive to the roughness of the walls and hence the amplitude of introduced random perturbations.

Since the experimental and numerical studies of instability in the Hartmann layer in 2004, several numerical studies of straight and cylindrical ducts have established the picture of bounded low-Rm MHD flow [Zhao et al., 2011, Zhao and Zikanov, 2012, Vantieghem and Knaepen, 2011, Krasnov et al., 2012, 2013]. Increasing Re from the laminar state at a given M, first the side layers become unstable while the Hartmann layers and the core flow remain laminar. The first side layer instabilities occur as patterned turbulence with puffs as in hydrodynamic pipe flow at $R \approx 200$. Only for $R \gtrsim 250$ do the side layers become fully turbulent. Since dissipation is essentially concentrated in the Hartmann layers, this transition influences the friction factor F only marginally, and is not observed in experiments at large M. At $R \approx 380$, also the Hartmann layers become unstable by a finite-amplitude mechanism that can possibly be triggered by the unstable side layers. Increasing M at a given Re, it is always possible to relaminarize first the Hartmann layers and the core flow, and subsequently also the side layers. An interesting and yet unexplained point is the role of $R = Re/M$, which can be interpreted as the Reynolds number based on the Hartmann layer thickness δ_H, as the single important control parameter. This is even more surprising since R also appears to govern transitions in the side layers. A concise review on the laminar-turbulent transition in MHD duct, pipe and channel flows was presented by Zikanov et al. [2014] very recently.

1.3.8 Recent cylindrical duct experiments

Recently an experimental study of electrically-driven liquid metal MHD flow in a cylindrical annulus was conducted by Boisson et al. [2012]. They worked in the narrow-gap geometry; parameter values are given in Table 1.1. With increasing imposed electrical current I, first a stationary structure was observed. At higher forcing, two regimes of traveling waves occured, characterized by different frequencies and speeds. The slower waves exhibited frequencies up to 0.045 Hz whereas the faster ones occurring at higher magnetic fields were around 0.2 Hz. For the mean azimuthal flow $\overline{u_\phi}$, the authors observed a scaling of roughly $\overline{u_\phi} \sim (IB)^{1/2}$, and explained it by the fully nonlinear regime. These results will later be compared to our findings from ZUCCHINI.

A similar experimental setup was used by Mikhailovich et al. [2012] to study the decay of the mean velocity components and turbulent fluctuations. It was found that the temporal evolution of mean velocity did not follow a power law t^{-n} with constant exponent n, but rather n increased with time. From kinetic energy spectra, different slopes of -5/3, -3 and -7/3 were extracted tentatively. Two other cylindrical annulus experiments in the narrow-gap geometry are currently run at TU Ilmenau. The smaller one has an inner radius of 20 mm, an outer radius of 25 mm and a height of 65.7 mm. The larger one has $r_i = 68.25$‘mm, $r_o = 75$ mm and $h = 72$ mm. Both annuli are filled with liquid GaInSn and subject to a magnetic field of up to 0.5 T with interesting results to come (F. Samsami, pers. comm., 2014).

1.3.9 Related MRI experiments

Electrically-driven flow in annular channels was proposed as base flow for the study of the magnetorotational instability (MRI) by Khalzov et al. [2010]. For that purpose, the initial equilibrium rotation profile needs to be unstable with respect to the MRI, but stable to other instabilities, e.g. hydrodynamic ones. The authors concluded that this condition severely restricts the useful parameter regime. Not only does an electrically-driven MRI experiment have to operate in the inertialess regime, but it also needs to exhibit stable Hartmann and side layers. This restricts such an experiment to small Re at large M (small R).

Most MRI experiments, e.g. the one in Princeton proposed by Ji et al. [2001], are built as a Taylor-Couette setup with two concentric rotating cylinders rotating at different speeds. In this setup, the parameter regime suitable for the observation of the MRI is approached more easily. Still it is not a trivial task to create an appropriate rotation profile. This is mainly due to the problem of how to divide the end caps of the cylinder. Roach et al. [2012] and Spence et al. [2012] studied the instability of the free shear layer that occurs where the rotation speed of the fluid is discontinuous due to split end caps. The occurrence of this free Shercliff layer makes their study relevant to our experiment.

Roach et al. [2012] found that the free Shercliff layer was destabilized by a hydrodynamic Kelvin-Helmholtz-type instability which occurs for $\Lambda \gtrsim 1$, where Λ is the Elsasser number (Eq. 1.40) based on the difference $\Delta\Omega = \Omega_1 - \Omega_2$ between inner- and outer-ring rotation rates, Ω_1 and Ω_2. The resulting velocity fluctuations in the (r, ϕ)-plane exhibit an azimuthal mode number m which increases with Λ. Supported by numerical simulations, Spence et al. [2012] suggested that the pure hydrodynamic free shear layer (without applied magnetic field) is suppressed by increasing the Rossby number $Ro = \Delta\Omega/\Omega_2$ since the shear is pushed radially outwards by the secondary circulation. The free shear layer, which can become globally unstable, is re-established when imposing a magnetic field that suppresses the secondary circulation. When attempting to study the MRI, it is important to characterize the hydrodynamic instabilities where the role of the magnetic field is restricted to establish the base flow profile. In this respect, our characterization of the free shear layer instability in ZUCCHINI might be useful for the design of further experiments.

1.4 Composition of the thesis

This thesis is a cumulative dissertation containing one published paper and two manuscripts ready for submission as Chapters 3-5. All three parts are first-author work by the author of the thesis.

Besides the thesis contains a detailed description of the experimental setup, some relevant laboratory tests as well as the numerical method used in Chapter 2. The focus of this chapter lies on the experience we gained during our experimental and numerical work. Hopefully it will help future readers in reproducing our results or setting up similar experiments.

The manuscript in Chapter 3 gives a detailed description of the experimental setup of ZUCCHINI including references to ultrasound Doppler velocimetry in liquid metals. Subsequently it focuses on the base flow at low forcing current. Experimental results are complemented by a numerical study using the finite element method (FEM) sketched in Section 2.2. The follow-up manuscript in Chapter 4 focuses on the observed instabilities. Moreover it contains a description of velocity measurements via potential difference probes as well as a linear stability study using FEM. Our study of electrically-driven MHD flow was put into the historical context in Section 1.3 which gives an overview of previous experimental work.

Chapter 5 is a study on extracting scaling laws from numerical dynamo models using leave-one-out cross-validation. Sections 5.1-5.7 including Appendices 5.A-5.B have been published in the Geophysical Journal International as Stelzer and Jackson [2013]. The chapter is concluded by an overview of recent developments in this research area.

Chapter 6 summarizes my PhD work and gives an outlook including open questions.

References

T. Alboussiere, V. Uspenski, and R. Moreau. Quasi-2D MHD turbulent shear layers. *Experimental Thermal and Fluid Science*, 20:19–24, 1999.

S. Balbus and J. Hawley. A powerful local shear instability in weakly magnetized disks. i - linear analysis. ii - nonlinear evolution. *Astrophys. J.*, 376:214–233, 1991.

J. Baylis. Detection of the onset of instability in a cylindrical magnetohydrodynamic flow. *Nature*, page 563, 1964.

J. Baylis. Experiments on laminar flow in curved channels of square section. *Journal of Fluid Mechanics*, 48(03):417–422, 1971.

J. Baylis and J. Hunt. MHD flow in an annular channel; theory and experiment. *Journal of Fluid Mechanics*, 48(03):423–428, 1971.

J. Boisson, A. Klochko, F. Daviaud, V. Padilla, and S. Aumaitre. Travelling waves in a cylindrical magnetohydrodynamically forced flow. *Phys Fluids*, 24(4):044101, Jan 2012.

L. Bühler. *Magnetohydrodynamics - Historical Evolution and Trends*, chapter Liquid Metal Magnetohydrodynamics for Fusion Blankets, pages 171–194. Springer, 2007.

U. R. Christensen and J. Wicht. Numerical dynamo simulations. In G. Schubert, editor, *Treatise on Geophysics*, volume 8 on Core Dynamics. Elsevier Science Publishers, 2007.

P. Davidson. *An Introduction to Magnetohydrodynamics.* Cambridge University Press, 2001.

P. A. Davidson. Magnetohydrodynamics in materials processing. *Annu. Rev. Fluid Mech.*, 31:273–300, 1999.

W. Dean. Fluid motion in a curved channel. *Proc R Soc Lon Ser-A*, 121(787):402–420, 1928.

A. Gailitis, O. Lielausis, S. Dementev, E. Platacis, A. Cifersons, G. Gerbeth, T. Gundrum, F. Stefani, M. Christen, H. Hänel, and G. Will. Detection of a flow induced magnetic field eigenmode in the Riga dynamo facility. *Phys. Rev. Lett.*, 84(19):4365–4368, 2000.

A. Gailitis, O. Lielausis, E. Platacis, G. Gerbeth, and F. Stefani. The Riga dynamo experiment. *Surveys in Geophysics*, 24(3):247–267, Jan 2003.

J. Hartmann. Hg-dynamics i: Theory of the laminar flow of an electrically conductive liquid in a homogeneous magnetic field. *Mathematisk-fysiske Meddelelser, Det Kgl. Danske Videnskabernes Selskab*, XV(6):1–28, 1937.

J. Hartmann and F. Lazarus. Hg-dynamics ii: Experimental investigations on the flow of mercury in a homogeneous magnetic field. *Mathematisk-fysiske Meddelelser, Det Kgl. Danske Videnskabernes Selskab*, XV(7):1–45, 1937.

R. Hollerbach, X. Wei, J. Noir, and A. Jackson. Electromagnetically driven zonal flows in a rapidly rotating spherical shell. *Journal of Fluid Mechanics*, 725:428–445, 2013.

J. Hunt. Magnetohydrodynamic flow in rectangular ducts. *Journal of Fluid Mechanics*, 21(4):577–590, 1965.

J. Hunt and K. Stewartson. Magnetohydrodynamic flow in rectangular ducts. ii. *Journal of Fluid Mechanics*, 23(3):563–581, 1965.

J. Hunt and W. Williams. Some electrically driven flows in magnetohydrodynamics. part 1. theory. *Journal of Fluid Mechanics*, 31(04):705–722, 1968.

H. Ji, J. Goodman, and A. Kageyama. Magnetorotational instability in a rotating liquid metal annulus. *Mon. Not. R. Astron. Soc.*, 325, 2001.

I. Khalzov, A. Smolyakov, and V. Ilgisonis. Equilibrium magnetohydrodynamic flows of liquid metals in magnetorotational instability experiments. *Journal of Fluid Mechanics*, 644:257–280, 2010.

D. Krasnov, E. Zienicke, O. Zikanov, T. Boeck, and A. Thess. Numerical study of the instability of the Hartmann layer. *Journal of Fluid Mechanics*, 504:183–211, 2004.

D. Krasnov, O. Zikanov, and T. Boeck. Numerical study of magnetohydrodynamic duct flow at high Reynolds and Hartmann numbers. *Journal of Fluid Mechanics*, 704: 421–446, 2012.

D. Krasnov, A. Thess, T. Boeck, Y. Zhao, and O. Zikanov. Patterned turbulence in liquid metal flow: Computational reconstruction of the Hartmann experiment. *Phys. Rev. Lett.*, 110(8):084501, Feb 2013.

R. J. Lingwood and T. Alboussière. On the stability of the Hartmann layer. *Physics of Fluids*, 11(8):2058–2068, 1999.

W. McDonough. A compositional model for the earth's core. In *Treatise on Geochemistry*, volume 2, pages 547–568, 2004.

K. Messadek and R. Moreau. An experimental investigation of MHD quasi-two-dimensional turbulent shear flows. *J. Fluid Mech.*, 456:137–159, Jan 2002.

B. Mikhailovich, A. Shapiro, S. Sukoriansky, and I. Zilberman. Experiments with turbulent rotating MHD flows in an annular gap. *Magnetohydrodynamics*, 48(1):43–50, 2012.

R. Monchaux, M. Berhanu, M. Bourgoin, M. Moulin, P. Odier, J. Pinton, R. Volk, S. Fauve, N. Mordant, F. Petrelis, A. Chiffaudel, F. Daviaud, B. Dubrulle, C. Gasquet, L. Marie, and F. Ravelet. Generation of a magnetic field by dynamo action in a turbulent flow of liquid sodium. *Phys Rev Lett*, 98:044502, 2007.

R. Moreau and S. Molokov. *Magnetohydrodynamics - Historical Evolution and Trends*, chapter Julius Hartmann and His Followers: A Review on the Properties of the Hartmann Layer, pages 155–170. Springer, 2007.

P. Moresco and T. Alboussiere. Experimental study of the instability of the Hartmann layer. *J. Fluid Mech.*, 504:167–181, Jan 2004.

H. C. Nataf, T. Alboussiere, D. Brito, P. Cardin, N. Gagniere, D. Jault, and D. Schmitt. Rapidly rotating spherical couette flow in a dipolar magnetic field: An experimental study of the mean axisymmetric flow. *Phys Earth Planet Int*, 170(1-2):60–72, 2008.

V. Noskov, S. Denisov, R. Stepanov, and P. Frick. Turbulent viscosity and turbulent magnetic diffusivity in a decaying spin-down flow of liquid sodium. *Phys Rev E*, 85 (1):016303, Jan 2012.

P. Olson. Overview of core dynamics. In G. Schubert, editor, *Treatise on Geophysics*, volume 8 on Core Dynamics. Elsevier Science Publishers, 2007.

K. Rädler, M. Rheinhardt, E. Apstein, and H. Fuchs. On the mean-field theory of the Karlsruhe dynamo experiment I. Kinematic theory. *Magnetohydrodynamics*, 38(1-2): 39–69, 2002.

A. Roach, E. Spence, C. Gissinger, E. Edlund, P. Sloboda, J. Goodman, and H. Ji. Observation of a free-Shercliff-layer instability in cylindrical geometry. *Phys. Rev. Lett.*, 108, 2012.

D. Schmitt, T. Alboussiere, D. Brito, P. Cardin, N. Gagniere, D. Jault, and H. C. Nataf. Rotating spherical Couette flow in a dipolar magnetic field: experimental study of magneto-inertial waves. *J. Fluid Mech.*, 604:175–197, 2008.

J. Shercliff. Steady motion of conducting fluids in pipes under transverse magnetic fields. *Mathematical Proceedings of the Cambridge Philosophical Society*, 49(01):136–144, 1953.

E. Spence, M. Nornberg, R. Bayliss, R. Kendrick, and C. Forest. Fluctuation-driven magnetic fields in the Madison dynamo experiment. *Phys Plasmas*, 15:055910, 2008.

E. Spence, A. Roach, E. Edlund, P. Sloboda, and H. Ji. Free magnetohydrodynamic shear layers in the presence of rotation and magnetic field. *Phys Plasmas*, 19(056502), 2012.

E. J. Spence, K. Reuter, and C. B. Forest. A spherical plasma dynamo experiment. *The Astrophysical Journal*, 700(1):470–478, 2009. doi: doi:10.1088/0004-637X/700/1/470.

Z. Stelzer and A. Jackson. Extracting scaling laws from numerial dynamo models. *Geophysical Journal International*, 193(3):1265–1276, 2013.

R. Stieglitz and U. Muller. Experimental demonstration of a homogeneous two-scale dynamo, Jan 2001.

P. Tabeling and J. Chabrerie. Magnetohydrodynamic secondary flows at high Hartmann numbers. *Journal of Fluid Mechanics*, 103:225–239, 1981.

G. Taylor. The spectrum of turbulence. *Proc R Soc Lon Ser-A*, 164(919):476–490, 1938.

S. Vantieghem. Numerical simulations of quasi-static magnetohydrodynamics using an unstructered finite volume solver: development and applications. *PhD Thesis*, 2011.

S. Vantieghem and B. Knaepen. Numerical simulation of magnetohydrodynamic flow in a toroidal duct of square cross-section. *International Journal of Heat and Fluid Flow*, 32(6):1120–1128, 2011.

E. Velikhov. Stability of an ideally conducting liquid flowing between cylinders rotating in a magnetic field. *J. Exptl. Theoret. Phys.*, 36:1398–1404, 1959.

T. Weier, V. Shatrov, and G. Gerbeth. *Magnetohydrodynamics - Historical Evolution and Trends*, chapter Flow Control and Propulsion in Poor Conductors, pages 295–312. Springer, 2007.

Y. Zhao and O. Zikanov. Instabilities and turbulence in magnetohydrodynamic flow in a toroidal duct prior to transition in Hartmann layers. *J. Fluid Mech.*, 692:288–316, 2012.

Y. Zhao, O. Zikanov, and D. Krasnov. Instability of magnetohydrodynamic flow in an annular channel at high Hartmann number. *Phys. Fluids*, 23(8):084103–084103–8, Aug 2011.

O. Zikanov, D. Krasnov, T. Boeck, A. Thess, and M. Rossi. Laminar-turbulent transition in magnetohydrodynamic duct, pipe and channel flows. *Applied Mechanics Reviews*, 66, 2014.

D. Zimmerman, S. Triana, and D. Lathrop. Bi-stability in turbulent, rotating spherical Couette flow. *Phys. Fluids*, 23:065104, 2011.

Chapter 2

Experiments and simulations

In this chapter, I present information on the experimental setup of ZUCCHINI and tests that we have performed to study specific topics concerning the experiment (Section 2.1). Section 2.2 adds details about the finite element method which we use to numerically complement our experimental study of the flow in our container. An integral part of the two sections is the experience that we gained during handling experiment and numerics, which can not be presented in the condensed form of paper manuscripts like Chapters 3 and 4. In this sense, this chapter is more a lab report. I hope that the reader will get an impression of our laboratory and numerical work, and excuse partial duplications that are unavoidable due to the layout.

2.1 Experimental setup and tests

This section details our experimental setup. It is subdivided into the different units of the experiment: the actual tank, the coil systems generating the magnetic field, the power supplies for the forcing current, the liquid metal alloy GaInSn with the argon system used to prevent oxidation, and finally the measurement techniques.

2.1.1 The ZUCCHINI tank

We start our description of the experimental setup with its essential part, the tank which contains the liquid metal. The container is a cylindrical annulus with rectangular cross-section, and has an inner height of $h = 2a = 10$ cm (cf. Fig. 1.1). The radii of the inner and outer cylinders are $r_i = 4.5$ cm and $r_o = 20.5$ cm respectively. The disk electrode protruding the inner cylinder has a radius of $r_d = 7.5$ cm. The thickness of the central disk electrode is 1 cm, the ring electrode along the outer cylinder is 1.5 cm wide. The dimensions are detailed in the technical drawings in Figures 2.1 and 2.2.

The different components of the tank are shown in Figure 2.3. The choice of wall materials was made in order to be compatible with the GaInSn which prohibits the use

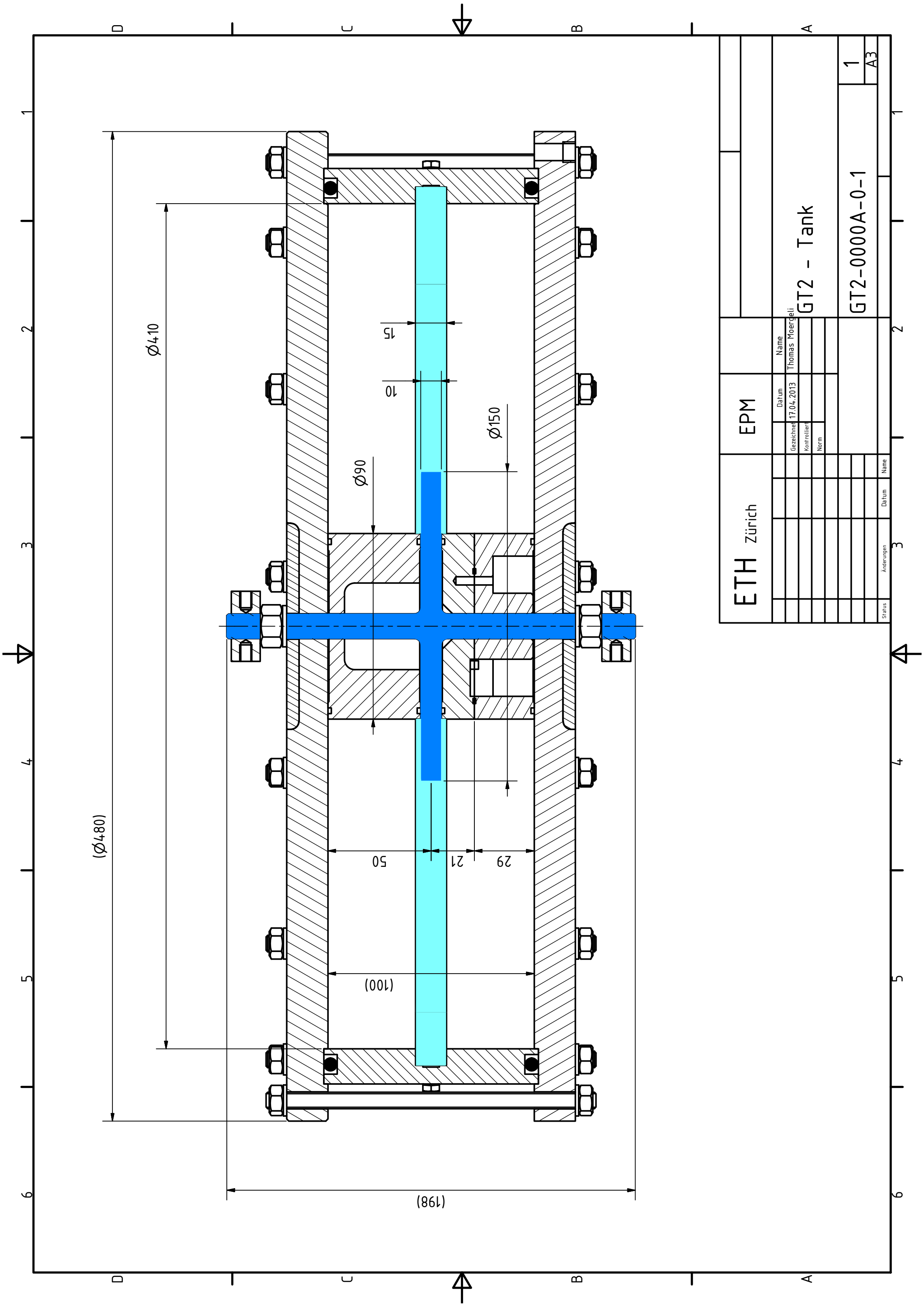
Ø410
(Ø480)
15
10
Ø150
Ø90
50
21
29
(100)
(198)
ETH Zürich
EPM
GT2 - Tank
GT2-0000A-0-1
1
A3
Gezeichnet
Kontrolliert
Norm
Datum
17.04.2013
Name
Thomas Moergeli
Status
Änderungen
Datum
Name
A
B
C
D
1
2
3
4
5
6

FIGURE 2.1: Vertical cross-section of the ZUCCHINI container. The inner electrode is shown in dark blue, the outer one in light blue. Relevant dimensions are given in mm. Courtesy of T. Mörgeli.

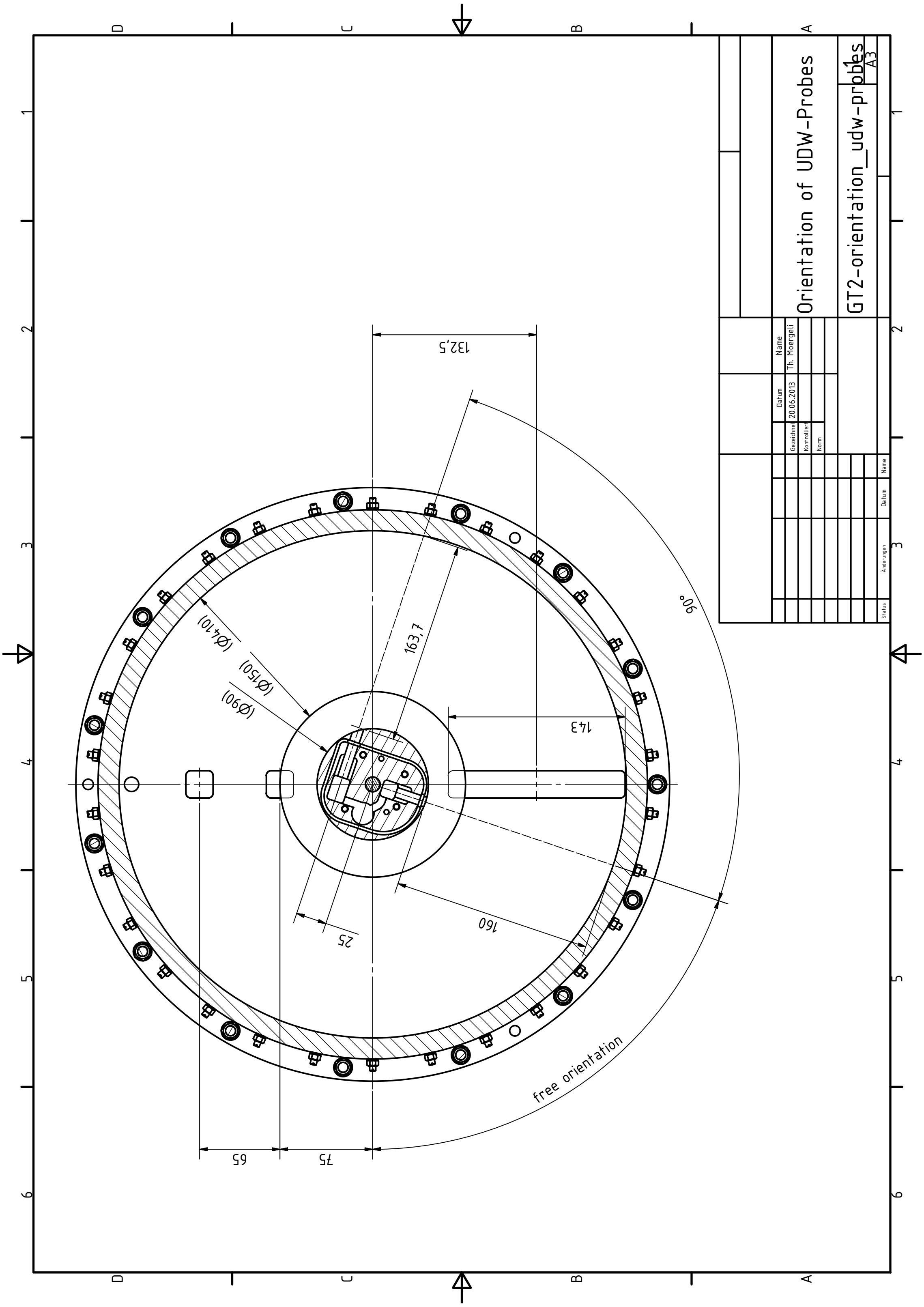
Orientation of UDW-Probes
GT2-orientation_udw-probes
A3
1
Gezeichnet
Kontrolliert
Norm
Datum
20.06.2013
Name
Th. Moergeli
Status
Änderungen
Datum
Name
132,5
163,7
143
160
25
65
75
90°
(Ø410)
(Ø150)
(Ø90)
free orientation
A
B
C
D
1
2
3
4
5
6

FIGURE 2.2: Top view of the container with orientation of UDV probes 1 (radial) and 2 (chordwise). Relevant dimensions are given in mm. Courtesy of T. Mörgeli.

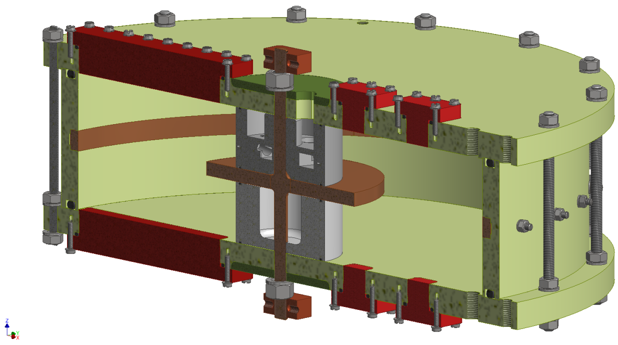

(a)

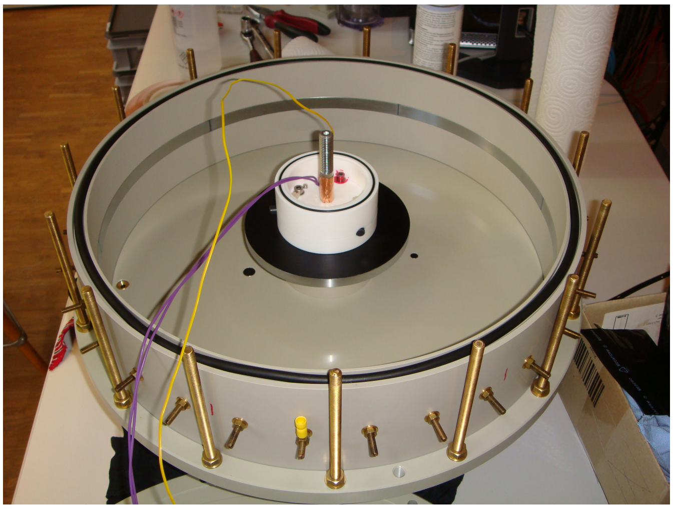

(b)

FIGURE 2.3: Components of the ZUCCHINI tank. (a) Technical drawing. The outer part of the tank (yellow-green) is made from polypropylene (PP), the inner cylinder (grey) is polyethylene terephtalate (PET). The inner and outer electrodes (brown) are copper coated with 20 μm NiP12 (nickel with 12 weight percent phosphor) and 2 μm chromium to prevent the copper from dissolving in the GaInSn. Additionally the inner electrode is insulated on its top and bottom surfaces. The replacable inserts (red) are made of plexiglass and epoxy resin. (b) Photo of the tank in open and empty state.

of copper and especially aluminium. All walls apart from the electrodes would ideally be electrically insulating ($\sigma_e = 0$). This requirement is relatively well fulfilled for the plastics used, and their mechanical strength is sufficient up to the fluid speeds of roughly 1.5 m/s that we achieve inside the container. Top and bottom lid as well as the outer cylinder of the tank are made of polypropylene (yellow-green in Fig. 2.3). The inner cylinder (grey) is made of polyethylene terephtalate, and the inserts for measurement probes (red) are made of plexiglass and epoxy resin. The latter polyester casting resin HT 1812 with MEKP-20 hardener turned out to be less suitable since it is slightly deformed over time under the pressure of the plastic screws. The inserts as well as the whole container of ZUCCHINI are designed in a modular way which enables us to exchange components, e.g. replace the large inserts by large grids of potential probes which is a modification envisaged for the future.

The inner disk and the outer ring electrode (brown) are copper plated with nickel and chromium to prevent the copper from dissolving in the GaInSn. The inner electrode is electrically conducting only around its outer radius, the remaining surface has been insulated by spraying black lake on it. The outer electrode is separated into six segments to improve control on the current distribution, see also the concerning test in Section 2.1.3.2. Gas- and water-tightness of the tank is achieved by nitrile butadiene rubber (NBR) O-rings. In preparation for the filling of the experiment, we cleaned and degreased all parts of the tank both mechanically and chemically with isopropyl alcohol, and performed extensive tightness tests using an argon overpressure of 0.5 bar and a water bath; in operation conditions, we have 0.2 bar of argon overpressure.

An issue that potentially plays an important role for the dynamics of the flow is the roughness of the Hartmann walls (top and bottom). Moresco and Alboussiere [2004] found in their experiment that roughness has an effect when $\delta_r/\delta_H > 0.3$ where δ_r is the size of the roughness (cf. Sec. 1.3.6). Their Hartmann walls had an rms (root-mean-square) roughness height of $R_Q = 0.1\ \mu$m and $0.6\ \mu$m for the polished copper and the ceramic plates, respectively, and maximum peak-to-trough distances of $R_t = 2\ \mu$m and $9\ \mu$m. We used the mechanical measurement device Diavite DT-15 with a Diavite T-780 probe to determine the roughness of our polypropylene top and bottom lids. This yields an average absolute roughness of $R_a = 0.1\ \mu$m and an rms roughness of $R_t = 2\ \mu$m. These values are valid when neglecting rare scratches that can have up to $R_t = 10\ \mu$m. We appear to operate in a roughness range similar to the smoother plates of Moresco and Alboussiere [2004]. For comparison, the thinnest Hartmann layer achieved in ZUCCHINI (at $M = 2022$) has a theoretical thickness of $\delta_H = 25\ \mu$m. Hence we do not expect to observe effects of the wall roughness at low and moderate M. Even at large M, we do not expect any significant influence of the wall roughness, but this criterion needs to be kept in mind.

2.1.2 Magnetic coil systems

One of the important ingredients of the ZUCCHINI experiment is the magnetic field. Not only is it necessary for the driving of the flow by the Lorentz force, but it also strongly influences the flow by making it quasi-2D along the field direction (cf. Sec. 1.2.5). During our experiments, we employed two different coil systems for the generation of the magnetic field. For the lower magnetic field strengths up to 0.1 T, we used a modified Helmholtz coil system with resistive copper coils manufactured by Caylar (‘Caylar’ setup). For the larger field strengths up to 1 T, we use a single superconducting coil from Cryomagnetics, Inc. (‘Cryo’ setup).

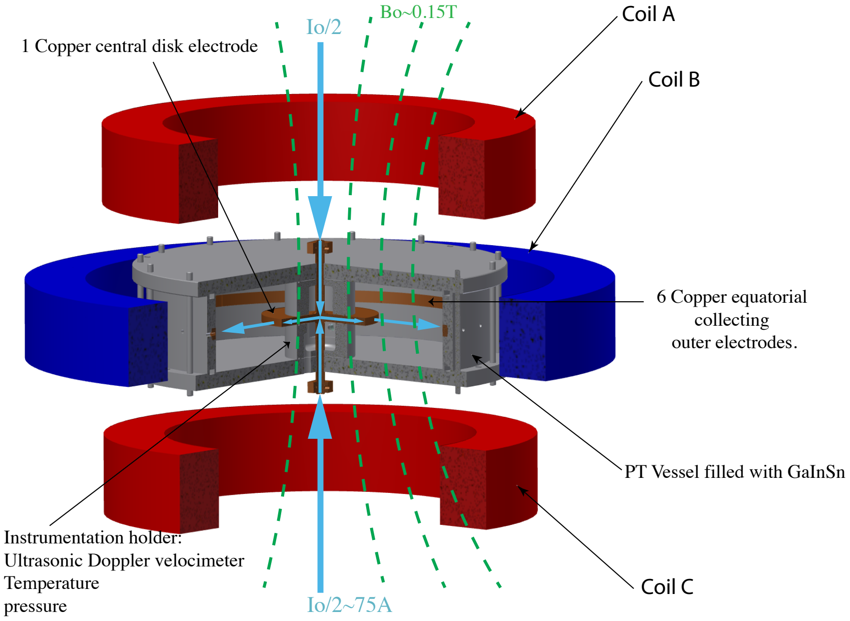
Bo~0.15T
Io/2
Coil A
1 Copper central disk electrode
Coil B
6 Copper equatorial
collecting
outer electrodes.
PT Vessel filled with GaInSn
Instrumentation holder:
Ultrasonic Doppler velocimeter
Temperature
pressure
Io/2~75A
Coil C

(a)

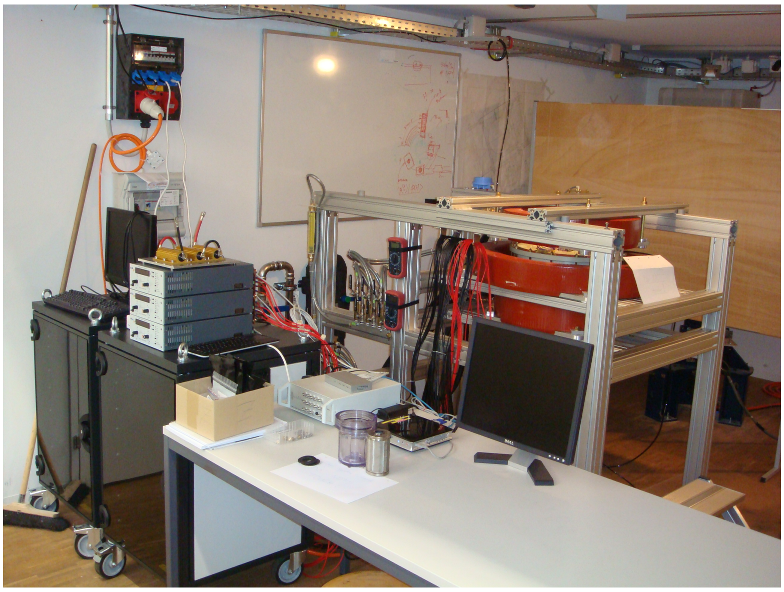

(b)

FIGURE 2.4: (a) Sketch of ZUCCHINI in the ‘Caylar’ magnetic coil setup. The field strength $B = 0.14$ T was never reached in this setup due to insufficient cooling of the resistive coils. (b) ‘Caylar’ setup with the red coils on the right and the power supplies on the left.

2.1.2.1 Caylar coils

The ‘Caylar’ setup consists of two small outer coils (inner diameter 40 cm) and a bigger central coil (inner diameter 60 cm) stacked coaxially with a mid-plane distance of 17 cm as shown in Figure 2.4. According to the manufacturer’s specifications, the three coils should generate a field of up to 0.14 T at 400 A of current. However, insufficient water

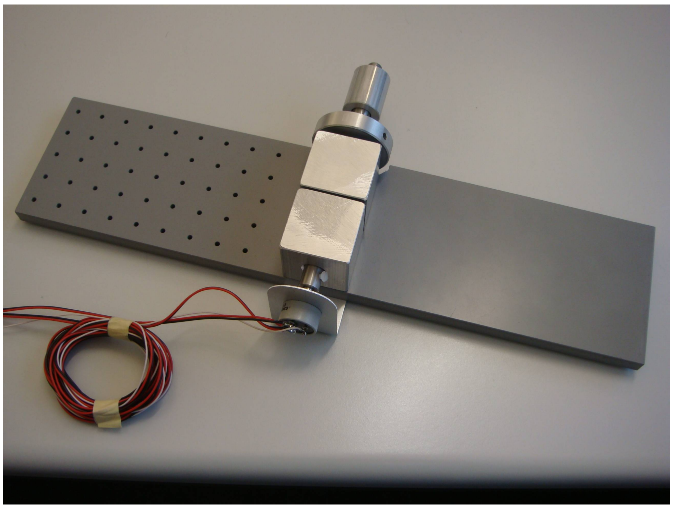

FIGURE 2.5: Rotatable lever for magnetic measurements in the Caylar setup. The potentiometer on top of the axis is used to record angular position. The 3-component Hall probe (Fig. 2.6) is fixed to the PVC plate by two aluminium screws.

cooling causes the copper coils to heat up in continuous operation, partially above 70°C as measured with our infrared camera testo 875. Due to the rising resistance, the maximum voltage of 15 V at the coils is reached already at 260 to 300 A. Hence we are limited to a field strength of 0.1 T in the 'Caylar' setup. The field strength was measured by two calibrated Hall probes provided by Caylar with a precision of < 0.1 mT on the top lid of the container. We used the 'Caylar' setup for our measurements up to $M = 169$.

In order to have an axisymmetric field, we made a great effort to align the coils and the GaInSn tank precisely not only according to geometric but also to magnetic measurements. For that purpose, we used a rotatable lever made of PVC and aluminium and shown in Figure 2.5 whose angular position was recorded by a potentiometer. The 1 kΩ-potentiometer of series 6180 has an electrical travel of $(340 \pm 1)^\circ$ and an independent linearity of $\pm 1\%$. A PVC cuboid with three mutually perpendicular Hall probes shown in Figure 2.6 was mounted on the rotatable lever. The probes were low-noise, linear Hall effect sensor ICs with analog output, model A1326 by Allegro, with a sensitivity of 25 mV/mT and a typical supply voltage of 5 V at 6.9 mA current. The Hall probes had been calibrated beforehand in the known field of a long coil at the Laboratory of Natural Magnetism of ETH Zürich, and have a precision of 0.08 mT at a resolution of 0.024 mT in connection with the data acquisition system (DAQ). The data were recorded by a NI USB-6009 DAQ. The thorough centering of the Caylar coils and the tank lead to a reduction in the axial asymmetry of B_z at a given radial and axial position from 1% to 0.1%. The azimuthal component B_ϕ was brought down to virtually zero.

We performed a magnetic field mapping with the Hall probes on the rotatable lever covering virtually the entire volume of the tank. The tank was not in place during the measurements. This should not make a significant difference since it contains no

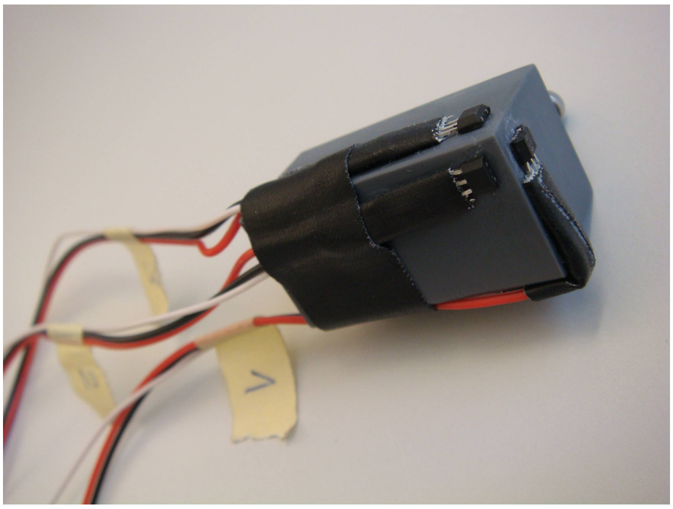

FIGURE 2.6: PVC cuboid with three mutually perpendicular Hall probes glued onto it measuring B_z, B_r and B_ϕ.

ferromagnetic parts. The current through the three coils was set to 240 A since this value was known to be achieved stably over two hours. In the thermal equilibrium between Joule heating and water cooling, the voltage at the small and big coils reached 13.6 and 9.7 V respectively. The measurements were performed with a sampling rate of 100 Hz at all 40 possible positions in the $(r,\ z)$-plane. They are summarized in Figure 2.7. The z-component is clearly the dominant component of the magnetic field. With increasing radius, it decreases by 7%. Also there seems to be a small dependence of the field strength on the axial position with higher values in the lower part of the tank. The radial and especially the azimuthal components are weak. We define the angle of deviation of the magnetic field direction from the vertical as

$$\alpha = \arctan \frac{B_h}{B_z} \tag{2.1}$$

where $B_h = \sqrt{B_r^2 + B_\phi^2}$ is the horizontal magnetic field strength. We find that deviations of the magnetic field direction from the vertical are smaller than 4° in most of the volume of the tank.

These results show a virtually uniform axial field within the volume of the ZUCCHINI tank in the Caylar setup. This field geometry should not only hold for the given value of current through the coils. By linear superposition, it is also valid for other magnetic field values as long as the currents through all Caylar coils are equal, which is true for all measurements presented in this work.

2.1.2.2 Cryomagnet

The ‘Cryo’ magnetic setup consists of a single superconducting coil with an inner diameter of 60 cm and a maximum field strength of 1 T manufactured by Cryomagnetics, Inc.

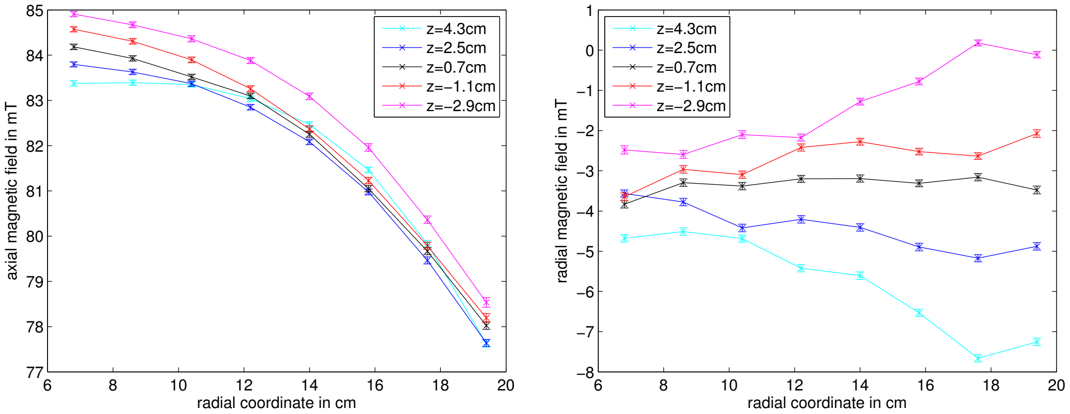

(a) B_z (b) B_r

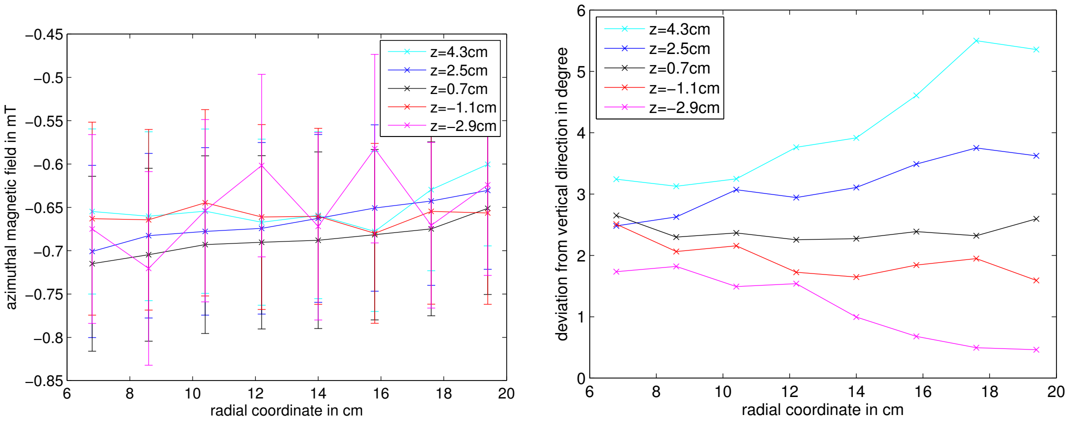

(c) B_ϕ (d) α

FIGURE 2.7: (a-c) Measurements of the three components B_z, B_r and B_ϕ of the magnetic field at different positions in the Caylar setup. The values and error bars shown are mean values and standard deviations over the azimuthal direction. (d) Angle α of deviation of the field direction (azimuthal mean) from the axial one, defined in Equation 2.1. The coordinates are: radial (r) from the symmetry axis and axial (z) from the mid-plane of the ZUCCHINI tank.

The coil is made from twisted multi-filamentary NbTi/Cu and cooled down to roughly 3 K using liquid helium and a Gifford-McMahon refrigeration cycle. The maximum field strength of 1 T is reached for an electrical current of 83 A. We centered the ZUCCHINI tank geometrically within the coil with its mid-plane 1 cm below the one of the coil due to construction reasons. In fact we do not know the extent and exact location of the actual NbTi/Cu coil inside its housing. When transferring the experiment from the ‘Caylar’ to the ‘Cryo’ setup, we had to cut the supporting aluminium frame around the tank with the tank filled in order to fit it into the cryomagnet. An impression of this process is given in Figure 2.8.

In the ‘Cryo’ setup, we characterized the field while the tank was in place. Hence we relied on measurements of B_z and B_r along lines above the top lid of the tank. We used Hoeben HE 244 analog Hall sensors with an open-circuit sensitivity of 190 V/(AT) at a

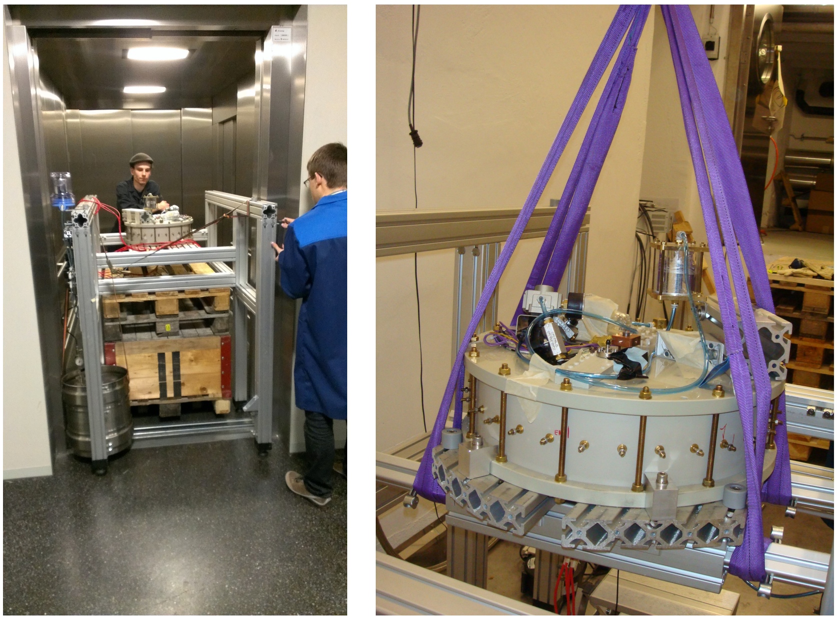

Figure 2.8: Impressions of transferring ZUCCHINI to the Cryo configuration which required precision work at the elevator and cutting the aluminium frame around the full tank using a jig saw.

supply current of 3 mA which was supplied by a NI 9265 card. The data were recorded by a NI-USB 4065 DAQ with a range of 1 V, a resolution of 6.5 digits and 0.3 s sampling interval.

Figure 2.9 shows the measured values for the components B_z and B_r at nominal center field strengths of 83.5 and 1000 mT. The recordings of B_z were taken 10.7 cm above the mid-plane of the coil housing on two perpendicular radial rays. The measurements of B_r were taken 11.5 cm above the mid-plane. We observe that the magnetic field strength in the 'Cryo' setup increases with the radius, e.g. at the location of the B_z-measurements by more than 15%. This is expected for the field inside a single short coil. Deviations with azimuth are small, with B_z varying by 1% between the perpendicular radial rays. Also in this setup, the magnetic field is characterized by a dominant axial component. However, the field is less uniform than in the 'Caylar' setup with a significant radial component, especially far from the mid-plane.

For our numerical study in Section 3.4.4.2, we approximate the 'Cryo' field by an analytic field of a single wire loop. Figure 2.10 shows a field of this type where we adjusted the parameters to get a field that fits our measurements. The fit to the measured data is depicted also in Figure 2.9 as solid lines. Not surprisingly, the behaviour of B_z with radius can be modelled quite well, whereas the model is too simple to achieve a good fit in B_r. However, since we are only interested in the general effect of a realistic single coil field, the single wire loop model is sufficient. It is obvious that the increase in field strength and the field curvature near the outer wall of the tank alter the Lorentz forcing

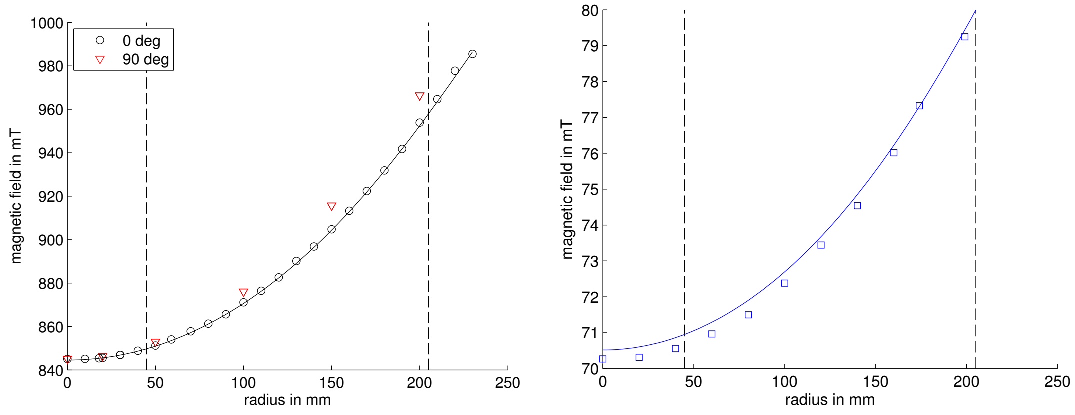

(a) B_z at 1000 mT (b) B_z at 83.5 mT

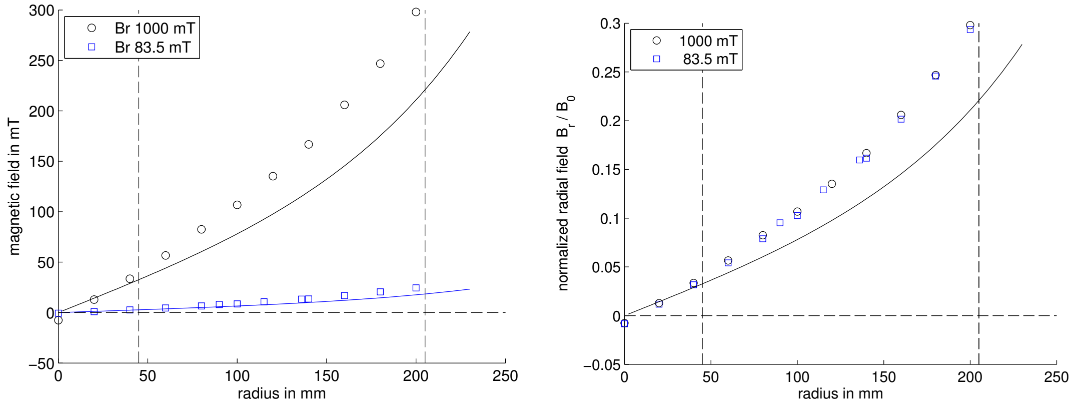

(c) B_r at 83.5 and 1000 mT (d) B_r/B_0 at 83.5 and 1000 mT

FIGURE 2.9: Line measurements of B_z (a-b) and B_r (c-d) at a center field strength of $B = 83.5$ mT and 1000 mT (maximum) in the single-coil cryomagnetic setup. The data were recorded 10.7 cm (a-b) and 11.5 cm (c-d) above the mid-plane of the coil. The solid lines depict an analytic magnetic field of a single current loop of the type used in Section 3.4.4.2. The relative dependence of the analytic field from the measured B_r-data is independent of the field strength (plot d). The dashed lines indicate the location of the inner and outer radii of the tank.

and can influence the flow, giving rise to a jet in the outer Shercliff side layer. For the actual numerical model in Section 3.4.4.2, we used a bigger single-loop radius than in the experiment in order to recover realistic jet amplitudes.

2.1.3 Current supply

The second ingredient in the Lorentz force besides the magnetic field is the electrical current I. In ZUCCHINI, we impose a current between inner and outer electrodes which is as axisymmetric as possible. For that purpose, we use switched-mode power supplies of type SM 18-50 from Delta Elektronika. They have an output voltage of 0-18 V, an output current of 0-50 A, and are characterized by an rms ripple and noise as low as 5 mA. We chose the power supplies such that the switching frequencies lie in a different range than our signal frequencies, especially the 8 MHz ultrasonic signal.

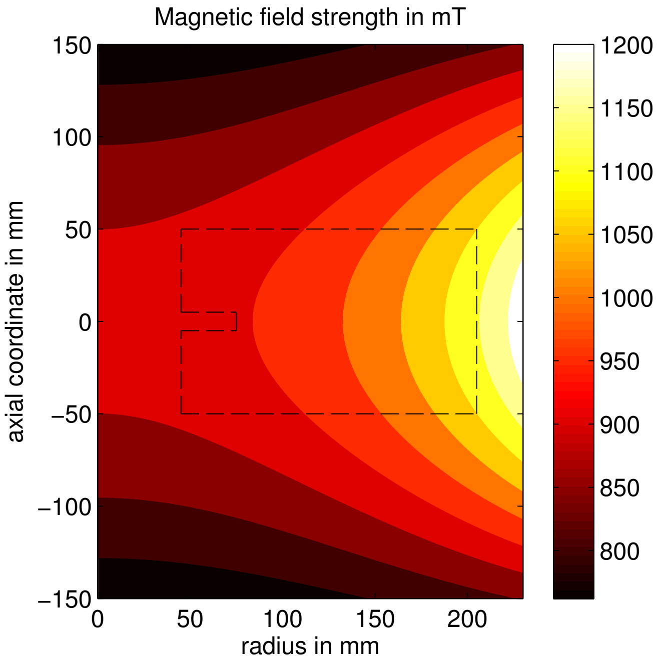

FIGURE 2.10: Map of magnetic field strength of a single loop approximating the field of the 'Cryo' setup at 1 T. The cross-section of the tank is shown in dashed lines. A field of this type is used for the numerical recovery of the jet in Section 3.4.4.2.

2.1.3.1 Caylar setup

In the 'Caylar' setup, we use three SM 18-50 power supplies in parallel master/slave mode and digital control, achieving a maximum current of $I_{max} = 150$ A. The connections between power supplies and experiment are made by copper busbars, see Figure 2.11, distributing the current to the different electrodes via copper cables with a cross-section of 4 mm^2 which are rated for 25 A each. The inner electrode is contacted with four cables from above and four from below. Each of the six outer electrode segments is connected at three points in order to make the potential homogeneous across the surface of the electrodes. The resulting electric circuit which is closed through the liquid GaInSn creates a non-axial magnetic field. Its strength, however, is negligible compared to the externally imposed predominantly axial field.

The usage of three power supplies means that every unit has to feed two segments of the outer electrode ring. This brings about the challenge of ensuring the axisymmetric distribution of the current. In principle, all cables should have equal length and resistance. Small variations in the cable resistance and the contact resistances (e.g. by wetting problems with the liquid GaInSn), however, lead to differing currents through the different cables. We made great efforts to equalize the resistances of the pathways by inserting washers between the busbars and the cables. In that way, we were able to reduce the difference in current flowing through different outer electrode segments from roughly 30% to less than 4%. Hence we assume a homogeneous distribution of

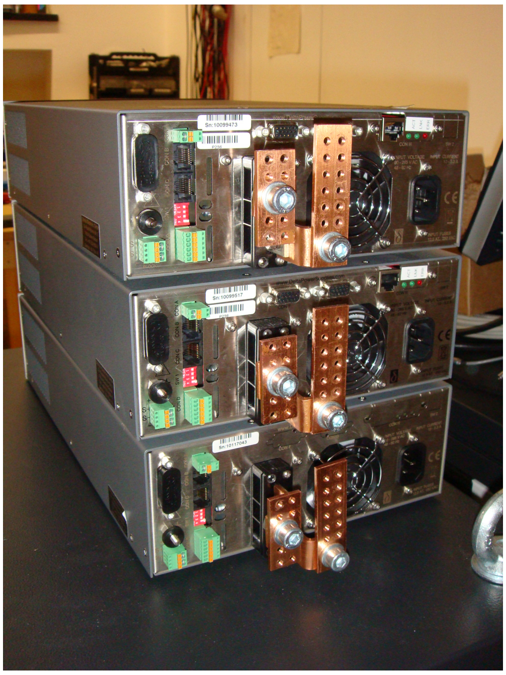

Figure 2.11: Photo of the copper busbars distributing the forcing current from the power supplies to the cables (not attached).

the forcing current as long as wetting issues can be neglected. A persistent problem was the temperature-dependence of our resistance-compensation since the cables were heated considerably by the current. The following test series, however, confirms that even a considerable amount of non-axisymmetry in the current distribution does not significantly alter the observed flow.

2.1.3.2 Effects of non-axisymmetric current distribution

In the experiment, it is inevitable to have a certain amount of non-axisymmetry in the forcing current due to resistance differences in the cables, contact resistances and wetting issues with the GaInSn. Hence it seems in order to have a test series dedicated to this topic. Instead of trying to minimize the degree of non-axisymmetry, we make it larger on purpose in order to study its effects on the flow.

Figure 2.12 shows space-time diagrams of the radial velocity measurements of UDV probe 1 for different current distributions on the six outer electrode segments. Starting from case (a) which is the symmetric standard configuration, we take out more and more electrodes while maintaining the total forcing current at 60 A. In the extreme case (f), we are left with only one electrode connected to the power supplies; case (f) also differs from the others in the current which is limited to 50 A here. We observe that the radial flow is largely unchanged in cases (a) to (c) which either have a large amount of electrodes connected or preserve axisymmetry. The one-sided forcing configurations (d) to (f) show

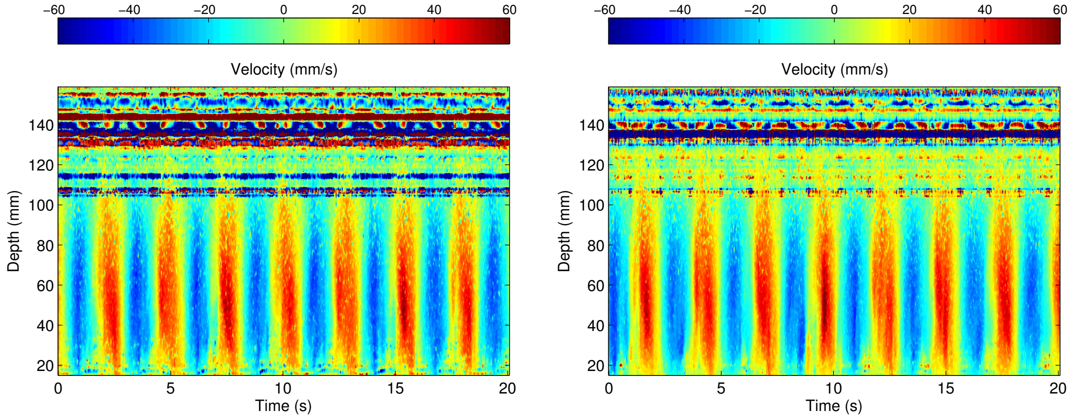

(a) standard configuration at 60 A (b) 5 electrodes connected

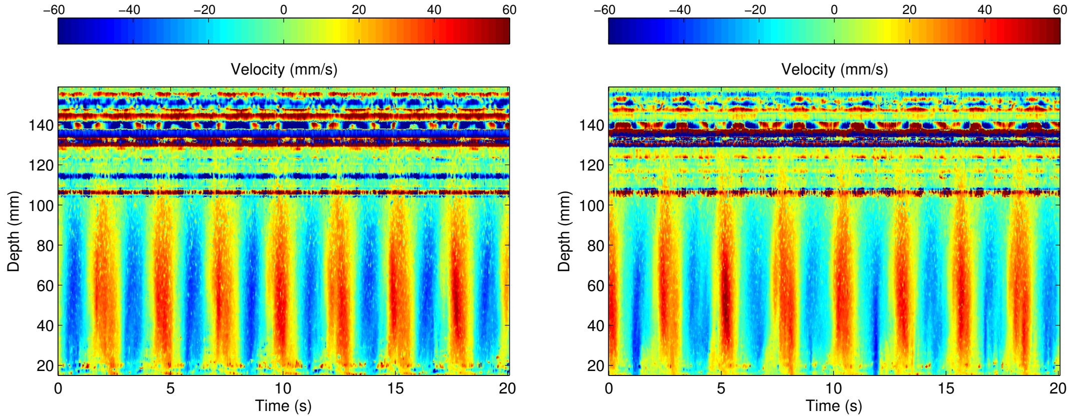

(c) 2 opposite electrodes (d) 3 neighbouring electrodes

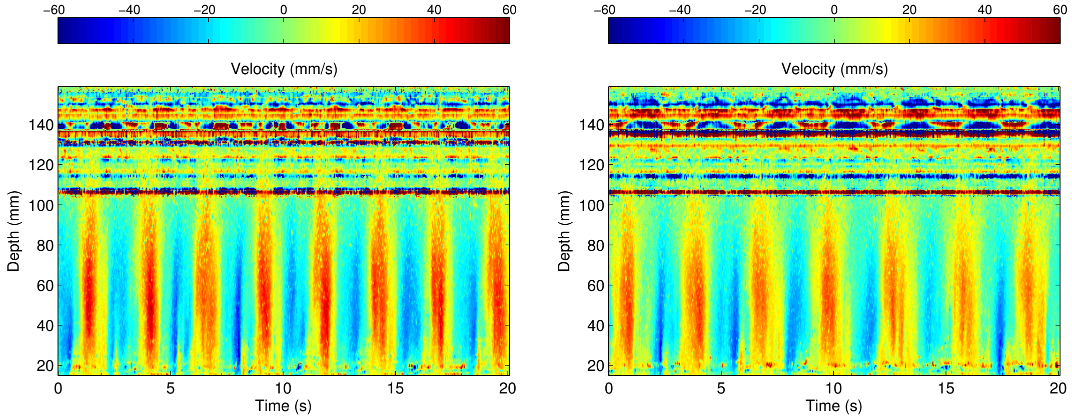

(e) 2 neighbouring electrodes (f) 1 electrode at 50 A

FIGURE 2.12: Effects of non-axisymmetric current distribution on radial velocity measurements. Plots (a)-(f) show configurations with different electrodes connected in order of decreasing similarity with the symmetric standard setup (a). The magnetic field strength is $B = 68.6$ mT, the forcing current is $I = 60$ A apart from case (f) which is at 50 A. Note the noise contamination in the range of depths greater than 100 mm which we were able to get rid of for our actual measurement series presented later.

decreasing oscillation amplitudes. The smaller oscillation frequency in case (f) is due to the smaller forcing current.

From this deliberate breaking of the axisymmetry of the forcing, we conclude that even taking out entire electrode segments does not significantly change the flow as long as a certain degree of axisymmetry is preserved. Hence we assume that we do not modify the flow by wetting problems and currents varying up to 4% between electrodes. Another issue that we tested on this occasion is the dependence of the flow on the initial conditions. It turns out that we observe no influence within the error bars.

2.1.3.3 Cryo setup

In the 'Cryo' setup, we employ six SM 18-50 power supplies to reach a maximum current of $I_{max} = 300$ A. Compared to the 'Caylar' setup, this doubling of the current leads to a doubling of the maximum velocities in the large-M limit (cf. Eq. 1.50). At the same time, we avoid a large part of the problem of uneven current distribution since every outer electrode segment is now fed by a separate power supply. Otherwise the cabling of the experiment is the same as in the 'Caylar' setup implying a stronger heating of the copper cables. Since the magnetic field strength is increased by an order of magnitude, it is more important to fix the cables in order to prevent shifting due to the Lorentz force acting on them in a magnetic field.

2.1.4 GaInSn and the argon system

ZUCCHINI is filled with roughly 12.5 l (80 kg) of the eutectic alloy GaInSn. We use MCP 11 alloy from 5N Plus UK Ltd. According to the certificate of analysis, it contains 65.9% gallium, 20.8% indium and 13.3% tin. Table 2.1 gives its relevant physical properties. Besides being liquid at room temperature, GaInSn has the advantage of not being hazardous to human health and the environment. This makes it the liquid metal of choice for an experiment without the safety precautions that are required for e.g. sodium. GaInSn may, however, be corrosive to metals, it weakens especially aluminium, and it is quite expensive. Additionally it is easily oxidized forming a sludge of mainly gallium oxides (Ga_2O_3, Ga_2O) which degrades or precludes experimental measurements.

We encountered problems with the sludge ourselves when we got our first load of GaInSn. For some reason, the content of the bottles consisted of up to one quarter sludge. This is certainly not desirable for a fluid dynamics experiment. Also our first handling of the GaInSn in contact with the surrounding air was not helpful. Consequently we were not able to get reliable UDV data in our first tests. For the second load of GaInSn, we had the bottles sealed with argon as cover gas prior to shipment, and precluded air contact in our laboratory.

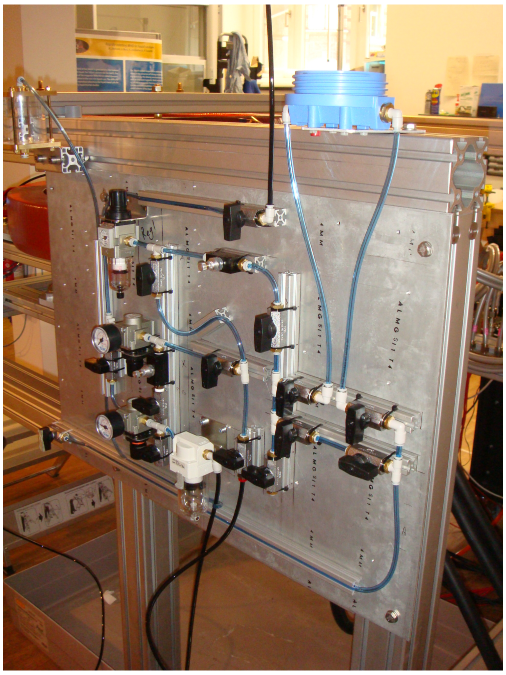

Figure 2.13: Photo of the argon overpressure system to prevent the GaInSn from oxidation. The pneumatic board is used for filling and emptying the tank and holding the GaInSn under an argon atmosphere.

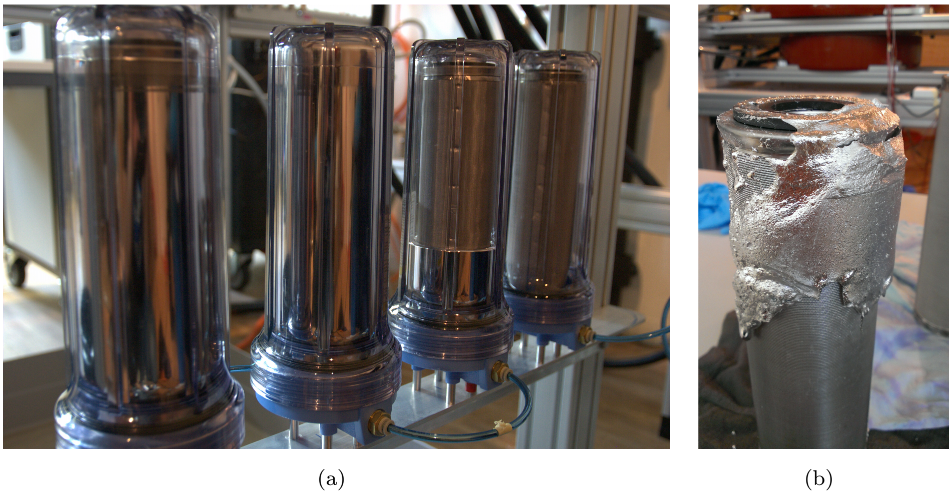

(a) (b)

Figure 2.14: Photos of the filter system to remove sludge from the GaInSn. (a) Filters with mesh sizes of 100, 50, 30 and 15 μm to remove sludge during the first filling. (b) Sludge remaining in the 100 μm-filter.

TABLE 2.1: Physical properties of GaInSn from Morley et al. [2008] who provide data for various composition ratios. We present the data set resembling most the MCP11 alloy from 5N Plus we use.

kinematic viscosity ν	$2.98 \cdot 10^{-7}$ m^2/s
electrical conductivity σ_e	$3.1 \cdot 10^6$ $(\Omega\text{m})^{-1}$
density ρ	6360 kg/m^3
melting point T_m	10.5°C
sound speed c	2730 m/s

TABLE 2.2: Operation sequence of the pneumatic system for filling, emptying and flushing the ZUCCHINI tank with argon. The valves are indicated in Figure 2.15. In operation, valve 11 should be closed. Courtesy of P. Scarfe.

Filling	Emptying	Flushing
close all (except 11)	close all (except 11)	close all
open 2	open 1	open 10
open 12	open 12	open 9
(allow storage tank	open 13	open 8
to pressurize)	allow storage tank	open 5
open 4	to depressurize	open 6 and 7 too, if
open 6	open 9	flushing filters as well
open 7	open 8	open 3
open 9	open 5	after sufficient argon has been
(check pressure in tank)	open 4	vented through valve 10...
then, when tank is full...	then, when tank is empty	open 11
close 9	close 4	wait a few seconds...
close 6	close 8	close 10
close 7	close 5	
close 4	close 9	
	re-pressurize storage tank	
	close 1	
	open 2	

Various procedures have been reported for the treatment of GaInSn. Morley et al. [2008] thoroughly clean all pipes mechanically and chemically using brushes as well as alcohol and acetone before putting GaInSn through them. Additional to the cleaning with isopropyl alcohol, we adopt their usage of argon as cover gas to prevent oxidation. For this reason, we have designed an elaborate pipe system which is shown in Figure 2.13 and keeps the GaInSn under an argon overpressure of at least 0.15 bar at every time. Also it allows us to fill and empty ZUCCHINI without the GaInSn ever coming into contact with the surrounding air by applying different pressures to the storage and working tanks. The schematic setup is shown in Figure 2.15; Table 2.2 reports the operation sequences for filling and emptying as well as flushing with argon.

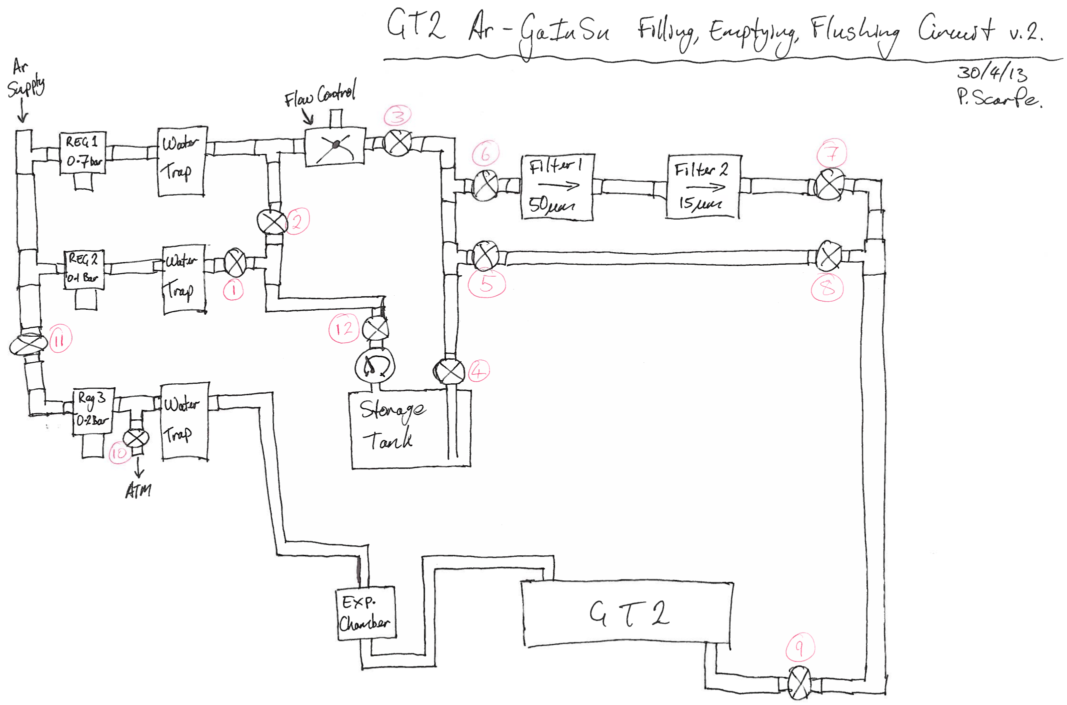
GT2 Ar-GaInSn Filling, Emptying, Flushing Circuit v.2.
30/4/13
P.Scarfe.
Ar Supply
Flow Control
REG 1 0-7bar
REG 2 0-1 Bar
Reg 3 0-2bar
Water Trap
Water Trap
Water Trap
ATM
Storage Tank
Filter 1 50µm
Filter 2 15µm
EXP. Chamber
GT2
1
2
3
4
5
6
7
8
9
10
11
12

FIGURE 2.15: Scheme of the pneumatic board controlling the argon overpressure system used for filling and emptying the ZUCCHINI tank alias GT2. Courtesy of P. Scarfe.

Prior to the first filling, we press the GaInSn through four filters with mesh sizes of 100, 50, 30 and 15 μm (Fig. 2.14) to remove oxides. Around 90% of the sludge stays in the coarsest mesh, and after the 50 μm mesh, hardly any sludge remains. Using this procedure, we have been able to run the experiment continously for one year up to now without any cleaning.

The argon overpressure system posed one difficulty to us which was a bubble of argon that remained in the tank leading to a partly free surface. In the beginning this hindered the contact between potential difference probes and GaInSn. We were able to transfer a part of the bubble to the expansion chamber by tilting the entire aluminium frame of the experiment using a lifting jack. It turned out that it would be convenient to connect the expansion chamber to the tank at the smallest radius possible instead of the biggest. In this case, one could use the centrifugal force acting on the liquid metal to drive the surplus argon into the expansion chamber.

A problem of most liquid metals is that they do not wet new surfaces easily. Morley et al. [2008] suggest to scrub the stainless steel container with diluted phosphoric acid (5% concentration), rinse with water and alcohol and dry with a heat gun. Another possibility is to rub the GaInSn into the metal surface at room temperature in order to get a well-defined electrical contact, e.g. Stefani et al. [2006].

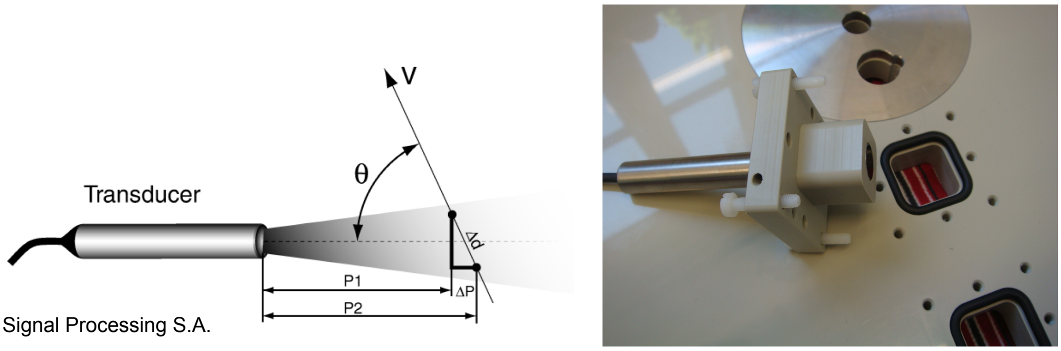

(a) (b)

Figure 2.16: UDV probes. (a) Sketch of probe with ultrasound beam, taken from [DOP]. (b) Photo of vertical probe 3 before mounting the insert in the bottom lid of the tank.

We encountered various problems with electrical contact and especially ultrasonic wave transmission to the GaInSn (bubbles forming at the probe surface). In our final setup, however, we thoroughly clean all surfaces with isopropyl alcohol and let them dry which appears to be sufficient to solve all problems related to surface wetting. For the cleaning of GaInSn spills, it is convenient to use WD-40 or a similar penetrating oil in addition to isopropyl alcohol.

2.1.5 Measurement techniques

We employed several measurement and monitoring methods in the ZUCCHINI experiment. Velocity measurements were performed by ultrasonic Doppler velocimetry (UDV) and potential difference probes (PDP). Moreover we tested recording dynamic pressure and induced magnetic fields, and we monitored the static pressure as well as the temperature in the tank. This section is meant as a collection of our experience with the different methods.

2.1.5.1 Ultrasonic Doppler velocimetry

UDV as used in our experiment is based on the pulsed emission of ultrasonic waves that are reflected by particles in the fluid. Velocities are derived from shifts in position between pulses resulting in a profile of the velocity component along the ultrasound beam. Earlier usage and our setup with the DOP3010 box from Signal Processing S.A. as well as two horizontally mounted and one vertical probe is described in detail in Section 3.4.2.1 (see especially Fig. 3.8).

Figure 2.16 shows a sketch and a photo of a UDV probe. The radial probe 1 and the chordwise probe 2 were custom-made for us with a polyurethane casing, lengths of 35 and 37 mm, and an outer diameter of 8 mm. The choice of material and length is due to the probes' locations within the inner insulating cylinder. The emitting frequency of probes 1-3 is 8 MHz. Probe 3 has a standard metal casing, and is mounted flush in the bottom plate of ZUCCHINI just outside the edge of the central disk electrode, $r_d = 7.5$ cm. Hence it measures a vertical profile of the axial velocity u_z over the entire height of the free Shercliff layer. At the beginning, we also had a fourth UDV probe looking from the bottom to the top at a radius of roughly 7 cm below the inner electrode with an azimuthal offset of 180° to probe 3. Due to its lower emitting frequency of 4 MHz, however, it turned out to be not very useful, so no data from this probe are shown in this work.

As mentioned earlier, getting reliable UDV measurements was not an easy task at all in the beginning. Tests in water seeded with e.g. pollen always yielded the desired results. In liquid GaInSn, however, we have to deal with the added complication of wetting and oxides. The wetting problem was only overcome when we adapted the thorough cleaning procedure described in Section 2.1.4. Concerning the oxides, on the one hand it is important to have a sufficient amount of them in the fluid as scatterers. Somewhat surprisingly, this was still true after we had filtered the GaInSn with mesh sizes as small as 15 μm. On the other hand, too many scatterers will lead to a fast energy loss of the ultrasound beam prohibiting velocity measurements at the far end of the profile. We were lucky enough to have an appropriate amount of oxides in our final setup with the argon system. However, also a good mixing of the oxides in GaInSn is essential since they would settle down or float after a while. Hence we mixed up the fluid between runs by high forcing currents.

Despite the reported procedure, we encountered loss of the UDV signal on the far-half of the profile on probes 1 and especially 2. First we attributed this problem to gas bubbles trapped at the surface of the probes. However, it turned out that this problem was actually related to electromagnetic noise from the Delta Elektronika power supplies despite thorough grounding. The good signal quality was recovered when keeping a distance of at least 1 m between power supplies and UDV box including cables. When all above mentioned points are taken into account, our UDV recordings in liquid GaInSn have a very good quality with high signal-to-noise ratio.

2.1.5.2 Potential difference probes

Electrical potential differences have been used to measure velocities for a long time. According to Shercliff [1987], the first suggestion of such a device was by Smith and Slepian for measuring the speed of ships in 1917. Our PDPs as well as the underlying theory are described in Section 4.4.2.1. Figure 2.17 shows a photo of the two 5 × 5 PDP arrays made from plexiglass and epoxy resin, respectively, that we mounted flush in the top lid of the GaInSn tank. The brass pins are standard PCB pin header strips that are held in place and made tight by casting epoxy resin into the gaps of the insert. Finally the inserts were machined flush and polished.

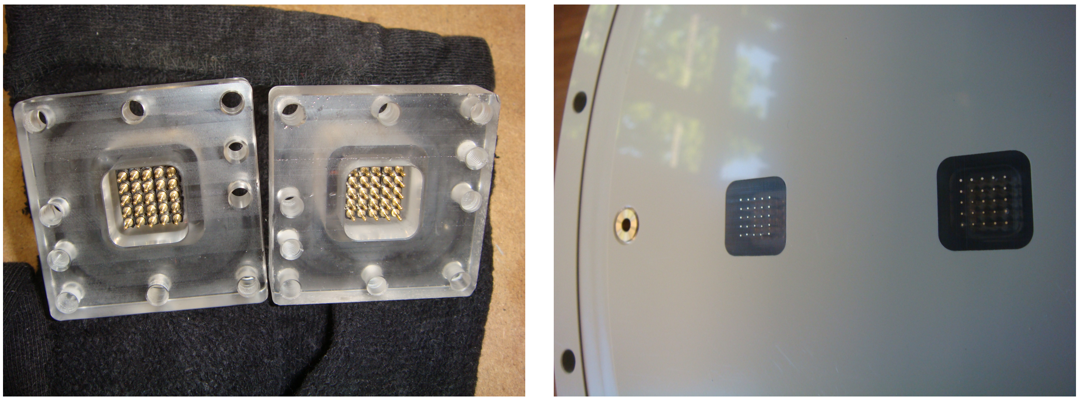

FIGURE 2.17: PDP probes. (a) Top view of the two inserts containing the two 5 × 5 PDP arrays. (b) Lower side of the top lid with the two inserts mounted flush. We only used data from the corners of the two arrays.

Obviously a good wetting and electrical contact with the liquid metal is crucial for the voltage measurements between the single pins. Here again, thorough cleaning is important. As described above, we were also concerned for a while with getting rid of the argon bubble trapped inside the container which prevented electrical contact. Another important observation was that using shielded cables (e.g. LAN cables, category 5e) alone is not enough to get optimal PDP recordings. When performing differential measurements, the cable to the reference (the inner electrode), which the electric potentials are measured against, should run in the same shielded cable. Only in this way, the ambient electromagnetic noise is cancelled out be differencing, and we can decrease the noise by roughly an order of magnitude to approximately 0.4 μV.

2.1.5.3 Further measurements

Further quantities that we tried to measure in the course of our experiments included dynamic pressure and induced magnetic fields. Both were tested only in the Caylar setup. The pressure probe 106B52 from PCB Piezotronics has a lower cut-off frequency of 2.5 Hz. Hence it could be possible to observe some of our signals at the highest forcing in the pressure recordings. Due to measurement noise, however, we were not able to get a useful signal.

For measurements of the induced magnetic field, the detectability of a signal depends a lot on the measured field component. Depending on the working principle of the sensor, it is not easy to measure a small induced b_z top of the large imposed B_z. A more convenient quantity to diagnose the flow is the radial component b_r or for instabilities even the azimuthal component b_ϕ. We tried to detect useful signals with the HE244 Hall sensors from Hoeben and Honeywell's anisotropic magnetoresistive (AMR) sensors HMC 1002 and 1022 which are even more sensitive. However, also for the induced magnetic field, we did not succeed in retrieving a useful signal in the Caylar setup. This might be due to the very small magnetic Reynolds numbers $Rm = \mathcal{O}(10^{-2})$ which prohibit having large induced fields. In the Cryo setup with $Rm = \mathcal{O}(10^{-1})$, it should be possible to detect induced signals.

During operation, we monitor continuously the temperature of the GaInSn tank. This is done by a K-type thermocouple mounted on the shaft of the central disk electrode using copper tape, and a standard multimeter. In the Caylar setup, the temperature of the tank was rising above 30°C in continuous operation due to the insufficient cooling of the resistive coils. In the Cryo setup, the room temperature was already lower due to the cooling of the superconductor. Due to the high forcing current up to 300 A, the GaInSn was heated up to 30°C.

2.2 Numerical techniques in complex geometries

In our study of the flow in ZUCCHINI, we use numerical simulations of the liquid metal MHD flow by the finite element method (FEM) to complement our experimental findings. For other numerical approaches to liquid metal MHD like effective two-dimensional models, we refer the reader to the references in Section 4.1. Based on the books by Hirsch [2007] and Zimmerman [2006], this section provides a short introduction to the FEM and motivates the use of COMSOL Multiphysics for our case.

2.2.1 Finite elements

The world around us is (at least macroscopically) a continuum in space and time. In the natural sciences, we try to capture phenomena and processes in empirical physical models. Typically these become manifest in mathematical equations. For liquid metal MHD flow, we find a system of partial differential equations (PDEs) consisting of the conservation of momentum (Navier-Stokes equation), mass (continuity equation) and charge complemented with Ohm's law (cf. Eqs. 1.41-1.44). It is rarely possible to find analytic solutions in arbitrary domains. For general flows, we need to turn to numerical solutions where we approximate continuous space and time by their discretized equivalents. One of these numerical methods is the finite element method.

The FEM originated from the field of structural analysis in the 1940s to 60s [Hrennikoff, 1941, Courant, 1943, Turner et al., 1956] where it was used to compute the distribution of stresses. It is, however, not restricted to this area but can be used to tackle various physical problems in arbitrary geometries. In the FEM, the model space is discretized into a number of contiguous elements of arbitrary shape. These elements form the mesh which need not be regular but can instead be unstructured. This makes the FEM convenient for modelling complex geometries.

The simplest elements in 2D and 3D are triangular and tetrahedral, respectively. In our 2D study of ZUCCHINI, we use triangular and quadrilateral elements for the core

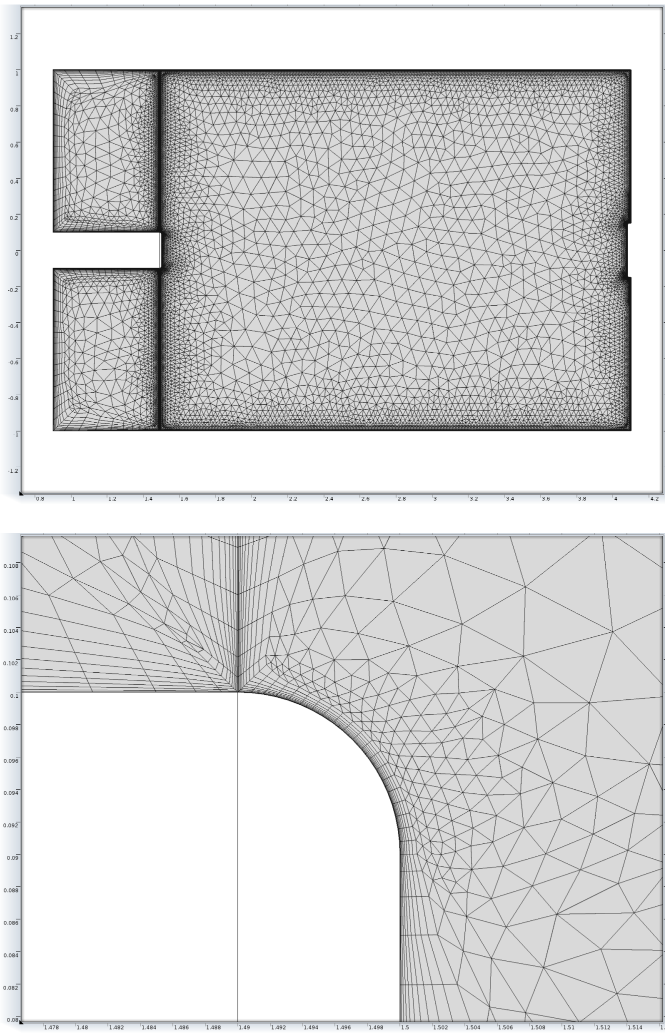
1.2
1
0.8
0.6
0.4
0.2
0
-0.2
-0.4
-0.6
-0.8
-1
-1.2
0.8
1
1.2
1.4
1.6
1.8
2
2.2
2.4
2.6
2.8
3
3.2
3.4
3.6
3.8
4
4.2
0.108
0.106
0.104
0.102
0.1
0.098
0.096
0.094
0.092
0.09
0.088
0.086
0.084
0.082
0.08
1.478
1.48
1.482
1.484
1.486
1.488
1.49
1.492
1.494
1.496
1.498
1.5
1.502
1.504
1.506
1.508
1.51
1.512
1.514

FIGURE 2.18: Finite element mesh used for our 2D axisymmetric parameter study, with appropriate resolution up to $M = 200$. It consists of 25308 triangular domain elements and 900 quadrilateral boundary elements. The boundary as well as the shear layers and the edges of the electrodes are refined.

of the flow and the boundary layers, respectively. An example mesh from our base flow study (Chapter 3) at a Hartmann number of $M = 200$ is shown in Figure 2.18. The use of different elements in the core and the boundary layers is due to desired properties for the different regions. In boundary layers, physical quantities have strong gradients along the direction perpendicular to the wall but not along it. It is desirable to decouple the errors in the two directions. Quadrilateral elements which can be conveniently elongated along the wall direction fulfill this requirement. In contrast, a coupling of the errors in different directions is desirable for more isotropic regions of the flow for better convergence. This is achieved by the usage of triangular elements for the core flow. Triangular elements also allow for unstructured meshes, thus facilitating the meshing of complex geometries.

The question remains where to change from triangular to quadrilateral elements. We determine the extent of the boundary layers by the theoretical scaling of their width which is $\delta_H = aM^{-1}$ and $\delta_S = aM^{-1/2}$ for the Hartmann and Shercliff layers, respectively, as reported in Sections 1.3.1f.; a is the half-height of the container and M the Hartmann number as discussed in the previous chapter. This approach is justified a posteriori by the retrieval of the scalings in the simulations at large M (cf. Fig. 3.7). A major issue is the numerical simulation of regions with strong gradients like the boundary layers of bounded flows. In our case, this is especially true for the Hartmann layers and the neighborhood of the electrodes where current is injected. Following Tagawa et al. [2002], we made sure that Hartmann layers are resolved by at least 5 elements in the wall-normal

Every finite element has the relevant material properties (ρ, ν and σ_e in our case) or nondimensional parameters (M and Re) prescribed. The corners of elements are called nodes. In the case of higher-order elements as used in our study, there are also nodes in between element corners which are then called edge nodes. For the unknown variables collected in the state vector $\mathbf{y}$, which in our case are the three velocity components $\mathbf{u}$, the pressure p and the potential Φ, a parametric representation is defined on every element based on a set of basis functions ϕ (also called interpolating or shape functions). For a simple one-dimensional problem this representation is given by

$$y(x) = \sum_i y_i \phi_i(x) \tag{2.2}$$

where i indexes the different elements. In constrast to e.g. spectral methods, this expansion is done element-wise with $\phi_i = 0$ in all elements but one. In our study, the basis functions ϕ are Lagrange polynomials

$$L_n(x) = \prod_{M=1, N \neq M}^{n} \frac{x - x_M}{x_N - x_M} \tag{2.3}$$

of orders $n = 1$ to 5, which explains the terms 'linear',... 'quintic Lagrange element'. The terms 'Pm + Pn' for the elements in the Navier-Stokes equation mean that velocity and pressure are parametrized by basis functions of order m and n, respectively. The order of an element influences the number of degrees of freedom (DOF) which essentially gives the number of unknown variables times the number of nodes they are defined on. The simplest element used in our study is P2+P1 which at the same time is the simplest element fulfilling the Ladyzhenskaya-Babuska-Brezzi condition which states that the basis functions for the pressure must be of lower order than the basis functions for the velocity; for details see Girault and Raviart [1986].

2.2.2 Weak formulation and solution

After the discretization of the model space and the parametrization of the unknown variables y by suitable basis functions ϕ, the governing equations need to be solved in the finite elements. This is often done by transforming the equations to their weak form. We will detail what that means. In our case, the 'strong form' of the equations is given by the system in 1.45-1.47. It is called 'strong' because variables y have to be continuous and have continuous derivatives up to the order of the equation, which is a strong constraint. The 'weak form' relaxes this condition to the weaker one that discontinuities must be integrable. This makes it a convenient tool to study e.g. shock phenomena.

The weak form is derived from the strong form through multiplication by a weight function w and integration over the domain Ω. In this way, a general example PDE in one dimension

$$\frac{\partial}{\partial x}\Gamma(y) = F(y) \tag{2.4}$$

with potentially nonlinear functions $\Gamma(y)$ and $F(y)$ is transformed to its weak form

$$\int_{\Omega} w \, \frac{\partial}{\partial x}\Gamma(y) \, \mathrm{d}x = \int_{\Omega} w \, F(y) \, \mathrm{d}x. \tag{2.5}$$

Equation 2.5 must hold for every weight function w. Different choices of w lead to different methods. We use Galerkin's method in which the weight functions w are chosen to be the same as the basis functions ϕ in the expansion of the unknown variables (Eq. 2.2). The terms resulting from the evaluation of Equation 2.5 on the different elements are assembled in a matrix and inverted numerically. The whole process is conveniently handled internally in COMSOL Multiphysics.

In our study, we used the matrix solvers MUMPS (MUltifrontal Massively Parallel sparse direct Solver, `http://mumps.enseeiht.fr/`) and PARDISO (PARallel DIrect sparse SOlver, `www.pardiso-project.org/`). Time stepping was done by the BDF (Backward Differentiation Formula)

$$\sum_{i=0}^{q} \alpha_{l,i} \, y_{l-i} = h_l \, \dot{y}_l \tag{2.6}$$

where y_l and $\dot{y}_l$ are the computed approximations to $y(t_l)$ and $\dot{y}(t_l)$, respectively, and the step size is $h_l = t_l - t_{l-1}$. The coefficients $\alpha_{l,i}$ are uniquely determined by the order q and the history of the step sizes, see Hindmarsh et al. [2005]. We used BDF with variable order q from 1 to 5 which is adjusted automatically in COMSOL Multiphysics. Choosing higher orders q allows for bigger step sizes and hence less computation time. Although BDF is known to be absolutely stable only up to order 2, we did not encounter problems with instabilities caused by the time stepping.

2.2.3 Specific options in COMSOL

In this section, we give a short overview of the model setup in COMSOL and special options used. The geometry, which in our case is a 2D cross-section through the ZUCCHINI tank, is created by adding and subtracting simple geometrical shapes to and from each other. Monitoring and output quantities (e.g. kinetic energy) can be defined as 'probes' in the model, i.e. functions evaluating the solved variables y on a defined volume. It is convenient to define fixed parameters and variables coupling the different physics modules globally.

We use the modules 'Laminar Flow' and 'Electrostatics' which contain the relevant Equations 1.45-1.47 for liquid metal MHD when coupled by the Lorentz force and the right-hand side term of the Poisson equation 1.47. We simulate a 2D cross-section of ZUCCHINI but we need to retain all 3 velocity components in order to have the dominant u_ϕ, which explains the name '2D3C simulations'. This is achieved by ticking the box 'Swirl flow' in the laminar flow module. Boundary and initial conditions are specified in the relevant menu items. The Lorentz force term in Equation 1.45 is introduced as a volume force in the laminar flow module. The coupling term on the right-hand side of Equation 1.47 is introduced as a space charge density in the electrostatics module. Finally it is advantageous to define a pressure point constraint e.g. in the middle of the channel in the laminar flow module since the pressure otherwise is only defined up to an additional constant which can cause problems in COMSOL looking for an initial state.

The meshing is taken care of automatically in COMSOL. However, it can be useful to refine the mesh in certain regions, e.g. boundary and shear layers as discussed above. The meshing options can be defined on parameters. This is convenient when performing a parametric sweep over various parameter values of e.g. the Hartmann number M, the Reynolds number Re or the number of boundary elements during the solution. The menu items under 'Study' also facilitate the choice of various direct and iterative solvers as well as their options. Also it is convenient to define output tables and data sets at this stage. In the 'Results' section, post-processing is implemented including various plotting routines.

The first step in our numerical simulations of the base flow (Section 3.3) and the linear stability (Sec. 4.3) in ZUCCHINI was a convergence study (cf. Sec. 3.C). There we determine the numerical convergence when changing various features of the mesh and the geometry as well as the order of the elements. In general, it is a good idea to avoid abrupt changes in space and time by e.g. rounding the electrode edges and applying ramps to time-dependent signals as discussed in the concerning sections. Mostly the smoothed features are also closer to reality where discontinuities are rare.

Moreover it can be useful to apply consistent stabilization to the Navier-Stokes equation by streamline and crosswind diffusion as offered in COMSOL (cf. Section 3.C).

Adding a small amount of artificial diffusion in the streamline and cross direction, respectively, can help to avoid numerical instabilities (oscillations) for convection-dominated transport problems [Hauke and Hughes, 1994]. This can discard spurious solutions which are true solutions of the weak form but not the strong form of the equations. The amount of artificial diffusion added depends on the mesh size, and is handled automatically by COMSOL. Streamwise and crosswind diffusion are especially useful in areas of imperfect meshing like sharp edges and boundary layers. Both are consistent stabilization methods, meaning that they give less numerical diffusion the closer the numerical solution comes to the exact one. In this way, the numerical solution is aided to converge faster (or at all) to the real one.

We ran our computations on a Macintosh Pro with two 6-core Intel Xeon processors of 2.66 GHz each and 32 GB memory. The models in the parameter study of the base flow (Section 3.3.2) have 10^6 DOF which was found to be a good compromise between accuracy and computation time in the convergence study (Section 3.C). In the linear stability study (Section 4.3.3), the larger number of computations required a reduction of the models to $[1.6, 3.1] \cdot 10^5$ DOF depending on the Hartmann number M while retaining a good level of accuracy.

2.2.4 Concluding remarks on the FEM

In conclusion, the FEM is a flexible method to solve the governing equations of multiple interacting physical processes in arbitrary geometries. However, one drawback that should not be omitted here, is that the FEM with Lagrange elements as used here, in contrast to the finite volume method (FVM) or Nédélec elements, does not inherently conserve flux. This becomes apparent in our convergence study (Section 3.C) where charge conservation is violated in the range of up to a few percent. Avoiding this, however, would come at the price of more complicated boundary conditions and having to deal with three components of a vector potential instead of only one electric potential as in our case.

An important advantage of the FEM implementation in COMSOL Multiphysics is that high-order accuracy is readily provided. Moreover the implementation facilitates the setup of realistic geometries, and takes care of the meshing, assembling and numerical solution including stability issues as well as the post-processing, which makes its use efficient in terms of user time. Hence the FEM is very handy for our engineering-type problem.

References

R. Courant. Variational methods for the solution of problems of equilibrium and vibrations. *Bulletin of the American Mathematical Society*, 49:1–23, 1943.

DOP3000 series User's manual. DOP Signal Processing S.A., www.signal-processing.com, software 4.01 edition.

V. Girault and P. Raviart. *Finite Element Methods for Navier-Stokes Equations. Theory and Algorithms.* Springer, 1986.

G. Hauke and T. Hughes. A unified approach to compressible and incompressible flows. *Comp. Meth. Appl. Mech. Engrg.*, 113:389–395, 1994.

A. Hindmarsh, P. Brown, K. Grant, S. Lee, R. Serban, D. Shumaker, and C. Woodward. Sundials: Suite of nonlinear and differential/algebraic equation solvers. *Transactions on Mathematical Software*, 31(3):363–396, 2005.

C. Hirsch. *Numerical Computation of Internal and External Flows.* Elsevier Science Publishers, 2007.

A. Hrennikoff. Solution of problems of elasticity by the framework method. *Journal of Applied Mechanics*, 8(4):169–175, 1941.

P. Moresco and T. Alboussiere. Experimental study of the instability of the Hartmann layer. *J. Fluid Mech.*, 504:167–181, Jan 2004.

N. B. Morley, J. Burris, L. C. Cadwallader, and M. D. Nornberg. Gainsn usage in the research laboratory. *Review of Scientific Instruments*, 79(5), 2008.

J. Shercliff. *The theory of electromagnetic flow-measurement.* Cambridge University Press, 1987.

F. Stefani, T. Gundrum, G. Gerbeth, G. Rüdiger, M. Schultz, J. Szklarski, and R. Hollerbach. Experimental evidence for magnetorotational instability in a taylor-couette flow under the influence of a helical magnetic field. *Phys. Rev. Lett.*, 97(18), Nov 2006.

T. Tagawa, G. Authie, and R. Moreau. Buoyant flow in long vertical enclosures in the presence of a strong horizontal magnetic field. Part 1. Fully-established flow. *European Journal of Mechanics - B/Fluids*, 21(4):383–398, 2002.

M. Turner, R. Clough, H. Martin, and L. Topp. Siffness and deflection analysis of complex structures. *Journal of the Aeronautical Sciences*, 23(9):805, 1956.

W. B. J. Zimmerman. *Multiphysics Modelling with Finite Element Methods.* World Scientific, 2006.

Chapter 3

The base flow in ZUCCHINI

Manuscript:

Experimental and numerical study of electrically-driven MHD flow in a modified cylindrical annulus: (1) Base flow

by **Zacharias Stelzer**, David Cébron, Sophie Miralles, Stijn Vantieghem, Jérôme Noir, Peter Scarfe and Andrew Jackson

For submission to *Physics of Fluids.*

Summary

Shear layers in confined liquid metal MHD flow play an important role in geo- and astrophysical bodies as well as in engineering applications. We present an experimental and numerical study of liquid metal MHD flow in a modified cylindrical annulus which is driven by an azimuthal Lorentz force resulting from a forced electric current under an imposed axial magnetic field. Hartmann and Reynolds numbers reach $M_{max} = 2022$ and $Re_{max} = 2.23 \cdot 10^5$ respectively. The peculiarity of our model geometry is the inner disk electrode which gives rise to a free Shercliff layer at its edge. The flow of liquid GaInSn in the experimental device ZUCCHINI (ZUrich Cylindrical CHannel INstability Investigation) is probed with ultrasound Doppler velocimetry. The threshold of instability, which is studied in a follow-up paper [Stelzer et al., in prep.], occurs at a few Amperes.

We establish the base flow in ZUCCHINI and study the scaling of velocities and the free Shercliff layer in both experiment and finite element simulations. Experiment and numerics agree well on the mean azimuthal velocity $\overline{u_\phi}(r)$, but differ in radial and axial velocities, u_r and u_z. In the numerics, we recover the theoretical free Shercliff layer width $\delta_S \sim M^{-1/2}$ whereas δ_S does not appear to depend on M in the experiment. In general, the transition to the theoretically predicted large-M limit, which is equivalent to neglecting inertial effects and the recirculation flow (u_r, u_z), occurs at larger $M \gtrsim 1000$

in the experiment than in the numerics ($M \gtrsim 50$). A special flow feature, only appearing in the experiment at large M, is the jet near the outer cylinder which is shown to be caused by the field inhomogeneity in the coil.

3.1 Introduction

Magnetohydrodynamics (MHD) is the subject concerned with the interplay of electrically conducting fluids and magnetic fields. Interest in MHD arises from geo- and astrophysical contexts as well as from engineering applications. In the field of geo- and astrophysics, Larmor [1919] proposed an MHD dynamo to explain the generation of magnetic fields in the Sun and the Earth. Today this theory is widely accepted and supported by numerical and experimental evidence; for a review see Olson [2007].

In the area of engineering, the advent of liquid metal MHD came with Hartmann's invention of the electromagnetic conduction pump around 1915 [Moreau and Molokov, 2007] and his two seminal articles on 'Hg dynamics' [Hartmann, 1937, Hartmann and Lazarus, 1937]. Since then MHD has found various applications in metallurgy and material processing, liquid metal blankets of fusion reactors as well as electromagnetic flow meters and pumps [Davidson, 2001].

Most liquid metal experiments operate in the 'quasi-static' regime where the induced magnetic field is negligible compared to the imposed field. It is characterized by small magnetic Reynolds numbers $Rm = \mu_0 \sigma_e U_0 a \ll 1$ where $\mu_0 = 4\pi \cdot 10^{-7}$ Hm^{-1} is the permeability of free space, σ_e the conductivity of the fluid, a the half-height of the container and U_0 a typical velocity in the system. Despite not being dynamo-capable, this regime is relevant for the dynamics of Earth's core since it governs the small-scale motions [Davidson and Siso-Nadal, 2002]. The Hartmann number is defined as

$$M = aB_0 \sqrt{\frac{\sigma_e}{\rho\nu}} \tag{3.1}$$

where B_0 is the imposed magnetic field strength, ρ the mass density and ν the kinematic viscosity of the fluid. Strong magnetic fields ($M \gg 1$) tend to make the flow uniform (quasi-2D) along the direction of the field $\mathbf{B}$. The presence of walls perpendicular and parallel to $\mathbf{B}$ leads to Hartmann and Shercliff layers (also called 'side layers'). The thickness of these layers scales as $\delta_H \sim M^{-1}$ and $\delta_S \sim M^{-1/2}$ respectively for large M [Hartmann, 1937, Shercliff, 1953].

Since the pioneering work of Hartmann, various studies considered laminar pressure-driven MHD flow in straight channels and ducts subject to different electrical boundary conditions [Shercliff, 1953, Hunt, 1965, Hunt and Stewartson, 1965, Hunt and Williams, 1968]. Using a boundary-layer technique, Hunt and Stewartson [1965] studied a duct with walls perpendicular to $\mathbf{B}$ being electrically insulating and parallel walls conducting, and derived expressions for the flow rate in the form of an asymptotic expansion in the limit of large M (neglecting secondary flows). Amongst other setups, they considered the purely electrically-driven case of an MHD pump, which is also the driving mechanism in ZUCCHINI.

In order to avoid entrance effects which are always present in straight duct experiments, other studies employed closed geometries like cylindrical ducts or spherical shells. Following the narrow-gap experiment of Baylis [1964], Baylis and Hunt [1971] performed the first concise study of flow in a cylindrical annulus with rectangular cross section. Walls perpendicular to $\mathbf{B}$ were again electrically insulating, parallel walls conducting used to force the flow. As in [Hunt and Stewartson, 1965], Baylis and Hunt [1971] worked in the large-M limit in order to neglect secondary (radial and axial) flows. Their condition for inertial effects to be negligible was $\left(K/M^2\right)^2 \lambda \ll 1$ with the Dean number $K = \lambda^{1/2} Re$ measuring curvature effects, the curvature ratio $\lambda = b/r_m$ of channel half-width b to mean radius r_m, and the Reynolds number Re (Eq. 3.9). Under these assumptions, they found an expression for the azimuthal velocity in the core of the flow (cf. Eq. 3.13). In their theoretical model, Baylis and Hunt [1971] additionally took into account the Hartmann and side layers. By comparing the resulting flow rate with experimental data from Baylis [1971], they confirmed the asymptotic theory for the side layer [Hunt and Stewartson, 1965].

A further theoretical study of laminar MHD flow in annular ducts with rectangular cross section was undertaken by Tabeling and Chabrerie [1981]. Also using a boundary-layer technique, they focused on the secondary flows, which Baylis and Hunt [1971] had neglected, in the high-M regime. Tabeling and Chabrerie [1981] employed a perturbation method containing expansions in ascending powers of the curvature ratio λ. They derived the velocities in the core and the Hartmann layers, and found that secondary flows in these regions are dominantly one-dimensional (suppression of u_z). For the side layers, secondary flows are far more intense. The secondary flow structure and the number of eddies in the side layer depends on the conductivities of the walls. In the case applying to ZUCCHINI (Hartmann walls insulating, side walls partly insulating), the secondary flow in this region was predicted to consist of a single eddy. The expansion in terms of ascending powers of λ in the perturbation method of Tabeling and Chabrerie [1981] converges if $K/M^{5/4} \ll 1$ which is a more stringent criterion for inertial effects to be negligible than the one in [Baylis and Hunt, 1971].

Numerical studies of quasi-static MHD flow in cylindrical geometries were performed using direct numerical simulation [Krasnov et al., 2004, Vantieghem and Knaepen, 2011, Zhao and Zikanov, 2012]. Other authors [Khalzov et al., 2010] employed the effective 2D model for low-Rm MHD flows which conveniently incorporates boundary layer and recirculation effects [Potherat et al., 2000]. We will reference these studies in more

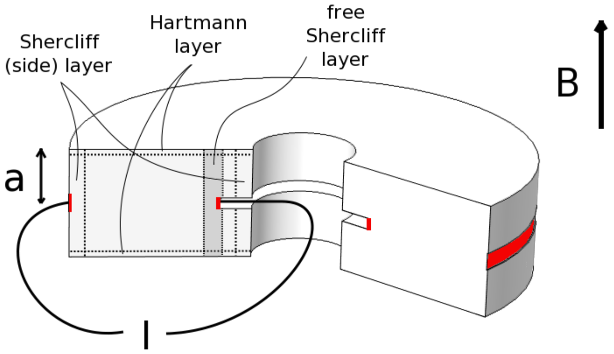

FIGURE 3.1: Sketch of the modified cylindrical annulus ZUCCHINI. Forcing an axisymmetric electrical current I through the liquid metal under an imposed magnetic field $\mathbf{B}$ gives rise to a Lorentz force which drives an azimuthal flow. The electrodes are coloured in red, the remaining walls are insulating. The half-height a is used as length scale.

detail in the follow-up paper [Stelzer et al., in prep.] termed 'Paper 2' which addresses instabilities and flow transitions in our experiment.

In recent years, there have been three experimental studies of electrically-driven MHD flow in cylindrical annuli: Moresco and Alboussiere [2004] studied the stability of the Hartmann layer which we will come back to in Paper 2. Boisson et al. [2012] observed travelling waves in a narrow-gap annulus. Mikhailovich et al. [2012] studied the decay of mean velocity components and turbulent fluctuations. All of these experiments have in common with Baylis and Hunt [1971] the simple geometry with straight conducting side walls.

In contrast, ZUCCHINI features modified cylindrical side walls with a disk electrode at the inner cylinder and a ring electrode at the outer one, coloured in Figure 3.1; all remaining walls are insulating. This gives rise to a free shear/Shercliff layer at the edge of the disk electrode. In this respect, our experiment is more similar to the MATUR experiment of Messadek and Moreau [2002] who studied the quasi-2D turbulent behaviour occuring in cylindrical shear flow resulting from the injection of electrical current in the bottom plate. As a consequence of energy transfer to the large scales, they observe a relatively small number of large coherent structures.

An overview of the dimensions and parameters of the previous experiments and ZUCCHINI is given in Table 3.1; the latter reaches Hartmann numbers that are more than double the ones of the other experiments. Another novel feature of our experiment is that we employ three UDV probes which enable us to recover profiles of radial and axial velocities through the free shear layer as well as the radial profile of mean azimuthal velocity in the core flow.

ZUCCHINI serves as a prelude and comparison point for an experiment of electrically-driven liquid sodium flow in a rapidly rotating spherical shell along the lines of Hollerbach

Table 3.1: Parameter values of experimental studies. Height $h = 2a$, outer radius r_o and width d of duct, maximum magnetic field strength B_{max}, as well as resulting maximum Hartmann number M^*_{max} and liquid metal used. Note: The definition of the Hartmann number used in this table is $M^* = 2M$, double the Hartmann number M (Eq. 3.1) used throughout the paper, since M^* was reported in the previous studies. Hg is mercury, PD(P) potential difference (probes).

	h in cm	r_o in cm	d in cm	B_{max} in T	M^*_{max}	I in A	fluid	measurements
Baylis [1964]	5	2.7	0.12	0.5	15	up to 30	Hg	global PD
Baylis [1971]	0.39-3.1	7	0.39-3.1	0.4	128	0.1-110	Hg	global PD
Moresco and Alboussiere [2004]	1	5	1	13	1690	650	Hg	global PD, pressure
Boisson et al. [2012]	12	4	1.2	0.15	460	50	GaInSn	UDV
Mikhailovich et al. [2012]	6.25	3.525	3.125	0.125	160	120	GaInSn	local PDP
Messadek and Moreau [2002]	1	11	5.6, 1.7 (11)	6	1800	10-70	Hg	local PDP
ZUCCHINI (this work)	10	20.5	13 (16)	1	4000	300	GaInSn	UDV, local PDP

et al. [2013]. The latter with its acronym SpiNaCH is designed to study the 'magnetostrophic regime', i.e. a balance between Coriolis and Lorentz forces, which is believed to govern the motions of liquid metal in the Earth's outer core. In this sense, it is similar to the DTS experiment [Nataf et al., 2008].

This paper focuses on the steady and axisymmetric base flow in ZUCCHINI; instabilities are considered in the follow-up Paper 2. We describe the physical model underlying this work in Section 3.2. The model is studied numerically (3.3) and experimentally (3.4). Since it is relevant also for Paper 2, it seems in order to detail the experimental setup and our handling of liquid GaInSn (3.4.1) as well as the measurements devices and procedure (3.4.2). We finish the paper by comparing numerical and experimental results (3.4.4) and drawing some conclusions on the base flow (3.5).

3.2 Model description

The physical model studied here by numerical simulations and laboratory experiments is a cylindrical annulus filled with an electrically conducting fluid. The basic setup is shown in Figure 3.1. Container and fluid are subject to an imposed axial magnetic field $\mathbf{B} = B_0\mathbf{e}_z$ with a strength of up to 1 T. We force an electrical current I of up to 300 A between the edge of the disk electrode at the center and the ring electrode at the outer cylinder. The remaining walls of the container are electrically insulating. The radial current in an axial magnetic field gives rise to a Lorentz force $\mathbf{f_L} = \mathbf{j} \times \mathbf{B}$ in azimuthal direction resulting in an azimuthal fluid flow.

The governing equations of the system are the Navier-Stokes equation including the Lorentz force $\mathbf{f_L}$, the incompressible continuity equation, Ohm's law and the equation of charge conservation,

$$\rho\left(\frac{\partial \mathbf{u}}{\partial t} + \mathbf{u}\cdot\nabla\mathbf{u}\right) = -\nabla p + \rho\nu\nabla^2\mathbf{u} + \mathbf{j}\times\mathbf{B} \tag{3.2}$$

$$\nabla\cdot\mathbf{u} = 0 \tag{3.3}$$

$$\mathbf{j} = \sigma_e\left(\mathbf{E} + \mathbf{u}\times\mathbf{B}\right) \tag{3.4}$$

$$\nabla\cdot\mathbf{j} = 0, \tag{3.5}$$

where $\mathbf{u}$ is the velocity vector, $\mathbf{E}$ is the electric field and p is the pressure. We are working in the quasi-static approximation ($Rm \ll 1$) where induced magnetic fields are negligible and the field is entirely given by the imposed field $\mathbf{B}$. In this case, $\nabla\times\mathbf{E} = -\partial\mathbf{B}/\partial t = 0$, so that the electric field can be written as the gradient of a potential Φ as $\mathbf{E} = -\nabla\Phi$.

Charge conservation (Eq. 3.5) can be exploited to eliminate the current density $\mathbf{j}$ from Ohm's law (Eq. 3.4). In contrast to the full MHD equations, the system then only contains one electromagnetic variable. Following this path and using the half-height a, the imposed magnetic field strength B_0 and a typical velocity U_0 as scales, Eqs. 3.2-3.5 are rewritten in nondimensional form,

$$\begin{aligned}\frac{Re}{M^2}&\left(\frac{\partial \mathbf{u}}{\partial t}+\mathbf{u}\cdot\nabla\mathbf{u}\right)\\ &=-\nabla p+\frac{1}{M^2}\nabla^2\mathbf{u}+(-\nabla\Phi+\mathbf{u}\times\mathbf{B})\times\mathbf{B} \qquad (3.6)\\ \nabla\cdot\mathbf{u}&=0 \qquad (3.7)\\ \nabla^2\Phi&=\nabla\cdot(\mathbf{u}\times\mathbf{B})\,. \qquad (3.8)\end{aligned}$$

Appendix 3.A states the governing equations explicitly in cylindrical coordinates. The nondimensional parameters governing the system are the Hartmann number M (Eq. 3.1) and the Reynolds number

$$Re=\frac{U_0 a}{\nu}. \qquad (3.9)$$

The square of the Hartmann number M^2 gives the ratio of Lorentz to viscous forces. The Reynolds number Re is the ratio of inertial to viscous forces. Alternatively the interaction parameter $N=M^2/Re$ can be used which gives the ratio of Lorentz to inertial forces. Using mean azimuthal velocities $\langle\overline{u_\phi}\rangle$ as velocity scale U_0, we reach $Re=2.23\cdot10^5$ at highest current and magnetic field ($M=2022$) in the experiment.

3.3 Numerical simulation

We perform numerical simulations using the commercial finite element (FE) code Comsol Multiphysics (version 4.3b) in order to gain a more detailed insight into the structure of the base flow encountered in the experiment. The FE method facilitates the implementation of complex geometries. A drawback is that flux is not automatically conserved.

3.3.1 Numerical model

The system of equations to be solved in the geometry of our modified cylindrical annulus is given in Eqs. 3.6-3.8 with $\mathbf{B}=\mathbf{e}_z$. In the first step (this paper), we are only interested in the base flow which in ZUCCHINI is assumed to be steady and axisymmetric. Hence we choose to perform axisymmetric simulations ($\partial/\partial\phi=0$) of a cross-section in the (r,z)-plane, but allowing for non-zero u_ϕ; such calculations are often referred to as 2D3C (2 dimensions, 3 components) simulations.

The nondimensional Navier-Stokes Equation (Eq. 3.6) contains the Reynolds number Re as a control parameter which by definition (Eq. 3.9) requires a choice of velocity scale U_0. However, the velocity is an output of the simulation rather than an input. Hence we use dimensional considerations to define the velocity scale as $U_0=j_0(\sigma_e B_0)^{-1}$ yielding an ‘input Reynolds number’

$$Re_i = \frac{U_0 a}{\nu} = \frac{j_0 a}{\nu \sigma_e B_0} \tag{3.10}$$

which controls the inertial term in Eq. 3.6. The scale j_0 is taken as the electric current density at the inner electrode $j_0 = I_0/A_{ei}$ where I_0 is the imposed current and A_{ei} the surface area of the inner electrode. Our study will show that Re_i in general does not scale in a simple way with the output parameter Re.

The governing equations need to be amended with mechanical as well as electrical boundary conditions. The mechanical boundary condition for all walls is no slip, $\mathbf{u} = \mathbf{0}$. For the electrical boundary conditions, we choose $-\nabla\Phi = \mathbf{e_r}$ which means that we impose j_0 at the inner electrode. The outer electrode is set to ground, $\Phi = 0$. A detailed reasoning for this choice is given in Appendix 3.B. The remaining walls are insulating and have to fulfill the dimensionless electrical boundary condition $-\mathbf{n} \cdot \nabla\Phi = 0$. The initial conditions are $\mathbf{u} = \mathbf{0}$ and $p, \Phi = 0$ in the whole geometry.

The model geometry is a cross-section in the (r, z)-plane of the container (Fig. 3.1) chosen to be as close to the experimental setup as possible meaning that it has the same shape and aspect ratio. Two minor differences have been introduced. The first is that in the numerics also the outer electrode protrudes the wall whereas in the experiment it is mounted flush. Translated into dimensional units, however, this modification amounts to only 1 mm of prominence. The second difference consists in a specified rounding of the electrode edges with a curvature radius of 0.5 mm (dimensionalized) in the numerics. This additional part with conducting boundary conditions was found to yield a higher degree of charge conservation (Eq. 3.5). The amount of rounding on the experimental disk electrode might, however, be of similar size.

As a result of the convergence study (Appendix 3.C), we use Lagrange elements of orders three and two for the discretization of velocity and pressure, and quintic elements for the electrical potential. The mesh is triangular and quadrilateral in the core and the boundary layers respectively.

3.3.2 Parameter study

We conduct a parameter study varying Hartmann and ‘input Reynolds’ (Eq. 3.10) number over two to three orders of magnitude, $M = \{1, 3, 10, 20, 50, 100, 150, 200\}$ and $Re_i = \{1, 3, 10, 30, 100, 300, 1000\}$ resulting in 56 parameter combinations. The numerical model is the one described in Section 3.3.1 which was found from the convergence study where mainly the order of discretization and the mesh size were varied (Appendix 3.C). It consists of 25308 domain elements and 900 boundary elements, and has roughly 10^6 degrees of freedom. The advantage of 2D3C simulations is that they can be run on a single node with every model running for less than 2 CPU hours. After applying the

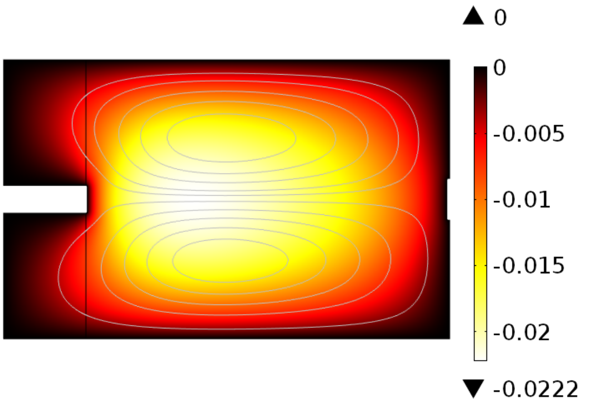

(a)

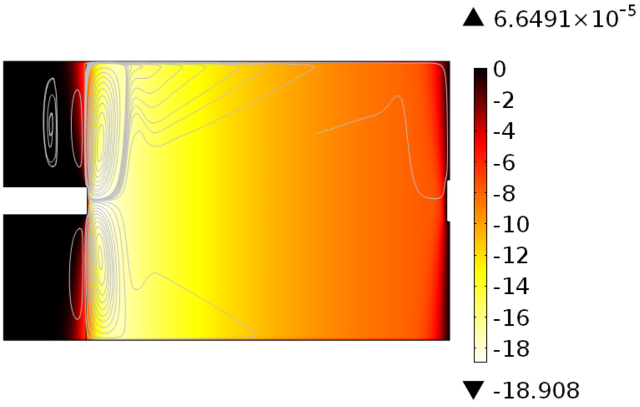

(b)

FIGURE 3.2: Nondimensional velocity **u** in the numerical simulation at $Re_i = 10$ and varying M: (a) $M = 1$, (b) $M = 200$. The colour scale shows u_ϕ, the streamlines u_r and u_z. At large M, thin Hartmann and Shercliff layers develop, and the core flow becomes uniform along the direction of the magnetic field.

quality criteria described in Appendix 3.C, we are left with 51 models which have all reached a steady state solution ($\partial/\partial t = 0$).

3.3.2.1 Flow structure

One major reason for the numerical study of the base flow expected in ZUCCHINI is to find the distribution of velocities for different magnetic field strengths. Figure 3.2 shows u_ϕ (colour) as well as u_r and u_z (streamlines) for models with $Re_i = 10$ and different M. It is $u_\phi \gg u_r, u_z$, and the flow structure is similar at other Re_i. Increasing M leads to thinner Hartmann and Shercliff layers (for their scaling, see Section 3.3.2.4), and the core flow is more and more two-dimensionalized along the direction of the magnetic field (z-direction). In the regime of large M, the electric current does not flow through the bulk of the fluid but is concentrated in the Hartmann and Shercliff layers as shown in Figure 3.3.

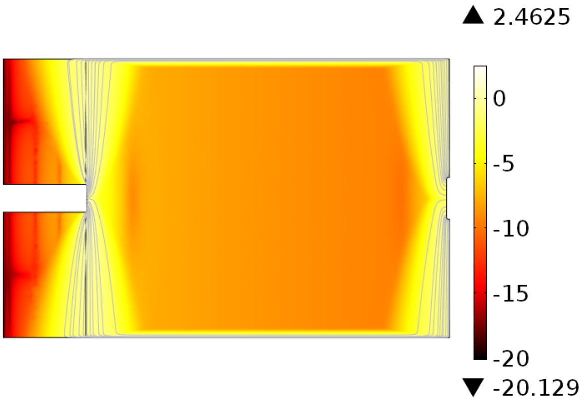

FIGURE 3.3: Nondimensional electrical current density in the numerical simulation at $M = 200$, $Re_i = 10$ (cf. Fig. 3.2b). The colour-coded quantity is $\log_{10} \mathbf{j}^2$ with grey streamlines of (j_r, j_z) superimposed to make the Hartmann and Shercliff layers visible which contain virtually the entire electrical current.

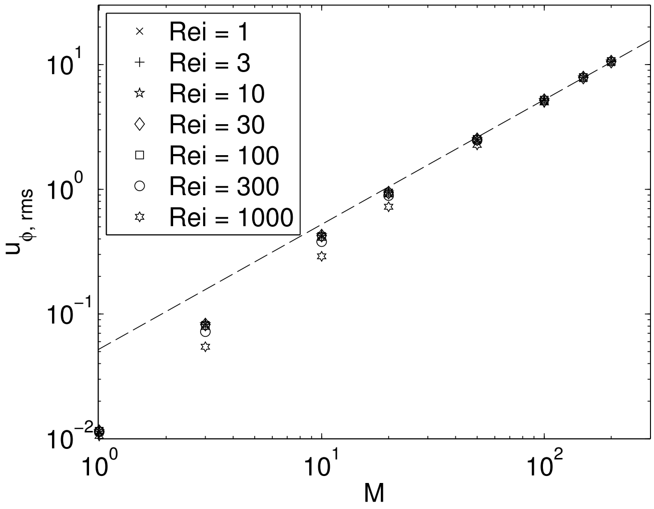

FIGURE 3.4: Nondimensional azimuthal rms velocity $u_{\phi,rms}$ as function of the Hartmann number M. For large M, $u_{\phi,rms} = 0.0523\,M$ (dashed line). At moderate $M = \mathcal{O}(1-10)$, the scaling exponent of M is larger than 1 (at least 1.5), and high Re_i show lower $u_{\phi,rms}$.

The (weak) recirculation flow in the (r, z)-plane has almost the same strength between inner and outer electrode at moderate $M = \mathcal{O}(1)$. But it becomes concentrated near the inner electrode for large M. The two large recirculation cells ($z < 0$ and $z > 0$) present at moderate M break up into several cells when increasing M.

3.3.2.2 Scaling of azimuthal velocity

For the study of the velocity scaling with the input parameters, we define nondimensional rms (root-mean-square) velocities as $u_{i,rms} = (2E_{kin,i}/S)^{1/2}$ where S is the nondimensional area of the 2D section, and the component-wise kinetic energy is $E_{kin,i} = 0.5 \int u_i^2 \mathrm{d}S$ with $i = \{r, \phi, z\}$.

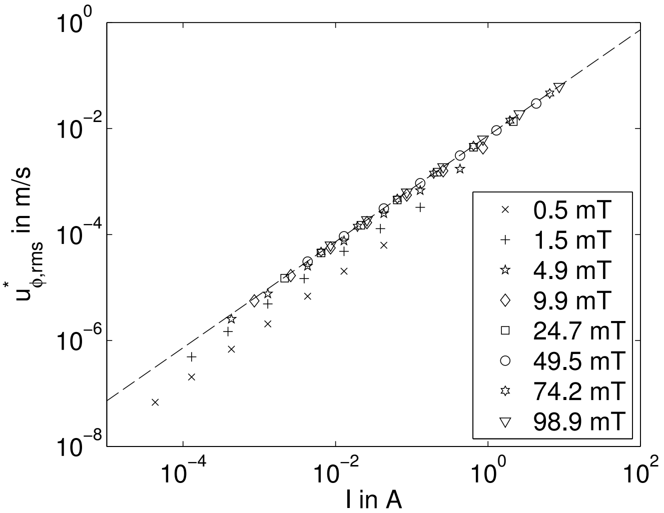

FIGURE 3.5: Dimensional azimuthal velocity $u^*_{\phi,rms}$ as function of the forcing current I. The dashed line shows a linear fit $u^*_{\phi,rms} = 7.32 \cdot 10^{-3}$ m(As)$^{-1} \cdot I$ to the data at highest magnetic field value used in the parameter study, $M = 200$.

Figure 3.4 shows $u_{\phi,rms}$ as a function of M for different values of Re_i. For large M, the dominant dependency is linear,

$$u_{\phi,rms} = (5.23 \pm 0.02) \cdot 10^{-2}\, M. \tag{3.11}$$

In the linear regression, the offset and exponent were forced to zero and one respectively. Departures from the linear scaling are observed at moderate $M = \mathcal{O}(1-10)$, where $u_{\phi,rms}$ scales with an exponent of at least 1.5. For moderate M and low Re_i, the scaling of $u_{\phi,rms}$ with M is even steeper. In the regime of moderate M and high $Re_i \gg 1$, $u_{\phi,rms}$ also depends on Re_i.

In the experimental study (Sec. 3.4), it will be easier to extract mean quantities than rms values. A comparison of the nondimensional mean azimuthal velocity $\overline{u_\phi}$ with the rms velocity $u_{\phi,rms}$ considered here is given in Appendix 3.D. In conclusion, $\overline{u_\phi}$ scales in the same way as $u_{\phi,rms}$.

For the comparison with theory and experiments, we also give the dimensional azimuthal velocity $u^*_{\phi,rms}$. The scaling of the nondimensional azimuthal velocity, $u_{\phi,rms} = \beta_1 M$, transforms to a scaling for $u^*_{\phi,rms}$ as

$$\begin{aligned} u^*_{\phi,rms} &= U_0 u_{\phi,rms} = \beta_1 M U_0 \\ &= \beta_1 \frac{a j_0}{\sqrt{\sigma_e \rho \nu}} = \beta_1 \frac{a I_0}{A_{ei}\sqrt{\sigma_e \rho \nu}}. \end{aligned} \tag{3.12}$$

This implies that the dimensional velocity $u^*_{\phi,rms}$ does not depend on the magnetic field strength at first order, but scales linearly with j_0 or the imposed current I_0 instead.

Figure 3.5 shows the scaling of the dimensional azimuthal velocity $u^*_{\phi,rms}$ with the forcing current I. In the limit of high magnetic fields ($B_0 \gtrsim 25$ mT, $M \gtrsim 50$), the linear scaling $u^*_{\phi,rms} = \beta^*_1 I$ is confirmed where the proportionality factor is $\beta^*_1 = 7.32 \cdot 10^{-3}$ m(As)$^{-1}$. For lower magnetic fields, the azimuthal velocity only reaches a fraction of this value.

A short comparison to a simple theoretical model for u^*_ϕ seems in order. Baylis and Hunt [1971] studied electrically-driven MHD flow in a rectangular annulus with two differences to our setup. Firstly the aspect ratio was different in their model, and secondly their electrodes extended over the whole surface of the inner and outer side walls at radii r_1 and r_2 (their nomenclature), respectively. Considering the limit of high M and neglecting axial and radial velocities, they found

$$u^*_\phi(r) = \frac{I}{4\pi r\sqrt{\sigma_e \rho \nu}} \tag{3.13}$$

for the azimuthal velocity in the core of the flow. Integration leads to

$$u^*_{\phi,rms} = \frac{\sqrt{2\ln\left(r_2/r_1\right)}}{4\pi\sqrt{\sigma_e \rho \nu (r_2^2 - r_1^2)}} I. \tag{3.14}$$

This gives the same linear dependence on I as observed in our simulations for large M. The prefactor depends only on physical properties and the geometry should be similar to β^*_1 from the linear regression. Taking $r_1 = r_d$, the radius of the inner electrode, the prefactor is 6% larger than β^*_1 found above in the linear regression, which is a good agreement.

The linear scaling $u_{\phi,rms} = \beta_1 M$ (equivalent to $u^*_{\phi,rms} = \beta^*_1 I$) can also be explained by a scaling argument based on the balance between dissipation in the Hartmann layer and driving by the Lorentz force. We give this reasoning in Appendix 3.E.

3.3.2.3 Scaling of radial and axial velocities

Radial and axial velocities are smaller compared to the dominant azimuthal flow by more than two order of magnitude in all models of our base flow study. Nevertheless the scaling of the recirculation flow is interesting. Figure 3.6a shows the rms velocities $u_{r,rms}$ and $u_{z,rms}$ normalized by the input Reynolds number Re_i as a function of the Hartmann number M. For not too high $Re_i \lesssim 100$, the normalization collapses the data well which points to a linear scaling $u_{rms,r}, u_{z,rms} \sim Re_i$. This is in contrast to the scaling of the azimuthal velocity $u_{\phi,rms}$ which becomes independent of Re_i at large M. In the limit of large M, the exponent in a scaling law $u_{z,rms} \sim M^{\beta_z}$ is larger than the one in $u_{r,rms} \sim M^{\beta_r}$ as $\beta_z \approx \beta_r + 0.5$.

Since u_r and u_z are concentrated in the Hartmann and the Shercliff layers for high M (Fig. 3.2b), the integral quantities $u_{r,rms}$ and $u_{z,rms}$ might not be the appropriate

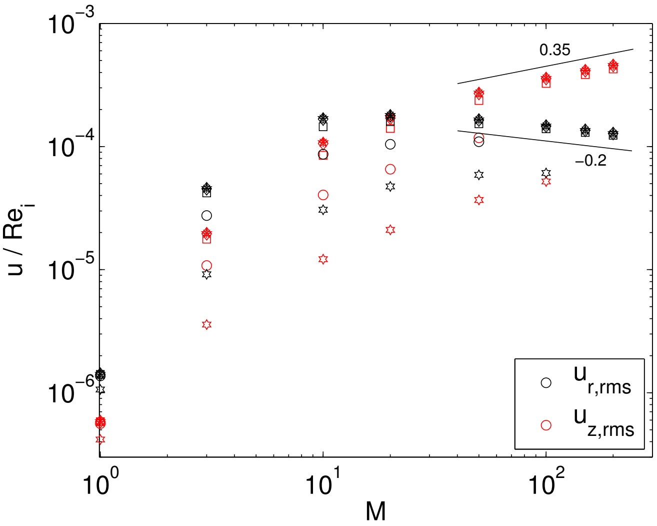

(a)

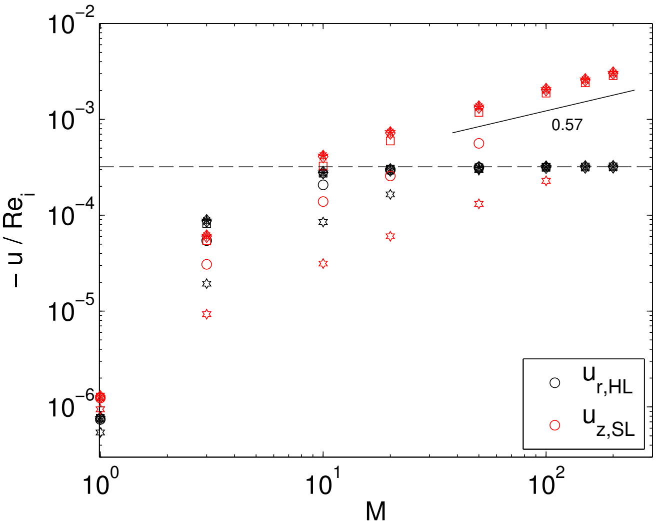

(b)

FIGURE 3.6: Nondimensional radial velocities u_r (black) and axial velocities u_z (red) normalized by the input Reynolds number Re_i as function of the Hartmann number M. (a) Global rms velocities $u_{r,rms}$ and $u_{z,rms}$. (b) Local velocities $u_{r,HL}$ and $u_{z,SL}$ measured at a point in the Hartmann and Shercliff layer respectively. Symbols indicate the value of Re_i and are the same as in Fig. 3.4.

Table 3.2: Scaling of nondimensional velocities in the limit of large M. Rms velocities $u_{i,rms}$ with $i = \{r.\phi, z\}$ are integrated quantities whereas velocities $u_{r,HL}$ and $u_{z,SL}$ are point measurements in the Hartmann and Shercliff layer respectively.

i	$u_{i,rms}$	$u_{i,BL}$
ϕ	$\sim M$	-
r	$\sim M^{-0.2} Re_i$	$\sim Re_i$
z	$\sim M^{0.35} Re_i$	$\sim M^{0.57} Re_i$

indicators to look at. Figure 3.6b shows the non-dimensional $u_{r,HL}$ and $u_{z,SL}$ measured locally at a point in the Hartmann and the Shercliff layer respectively. The measurement point in the Hartmann layer is located at ($r_m = 2.5$, $z_H = 1-0.5M^{-1}$); the measurement point in the Shercliff layer is at ($r = r_d + 0.5M^{-1/2}$, $z_m = 0.5$). The scaling of the measurement location with M^{β} was chosen in order to always be at a similar point in the boundary or shear layer whose thickness scales with M^{β} (cf. Sec. 3.3.2.4). The general behaviour of the local radial and axial velocities is similar to the rms velocities. However, the scaling with M at large M differs. It is $u_{z,SL} \sim M^{0.57}$ whereas $u_{r,HL}$ is independent of M. A surprising observation is that for the two exponent, it again holds that $\beta_z \approx \beta_r + 0.5$. The scalings are summarized in Table 3.2.

We explain the observation that the exponent of M in the scaling laws for radial and axial velocities differ by roughly 1/2 by the following considerations. From the continuity equation (Eq. 3.7), applying $\partial/\partial\phi = 0$, we find

$$u_r \sim \frac{l_r}{l_z} u_z \tag{3.15}$$

where l_r and l_z are the radial and vertical length scales of the flow respectively. For moderate $M = \mathcal{O}(1-10)$, these length scales are defined by the geometry of the container and constant, so $u_r \sim u_z$. For large M, we need to consider the length scales of the Hartmann and Shercliff layers where the gradients are largest. We use $l_r = \delta_S \sim M^{-1/2}$ and $l_z = \delta_H \sim M^{-1}$ (see Section 3.3.2.4). Hence we find $u_r \sim M^{1/2} u_z$ for $M \gg 1$. Both, the low- and the high-M relation between u_r and u_z are roughly observed in the data.

3.3.2.4 Boundary and shear layer scaling

Hartmann and Shercliff layers in large-M MHD flow typically obey scaling laws depending on the Hartmann number M (cf. Sec. 3.1). We study to what extent the scalings of the boundary layers and especially the free shear layer in our model agree with these laws. The models studied in this section have $Re_i = 100$. At different $Re_i \in [1, 1000]$, the flow structure is similar.

Figure 3.7a shows profiles of the velocity magnitude $U = (u_r^2 + u_\phi^2 + u_z^2)^{1/2}$ along z at the half-radius $r_m = 2.5$ of the tank for different Hartmann numbers M. The

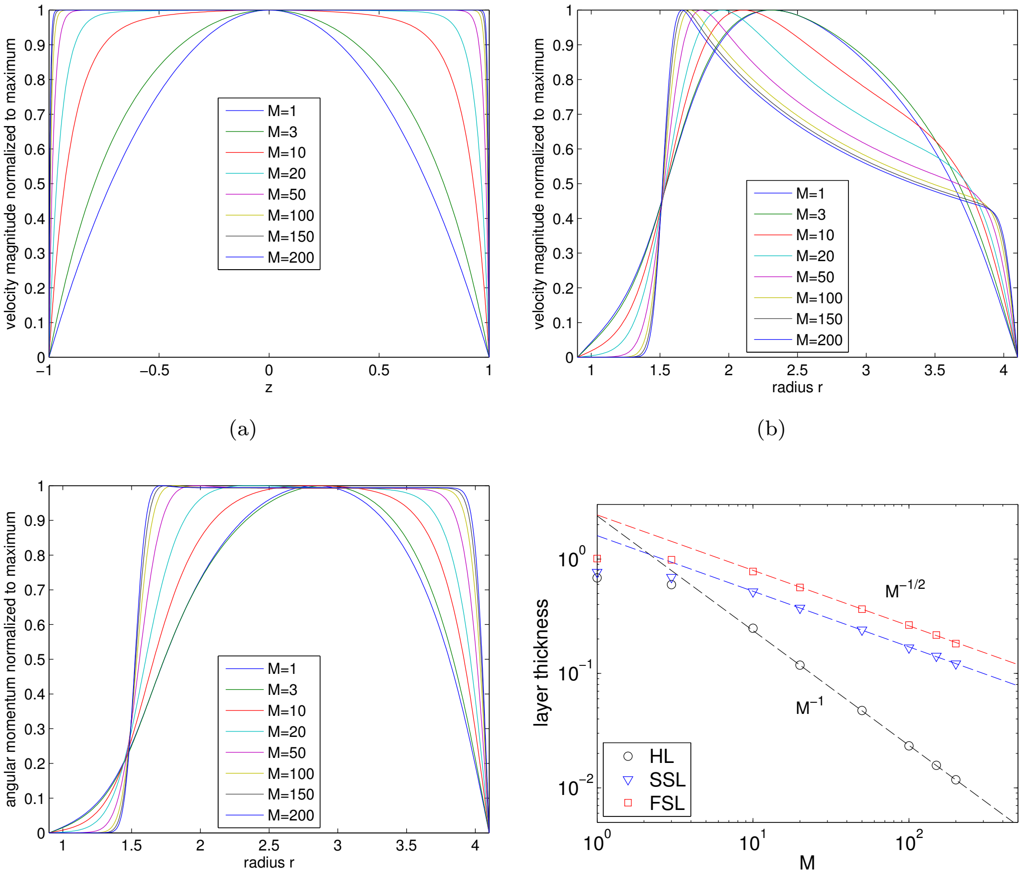

(a) (b)

(c) (d)

Figure 3.7: Scaling of the Hartmann and Shercliff layers in the numerical models. (a) Profiles of the velocity magnitude U normalized to its maximum value along the z-direction at the half-radius of the container for different Hartmann numbers M. (b) Profiles of the velocity magnitude U normalized to its maximum value along the r-direction at nondimensional height $z_i = 0.42$; z_i is where the radial and chord-wise UDV probes are located in the laboratory experiment. (c) Profiles of the angular momentum $L = r \cdot U$ normalized to its maximum value along the r-direction at height z_i. All models shown have $Re_i = 100$. (d) Scaling of the thickness of the Hartmann (HL), side (SSL) and free Shercliff (FSL) layers with the Hartmann number M.

velocity profile in the core of the flow is almost parabolic for $M = 1$ (hydrodynamic limit $M \to 0$), and becomes flatter with increasing M. For high magnetic fields ($M \gg 1$), the core flow is two-dimensionalized. Figure 3.7d shows the Hartmann layer thickness δ_H as a function of M (black circles). The thickness of the boundary layer is defined as the distance from the wall where the velocity magnitude U reaches 90% of its maximum (core) value. Fitting the data that have $M \geq 20$, the scaling found by linear regression is $\delta_H \sim M^{-1.003\pm0.004}$. This confirms the theoretical scaling of M^{-1} for $M \gg 1$.

We are particularly interested in the free Shercliff layer extending vertically from the inner electrode observed in Figure 3.7b at $r = 1.5$. We define its thickness δ_{Sh} as the radial distance between 5% and 95% of the maximum velocity magnitude. Figure 3.7d shows the scaling of the free Shercliff layer thickness (red squares) as $\delta_S \sim M^{-0.485\pm0.009}$

agreeing well with the simple scaling $\delta_S \sim M^{-1/2}$. The scaling exponent varies little when using different percentages in the criteria for the layer thicknesses.

In our model, the boundary layer at the outer wall is not a typical side or parallel layer since only the central part of the outer cylinder is electrically conducting. In standard examples like Baylis and Hunt [1971], the whole outer cylinder would be conducting. In Figure 3.7b, the boundary layer at $r = 4.1$ gets thinner with increasing M. Due to the cylindrical geometry, the profile of U is not flat within the core. From Equation 3.13 we know that the azimuthal velocity which is by far the dominant velocity component scales as $u_\phi \sim 1/r$. Hence we use the angular momentum profile $L = r \cdot U$ in Figure 3.7c which has a flat profile in the core of the flow for the determination of the layer thickness. On this profile, we again simply apply the 90%-criterion. The scaling for $M \geq 20$ is $\delta_S \sim M^{-0.486\pm0.007}$ (blue triangles in Fig. 3.7d) which is close to $\delta_S \sim M^{-1/2}$ from the geometrically simpler theoretical model. Hence both the free and the side Shercliff layers scale in the same way for the steady base flow in the numerics, as predicted for layers parallel to the magnetic field.

3.4 Experiment

The ZUCCHINI experiment is designed to study electrically-driven MHD flow in a modified cylindrical annulus. In this paper, we are interested in the base flow; the free shear layer that develops at the edge of the inner electrode as well as its instability are the scope of Paper 2. The main principles and features of ZUCCHINI were described in Section 3.2. Here we discuss more in detail the experimental setup and procedure as well as the measurements and results as far as they concern the steady base flow.

3.4.1 Setup

The experimental setup of ZUCCHINI consists of three essential parts: the tank itself, the coils creating the magnetic field and the current supply. Moreover we use an argon overpressure in the container to keep the working liquid GaInSn pure, and ultrasonic Doppler velocimetry (UDV) to diagnose the flow. In the following, we describe these parts and procedures separately.

The ZUCCHINI container has an inner height of $h = 2a = 10$ cm (cf. Fig. 3.1). The radii of the inner and outer cylinders are $r_i = 4.5$ cm and $r_o = 20.5$ cm respectively. The disk electrode protruding the inner cylinder has a radius of $r_d = 7.5$ cm. The thickness of the central disk electrode is 1 cm, the ring electrode along the outer cylinder is 1.5 cm wide. The materials of the different components are detailed in Appendix 3.F.

During our experiments, we employed two different coil systems for the generation of the magnetic field. For the lower magnetic field strengths up to 0.1 T, we used a modified Helmholtz coil system with three resistive copper coils manufactured by Caylar

Table 3.3: Overview of the measurements taken in the two setups ‘Caylar’ and ‘Cryo’. $\#(B)$ gives the number of sweeps of $I \in [I_{min}, I_{max}]$ performed in the range $B \in [B_{min}, B_{max}]$; $\mathbf{B}$ describes the geometry of the field.

	B_{min}	B_{max}	$\#(B)$	$\mathbf{B}$	I_{min}	I_{max}
‘Caylar’	17.5 mT	83.4 mT	5	$\partial B_{r,z}/\partial r \lesssim 0$	0 A	150 A
‘Cryo’	83.5 mT	1000 mT	9	$\partial B_{r,z}/\partial r > 0$	0 A	300 A

Table 3.4: Physical properties of GaInSn from Morley et al. [2008] who provide data for various composition ratios. We present the data set resembling most the MCP11 alloy from 5N Plus we use.

kinematic viscosity ν	$2.98 \cdot 10^{-7}$ m^2/s
electrical conductivity σ_e	$3.1 \cdot 10^6$ $(\Omega\text{m})^{-1}$
density ρ	6360 kg/m^3
melting point T_m	10.5°C
sound speed c	2730 m/s

(‘Caylar’ setup). For the higher fields up to 1 T, we employed a single superconducting coil from Cryomagnetics, Inc. (‘Cryo’ setup). The two systems not only differ in their maximum field strength but also in the field geometry. The ‘Caylar’ setup creates a roughly uniform field within the tank volume which decreases in strength by only 7% with the radius. The ‘Cryo’ setup is characterized by increasing field strengths with radius and a considerable amount of field curvature near the outer cylinder. The two magnetic field geometries are summarized in Table 3.3 and detailed in Appendix 3.G. We will show how the differences influence the resulting flow in Section 3.4.4.2.

The forcing current I between inner and outer electrodes is generated by power supplies of type SM 18-50 from Delta Elektronika. These have an output voltage of 0-18 V and an output current of 0-50 A. They are characterized by an rms ripple and noise as low as 5 mA. In our first setup ‘Caylar’ ($B_{max} = 0.1$ T), we employ three power supplies resulting in $I_{max} = 150$ A whereas for the ‘Cryo’ setup ($B_{max} = 1$ T), we double the number of power supplies to reach $I_{max} = 300$ A. Details about the current distribution are given in Appendix 3.H.

ZUCCHINI is filled with roughly 12.5 l (80 kg) of the eutectic alloy GaInSn. We use MCP 11 alloy from 5N Plus UK Ltd. According to the certificate of analysis, it contains 65.9% gallium, 20.8% indium and 13.3% tin. Table 3.4 gives its relevant physical properties. Besides being liquid at room temperature, GaInSn has the advantage of not being hazardous to human health and the environment. It may, however, be corrosive to metals, it weakens especially aluminium, and it is expensive. Additionally it is easily oxidized forming a sludge from mainly gallium oxides (Ga_2O_3, Ga_2O) which degrades or precludes experimental measurements.

From the treatment of GaInSn reported in Morley et al. [2008], we adopt the cleaning with isopropyl alcohol and the suggested usage of argon as cover gas to prevent oxidation. For this reason, we have designed an elaborate pipe system which keeps the GaInSn under an argon overpressure of at least 0.15 bar at all times. Also it facilitates filling and emptying the tank without the GaInSn ever coming into contact with the surrounding air by applying different pressures to the storage and working tanks. Prior to the first filling, we press the GaInSn through four filters with mesh sizes of 100, 50, 30 and 15 μm to remove oxides. Around 90% of the sludge stays in the coarsest mesh, and after the 50 μm mesh, hardly any sludge remains. Following Morley et al. [2008] and Stefani et al. [2006], we take care that the liquid GaInSn is properly wetting the electrodes and the UDV probes to ensure a good electric and acoustic contact. This is achieved by a thorough cleaning of all surfaces with isopropyl alcohol.

3.4.2 Methods

The flow in ZUCCHINI is diagnosed with Ultrasonic Doppler Velocimetry (UDV). The temperature of the tank is monitored by a K-type thermocouple mounted on the central disk electrode. In the following section, we describe our experimental measurements from methods and devices to data processing and a data example.

3.4.2.1 Measurements

UDV as used in our experiment is based on the pulsed emission of ultrasonic waves that are reflected at particles in the fluid. Velocities are derived from shifts in position between pulses resulting in a profile of the velocity component along the ultrasound beam. We use a DOP3010 box from Signal Processing S.A., and multiplex three channels. The emitting frequency f_e of the probes is selected according to the desired maximum profile depth p_{max} and velocity v_{max} which are related by

$$p_{max} v_{max} = \frac{c^2}{8 f_e} \tag{3.16}$$

where c is the speed of sound (cf. Table 3.4) in the fluid [DOP]. We use three UDV probes with $f_e = 8$ MHz to achieve sufficient resolution. The wave length of the 8 MHz-wave in GaInSn is 0.34 mm. The maximum achievable velocity measurement in ZUCCHINI is of the order of 1 m/s which is sufficient since we do not measure u_ϕ directly. The (half-)angle of divergence of the ultrasonic beam is 4.8°. The near field characterized by corrupted signals goes up to 1.8 cm distance from the probe.

Two probes are pointing outwards from the inner cylinder in a horizontal plane 2.1 cm above the central plane of the tank. Probe 1 (‘radial’) is measuring purely the radial velocity u_r along a radial profile. Probe 2 (‘chordwise’) has an offset of 90° to probe 1 in azimuthal direction, and points outward forming a skew angle with the radial rays intersecting it (Fig. 3.8). It also measures mainly u_r but additionally picks up the azimuthal component u_ϕ. This is exploited to construct radial profiles of mean azimuthal velocity $\overline{u}_\phi$ (Section 3.4.2.2). Probe 3 is mounted flush in the bottom plate of ZUCCHINI just outside the edge of the central disk electrode, $r_d = 7.5$ cm. Hence it measures a vertical profile of the axial velocity u_z over the entire height ($h = 10$ cm) of the free shear layer.

Measurements with UDV in liquid metals have been conducted since more than a decade, including a pioneering study in gallium by Brito et al. [2001]. We rely on the unavoidable oxides in GaInSn as scatterers of the ultrasonic beam, mainly Ga_2O_3 (6440 kg/m^3) and GaO_2 (4770 kg/m^3) [Cramer et al., 2004, Andreev et al., 2009, Boisson et al., 2012]. Some previous studies used UDV through the container wall [Brito et al., 2001, Boisson et al., 2012], others brought the probes in direct contact with the GaInSn as is done in our experiment [Andreev et al., 2009]. A good mixing of the oxides in GaInSn is essential. Hence we mix up the fluid between runs by high forcing currents.

3.4.2.2 Processing

For comparison with theory and numerics, we are interested in the radial profile of azimuthal velocity $u_\phi(r)$. However, we do not directly measure azimuthal velocities with the UDV probes. Instead, probe 1 records $u_1 = u_r$, and probe 2 the chordwise velocity u_2 as shown in Figure 3.8. Data of the latter UDV probe contain mostly information on the radial velocity, but the azimuthal component contributes to the measurement as well. This contribution from u_ϕ to u_2 is dependent on the radial distance from the inner cylinder.

It is impossible to reconstruct the velocity vector at a certain point in the horizontal (r, ϕ)-plane since the UDV beams of the radial and chordwise probes do not cross each other. Nevertheless we can derive a mean azimuthal velocity profile $\overline{u_\phi}(r)$ from the mean radial and chordwise profiles, $\overline{u_1}(r)$ and $\overline{u_2}(r)$; the overline denotes a temporal mean. For the steady base flow in this paper, it is $u_\phi(r) = \overline{u_\phi}(r)$. The angle α between the chordwise UDV beam and a radial ray intersecting it, is

$$\alpha = \arctan\frac{r_p}{l_{cs} + \xi}, \tag{3.17}$$

where ξ is the coordinate from probe 2 along the beam, $r_p = 25$ mm and $l_{cs} = (r_i^2 - r_p^2)^{1/2} = 37.4$ mm. This means that α varies in the range of 33.7° to 7° between the inner and outer cylinder. Using Equation 3.17, the mean azimuthal velocity is calculated as

$$\overline{u_\phi}(\xi) = -\frac{l_{cs} + \xi}{r_p}\,\overline{u_1}(\xi) + \sqrt{1 + \left(\frac{l_{cs} + \xi}{r_p}\right)^2}\,\overline{u_2}(\xi). \tag{3.18}$$

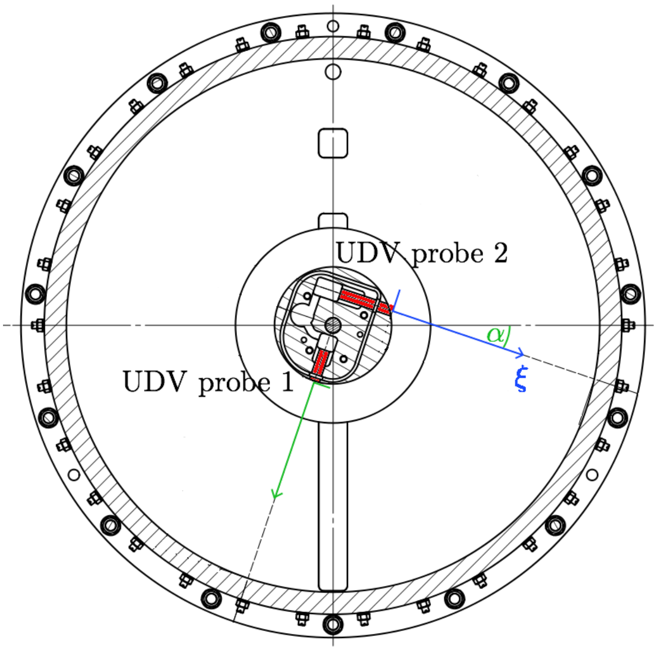

FIGURE 3.8: Top view of tank with orientation of UDV probes 1 (radial) and 2 (chordwise) in red. The angle α of the chordwise beam with the radial direction decreases with the distance ξ from probe 2 (cf. Eq. 3.17).

Then $\overline{u_\phi}(\xi)$ is transformed into a profile $\overline{u_\phi}(r)$ dependent on true radius, also taking into account the offsets of the UDV probes with respect to the inner cylinder. The radial UDV probe sticks approximately 5 mm out of the inner cylinder, whereas it is 1.5 mm for the chordwise probe.

From mean azimuthal velocity profiles $\overline{u_\phi}(r)$, we determine a characteristic value $\langle\overline{u_\phi}\rangle$ for the azimuthal velocity by taking the spatial average over the radial range $r \in [58, 195]$ mm. This is used to define a Reynolds number as

$$Re = \frac{\langle\overline{u_\phi}\rangle a}{\nu}, \tag{3.19}$$

which is essentially a nondimensional velocity measured in the system, and as such an output quantity, in contrast to the control parameter Re_i (Eq. 3.10) in the numerical study.

3.4.2.3 Data example

A typical experimental run begins by ramping up the current in the magnetic coils. The fluid and the oxides are mixed up by a strong electrical current through the tank, typically 150 A or more. After the fluid has come to rest, we record with UDV and PDP at a given magnetic field strength stepwise increasing the electrical current. At every parameter setting, we let the flow reach its new equilibrium state. The settling time decreases with increasing magnetic field and current.

The sampling rate of the UDV is adjusted according to signal quality and the ability to resolve the observed oscillations (scope of Paper 2). In general it increases from ~ 1 Hz at a few A (steady flow) to ~ 30 Hz at 150-300 A. The recording time is set such that the noise is largely canceled out (steady state) and the frequency resolution is sufficient (~ 0.01 Hz for the oscillations). In general it decreases from ~ 150 s to ~ 60 s with increasing current.

Figure 3.9 shows an example of radial and chordwise UDV recordings from the 'Cryo' setup, together with the mean azimuthal velocity profile $\overline{u_\phi}(r)$ calculated according to Eq. 3.18. By definition, velocities are positive when directed away from the probe. The thin lines are 256 raw data profiles, the bold lines their temporal means. The noise increases towards the far end of the profiles near the outer wall. In general the signal quality of the radial and chordwise UDV probes is remarkable.

At large B and low I in the 'Cryo' setup, we observe a jet near the outer wall. The detection of this flow feature around $r = 184$ mm in Figure 3.9b relies on the measurements of radial velocities and their contribution to Equation 3.18 since it is surprisingly not seen in the chordwise recordings. Nevertheless we take the jet for real due to its small propagated errors and a possible explanation by numerical simulations in Section 3.4.4.2. In order to quantify the jet in the experimental data, we use a power law of the form $\overline{u_\phi}(r) = cr^{-\alpha}$ fitted to the radial range $r \in [100,\ 140]$ mm (dashed red line in Fig. 3.9b). The half-width $\delta_{jet} = \overline{u_\phi}(r_j) - r_s$ of the jet is defined by the distance between the location of the maximum jet amplitude r_j and the intersection of the fitted curve and $\overline{u_\phi}(r)$ at r_s. The normalized jet amplitude is $A_{jet} = \overline{u_\phi}(r_j)/(cr_j^{-\alpha})$.

Axial UDV measurements (not shown in the example) contain a similar absolute amount of noise of roughly 1 mm/s as u_1 and u_2. This makes them relatively noisier than radial and chordwise recordings due to velocities being an order of magnitude smaller. The rms value $\langle\cdot\rangle_{rms}$ of the mean axial velocity profile $\overline{u_z}(z)$ is defined as

$$\langle\overline{u_z}\rangle_{rms} = \sqrt{\frac{1}{z_2 - z_1}\int_{z_1}^{z_2} \left(\overline{u_z}(z)\right)^2 \mathrm{d}z} \tag{3.20}$$

between $z_1 = 5.5$ mm and $z_2 = 97$ mm. Spatial rms values $\langle\overline{u_r}\rangle_{rms}$ of the mean radial velocities are calculated analogously with $r_1 = 58$ mm and $r_2 = 200$ mm.

3.4.3 Results

Measurements have been conducted along the lines described in the previous sections in the two setups 'Caylar' and 'Cryo'. The parameters of the recordings are specified in Table 3.3. As a consistency check for our data set, we took measurements at $B = 83.5$ mT ($M = 169$) in both setups. The mean azimuthal flow $\overline{u_\phi}(r)$ turns out to be similar in magnitude and also in structure. This allows us to combine the two data sets despite the

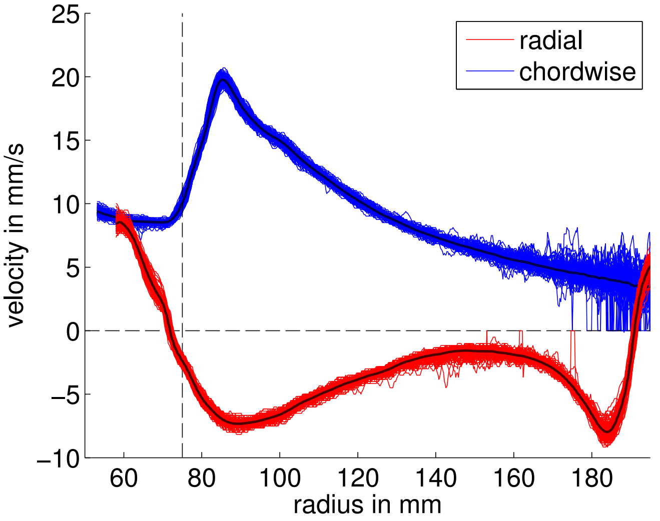

(a)

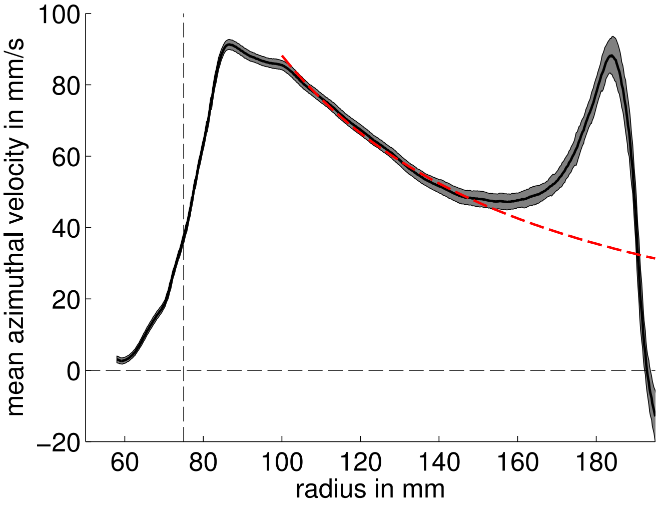

(b)

FIGURE 3.9: UDV data example of steady flow recorded at $B = 875$ mT, $I = 7$ A ($M = 1770$, $Re = 9570$). (a) Profiles of radial velocity $u_1 = u_r$ in red and chordwise velocity u_2 in blue. The bold lines are temporal means $\overline{u_i}$ of all recorded profiles during roughly 90 s with a sampling interval of approximately 0.35 s in both cases. (b) Mean azimuthal velocity profile $\overline{u_\phi}(r)$ in black calculated according to Eq. 3.18. The grey shaded area indicates the standard error propagated from the measurements of u_1 and u_2. The red line is a power law $\overline{u_\phi}(r) \sim r^{-\alpha}$ fitted to the radius range of roughly [100, 140] mm, yielding $\alpha = 1.55$. The jet around $r = 184$ mm has normalized amplitude $A_{jet} = 1.57$ and half-width $\delta_{jet} = 6.8$ mm. The dashed vertical lines indicate the location of the inner electrode edge.

differing distributions of magnetic field in the two setups (cf. Sec. 3.4.1 and App. 3.G). For the base flow studied in this paper, the 'Cryo' data set provides more relevant information due to its larger M. The first instability is not observed below a forcing current of roughly 10 A at $B = 1$ T ($M = 2022$), while the flow is already unstable at 2 A for the lower values of B in the 'Caylar' setup (cf. Paper 2).

3.4.3.1 Mean azimuthal flow

Profiles of the mean azimuthal velocity $\overline{u_\phi}(r)$ derived using Eq. 3.18 are shown in Figures 3.9b and 3.10. The profiles share some characteristics, the most prominent one being the strong increase in $\overline{u_\phi}$ roughly in the radial range $r \in [70, 90]$ mm. This is the free Shercliff layer associated to the current injection at the edge of the disk electrode at $r_d = 75$ mm. Varying B (M) by more than a factor 50 in Figure 3.10, the Shercliff layer width $\delta_S \approx 15$ mm is not observed to vary substantially. For smaller radii $r < r_d$, there is no forcing, and the fluid is only entrained viscously by the outer part. For $r > 90$ mm, $\overline{u_\phi}$ falls off again due to the geometrical spreading of the forcing current over a larger circumference, theoretically expressed by Eq. 3.13 for large M [Baylis and Hunt, 1971]. The observed deviation from $\overline{u_\phi} \sim r^{-1}$ at moderate M is studied in the next section. A feature that only appears for $M \gtrsim 200$ in the 'Cryo' setup is the jet in the radial range of roughly $r \in [165, 190]$ mm, which is considered in more detail later.

Figure 3.10 shows profiles of $\overline{u_\phi}$ at $I = 1$ A at all magnetic field values measured. In the 'Caylar' setup (a), the maximum of $\overline{u_\phi}$ is increasing with the magnetic field up to $M = 169$. It is exceeding the theoretical profile (dotted line) from the large-M theory (Eq. 3.13) which predicts a scaling as $\overline{u_\phi} \sim r^{-\alpha}$ with $\alpha = 1$ between the inner and outer electrodes [Baylis and Hunt, 1971]. Fitting power laws of this form to the data in the radial range of roughly [100, 190] mm yields exponents of $\alpha \in [1.5, 1.7]$ for $M \in [106, 169]$. The asymptotic large-M regime is not reached yet. In the 'Cryo' setup (Fig. 3.10b), the local maximum at the free Shercliff layer generally decreases with growing M. An exception is the outlier profile for $M = 253$. The profiles of $\overline{u_\phi}$ approach the theoretical curve in the range of $r \in [100, 140]$ mm for $M \gtrsim 1000$. It appears that the large-M regime assumed in the theory of Baylis and Hunt [1971] is finally reached.

The jet at $r \in [165, 190]$ mm in the 'Cryo' setup (cf. Fig. 3.10b) is a feature which does not appear in the simple theoretical case which has straight conducting side walls [Baylis and Hunt, 1971]. It is observed for $M \gtrsim 250$, but not for $M \leq 169$ even in the same configuration. The jet half-width $\delta_{jet} \approx 7$ mm is not observed to vary significantly with M. The normalized jet amplitude A_{jet}, however, depends on M. Figure 3.11 shows A_{jet} for the steady base flow. The instability occurring at the free Shercliff layer (Paper 2) does not modify the jet near the outer wall. Besides significant changes of A_{jet} with the current I, a slightly sublinear scaling $A_{jet} \sim M^\alpha$ with $\alpha \lesssim 1$ is observed. Since the growth of A_{jet} with M is accompanied by a decrease of the free Shercliff layer maximum, quantities that are ideally conserved, like total angular momentum and kinetic energy, tend to a constant value for large M.

Figure 3.12 shows the radial mean $\langle \cdot \rangle$ of $\overline{u_\phi}(r)$ versus the forcing current. The dashed black line indicates the theoretical value obtained from the simplified model with entirely conducting side walls at $r_1 = 75$ mm and $r_2 = 195$ mm [Baylis and Hunt, 1971]. Taking

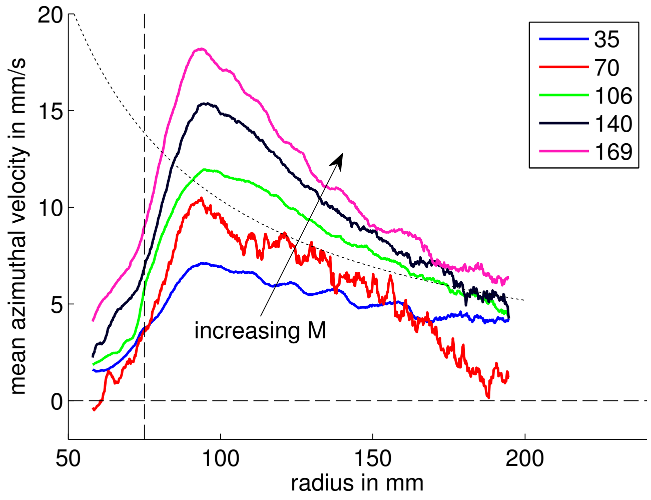

(a)

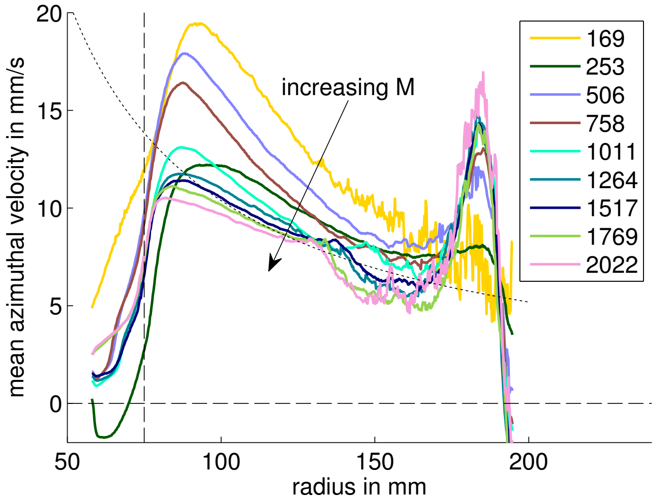

(b)

FIGURE 3.10: Profiles of $\overline{u_\phi}(r)$ measured at 1 A and varying B (numbers give M). (a) ‘Caylar’ setup with $Re \in [830, 1780]$. (b) ‘Cryo’ setup with $Re \in [1310, 1960]$. All runs are observed to be stable up to the noise level. The vertical dashed line indicates the inner electrode. The dotted line is the theoretical prediction of Eq. 3.13 for large M. The experimental data seem to reach the large-M regime only at $M \gtrsim 1000$.

the radial mean $\langle\cdot\rangle$ of Eq. 3.13 yields

$$\langle\overline{u_\phi}\rangle_{BH71} = \frac{I}{4\pi\sqrt{\sigma_e\rho\nu}}\frac{\ln(r_2/r_1)}{r_2-r_1}. \tag{3.21}$$

The experimental data follow a linear scaling $\langle\overline{u_\phi}\rangle \sim I$ with arbitraty slope in the steady flow regime. The slope of the theoretical prediction (dashed line, Eq. 3.21) is, however, only reached for large $M \gtrsim 1000$.

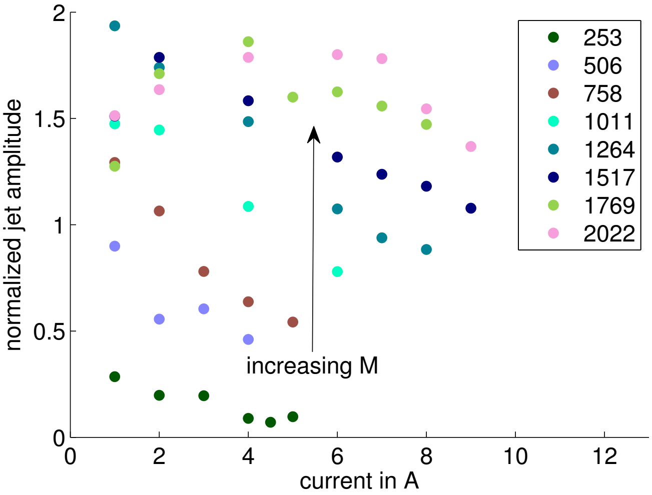

FIGURE 3.11: Normalized jet amplitude A_{jet} observed in steady flow for $M \gtrsim 250$. The jet amplitude scales slightly sublinear with M, $A_{jet} \sim M^{\alpha}$ with $\alpha \lesssim 1$.

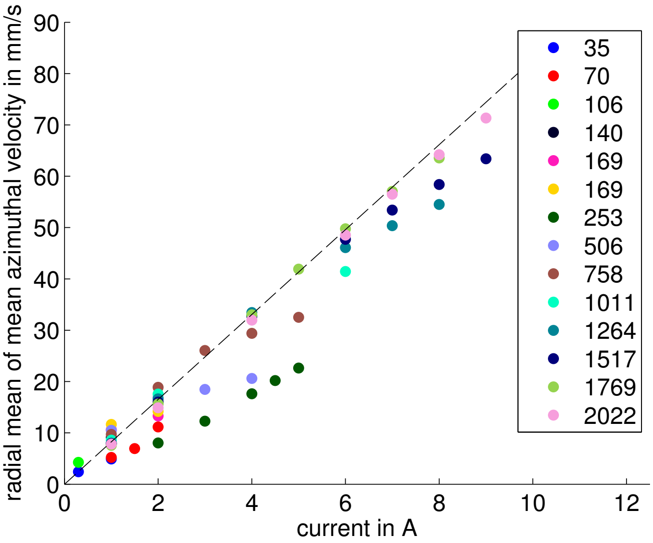

FIGURE 3.12: Radial mean of (temporal) mean azimuthal velocity $\langle \overline{u_\phi} \rangle$ depending on forcing current and magnetic field strength (colours). The dashed black line is $\langle \overline{u_\phi} \rangle_{BH71}$, the theoretical curve for a simple setup with straight conducting side walls (Eq. 3.21). Its slope is only reached for large M. The highest stable $\langle \overline{u_\phi} \rangle$ at $M = 2022$ ($B = 1$ T) and $I = 9$ A corresponds to $Re = 1.2 \cdot 10^4$.

3.4.3.2 Radial and axial recirculation

The dominant flow u_ϕ which is driven by the Lorentz force gives rise to a recirculation in the (r, z)-plane. This secondary flow is probed by a UDV-profile in either direction (probes 1 and 3). An example mean radial profile $\overline{u_r}(r)$ is shown in Figure 3.9. The data quality in the u_r-measurements at low forcing current I is only sufficient in the 'Cryo' data, so we restrict the study of the radial flow structure to $M \gtrsim 250$.

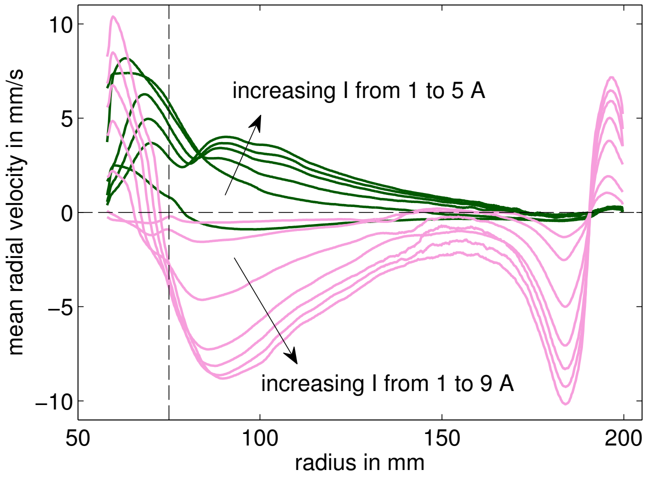

FIGURE 3.13: Profiles of mean radial velocity $\overline{u_r}(r)$ at $M = 253$ (green) and 2022 (pink). Positive values indicate outward directed flow.

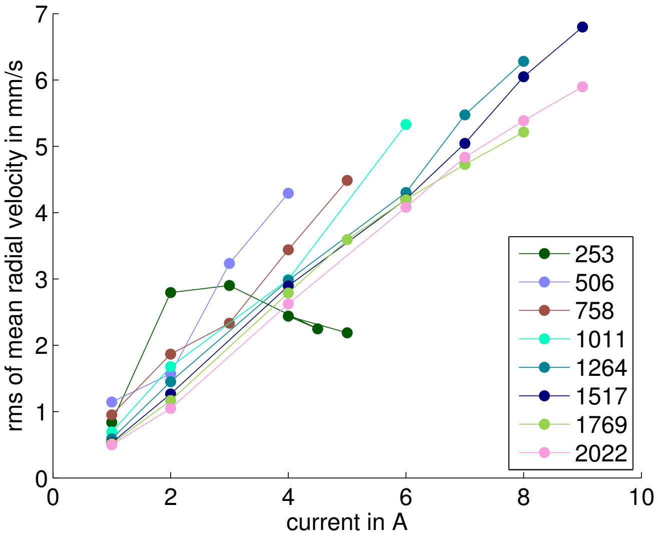

FIGURE 3.14: Radial rms values $\langle\cdot\rangle_{rms}$ of the mean radial velocity $\overline{u_r}(r)$ versus the forcing current. In general, $\langle\overline{u_r}\rangle_{rms} \sim I$ with a slightly suppressed flow at large M.

Profiles of mean radial velocity $\overline{u_r}(r)$ at $M = 253$ and $M = 2022$ are shown in Figure 3.13. At $M = 253$, the flow is directed radially outward at the location of probe 1, 2.1 cm above the mid plane of the tank, with its maximum in the free Shercliff layer. At $M = 2022$, $\overline{u_r}(r)$ exhibits two sign changes which appear to be connected to the free shear Shercliff near the inner electrode and the jet near the outer wall (cf. Fig. 3.10b). In between the free Shercliff layer and the jet, the radial flow is directed radially inward at large M.

Figure 3.14 shows radial rms values $\langle\overline{u_r}\rangle_{rms}$ of the mean radial profiles plotted versus the forcing current I. For large $M \gtrsim 750$, the scaling of the two quantities is linear, $\langle\overline{u_r}\rangle_{rms} \sim I$. In general, $\langle\overline{u_r}\rangle_{rms}$ appears to decrease only slightly with M, which can be seen as a suppression of the recirculation by the magnetic field; a clear power law scaling with M is not observed.

The UDV probe 3 located in the bottom plate of the ZUCCHINI tank measures vertical profiles of axial velocities $u_z(z)$ within the free Shercliff layer. Example profiles at minimum, medium and maximum magnetic field are given in Figure 3.15. At $M = 35$, the mean $\overline{u_z}$-profile is roughly antisymmetric around the mid plane. The flow is directed towards the mid plane where the disk electrode is located, with largest $\overline{u_z}$ near the top and bottom plates. The recirculation pattern is somewhat different at $M = 169$. A dominant downward component is superimposed on the antisymmetric axial flow. At $M = 2022$, the axial flow in the free Shercliff layer appears to be almost reversed at the location of the probe.

The scaling of the strength of the mean axial flow with I and M, given by its rms value $\langle\overline{u_z}\rangle_{rms}$, is shown in Figure 3.16. As for the radial flow, $\langle\overline{u_z}\rangle_{rms}$ scales linearly with I for the steady base flow, $\langle\overline{u_z}\rangle_{rms} \sim I$. In contrast to $\langle\overline{u_r}\rangle_{rms}$, however, $\langle\overline{u_z}\rangle_{rms}$ decreases significantly with M for large $M \gtrsim 250$. This is interpreted as an effect of the magnetic field which tends to suppress gradients along its direction, and hence leads to an almost vanishing axial flow.

3.4.4 Experiment versus numerics

3.4.4.1 General comparison

At this stage, a comparison between the laboratory experiment and the numerical simulations (Sec. 3.3) seems in order. Figure 3.17 shows mean profiles of the dominant velocity component $\overline{u_\phi}(r)$ measured at 1 A (cf. Fig. 3.10) together with results from numerical simulations at the same values of M and I, where the magnetic field is taken to be axial and uniform as in Section 3.3. The magnitude of $\overline{u_\phi}(r)$ agrees reasonably well in numerics and experiment. Also the general structure of the flow, with the inner part almost at rest, the free Shercliff layer and then a decreasing velocity with radius, is recovered. Between the electrodes, numerical and experimental profiles converge to the prediction of the large-M theory by Baylis and Hunt [1971]. Interestingly, the observation of a growing number of radial secondary flow cells in the numerics (Fig. 3.2) offers an interpretation for the experimentally recorded change in axial flow structure in the free Shercliff layer at large M (Fig. 3.15). The change in the cell structure of the secondary flow with M might lead to a reversal of the antisymmetric axial flow at the radial position of UDV probe 3.

Besides this agreement of the results of numerical simulations and experiments, three differences are observed. The first one concerns the magnitude of the flow which in the numerics reaches the asymptotic large-M limit, where $u_\phi \sim I$ and is independent of M, for $M \gtrsim 50$. In the experiment, the value of u_ϕ first grows above the theoretical

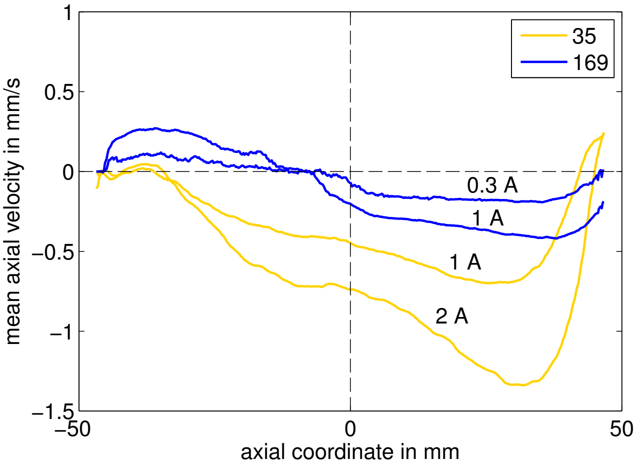

(a)

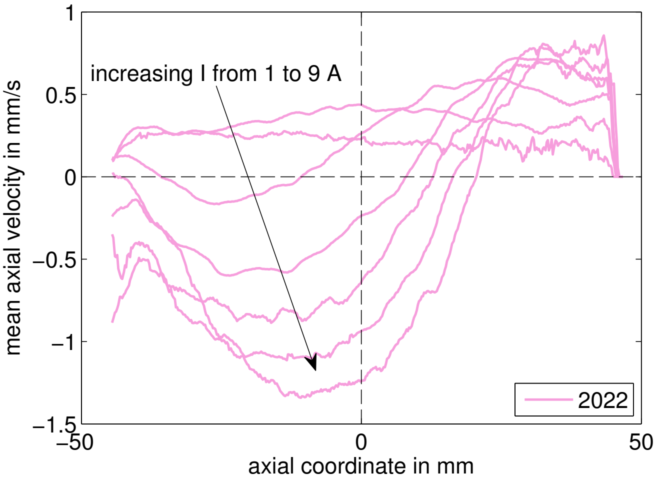

(b)

FIGURE 3.15: Profiles of mean axial velocity $\overline{u_z}(z)$ for stable flow at $M = 35$ and 169 (a), as well as 2022 (b). At $M = 35$, the recirculation in the free Shercliff layer is antisymmetric and directed towards the mid plane. At $M = 169$, a downward component appears to be superimposed, whereas the structure is roughly reversed at $M = 2022$.

and numerical prediction with increasing M, having its maximum at $M \approx 200$, and becomes similar again only for $M \gtrsim 1000$ (Fig. 3.10). The second difference concerns the thickness of the free Shercliff layer at the inner electrode. In the numerics, it is found to scale as $\delta_S \sim M^{-1/2}$ (Fig. 3.7), whereas in the experiment, it appears not to scale with M (Fig. 3.10). The thickness of the Hartmann and side layers can not be compared in numerics and experiment since it is not possible to probe these layers in the experiment due to UDV resolution and wall effects. The third difference is the jet near the outer cylinder which appears in the experiment at large M, but is not reproduced in the numerical simulations with homogeneous axial magnetic field. In Section 3.4.4.2, we

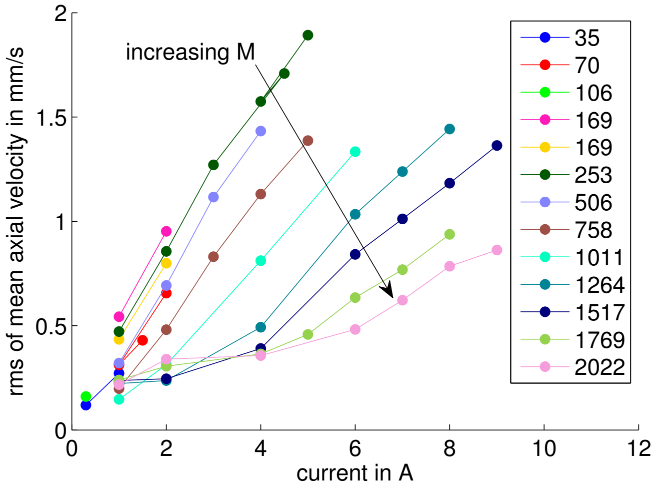

FIGURE 3.16: Axial rms values $\langle \cdot \rangle_{rms}$ of the mean axial velocity $\overline{u_z}(z)$ versus the forcing current I. The scaling of $\langle \overline{u_z} \rangle_{rms}$ with I is roughly linear. For large $M \gtrsim 250$, $\langle \overline{u_z} \rangle_{rms}$ decreases with increasing M.

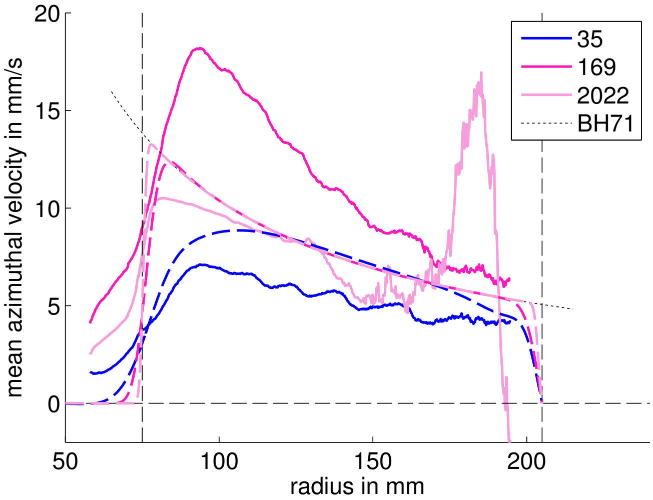

FIGURE 3.17: Comparison of azimuthal velocity profiles $\overline{u_\phi}(r)$ at 1 A in experiment, numerics and large-M theory. The experimental data (solid lines, coloured according to value of M) are the same as in Figure 3.10. The numerical simulations (dashed lines) at the same parameters approximate the theoretical large-M prediction (dotted line) of Eq. 3.13 increasingly well with growing M between the two electrodes (dashed vertical lines). The convergence of the experimental profiles to the prediction is slower and also imperfect due to the jet at $M = 2022$.

will show that a jet near the outer wall is also found in the numerical simulations when considering a more realistic magnetic field similar to the one in the 'Cryo' setup.

Comparing radial and axial velocities, $\overline{u_r}(r)$ and $\overline{u_z}(z)$, between experiment and numerics yields less agreement than for the mean azimuthal flow. Only at low $M \approx 35$, both are comparable in magnitude, at large M the experimentally measured velocities $\overline{u_r}$ and $\overline{u_z}$ are at least an order of magnitude larger than the numerical results. In terms of the rms velocity scaling with the dimensional control parameters $B \sim M$ and $I \sim Re_i M$,

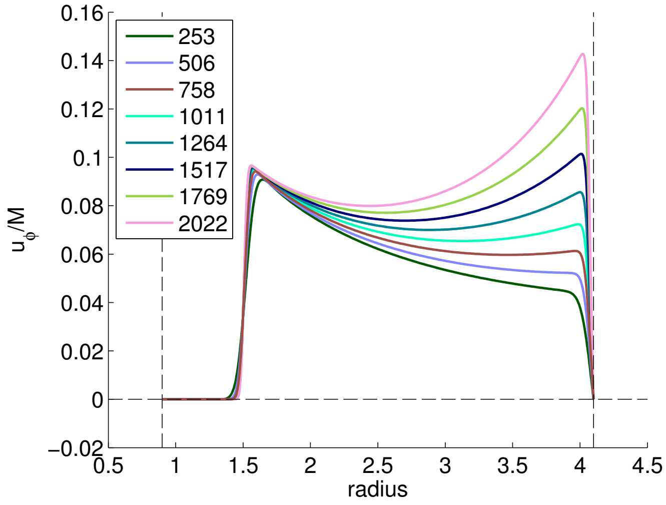

FIGURE 3.18: Nondimensional azimuthal velocity normalized by M from numerical simulations with a more realistic magnetic field of a single current loop at a forcing current of 1 A. The parameters of the field have been adjusted to fit magnetic field measurements from the 'Cryo' setup. The higher field strength and curvature near the outer electrode generate a jet growing with M similar to the experimentally observed one in Fig. 3.10b.

a similar dichotomy is observed. For the azimuthal velocity, $u_\phi \sim I$ is found in both, experiment and numerics, for sufficiently large M. For radial and azimuthal velocities, the numerical scalings in the limit of large M from Table 3.5 translate to dimensional units as $u_{r,rms} \sim B^{-2.2} I^2$ and $u_{z,rms} \sim B^{-1.65} I^2$. Experimentally, a linear scaling with the current I is observed (Figs. 3.14 and 3.16).

3.4.4.2 Numerical recovery of the jet

The 2D3C numerics of Section 3.3 were designed to match the parameters of the base flow in the 'Caylar' setup which is assumed to be steady and axisymmetric. In addition to some minor differences in geometry, boundary conditions and possibly material properties, there is a major difference in the magnetic field between numerics and experiment. While the field in the Helmholtz-like 'Caylar' setup (M up to 169) is relatively well approximated by a homogeneous axial field (Fig. 3.21), this is not the case for the 'Cryo' setup ($M \in [169, 2022]$). In the single-coil 'Cryo' setup, the field is stronger and curved outwards near the outer wall of the ZUCCHINI tank. We approximate the 'Cryo' magnetic setup by a single current loop whose magnetic field is analytically known. The two only free parameters, loop radius and current, are adjusted to roughly fit magnetic field measurements from the 'Cryo' setup and recover comparable jet amplitudes.

We conduct numerical simulations for $M \in [253, 2022]$ imposing this field of a single current loop (Fig. 3.22) in our numerical model; all other model parameters are the same as in Section 3.3. Figure 3.18 shows the resulting profile of azimuthal velocity at $I = 1$ A and different M. As in the experimental data (Fig. 3.10b), there is hardly any bump visible near the outer electrode at moderate M. With increasing M, the jet amplitude grows. The jet can hence be explained by a stronger Lorentz-forcing in the outer part of the tank due to larger magnetic field strength and the curvature of the field in this region.

3.5 Conclusions

We have studied the liquid metal flow that is generated by Lorentz-force driving in a modified cylindrical annulus by means of both laboratory experiments and numerical FE simulations. The peculiarity of the ZUCCHINI geometry compared to similar experimental studies [Baylis, 1971, Moresco and Alboussiere, 2004, Boisson et al., 2012, Mikhailovich et al., 2012] is the inner electrode which is built as a disk protruding into the flow. This results in a free Shercliff layer between the inner and outer part without and with electrical forcing, which becomes unstable at currents of a few Amperes. This paper focuses on the steady axisymmetric base flow below this threshold.

Two experimental setups are used, characterized by different magnetic field strength and geometry with Hartmann numbers M up to 169 for the 'Caylar' and 2022 for the 'Cryo' setup. The flow is probed by ultrasound Doppler velocimetry. To our knowledge, this is the first time, that the radial profile of electrically-driven azimuthal flow with a free Shercliff layer is established using UDV.

The structure of the base flow consists of a dominant azimuthal component and a secondary recirculation flow in the (r, z)-plane which is an order of a magnitude slower. The azimuthal flow is characterized by the inner non-driven part of the fluid, the free Shercliff layer, and a drop-off with increasing radius as $u_\phi(r) \sim r^{-\alpha}$ with $\alpha \in [0.6, 1.7]$ in the experimental data; the numerical results yield similar velocities and obey $\alpha = 1$ more closely, which is the theoretical prediction for large M from Baylis and Hunt [1971]. Their theory neglects secondary (radial and axial) flows which is a condition that appears to be much better fulfilled by the numerical rms velocities than by the experimental ones. The theory predicts $u_\phi(r) \sim I$ which we observe in both numerical and experimental data. At large M, even the proportionality constant in the experimental and numerical scalings agrees with the theoretical prediction. In the experiment, also radial and axial velocities are observed to scale linearly with the current for large M. The large-M threshold implying negligibility of the secondary flow and independence of M, however, appears to be reached at higher $M \gtrsim 1000$ in the experiment than in the numerics ($M \gtrsim 50$). Similarly, numerics and experiment differ in the observed thickness of the free Shercliff layer. In the numerical data, it scales as $\delta_S \sim M^{-1/2}$ like the Shercliff (side) layer under a strong magnetic field [Shercliff, 1953]. In the experimental data, the free Shercliff layer thickness $\delta_S \approx 15$ mm appears to be independent of M for a large range of M (cf. Fig. 3.10).

A special feature of the experimental flow at large $M \gtrsim 200$ is the occurrence of a jet near the outer cylinder wall. This jet does not appear in the numerical simulations with uniform magnetic field. But it can be reproduced in simulations with a magnetic field that is more similar to the one in our 'Cryo' setup, i.e. increasing in strength and slightly curved towards the outer wall. Hence the jet is probably generated by a stronger Lorentz-forcing near the outer cylinder. Its normalized amplitude is observed to scale slightly sublinear with M in the experiment, whereas its half-width $\delta_{jet} \approx 7$ mm appears to be independent of M.

With this experimental and numerical study, we have established the base flow in ZUCCHINI which allows us to study the instabilities, especially of the free Shercliff layer, in Paper 2 [Stelzer et al., in prep.].

Appendix

3.A Governing equations in cylindrical coordinates

The governing equations of our model (Eq. 3.6 - 3.8) in cylindrical coordinates are:

$$\begin{aligned}
&\frac{Re}{M^2}\left[\frac{\partial u_r}{\partial t} + u_r\frac{\partial u_r}{\partial r} + u_z\frac{\partial u_r}{\partial z} - \frac{u_\phi^2}{r} + \frac{u_\phi}{r}\frac{\partial u_r}{\partial \phi}\right]\\
&= -\frac{\partial p}{\partial r} + \frac{1}{M^2}\left[\frac{\partial^2 u_r}{\partial r^2} + \frac{1}{r}\frac{\partial u_r}{\partial r} + \frac{1}{r^2}\frac{\partial^2 u_r}{\partial \phi^2} + \frac{\partial^2 u_r}{\partial z^2} - \frac{u_r}{r^2} - \frac{2}{r^2}\frac{\partial u_\phi}{\partial \phi}\right]\\
&\quad + B_\phi\frac{\partial \Phi}{\partial z} - \frac{B_z}{r}\frac{\partial \Phi}{\partial \phi} + u_r(B_r^2 - 1) + B_r(u_\phi B_\phi + u_z B_z)
\end{aligned} \tag{3.22}$$

$$\begin{aligned}
&\frac{Re}{M^2}\left[\frac{\partial u_\phi}{\partial t} + u_r\frac{\partial u_\phi}{\partial r} + \frac{u_\phi}{r}\frac{\partial u_\phi}{\partial \phi} + u_z\frac{\partial u_\phi}{\partial z} + \frac{u_r u_\phi}{r}\right]\\
&= -\frac{1}{r}\frac{\partial p}{\partial \phi} + \frac{1}{M^2}\left[\frac{\partial^2 u_\phi}{\partial r^2} + \frac{1}{r}\frac{\partial u_\phi}{\partial r} + \frac{1}{r^2}\frac{\partial^2 u_\phi}{\partial \phi^2} + \frac{\partial^2 u_\phi}{\partial z^2} - \frac{u_\phi}{r^2} + \frac{2}{r^2}\frac{\partial u_r}{\partial \phi}\right]\\
&\quad + B_z\frac{\partial \Phi}{\partial r} - B_r\frac{\partial \Phi}{\partial z} + u_\phi(B_\phi^2 - 1) + B_\phi(u_r B_r + u_z B_z)
\end{aligned} \tag{3.23}$$

$$\begin{aligned}
&\frac{Re}{M^2}\left[\frac{\partial u_z}{\partial t} + u_r\frac{\partial u_z}{\partial r} + \frac{u_\phi}{r}\frac{\partial u_z}{\partial \phi} + u_z\frac{\partial u_z}{\partial z}\right]\\
&= -\frac{\partial p}{\partial z} + \frac{1}{M^2}\left[\frac{\partial^2 u_z}{\partial r^2} + \frac{1}{r}\frac{\partial u_z}{\partial r} + \frac{1}{r^2}\frac{\partial^2 u_z}{\partial \phi^2} + \frac{\partial^2 u_z}{\partial z^2}\right]\\
&\quad + \frac{B_r}{r}\frac{\partial \Phi}{\partial \phi} - B_\phi\frac{\partial \Phi}{\partial r} + u_z(B_z^2 - 1) + B_z(u_r B_r + u_\phi B_\phi)
\end{aligned} \tag{3.24}$$

$$\frac{u_r}{r} + \frac{\partial u_r}{\partial r} + \frac{1}{r}\frac{\partial u_\phi}{\partial \phi} + \frac{\partial u_z}{\partial z} = 0 \tag{3.25}$$

$$\begin{aligned}
&\frac{\partial^2 \Phi}{\partial r^2} + \frac{1}{r}\frac{\partial \Phi}{\partial r} + \frac{1}{r^2}\frac{\partial^2 \Phi}{\partial \phi^2} + \frac{\partial^2 \Phi}{\partial z^2}\\
&= -\frac{B_z}{r}\frac{\partial u_r}{\partial \phi} + B_\phi\frac{\partial u_r}{\partial z} + \frac{B_z}{r}u_\phi + B_z\frac{\partial u_\phi}{\partial r} - B_r\frac{\partial u_\phi}{\partial z} - \frac{B_\phi}{r}u_z - B_\phi\frac{\partial u_z}{\partial r} + \frac{B_r}{r}\frac{\partial u_z}{\partial \phi}
\end{aligned} \tag{3.26}$$

In our axisymmetric model of ZUCCHINI, all derivatives in the ϕ-coordinate ($\partial/\partial\phi$) are set to zero.

3.B Electrical boundary conditions

What are the appropriate electrical boundary conditions for the numerical simulations of ZUCCHINI? Imposing either the electric current density on or the voltage difference between the two electrodes leads to two different boundary conditions. Strictly speaking, neither of them is the boundary condition present in the lab experiment. There, the electrical current is kept fixed by controlling the potential of both electrodes. The electrical current density is free to rearrange on the electrodes while the potential difference between the two electrodes is not necessarily the same at all times. The corresponding boundary condition would be

$$\int_{\partial\Omega} \mathbf{j} \cdot \mathbf{n} \, \mathrm{d}S = I_{imp}, \tag{3.27}$$

where integration is performed over the conducting surface $\partial\Omega$ of the electrodes. It is, however, nonlocal and not easy to implement within a FE framework.

Instead, we choose to impose the current density j_0 at the inner electrode which leads to the dimensionless condition $\mathbf{j} = \mathbf{E} = -\nabla\Phi = \mathbf{e_r}$ (Neumann boundary condition for Φ). The outer electrode is set to ground, $\Phi = 0$ (Dirichlet boundary condition for Φ). At least on the outer electrode, the electrical current density is free to rearrange. Imposing j_0 on both electrodes appears to be physically impossible. All insulating walls have to fulfill the dimensionless electric boundary condition $\mathbf{n} \cdot \mathbf{j} = \mathbf{n} \cdot \mathbf{E} = -\mathbf{n} \cdot \nabla\Phi = 0$.

3.C Convergence study

On our numerical model of ZUCCHINI, we perform tests of numerical convergence by varying several parameters, especially the order of spatial discretization and the mesh. We do our tests at $M = 202.22$ and $Re = 114.86$. These numbers correspond to the highest magnetic field that can be reached in the 'Caylar' setup ($B_{max} = 0.1$ T), and an electrical current density j_0 that is based on an imposed current of 1 A on the inner electrode which in the experiment yields a steady flow. The physical properties of GaInSn used are given in Table 3.4. The convergence study is performed without rounded electrode edges.

On the one hand we vary the order of spatial discretization. For velocity we test P3 (cubic) and P2 (quadratic), for pressure P2 and P1 (linear), for the electric potential quintic, quartic and quadratic. Also we study the effects of streamline diffusion (SL) and crosswind diffusion (CW) which damp numerical oscillations by adding a small amount of artificial diffusion in the streamwise and crosswind direction respectively. On the

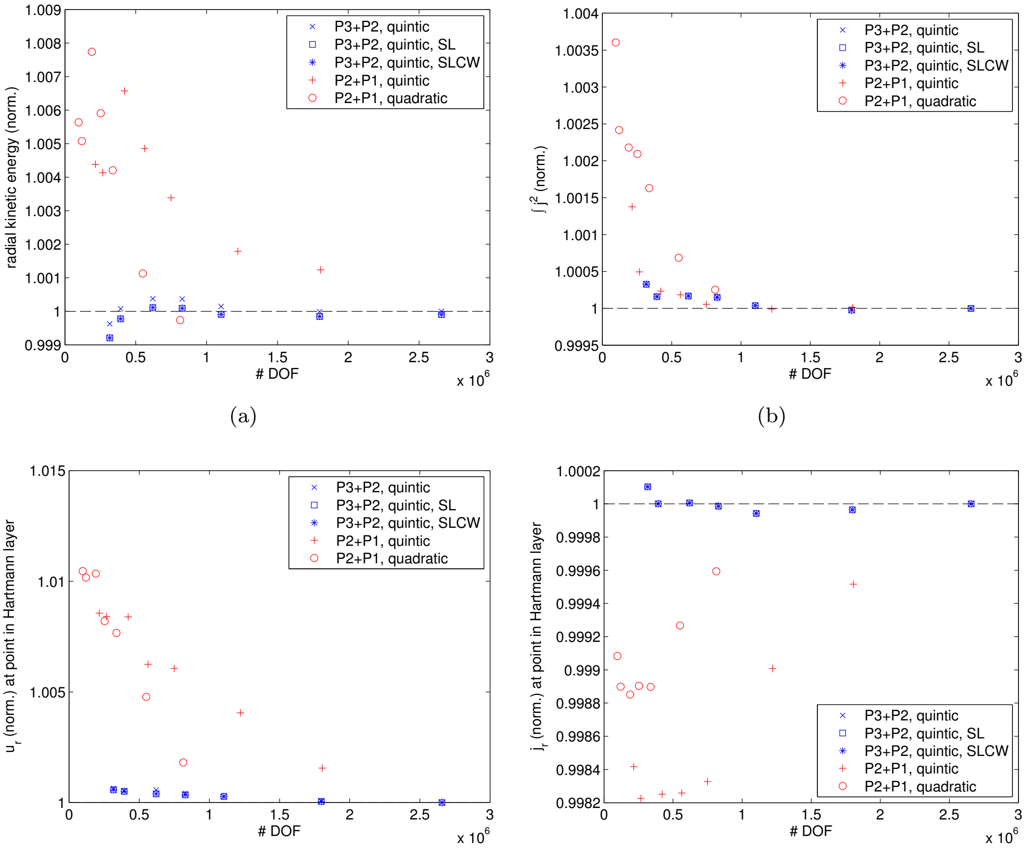

(a) (b)

(c) (d)

FIGURE 3.19: Convergence of global and local quantities. (a) Radial kinetic energy when decreasing the element size in the mesh. (b) 'Ohmic dissipation'. (c) Radial velocity u_r in the Hartmann layer. (d) Radial current density j_r in the Hartmann layer. Results are normalized by the best-resolved 'P3+P2, quintic' simulation.

other hand we parametrize the element size, resulting in meshes with different numbers of degrees of freedom (DOF).

Convergence is assessed using several global and local quantities related to velocity and current density. Besides we also test whether the divergence-free conditions for velocity and current density are fulfilled globally and locally. Examples of the convergence of global quantities are given in Figures 3.19a-b which show integrated radial kinetic energy $E_{kin,r} = 0.5 \int u_i^2 \mathrm{d}S$ and integrated 'Ohmic dissipation' $\int (j_r^2 + j_\phi^2 + j_z^2)\mathrm{d}S$. Figures 3.19c-d display the convergence of point measurements of u_r and j_r in the Hartmann layer. All quantities are normalized to the best-resolved simulation with discretization 'P3+P2, quintic'. In conclusion of this first part of the convergence study, we choose to use discretization 'P3+P2, quintic' with streamline diffusion. A model with roughly 10^6 DOF is observed to have a sufficient numerical convergence better than 0.1%.

In the second step of our convergence study, we refine the element size of the mesh in the core and the boundary layers independently from each other. It turns out that by decreasing boundary layer size we improve convergence further, whereas decreasing

Table 3.5: Comparison of the mean azimuthal velocity $\overline{u_\phi}$ with the rms azimuthal velocity $u_{\phi,rms}$ for the most extreme models in our data set. The ratio $-\overline{u_\phi}/u_{\phi,rms}$ does hardly scale with M and not at all with Re_i.

M	Re_i	$u_{\phi,rms}$	$\overline{u_\phi}$	$-\overline{u_\phi}/u_{\phi,rms}$
1	1	0.0115	−0.0095	0.83
1	1000	0.0107	−0.00898	0.84
200	1	10.33	−9.47	0.92
200	1000	10.21	−9.36	0.92

core element size does not make a difference. In general we make sure that the boundary and shear layers are resolved by at least 5 elements within their thickness Tagawa et al. [2002].

The quantity most difficult to conserve is $\nabla \cdot \mathbf{j} = 0$. For our interpretation, we only use simulations that have a ratio of inflowing over outflowing electrical current of $I_{in}/I_{out} \in [95\%, 105\%]$. In our parameter study (Section 3.3.2), this criterion discards the models highest in Re_i for $M \geq 100$ and leaves us with 51 out of 56 models. A convergence test along the same lines is performed for the simulations of the 'Cryo' setup ($B_{max} =$ 1 T) with up to $M = 2000$.

3.D Comparison mean versus rms azimuthal velocity

In Section 3.3.2.2, we used rms velocities defined by $u_{i,rms} = (S^{-1}\int u_i^2 \mathrm{d}S)^{1/2}$ to determine the scaling with the control parameters. Depending on the velocity distribution in the volume, their scaling might be different from the one of mean velocities $\overline{u_i} = S^{-1}\int u_i \mathrm{d}S$.

For the dominating azimuthal velocity $u_{\phi,rms}$, we found scalings in Section 3.3.2.2. We know that u_ϕ has a similar order of magnitude over the biggest part of the volume (especially at high M). Table 3.5 shows a comparison between $\overline{u_\phi}$ and $u_{\phi,rms}$ for the most extreme cases in our data set. The ratio $-\overline{u_\phi}/u_{\phi,rms}$ does hardly depend on M and not at all on Re_i. Hence we conclude that $\overline{u_\phi}$ scales in the same way as $u_{\phi,rms}$ (Table 3.2).

3.E Argument for the velocity scaling at high M

We give here an argument for the scaling of $u_\phi \sim M$ at large M (see Section 3.3.2.2). Starting from the Navier-Stokes equations for steady flow,

$$\nabla \cdot \mathbf{u} = 0 \tag{3.28}$$

$$Re\, \mathbf{u} \cdot \nabla \mathbf{u} = -\nabla p + M^2\, \mathbf{j} \times \mathbf{B} + \nabla^2 \mathbf{u}, \tag{3.29}$$

we integrate over the volume of the tank, and consider the ϕ-component of the momentum equation. We find:

- $\int_V \mathbf{u}\cdot\nabla\mathbf{u}\,\mathrm{d}V = \oint (\mathbf{u}\circ\mathbf{u})\cdot\mathrm{d}\mathbf{S} = 0$, which vanishes exactly given the no-slip boundary conditions; $\circ$ is the dyadic product.
- $\int_V r^{-1}\partial_\phi p\,\mathrm{dV} = \iint_{r,z} r\,\mathrm{d}r\,\mathrm{d}z \int_{\phi=0}^{2\pi} r^{-1}\partial_\phi p\,\mathrm{d}\phi = \iint_{r,z} r\,\mathrm{d}r\,\mathrm{d}z\,p|_{\phi=0}^{2\pi} = 0$, since $p(r,\phi=0,z) = p(r,\phi=2\pi,z)$.

Furthermore, we can also convert the viscous term into a boundary integral:

$$\int_V \nabla^2\mathbf{u}\,\mathrm{d}V = \int_V \partial_i\partial_i u_j \mathrm{d}V = \oint \partial_i u_j\,\mathrm{d}S_i \tag{3.30}$$

The dominant contributions to this term come from the walls where $\partial_i u_j$ is largest. For Hartmann and side walls, this term scales as Mu and $M^{1/2}u$ respectively, provided that $M \gg 1$. Therefore, we can say that:

$$\int_V \nabla^2\mathbf{u}\,\mathrm{d}V = \mathcal{O}(Mu). \tag{3.31}$$

Considering the Lorentz force, we may separate the current into two contributions: $\mathbf{j} = \mathbf{j}_1 + \mathbf{j}_2$, where $\mathbf{j}_1 = -\nabla\phi_1 + \mathbf{u}\times\mathbf{B}$ and $\mathbf{j}_2 = -\nabla\phi_2$. Here, ϕ_1 and ϕ_2 are respectively solution of:

$$\nabla^2\phi_1 = \nabla\cdot(\mathbf{u}\times\mathbf{B}) \tag{3.32}$$

with boundary conditions $\partial_n\phi_1 = 0$ everywhere, and

$$\nabla^2\phi_2 = 0 \tag{3.33}$$

with boundary conditions $\partial_n\phi_2 = 0$ at the insulating parts of the walls, and $\partial_n\phi = j_{in}(z)$ at the electrodes. Furthermore, we may transform the integral of the Lorentz force as follows:

$$\begin{aligned} \int_V \mathbf{j}\times\mathbf{B}\,\mathrm{dV} &= \int_V \varepsilon_{klm} j_l B_m\,\mathrm{d}V \\ = \int_V \varepsilon_{klm}\partial_n(j_n r_l B_m)\,\mathrm{dV} &= \oint_{\partial V} (\mathbf{r}\times\mathbf{B})\,(\mathbf{j}\cdot\mathrm{d}\mathbf{S})\,. \end{aligned} \tag{3.34}$$

We see that this term will cancel for $\mathbf{j}_1$, and will be of order-of-magnitude $\mathcal{O}(j_{in}B) = 1$ for $\mathbf{j}_2$. Summarizing, we find:

$$\mathcal{O}(Mu) = \mathcal{O}(M^2), \tag{3.35}$$

which gives the required scaling $u_\phi \sim M$.

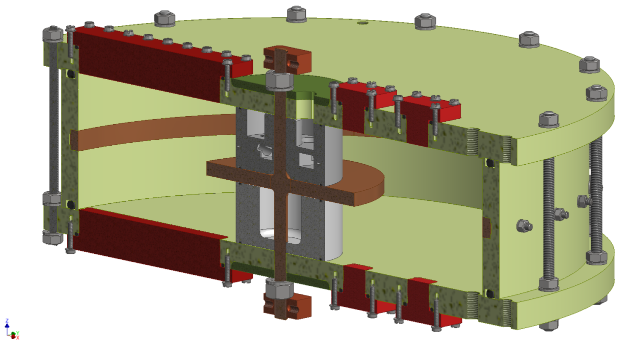

FIGURE 3.20: Components of ZUCCHINI. The outer part of the tank (yellow-green) is made from polypropylene (PP), the inner cylinder (grey) is polyethylene terephtalate (PET). The inner and outer electrodes (brown) are copper which has been coated with 20 μm NiP12 (nickel with 12 weight percent phosphor) and 2 μm chromium to prevent the copper from dissolving in the GaInSn. Additionally the inner electrode is insulated on its top and bottom surfaces. The replacable inserts (red) are made of plexiglass and epoxy resin.

3.F Details of the experimental setup

The different components of the tank are shown in Figure 3.20. The inner cylinder houses UDV probes 1 and 2. UDV probe 3 and the potential difference probes are mounted on the inserts at the top and bottom plates. The inserts as well as the whole container of ZUCCHINI are designed in a modular way which enables us to exchange components. The outer electrode is separated into six segments to improve control on the current distribution. Gas- and water-tightness of the tank is achieved by nitrile butadiene rubber (NBR) O-rings. In preparation for the filling with GaInSn, we cleaned and degreased all parts of the tank both mechanically and chemically with isopropyl alcohol, and performed extensive tightness tests using argon and a water bath.

3.G The magnetic setups ‘Caylar’ and ‘Cryo’

During our experiments, we employed two different coil systems for the generation of the magnetic field. For the lower magnetic field strengths up to 0.1 T, we used a modified Helmholtz coil system with resistive copper coils manufactured by Caylar (‘Caylar’ setup). It consists of two small outer coils (inner diameter 40 cm) and a bigger central coil (inner diameter 60 cm) stacked vertically. The coils were fed with up to 300 A (max. 15 V) generating fields up to 0.1 T in continuous operation. The field strength was measured by two calibrated Hall probes with a precision of < 0.1 mT on the top lid of the container.

During installation, we centered the ZUCCHINI tank not only geometrically but also more precisely according to the magnetic mapping. We mapped the magnetic field inside the coil volume by three perpendicular Hall effect sensors, model A1326 by Allegro,

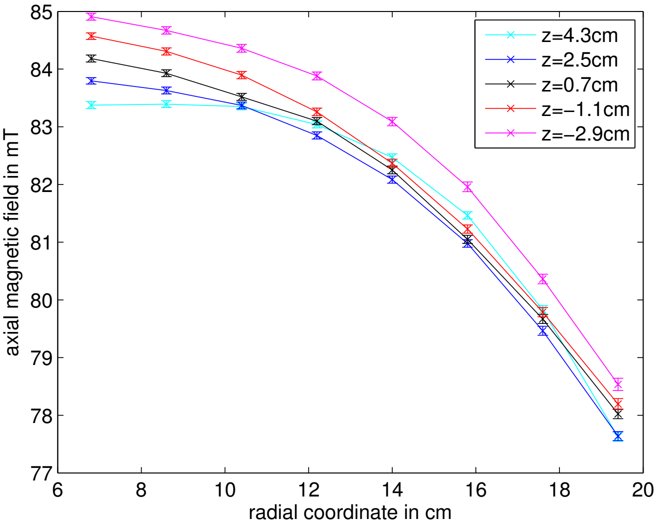

(a)

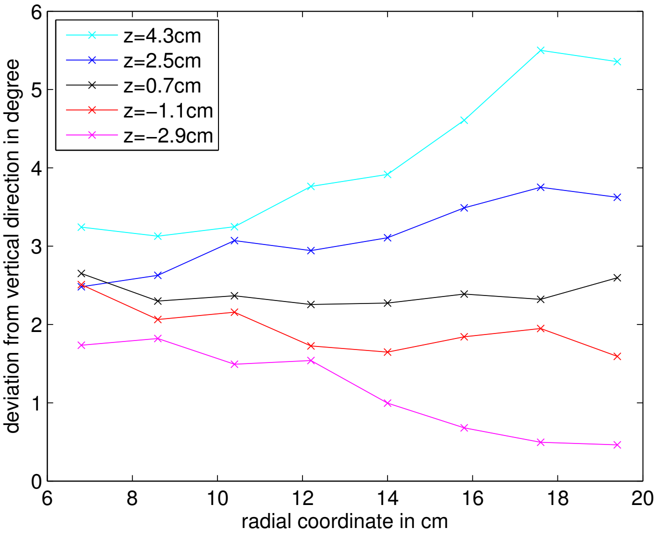

(b)

FIGURE 3.21: Characterization of magnetic field in 'Caylar' setup. (a) Measurements of the dominant axial component B_z at a current of 240 A through the three Caylar coils. The values and error bars shown are mean values and standard deviations over the azimuthal direction. (b) Angle of deviation of the direction of the magnetic field from the axial direction. The coordinates are: radial r from the symmetry axis, and axial z from the mid-plane of ZUCCHINI.

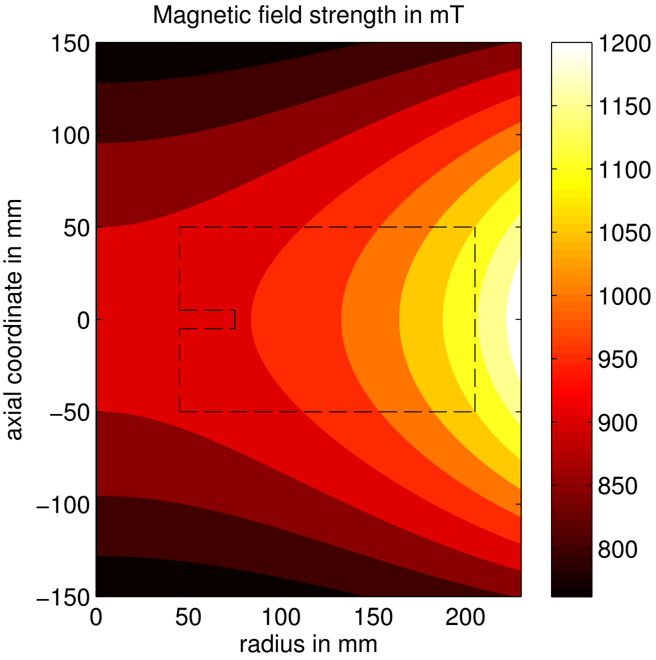

FIGURE 3.22: Map of magnetic field strength of a single loop approximating the field of the 'Cryo' setup at 1 T. The cross-section of the tank is shown in dashed lines. A field of this type is used for the numerical recovery of the jet in Section 3.4.4.2.

which are calibrated beforehand and have sensitivity of 25 mV/mT. Figure 3.21a shows the azimuthal mean of dominant the axial component B_z of the magnetic field. With increasing radius, it decreases by 7%. Also there seems to be a small dependence of the field strength on the axial position with higher values in the lower part of the tank.

The angle of deviation of the magnetic field direction from the vertical is defined as $\alpha = \arctan B_h/B_z$ where $B_h = (B_r^2 + B_\phi^2)^{1/2}$ is the horizontal magnetic field strength. We find that deviations of the magnetic field direction from the vertical are smaller than 4° in most of the tank volume (Fig. 3.21b). These results are the same for other magnetic field strengths as long as the currents through the three coils are equal (linear superposition).

The second setup 'Cryo' reaches magnetic field strengths up to 1 T. It consists of a single superconducting coil made from twisted multi-filamentary NbTi/Cu by Cryomagnetics, Inc. The coil is cooled down to roughly 3 K using liquid helium and a Gifford-McMahon refrigeration cycle. The required electrical current in the coil at 1 T is 83 A. As it is generated by a single (short) coil, the magnetic field is less uniform than in the Helmholtz-type 'Caylar' setup. The 'Cryo' setup shows an increase in magnetic field strength by roughly 15% with radius and a considerable amount of deviation from the axial direction at $z \neq 0$ near the outer cylinder. For our numerical study in Section 3.4.4.2, we approximate the 'Cryo' field by the field of a single wire loop similar to the one shown in Figure 3.22.

3.H Power supplies

In the ‘Caylar’ setup, each of the three used Delta Elektronika power supplies feeds two of the six segments of the outer ring electrode. The amount of current flowing through each segment has been adjusted by additional Ohmic resistors to vary by less than 4 % between segments. The copper electrodes have an electrical conductivity which is roughly 20 times higher than that of GaInSn. Hence we assume a homogeneous distribution of the forcing current as long as wetting issues can be neglected. In fact, we have tested the sensitivity of the flow to the distribution of forcing current. It turns out that as long as the distribution is reasonably symmetrical, the resulting flow is not affected significantly even if one or more segments are disconnected from the power supply.

In the ‘Cryo’ setup, we use six power supplies each feeding one segment of the outer electrode, thus avoiding the problem of uneven current distribution. Running the experiment at high currents over a longer time interval leads to an increase of the temperature in the system by up to 15 K. The temperature at the beginning of a data acquisition sequence differs between the two setups. In the ‘Caylar’ setup, it is standard room temperature ($\sim$ 22°C), whereas it is $\sim$ 15°C in the ‘Cryo’ setup due to the cooling of the superconducting coil.

Acknowledgments

We would like to thank P. Scarfe, R. Grimmer, F. Polli and T. Mörgeli for help with the design and manufacture of the experiment, as well as R. Hollerbach, T. Alboussière, A. Pothérat, F. Stefani, M. Seilmayer, T. Boeck and F. Samsami for fruitful discussions and advice on various topics within ZUCCHINI. Funding for for this work by the ERC grant 247303 ‘MFECE’ is gratefully acknowledged.

References

O. Andreev, Y. Kolesnikov, and A. Thess. Application of the ultrasonic velocity profile method to the mapping of liquid metal flows under the influence of a non-uniform magnetic field. *Exp Fluids*, 46(1):77–83, Jan 2009.

J. Baylis. Detection of the onset of instability in a cylindrical magnetohydrodynamic flow. *Nature*, page 563, 1964.

J. Baylis. Experiments on laminar flow in curved channels of square section. *Journal of Fluid Mechanics*, 48(03):417–422, 1971.

J. Baylis and J. Hunt. MHD flow in an annular channel; theory and experiment. *Journal of Fluid Mechanics*, 48(03):423–428, 1971.

J. Boisson, A. Klochko, F. Daviaud, V. Padilla, and S. Aumaitre. Travelling waves in a cylindrical magnetohydrodynamically forced flow. *Phys Fluids*, 24(4):044101, Jan 2012.

D. Brito, H. Nataf, P. Cardin, J. Aubert, and J. Masson. Ultrasonic doppler velocimetry in liquid gallium. *Exp Fluids*, 31(6):653–663, Jan 2001.

A. Cramer, C. Zhang, and S. Eckert. Local flow structures in liquid metals measured by ultrasonic doppler velocimetry. *Flow Measurement and Instrumentation*, 15:145–153, 2004.

P. Davidson. *An Introduction to Magnetohydrodynamics.* Cambridge University Press, 2001.

P. Davidson and F. Siso-Nadal. On the structure of small-scale motion in the core of the earth. *Geophysical and Astrophysical Fluid Dynamics*, 96(1):49–76, 2002.

DOP3000 series User's manual. DOP Signal Processing S.A., www.signal-processing.com, software 4.01 edition.

J. Hartmann. Hg-dynamics i: Theory of the laminar flow of an electrically conductive liquid in a homogeneous magnetic field. *Mathematisk-fysiske Meddelelser, Det Kgl. Danske Videnskabernes Selskab*, XV(6):1–28, 1937.

J. Hartmann and F. Lazarus. Hg-dynamics ii: Experimental investigations on the flow of mercury in a homogeneous magnetic field. *Mathematisk-fysiske Meddelelser, Det Kgl. Danske Videnskabernes Selskab*, XV(7):1–45, 1937.

R. Hollerbach, X. Wei, J. Noir, and A. Jackson. Electromagnetically driven zonal flows in a rapidly rotating spherical shell. *Journal of Fluid Mechanics*, 725:428–445, 2013.

J. Hunt. Magnetohydrodynamic flow in rectangular ducts. *Journal of Fluid Mechanics*, 21(4):577–590, 1965.

J. Hunt and K. Stewartson. Magnetohydrodynamic flow in rectangular ducts. ii. *Journal of Fluid Mechanics*, 23(3):563–581, 1965.

J. Hunt and W. Williams. Some electrically driven flows in magnetohydrodynamics. part 1. theory. *Journal of Fluid Mechanics*, 31(04):705–722, 1968.

I. Khalzov, A. Smolyakov, and V. Ilgisonis. Equilibrium magnetohydrodynamic flows of liquid metals in magnetorotational instability experiments. *Journal of Fluid Mechanics*, 644:257–280, 2010.

D. Krasnov, E. Zienicke, O. Zikanov, T. Boeck, and A. Thess. Numerical study of the instability of the Hartmann layer. *Journal of Fluid Mechanics*, 504:183–211, 2004.

J. Larmor. Possible rotational origin of magnetic fields of Sun and Earth. *Electrical Review*, 85:412ff., 1919.

K. Messadek and R. Moreau. An experimental investigation of MHD quasi-two-dimensional turbulent shear flows. *J. Fluid Mech.*, 456:137–159, Jan 2002.

B. Mikhailovich, A. Shapiro, S. Sukoriansky, and I. Zilberman. Experiments with turbulent rotating MHD flows in an annular gap. *Magnetohydrodynamics*, 48(1):43–50, 2012.

R. Moreau and S. Molokov. *Magnetohydrodynamics - Historical Evolution and Trends*, chapter Julius Hartmann and His Followers: A Review on the Properties of the Hartmann Layer, pages 155–170. Springer, 2007.

P. Moresco and T. Alboussiere. Experimental study of the instability of the Hartmann layer. *J. Fluid Mech.*, 504:167–181, Jan 2004.

N. B. Morley, J. Burris, L. C. Cadwallader, and M. D. Nornberg. Gainsn usage in the research laboratory. *Review of Scientific Instruments*, 79(5), 2008.

H. C. Nataf, T. Alboussiere, D. Brito, P. Cardin, N. Gagniere, D. Jault, and D. Schmitt. Rapidly rotating spherical couette flow in a dipolar magnetic field: An experimental study of the mean axisymmetric flow. *Phys Earth Planet Int*, 170(1-2):60–72, 2008.

P. Olson. Overview of core dynamics. In G. Schubert, editor, *Treatise on Geophysics*, volume 8 on Core Dynamics. Elsevier Science Publishers, 2007.

A. Potherat, J. Sommeria, and R. Moreau. An effective two-dimensional model for mhd flows with transverse magnetic field. *Journal of Fluid Mechanics*, 424:75–100, 2000.

J. Shercliff. Steady motion of conducting fluids in pipes under transverse magnetic fields. *Mathematical Proceedings of the Cambridge Philosophical Society*, 49(01):136–144, 1953.

F. Stefani, T. Gundrum, G. Gerbeth, G. Rüdiger, M. Schultz, J. Szklarski, and R. Hollerbach. Experimental evidence for magnetorotational instability in a taylor-couette flow under the influence of a helical magnetic field. *Phys. Rev. Lett.*, 97(18), Nov 2006.

Z. Stelzer, D. Cebron, S. Miralles, J. Noir, S. Vantieghem, and A. Jackson. Experimental and numerical study of electrically-driven MHD flow in a modified cylindrical annulus: (2) Instabilities. in prep.

P. Tabeling and J. Chabrerie. Magnetohydrodynamic secondary flows at high Hartmann numbers. *Journal of Fluid Mechanics*, 103:225–239, 1981.

T. Tagawa, G. Authie, and R. Moreau. Buoyant flow in long vertical enclosures in the presence of a strong horizontal magnetic field. Part 1. Fully-established flow. *European Journal of Mechanics - B/Fluids*, 21(4):383–398, 2002.

S. Vantieghem and B. Knaepen. Numerical simulation of magnetohydrodynamic flow in a toroidal duct of square cross-section. *International Journal of Heat and Fluid Flow*, 32(6):1120–1128, 2011.

Y. Zhao and O. Zikanov. Instabilities and turbulence in magnetohydrodynamic flow in a toroidal duct prior to transition in Hartmann layers. *J. Fluid Mech.*, 692:288–316, 2012.

Chapter 4

Characterization of the instabilities

Manuscript:

Experimental and numerical study of electrically-driven MHD flow in a modified cylindrical annulus: (2) Instabilities

by **Zacharias Stelzer**, Sophie Miralles, David Cébron, Jérôme Noir, Stijn Vantieghem, Peter Scarfe and Andrew Jackson

For submission to *Physics of Fluids*.

Summary

The stability of electrically conducting flows under the influence of an imposed magnetic field is relevant in geo- and astrophysical context as well as in engineering applications. We present an investigation of liquid metal flow by means of a laboratory experiment as well as a linear stability analysis of the setup using the finite element method. The experimental device ZUCCHINI is a modified cylindrical annulus with electrically-driven flow of liquid GaInSn operating at Hartmann and Reynolds numbers up to $M_{max} = 2022$ and $Re_{max} = 2.23 \cdot 10^5$ respectively. The magnetic field gives rise to a free Shercliff/ shear layer at the prominent inner electrode. The flow is probed by ultrasound Doppler velocimetry as well as potential difference probes.

In the experiment, we identify several flow regimes characterized by the nature of the instabilities and the behaviour of the friction factor F. The steady flow is destabilized by a Kelvin-Helmholtz mechanism at the free Shercliff layer. In the asymptotic large-M regime which is experimentally only reached for $M \gtrsim 500$, this transition scales as $Re_c/M \approx 6$ and is clearly seen in measurements of F. In agreement with the numerical linear stability study, the instability consists of counterrotating vortices which are restricted to the free Shercliff layer for low forcing. Their azimuthal wave number m grows with M and decreases with Re. The second transition is a significant increase in

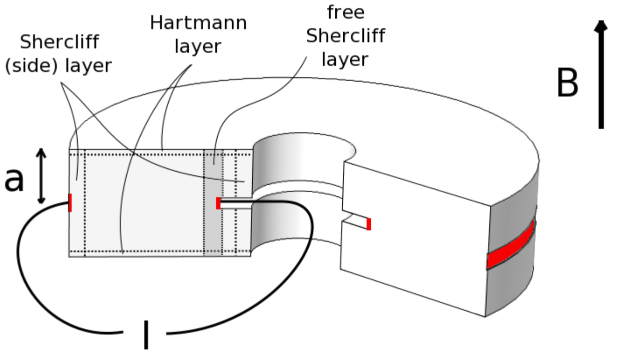

FIGURE 4.1: Sketch of the modified cylindrical annulus ZUCCHINI. Forcing an axisymmetric electrical current I through the liquid metal under an imposed magnetic field $\mathbf{B}$ gives rise to a Lorentz force which drives an azimuthal flow. The electrodes are coloured in red, the remaining walls are insulating. The half-height $a = 5$ cm is used as length scale.

the Shercliff layer thickness to a constant value of $\delta_S \approx 40$ mm associated with a change in radial flow structure and space-filling vortices at $Re_t \sim M^\beta$ with $\beta \in [1, 1.3]$. Further transitions are observed at $Re_f/M^2 \sim 1$ and $Re_h/M \approx 380$ in F-measurements; the first is attributed to a growth of the vortices, the second to the transition to turbulence in the Hartmann layer.

4.1 Introduction

In the context of geo- and astrophysics as well as engineering applications, it is of great interest to study the interaction between electrically conducting fluids and magnetic fields. This research area is called magnetohydrodynamics (MHD). Two MHD regimes can be distinguished by the value of the magnetic Reynolds number $Rm = \mu_0 \sigma_e U_0 a$ where μ_0 is the permeability of free space, σ_e the electrical conductivity, U_0 a typical velocity and a the length scale of the system. On the one hand is the regime of large Rm where e.g. planetary dynamos live [Olson, 2007]. It is characterized by a two-way interaction between flow and magnetic field. On the other hand is the regime of small $Rm \ll 1$ characterized by the absence of the reaction of the flow on the magnetic field since induced fields are negligible. Many liquid-metal experiments and engineering applications fall into this so-called quasi-static limit [Davidson, 2001]; it is also believed to govern the small-scale motions in the Earth's core [Davidson and Siso-Nadal, 2002].

The experiment ZUCCHINI (ZUrich Cylindrical CHannel INstability Investigation) allows us to study electrically-driven MHD flow at low Rm in the modified cylindrical annulus shown in Figure 4.1. All side walls are electrically insulating except the inner and outer ring electrodes. Forcing a radial electrical current I through the tank filled with liquid GaInSn under an imposed magnetic field $\mathbf{B}$ gives rise to a Lorentz force leading to a mainly azimuthal flow. The system is controlled by two nondimensional parameters, namely the Hartmann number M and the Reynolds number Re,

$$M = aB_0\sqrt{\frac{\sigma_e}{\rho\nu}}, \qquad Re = \frac{U_0 a}{\nu}. \tag{4.1}$$

where ρ is the mass density, ν the kinematic viscosity of the fluid and B_0 the strength of the imposed magnetic field. In the first part of this work [Stelzer et al., in prep.], hereafter referred to as 'Paper 1', we established the steady base flow experimentally as well as numerically. Also a detailed description of the setup and previous experiments are found there. In the current study, we focus on the instabilities of the flow which will be shown to originate from the free Shercliff layer near the inner electrode.

Most earlier experiments in similar geometries operated in the unstable regime and used global potential difference measurements to diagnose the flow [Baylis, 1964, Baylis and Hunt, 1971, Moresco and Alboussiere, 2004]. Transitions in flow regimes were diagnosed by the friction factor F (Eq. 4.16) or similar quantities. Some experiments probed the flow structure locally by potential difference probes (PDP) [Alboussiere et al., 1999, Messadek and Moreau, 2002] or ultrasonic Doppler velocimetry (UDV) [Boisson et al., 2012]. We employ both local and global measurements.

The most significant difference between ZUCCHINI and most other experiments is the presence of the inner electrode which protrudes into the flow. Since the magnetic field suppresses gradients along its direction, a free Shercliff (shear) layer develops at the edge of the electrode. In addition the Hartmann layers at walls perpendicular to the field with thickness $\delta_H \sim M^{-1}$ and Shercliff (side) layers at parallel walls scaling as $\delta_S \sim M^{-1/2}$ are important features of confined low-Rm MHD flow.

Due to the sparsity of experimental measurements, it is instructive to turn to numerical simulations in order to get a complementary picture of the flow. Consequently the famous Moresco and Alboussiere [2004] experiment (MA04) studying the instability of the Hartmann layer as well as the original Hartmann and Lazarus [1937] duct experiment have been the topic of intense numerical investigations. Krasnov et al. [2004] explained the discrepancy in the value for the threshold of instability between results of MA04 ($R_c = Re/M \approx 380$) and the linear stability analysis which is two orders of magnitude larger by finite-amplitude perturbations. Vantieghem and Knaepen [2011] found that the magnetic field suppresses turbulence in the core and the Hartmann layers and that unstable side layers can coexist with stable Hartmann layers. Zhao and Zikanov [2012] studied the MA04 setup below the threshold of Hartmann layer instability for a Hartmann number of $M = 260$ and input Reynolds numbers $Re_i \in [800, 90000]$ (definition based on the imposed voltage analogous to Eq. 4.9). They found that a first instability limited to the outer side layer does not change the friction factor F which is dominated by stresses at the Hartmann walls. This picture of subsequent relaminarization of the core flow, the Hartmann layers and finally the side layers with increasing magnetic field was confirmed by the straight duct simulations of Krasnov et al. [2012] at $Re = 10^5$ and $M \in [0, 400]$. Not only the critical parameters for the laminar-turbulent transition but also friction coefficients are in agreement with Hartmann's original data [Krasnov et al., 2013].

Another approach for the numerical simulation of MHD flow at large Hartmann numbers M and interaction parameters $N = M^2/Re$ is the effective two-dimensional model of Potherat et al. [2000, 2005]. It is based on the assumption of a quasi-2D core flow, and includes 3D effects due to the Hartmann layers in the averaged equations. It has been validated against experimental results, e.g. the free shear layer of Alboussiere et al. [1999]. A similar concept underlies the geostrophic-like model by Alboussiere [2004, 2007] for large-M flows.

Free MHD shear layers have been studied theoretically [Bühler, 1996, Lieutaud and Neel, 2001], experimentally [Alboussiere et al., 1999, Messadek and Moreau, 2002, Roach et al., 2012, Spence et al., 2012] and numerically [Potherat et al., 2005, Spence et al., 2012]. Lieutaud and Neel [2001] studied the stability of electrically-driven shear flow in a straight duct against two-dimensional perturbations, and found the limit of unconditional stability below which any arbitrary 2D perturbation decays. The MATUR experiment [Alboussiere et al., 1999, Moresco and Alboussiere, 2004] examined the structure as well as momentum transport of a quasi-2D MHD turbulent shear layer at $M = 42$ and up to 1800 respectively. It was found that the shear layer thickness is significantly increased and scales as $\delta_S \sim (M/Re)^{-1/2.3}$, the laminar prediction being $\delta_S \sim M^{-1/2}$. The velocity field is dominated by a small number of large coherent structures moving with a transit velocity of slightly above $u_{\phi,max}$. In the Princeton MRI experiment [Roach et al., 2012, Spence et al., 2012], a free Shercliff layer was studied in the presence of rotation and magnetic field in a Taylor-Couette apparatus. Another Taylor-Couette experiment, however in spherical geometry, is DTS [Nataf et al., 2008] where magneto-inertial waves were observed [Schmitt et al., 2008].

The present paper focuses on the instabilities in ZUCCHINI and their threshold. Section 4.2 summarizes the physical model which can be found in more detail in Paper 1. Section 4.3 describes our linear stability analysis that is based on 2D numerical simulations. The experimental setup, procedure and results are given in Section 4.4. A discussion in Section 4.5 concludes the work.

4.2 Model description

The physical model is a cylindrical annulus filled with an electrically conducting fluid. The basic setup is shown in Figure 4.1. Container and fluid are subject to an imposed axial magnetic field $\mathbf{B} = B_0\mathbf{e}_z$ with a strength of up to 1 T. We force an electrical current I of up to 300 A between the edge of the disk electrode at the center and the ring electrode at the outer cylinder. The remaining walls of the container are electrically insulating. The mainly radial current density $\mathbf{j}$ in an axial magnetic field gives rise to a Lorentz force $\mathbf{f_L} = \mathbf{j} \times \mathbf{B}$ in the azimuthal direction resulting in an azimuthal fluid flow.

With $Rm \lesssim \mathcal{O}(10^{-2})$ as an indicator of the ratio of induced to imposed magnetic fields, induced fields are negligible in ZUCCHINI. For this so-called quasi-static approximation ($Rm \ll 1$), the dimensional governing equations are the Navier-Stokes equation, the incompressible continuity equation, Ohm's law and the equation of charge conservation,

$$\rho \left(\frac{\partial \mathbf{u}}{\partial t} + \mathbf{u} \cdot \nabla \mathbf{u} \right) = -\nabla p + \rho \nu \nabla^2 \mathbf{u} + \mathbf{j} \times \mathbf{B} \tag{4.2}$$

$$\nabla \cdot \mathbf{u} = 0 \tag{4.3}$$

$$\mathbf{j} = \sigma_e \left(\mathbf{E} + \mathbf{u} \times \mathbf{B} \right) \tag{4.4}$$

$$\nabla \cdot \mathbf{j} = 0, \tag{4.5}$$

where $\mathbf{u}$ is the velocity vector, $\mathbf{E}$ is the electric field and p is the pressure. The relevant material properties are the mass density ρ, the kinematic viscosity ν and the electrical conductivity σ_e. The nondimensional equations are

$$\begin{aligned} \frac{Re}{M^2} \left(\frac{\partial \mathbf{u}}{\partial t} + \mathbf{u} \cdot \nabla \mathbf{u} \right) \\ = -\nabla p + \frac{1}{M^2} \nabla^2 \mathbf{u} + \left(-\nabla \Phi + \mathbf{u} \times \mathbf{B} \right) \times \mathbf{B} \end{aligned} \tag{4.6}$$

$$\nabla \cdot \mathbf{u} = 0 \tag{4.7}$$

$$\nabla^2 \Phi = \nabla \cdot \left(\mathbf{u} \times \mathbf{B} \right) \tag{4.8}$$

as derived in Paper 1. The nondimensional parameters governing the system are the Hartmann number M and the Reynolds number Re (Eq. 4.1). The square of the Hartmann number M^2 gives the ratio of Lorentz to viscous forces. The Reynolds number Re is the ratio of inertial to viscous forces. Alternatively the interaction parameter $N = M^2/Re$ can be used which gives the ratio of Lorentz to inertial forces. Note that we need to define a control parameter Re for the numerical study that depends on a fixed velocity scale U_0 since the actual velocity is an output of the simulations. We choose the 'input Reynolds' number,

$$Re_i = \frac{U_0 a}{\nu} = \frac{j_0 a}{\nu \sigma_e B_0}, \tag{4.9}$$

where j_0 is the imposed electric current density on the inner electrode.

4.3 Numerical simulation

We assume that the base flow in ZUCCHINI is steady and axisymmetric (cf. Paper 1). In reality, such a flow occurs only at low forcing. For a given Hartmann number M, the flow may be unstable to infinitesimally small perturbations in the velocity field above a critical value $Re_{i,c}$ of the input Reynolds number, called the linear onset of instability. These perturbations initially grow like $\mathrm{e}^{\sigma t}$ where σ is the growth rate. The flow is also unstable to finite-amplitude perturbations potentially already below the linear onset of instability, $Re_i < Re_{i,c}$, called a subcritical instability.

As for the base flow, we perform numerical simulations using the commercial finite element (FE) code Comsol Multiphysics, version 4.3b, which facilitates the implementation of the ZUCCHINI geometry. The brute force approach of recovering the unstable flow by 3D simulations is too costly since very thin boundary layers $\delta_H \sim M^{-1}$ have to be resolved. Hence we choose to study the linear onset of instability by simulating modes with different azimuthal wave numbers m separately. The separation is possible since modes with different m are not coupled in the linear problem. In this way, the problem reduces to 2D3C (2 dimensions, 3 components) simulations.

4.3.1 First-order perturbation equations

For the study of the linear onset of instability, the velocity field is expressed as a sum of the steady and axisymmetric base flow $\mathbf{u}^b$ and and a harmonic perturbation $\mathbf{u}'$ with an explicit ϕ-dependence using the azimuthal wave number m,

$$\mathbf{u} = \mathbf{u}^b(r, z) + \mathbf{u}'(r, z, t)\, \mathrm{e}^{\mathrm{i}m\phi}. \tag{4.10}$$

The perturbation is assumed to be small compared to the base flow, $|\mathbf{u}'| = \epsilon\, |\mathbf{u}^b|$ with $\epsilon \ll 1$. The same procedure is applied to the remaining variables pressure p and the electric potential Φ. Inserting these expressions into the governing Equations 4.6-4.8 yields terms of order ϵ^0, ϵ^1 and ϵ^2. Terms of order zero that constitute the base flow (equivalent to Eq. 4.6-4.8) are solved in Paper 1, second-order terms are negligible. The remaining terms of order one in ϵ make up the linearized perturbation equations. They are given in cylindrical coordinates in Appendix 4.C.

4.3.2 Numerical model

The linearized perturbation equations (Eq. 4.17-4.21) as well as the equations for the axisymmetric base flow (Eq. 4.6-4.8) are solved with the FE code Comsol Multiphysics. The 2D geometry corresponds to a (r, z)-plane section through the experimental setup of ZUCCHINI. Details of the implementation are found in Paper 1. We use quadratic and linear Lagrange elements for the discretization of velocity and pressure fields respectively in this study; the discretization of the electric potential is quadratic. In order to further reduce computation time, the mesh is adapted for every M. A validation with results from the better resolved base flow study is reported in Appendix 4.A.

Velocity boundary conditions are no slip, $\mathbf{u} = \mathbf{0}$. For the base flow, electrical boundary conditions are insulating, $-\mathbf{n} \cdot \nabla\Phi = 0$, at all boundaries apart from the electrodes; at the inner electrode, a radial current is forced, $-\nabla\Phi = \mathbf{e_r}$, the outer electrode is set to ground, $\Phi = 0$ (cf. Paper 1). For the linearized perturbation equations, the boundary conditions are the same as for the base flow apart from the electrical boundary condition for the inner electrode which is also insulating.

In order to have a perturbation in the linearized equations to begin with (which also satisfies the continuity equation), a flow is driven by the injection of a radial electrical current at the inner electrode which is shut off after some time. The function $f(t)$ in $-\nabla\Phi = f(t)\mathbf{e_r}$ needs to be sufficiently smooth, otherwise the time-stepping algorithm will greatly refine the time step which increases computation time. For our study, we applied

$$f(t) = \begin{cases} \frac{c}{2}\left(1 + \cos(10\pi t)\right) & \text{for } t < 0.1 \\ 0 & \text{for } t \geq 0.1, \end{cases} \tag{4.11}$$

which is smooth at $t_0 = 0.1$. The constant c is adjusted in the range from 0.5 for $M = 200$ to 10 for $M = 10$ such that the kinetic energy in the perturbation of the flow is small ($\sim 10^{-3}$) compared to the base flow.

In the linear instability study, first the base flow model at (M, Re) is run until it converges. Then the flow for every azimuthal wave number m is simulated separately. The number of degrees of freedom (DOF) ranges from roughly $1.6 \cdot 10^5$ at $M = 10$ to $3.1 \cdot 10^5$ at $M = 200$. Calculations were performed on a local computer with every run (M, Re_i, m) taking of the order of four hours of CPU time.

4.3.3 Parameter study

We perform a systematic parameter study on the first-order perturbation equations in order to calculate growth rates σ for the different modes and discover the threshold of linear stability. Moreover we study the spatial structure and behaviour of the unstable modes.

4.3.3.1 Parameters and processing

The parameter study of the base flow in Paper 1 contained models with $M \in [1...200]$ and $Re_i \in [1...1000]$. An asymptotic behaviour in terms of velocity scalings was found for $M > 20$. In this parameter regime, the axisymmetric base flow ($m = 0$) is stable up to the highest forcing of our study ($Re_i = 1000$). We restrict our linear stability analysis to

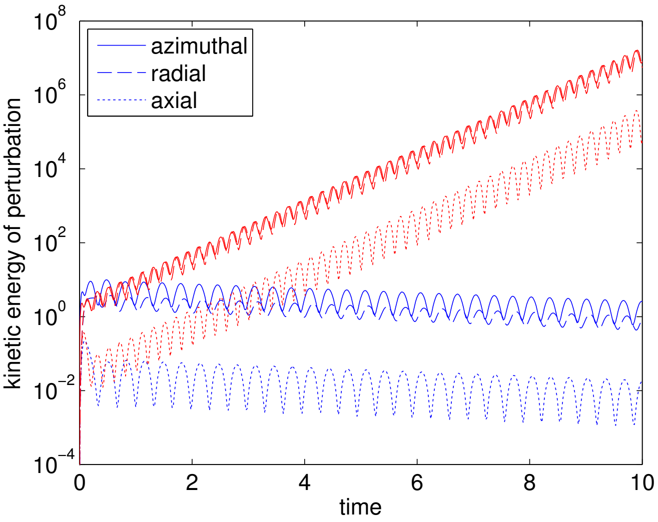

FIGURE 4.2: Temporal evolution of kinetic energies of perturbation $E'_{kin,i}$ where $i \in \{r, \phi, z\}$. The data are taken from runs with $M = 100$, $Re_i = 50$ and $m = 4$ (blue) and $m = 6$ (red) respectively.

Hartmann numbers $M \in \{10, 20, 35, 50, 70, 100, 140, 200\}$ while input Reynolds numbers are chosen mostly between 10 and 1000. For 48 parameter combinations (M, Re_i), we run models with azimuthal wave number $m \in [1...10]$. To check the behaviour of the growth rates at higher m, we perform simulations with m up to 50 for the case $(M = 20, Re_i = 500)$. We measure the temporal evolution of the spatial components of the kinetic energy of the perturbation,

$$E'_{kin,i} = 0.5 \int u_i'^2 \mathrm{d}V, \tag{4.12}$$

where $i \in \{r, \phi, z\}$ denotes the radial, azimuthal or axial component. Figure 4.2 shows the temporal evolution of the kinetic energies for $M = 100$, $Re_i = 50$, $m = 4$ and 6. After the shutdown of the initial excitation, the kinetic energies in the 2D section are oscillating around a curve of exponential decay $(m = 4)$ or growth $(m = 6)$. We fit an exponential function $A + B\mathrm{e}^{\sigma t}$ to the azimuthal kinetic energy of perturbation $E'_{kin,\phi}$ using linear regression. Extracting σ from $E'_{kin,r}$ or $E'_{kin,z}$ yields the same result. Positive growth rates $\sigma > 0$ mean that infinitesimal perturbations grow and the flow is unstable. Since the frequency of the instability is experimentally observable, we also measure the oscillation frequency $2f$ of the azimuthal kinetic energy which is two times the frequency f with which the azimuthal velocity u'_ϕ oscillates. The oscillation frequencies of radial and axial velocity components are the same as the azimuthal one. Since the data are unevenly sampled in time (adaptive time stepping), the Fourier transform can not be used to determine the frequency. Instead we apply the Lomb-Scargle periodogram [Press et al., 2007].

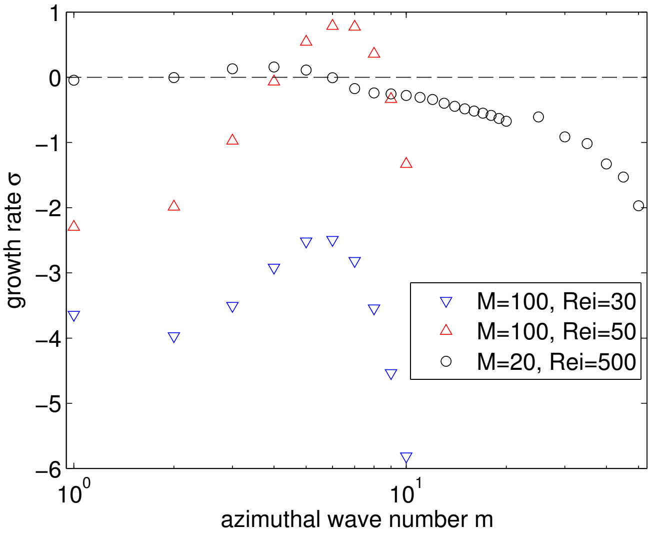

FIGURE 4.3: Growth rates σ versus azimuthal wave number m for $(M = 100, Re_i = 30$ and $50)$ as well as $(M = 20, Re_i = 500)$. Modes with $\sigma > 0$ are linearly unstable.

4.3.3.2 Growth rates and frequencies

We calculate growth rates σ and oscillation frequencies f for all models (M, Re_i, m). After sufficient time, only the mode with the largest growth rate $\sigma_{max}(M, Re_i)$ is observed. Figure 4.3 shows the growth rates of modes with different azimuthal wave numbers. For the case $(M = 100, Re_i = 30)$, we find $\sigma < 0$ for all m; this case is linearly stable. For the case $(M = 100, Re_i = 50)$, we have $\sigma > 0$ for $m \in \{5, 6, 7, 8\}$; these modes are linearly unstable with $m = 6$ being most unstable. Also shown are data for $(M = 20, Re_i = 500)$ including m up to 50. The growth rates are observed to first increase up to σ_{max} at $m(\sigma_{max})$ and then decrease again almost monotonically; we find $m(\sigma_{max}) \in [1...9]$ for the catalog of our runs. Hence we restrict our parameter study to $m \in [1...10]$; from the axisymmetric study of the base flow (Paper 1), $m = 0$ is known to be stable in the whole parameter range. The critical input Reynolds number $Re_{i,c}$ of the onset of linear instability is determined by interpolation in a plot of σ_{max} versus Re_i, e.g. $Re_{i,c}(M = 100) \approx 45$ for the data shown in Figure 4.3.

Figure 4.4a shows the nondimensional frequency f as a function of the Hartmann and input Reynolds number. The dimensional frequency f^* is plotted as a function of the electrical current in Figure 4.4b. For a given electrical current, frequencies are higher for larger magnetic field strengths. Note that only perturbations above the threshold of instability which is between 0.14 and 0.28 A depending on the magnetic field (cf. Fig. 4.5b) are growing and potentially observable. Frequencies near the onset of linear instability range from roughly 0.004 Hz at $M = 10$ (5 mT) to 0.025 Hz at $M = 200$ (99 mT).

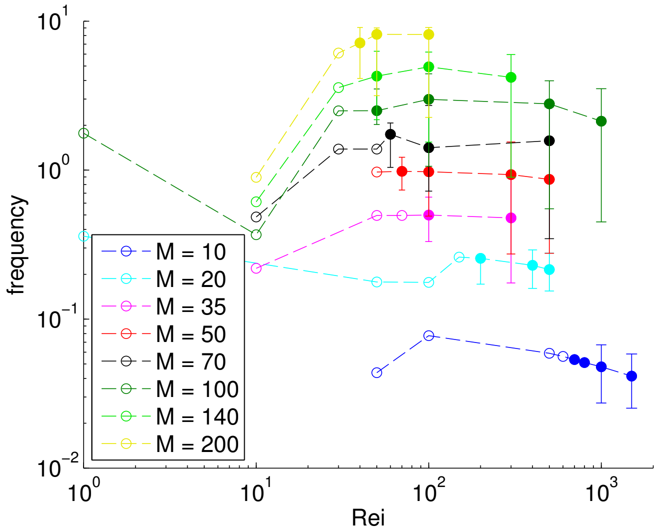

(a)

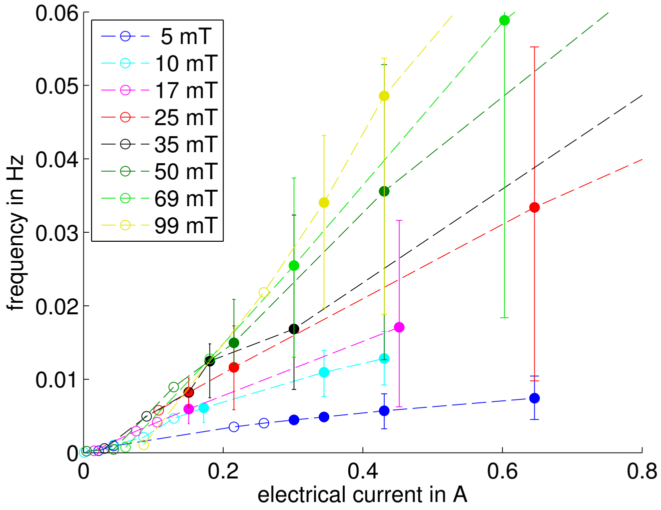

(b)

FIGURE 4.4: Frequencies of the oscillations of the azimuthal velocity u'_ϕ in the linear stability study. (a) Nondimensional f as a function of the input Reynolds number. (b) Dimensional f^* as a function of the forcing current. Colours indicate the value of the Hartmann number and magnetic field strength respectively. Empty symbols denote decaying modes ($\sigma < 0$), filled symbols the fastest growing modes. The error bars show the range of frequencies that corresponds to all growing modes ($\sigma > 0$) at a certain (M, Re_i).

4.3.3.3 Stability diagram

From roughly 480 simulations resulting from 48 parameter combinations (M, Re_i) with 10 values of m each, diagrams of linear stability and onset of instability are derived by applying the procedure described above. In the following plots, blue symbols denote a linearly stable flow whereas red ones are unstable. Figure 4.5 shows the diagram of linear stability in terms of nondimensional parameters as well as dimensional quantities. The critical input Reynolds number $Re_{i,c}$ for transition to instability decreases from 640 to 32 when increasing the Hartmann number M from 10 to 200. The value of $m(\sigma_{max})$, the wave number of the most unstable mode, grows when increasing M and when increasing Re_i. At transition, we find $m = 3$ for $M = 10$ and $m = 8$ for $M = 200$. At higher M, the value of σ changes more abruptly than at lower M. In terms of the physical quantities B and I, the curve of neutral stability looks somewhat different (Fig. 4.5b). The critical current I_c has a minimum of roughly 0.13 A at around $M \approx 30$ (15 mT). For larger magnetic fields, it grows to 0.28 A at $M = 200$ (99 mT); the scaling follows $I_c \sim B^{0.5}$. For $B < 15$ mT, I_c increases steeply with decreasing B.

We can also look at the curves of neutral stability ($\sigma = 0$) for every wave number m separately. Figure 4.6 shows curves of neutral stability in dimensional parameters. The lowest curve at a given M (B) corresponds to the mode which is the most linearly unstable. In these plots, the transition to higher m with increasing M (B) at the onset of linear instability comes out clearly.

4.3.3.4 Structure of the modes

After having established the linear instability of the base flow in ZUCCHINI, it is instructive to study where the growing modes are located and what they look like. Figure 4.7 shows a series of snapshots of the perturbation velocities u_i' with $i \in \{r, \phi, z\}$ over the duration of one period for the slightly supercritical case $(M = 20, Re_i = 200, m = 4)$. The instability is made up of a series of vortices meandering around the free Shercliff layer near the inner electrode. Figure 4.8 shows the shear rate γ of the axisymmetric base flow for the same parameters $(M = 20, Re_i = 200)$; it is defined as the magnitude $\gamma = |\boldsymbol{\gamma}|$ of the strain-rate tensor $\boldsymbol{\gamma} = \left(\nabla\mathbf{u} + (\nabla\mathbf{u})^T\right)$. The shear rate γ is largest in the Hartmann layers where also the highest electrical current density and dissipation is found (cf. Paper 1). But a significant amount of shear is also observed in the free Shercliff layer at the inner electrode which is the location of the unstable mode of Figure 4.7. Hence the observed instability is interpreted as a Kelvin-Helmholtz-type instability of the free Shercliff layer. Other instabilities as the centrifugal instability described by Rayleigh's criterion appear to occur at higher Re_i according to our linear stability analysis.

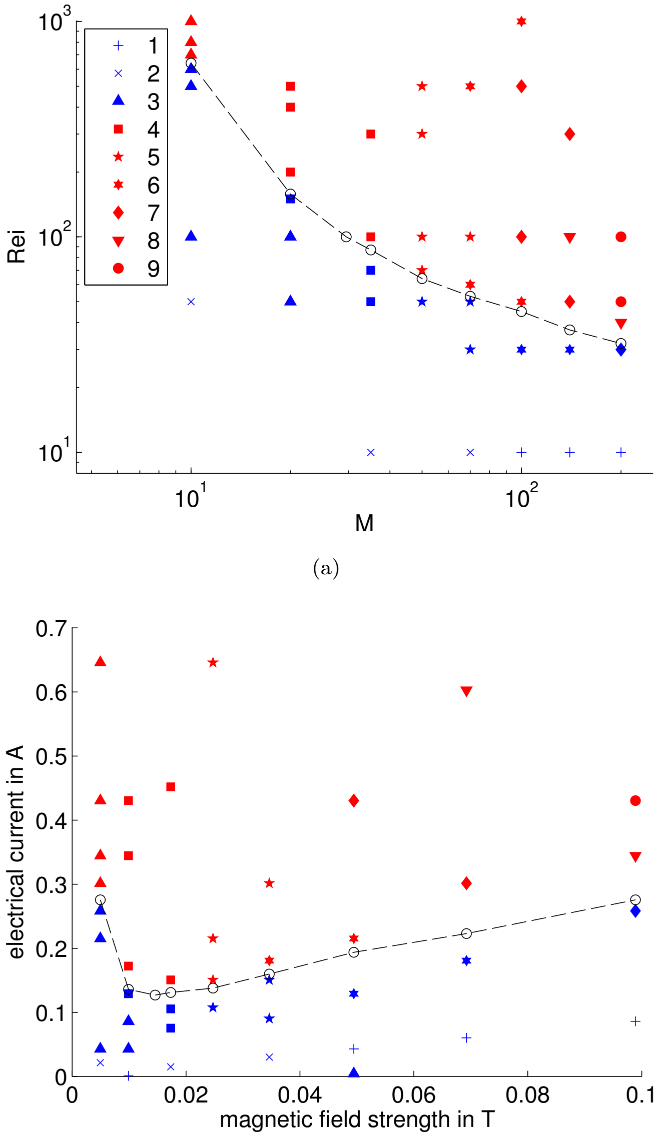

(a)

(b)

FIGURE 4.5: Diagrams of linear stability in terms of (a) nondimensional parameters M and Re_i and (b) dimensional quantities B and I. Blue symbols denote a linearly stable flow whereas red ones are unstable. The shape of the symbol indicates the azimuthal wave number m at which σ_{max} occurs for a given (M, Re_i) and (B, I) respectively. The black circles and dashed curve shows the onset of linear instability inferred by interpolation between the neighbouring points.

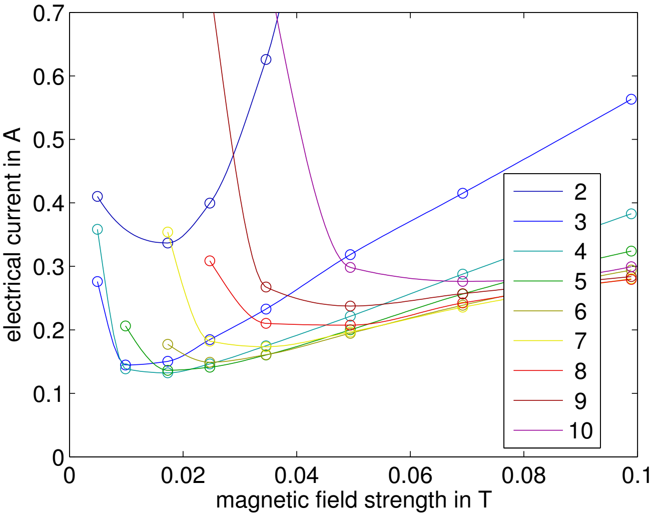

FIGURE 4.6: Curves of neutral stability ($\sigma = 0$) for different azimuthal wave numbers m in dimensional parameter space (B, I). The data points are derived from the measured growth rates by linear interpolation, the connecting lines are piecewise cubic Hermite interpolating polynomials (pchip).

4.4 Experiment

The ZUCCHINI experiment is designed for the study of electrically-driven MHD flow in a modified cylindrical annulus. In this work, we study the instabilities of the flow, especially the ones occurring in the free Shercliff layer at the inner electrode, but we also find indications for instability in the Hartmann layer. The base flow was investigated in Paper 1. The latter also describes the experimental setup and measurement procedure in more detail.

4.4.1 Setup

The experimental setup consists of three main parts: the tank filled with liquid GaInSn in the form of a modified cylindrical annulus, coils that create the imposed magnetic field $\mathbf{B}$, and power supplies generating the current I (cf. Fig. 4.1). Moreover the tank is equipped with ultrasonic Doppler velocimetry (UDV) and potential difference probes (PDP) to diagnose the flow. The working fluid is MCP 11 alloy from 5N Plus UK Ltd. consisting of 65.9% gallium, 20.8% indium and 13.3% tin. It is liquid at room temperature; its relevant physical properties are given in Table 4.1. Since it is easily oxidized, we keep the whole system under an argon overpressure of 0.15 bar at all times.

The data of this work come from two different realizations of this setup. The first one is the 'Caylar' setup which consists of three resistive magnetic coils in a modified Helmholtz arrangement. They generate a relatively uniform axial field within the tank volume, reaching a maximum field strength of $B_{max} = 0.1$ T. The 'Caylar' setup is

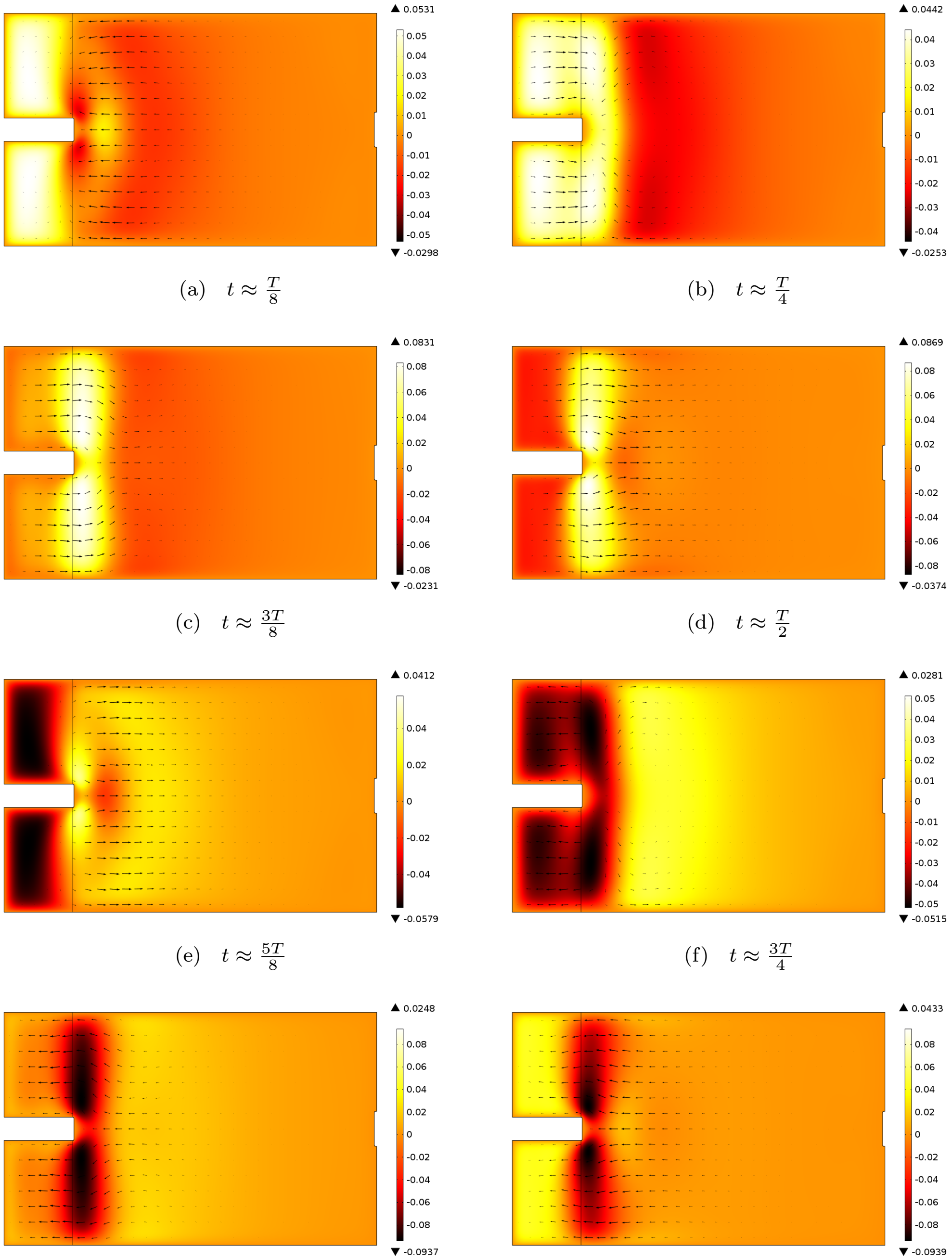

(a) $t \approx \frac{T}{8}$

(b) $t \approx \frac{T}{4}$

(c) $t \approx \frac{3T}{8}$

(d) $t \approx \frac{T}{2}$

(e) $t \approx \frac{5T}{8}$

(f) $t \approx \frac{3T}{4}$

(g) $t \approx \frac{7T}{8}$

(h) $t \approx T$

FIGURE 4.7: Temporal evolution of the perturbation velocities u'_i with $i \in \{r, \phi, z\}$ over one period for the slightly supercritical case ($M = 20, Re_i = 200, m = 4$). Colours indicate the azimuthal velocity u'_ϕ, arrows show u'_r and u'_z. The eight snapshots are taken with roughly equal time intervals over one oscillation period T. Originating from the Shercliff layer at the inner electrode, the perturbation flow appears to meander with all velocity components changing sign over one period. The structure consists of alternating vortices being swept with the mean flow, and thus is reminiscent of a Kelvin-Helmholtz-type instability.

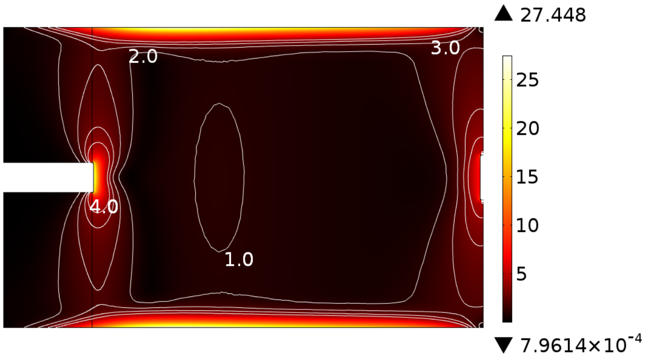

FIGURE 4.8: Shear rate γ of the axisymmetric base flow for the slightly supercritical case ($M = 20, Re_i = 200, m = 4$). Most shearing occurs in the Hartmann layers at the top and bottom walls, followed by the free Shercliff layer at the inner disk electrode and the outer side layer.

TABLE 4.1: Physical properties of GaInSn from Morley et al. [2008] who provide data for various composition ratios. We present the data set resembling most the MCP11 alloy from 5N Plus we use.

kinematic viscosity ν	$2.98 \cdot 10^{-7}$ m^2/s
electrical conductivity σ_e	$3.1 \cdot 10^6$ $(\Omega\text{m})^{-1}$
density ρ	6360 kg/m^3
melting point T_m	10.5°C
sound speed c	2730 m/s

TABLE 4.2: Overview of the measurements taken in the two setups 'Caylar' and 'Cryo'. $\#(B)$ gives the number of sweeps of $I \in [I_{min}, I_{max}]$ performed in the range $B \in [B_{min}, B_{max}]$; $\mathbf{B}$ describes the geometry of the field.

	B_{min}	B_{max}	$\#(B)$	$\mathbf{B}$	I_{min}	I_{max}
'Caylar'	17.5 mT	83.4 mT	5	$\partial B_{r,z}/\partial r \lesssim 0$	0 A	150 A
'Cryo'	83.5 mT	1000 mT	9	$\partial B_{r,z}/\partial r > 0$	0 A	300 A

equipped with three SM 18-50 power supplies from Delta Elektronika providing a total forcing current up to $I_{max} = 150$ A.

In the second setup, called 'Cryo', a single thick superconducting coil set from Cryomagnetics, Inc. provides a magnetic field up to $B_{max} = 1$ T. The electrical current between the electrodes is driven by six SM 18-50 power supplies in the 'Cryo' setup reaching a total forcing current of $I_{max} = 300$ A. An overview of the two setups and measurements taken therein is shown in Table 4.2. More detailed information on magnetic field geometry, current distribution and GaInSn handling is given in Paper 1.

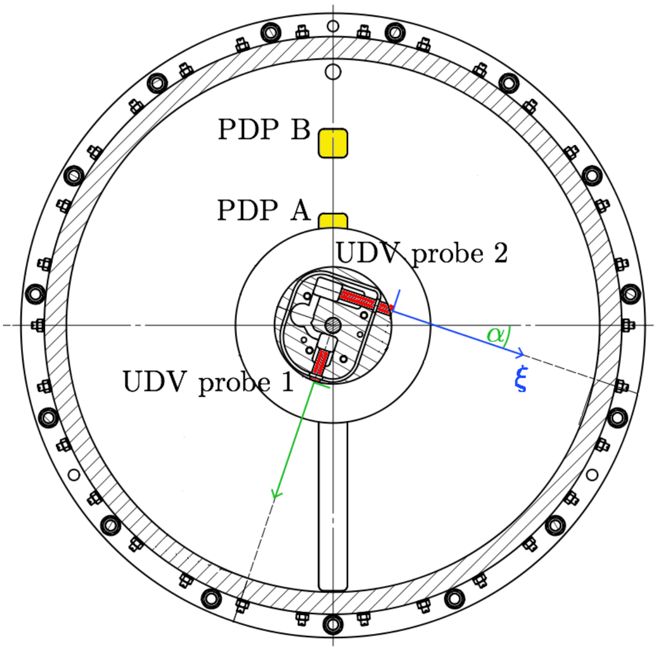

FIGURE 4.9: Top view of tank with orientation of UDV probes 1 (radial) and 2 (chordwise) in red and the location of the PDP A and B in yellow. For the derivation of the azimuthal velocity from measurements of u_1 and u_2, see Section IV B 2 in Paper 1

4.4.2 Methodology

The flow in ZUCCHINI is measured by UDV and PDP. Since both rely on different physical principles, they provide independent measurements allowing to mutually check the results. In the following section, we describe the measurement methods, the data processing, and present a data example.

4.4.2.1 Measurements

We use the UDV system DOP3010 from Signal Processing S.A. with three multiplexed channels connected [DOP]. The UDV probes have an emission frequency of $f_e = 8$ MHz resulting in a wave length of 0.34 mm in GaInSn which yields a sufficient resolution. UDV is based on measuring shifts in the position of particles suspended in the fluid between two consecutive ultrasonic pulses. It gives a profile of the velocity component along the ultrasonic beam. For technical details and procedures, see Paper 1.

Two of the three UDV probes are mounted in the inner cylinder of the tank (cf. Fig. 4.9). Probe 1 measures the radial velocity u_r along a radial profile to the outer wall. Probe 2 records the chordwise velocity u_2 which is also most sensitive to u_r, but additionally contains the azimuthal velocity u_ϕ. Both probes together can be used to reconstruct profiles of mean azimuthal velocity $\overline{u_\phi}(r)$ (cf. Section IV B 2 in Paper 1). UDV probe 3 is mounted flush in the bottom plate of the tank slightly outside the inner disk electrode. It records a profile of the axial velocity u_z over the entire height of the container.

PDP measurements have not been used in Paper 1. Hence we give here a more detailed overview of the method. There are essentially two different types of PDPs, one that contains its own small magnet, and another one which makes use of the externally imposed magnetic field as employed in ZUCCHINI. In both cases, the PDP measures the voltage drop $\Delta\Phi$ across the distance between the wires Δl induced by the flow of an electrically conducting fluid in a magnetic field. In the absence of electric currents $\mathbf{j}$, Ohm's law (Eq. 4.4) relates the electric field $E \approx \Delta\Phi/\Delta l$ linearly to the velocity [Eckert et al., 2007]. In specific cases, it is necessary to take thermoelectric effects into account due to the different materials of PDP and fluid when measuring $\Delta\Phi$ [Davoust et al., 1999, Sreenivasan and Alboussière, 2002]. Also it is known that PDPs perturb liquid metal flow [Mistrangelo and Bühler, 2010]. We consider these effects to be negligible in our experiment.

We use an array of wires mounted flush in the top lid of the container to measure $\Delta\Phi$ in the r- and ϕ-directions in a similar way to that of Kljukin and Thess [1998] and Messadek and Moreau [2002]. Our PDP arrays consist of 5×5 brass pins with a width of a few tenths of a mm and a spacing of 2.54 mm. Only the four edge pins of each array are recorded resulting in two radial and two azimuthal measurements per PDP array. The pins are held by inserts made from epoxy resin and plexiglass respectively. The PDP arrays A and B are located on a radial ray above the radial UDV beam at $r = 75$ mm and 140 mm respectively (cf. Fig. 4.9). Since $\mathbf{B} \approx B_0\mathbf{e}_z$, azimuthal and radial velocity are given by

$$u_{\{\phi,r\}} = \frac{\Delta\Phi_{\{r,\phi\}}}{B_0\,\Delta l}. \tag{4.13}$$

In the limit of high Hartmann numbers ($M \gg 1$), the electric potential is uniform along the direction of the magnetic field and does not significantly change over the Hartmann layer. Hence our measurements of $\Delta\Phi$ in the Hartmann layer do not only give local velocities but carry information about the core velocity. We have verified that the velocities calculated from PDPs agree relatively well with the ones measured by UDV. Nevertheless we report PDP measurements as voltages only in this study.

The PDPs are connected to a NI PXI-2501 multiplexer and a NI PXI-4070 data acquisition system through a LAN cable of category 5e or similar shielded cables. In the 0.1 V (resp. 1 V) range, the measurements have a resolution of 0.1 μV (resp. 1 μV). Sampling with roughly 50 Hz (resp. 750 Hz) leads to a noise level of less than ~ 1 μV (resp. ~ 10 μV). Potential differences are measured against the inner electrode as common reference, and later combined to yield local measurements.

UDV and PDP provide time series of velocity and voltage respectively. The sampling rate of the UDV is adjusted according to signal quality and the ability to resolve the observed oscillations. In general it increases from ~ 1 Hz at low currents (steady flow) to ~ 30 Hz at 150-300 A. The recording time is set such that the noise is largely canceled out

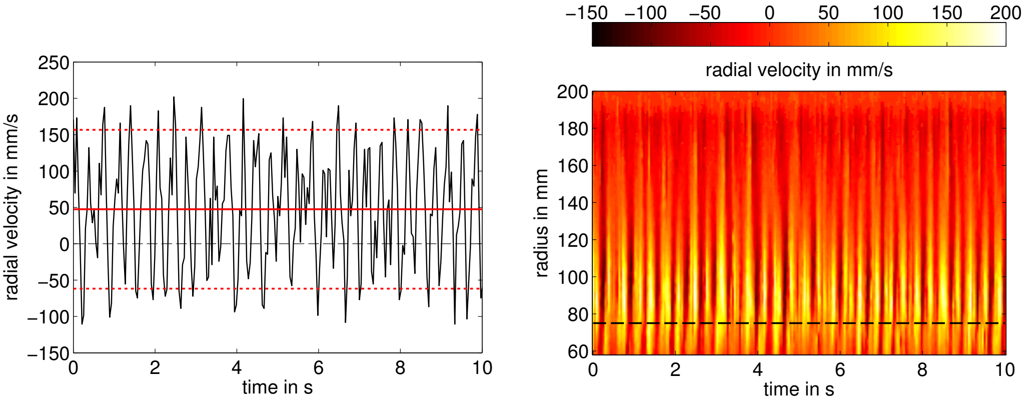

(a) Time series

(b) Space-time diagram

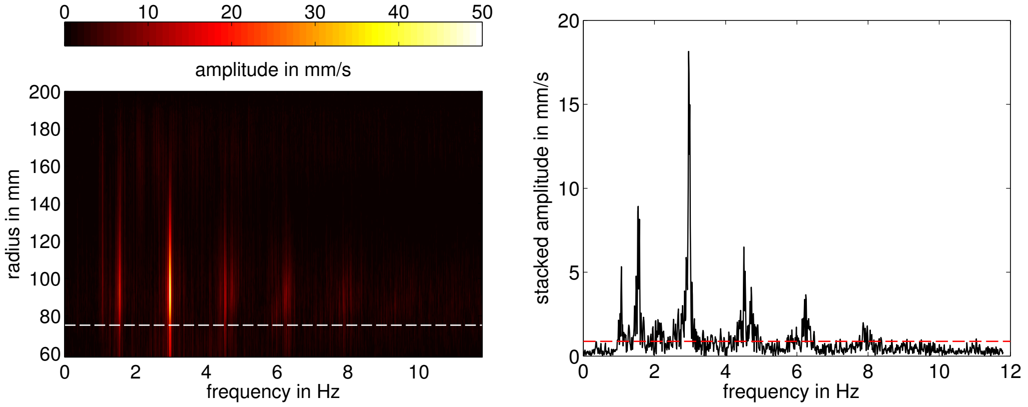

(c) Space-frequency diagram

(d) Stacked amplitude

FIGURE 4.10: UDV example data: u_r measured at 875 mT and 150 A ($M = 1769$, $Re = 1.10 \cdot 10^5$). (a) Detail of time series $u_r(t)$ at radius $r = 90$ mm. Solid and dotted red lines indicate $\overline{u_r}$ and $\overline{u_r} \pm \sqrt{2}s$ at this radius, respectively. (b) Space-time diagram $u_r(r,t)$ with the dashed line indicating the edge of the inner electrode. (c) Space-frequency diagram. (d) Radial mean of (c) with mean amplitude indicated by red dashed line.

(steady state) and the frequency resolution is sufficient (~ 0.01 Hz for the oscillations). In general it decreases from ~ 150 s to ~ 60 s with increasing current. The sampling rate of the PDPs is 5.2 Hz per channel for low forcing currents and 83.3 Hz for high currents.

4.4.2.2 Processing and data examples

UDV and PDP time series are treated in a similar way. In both cases, we calculate the temporal mean value $\overline{(\cdot)}$ and the standard deviation s, and study their evolution with the forcing current I and the magnetic field strength B. After detrending with a fitted linear function and applying a Hann window to the time series, we perform a fast Fourier transform (FFT) to find the two dominant frequency components f_i and their respective amplitudes A_i with $i \in \{1, 2\}$.

Figure 4.10 shows example data from UDV probe 1 measuring $u_r(r,t)$ along a radial profile. The data was recorded well above the threshold of instability where the oscillations fill the entire radial range of the container. The time series contains a strong harmonic component of frequency $f_1 = 2.96$ Hz. By stacking (taking the radial mean of) the amplitude for each frequency in the space-frequency diagram, its amplitude is determined as $A_1 = 18.2$ mm/s; the second maximum is found to be $f_2 = 1.54$ Hz with $A_2 = 8.9$ mm/s. Only spectral peaks with $A_i > 10\,\overline{A_i}$ are considered as significant frequency components where $\overline{A_i}$ is the mean value of the stacked amplitudes. Applying this procedure to the velocities u_2 and u_z recorded by UDV probes 2 and 3 yields the same main frequency components.

Combining the UDV measurements of $u_1 = u_r$ and u_2, it is possible to derive a mean azimuthal velocity profile $\overline{u_\phi}(r)$, cf. Section IV B 2 in Paper 1. This is used to define the Reynolds number,

$$Re = \frac{\langle \overline{u_\phi} \rangle a}{\nu}, \tag{4.14}$$

which in contrast to Re_i (Eq. 4.9) is an output parameter of the system.

PDP measurements are processed in a similar way. The extracted frequency spectrum agrees well with the one from UDV recordings. A data example is given in Appendix 4.B.

4.4.3 Results

First we present the flow structure as inferred from the UDV measurements, and compare it with the PDP recordings. Beginning from Section 4.4.3.5, we evaluate the oscillations and the threshold of unstable flow including friction factor measurements. In particular we find four transitions present in different recordings at Re_c, Re_t, Re_f and Re_h. In Section 4.4.3.7, we assemble all parts in a stability diagram for the parameter range covered in ZUCCHINI.

4.4.3.1 Mean azimuthal flow

The mean azimuthal flow is the dominant component due to the forcing mechanism in our experiment. Mean azimuthal flow profiles at low forcing have been shown to behave largely as $\overline{u_\phi}(r) \sim I/r^\alpha$ with $\alpha \in [0.6, 1.7]$ for $r \gtrsim 90$ mm and fixed M (Paper 1); $\alpha = 1$ is the theoretically predicted value for cylindrical Hartmann flow at large M [Baylis and Hunt, 1971]. Figure 4.11 shows the evolution of $\overline{u_\phi}(r)$ with increasing I also in the unstable regime for our lowest magnetic field and a large-M case. Only the lowermost curves correspond to stable base flow. The shape of $\overline{u_\phi}(r)$ changes to a more flat profile in the radial range $r \in [90, 180]$ mm. In some cases, we even observe an increase of $\overline{u_\phi}$ towards the outer cylinder. Also the forcing-free volume on the inside of the inner electrode exhibits significant velocities. This is due to enhanced angular momentum transport that was also observed by [Alboussiere et al., 1999], and is again increased

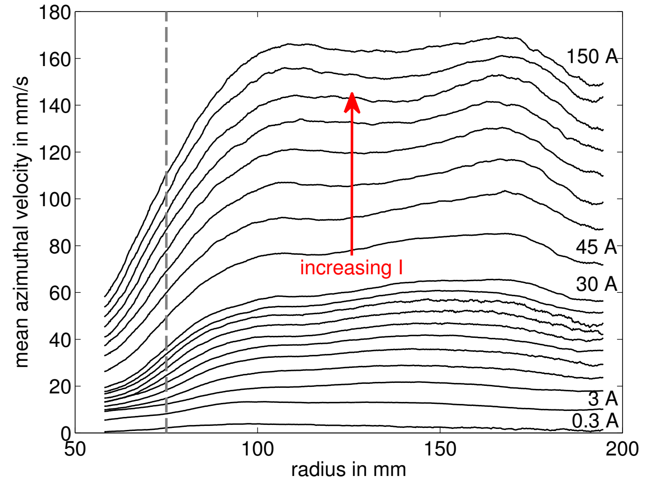

(a) $M = 35$ (17.5 mT), $Re(0.3\text{ A}) = 405$, $Re(150\text{ A}) = 2.50 \cdot 10^4$

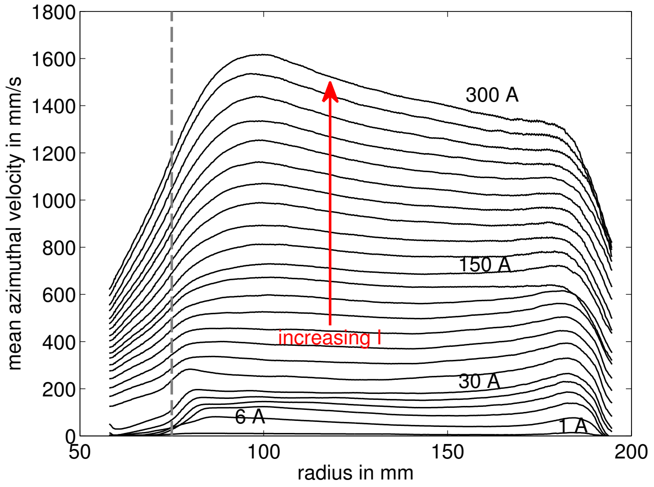

(b) $M = 1769$ (875 mT), $Re(1\text{ A}) = 1270$, $Re(300\text{ A}) = 2.26 \cdot 10^5$

FIGURE 4.11: Mean azimuthal velocity profiles $\overline{u_\phi}(r)$ at different magnetic fields. (a) $M = 35$: With increasing current I, the profile becomes flat outside the free Shercliff layer with a slight bump at $r \approx 175$ mm. (b) $M = 1769$: The jet at $r \approx 185$ mm that is present for low I disappears for stronger forcing, and $\overline{u_\phi}(r)$ decreases with r again. The dashed grey line indicates the location of the inner electrode edge.

when the instabilities kick in. This also influences the thickness δ_S of the free Shercliff layer which is investigated in the next section. The fast jet near the outside wall visible in the low-I profiles in Figure 4.11b (cf. Paper 1) disappears towards high forcing currents $I > 150$ A.

Figure 4.12 shows the radial mean value $\langle\overline{u_\phi}\rangle$ of the profile $\overline{u_\phi}(r)$. The evolution of $\langle\overline{u_\phi}\rangle$ with I (plot a) is different in different regimes. For large Hartmann numbers $M \gtrsim 500$, $\langle\overline{u_\phi}\rangle$ scales linearly with I and does not depend on M as predicted theoretically [Baylis and Hunt, 1971]. We only observe one clear change in slope at low $I < 10$ A which will be shown to correspond to the onset of the first instability. The maximum $\langle\overline{u_\phi}\rangle$ reached

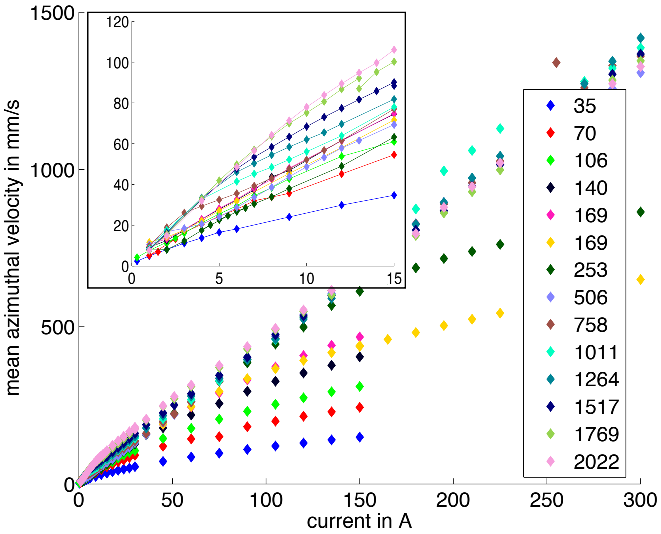

(a)

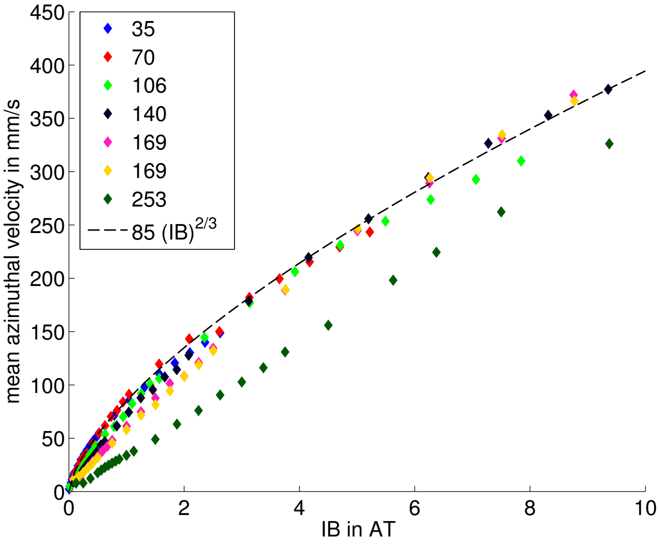

(b)

FIGURE 4.12: Radial mean of (temporal) mean azimuthal velocity $\langle\overline{u_\phi}\rangle$ vs. (a) the current I and (b) the forcing IB. The colour shows the value of M. The change in slope at low I (insert in a) is due to the onset of the first instability of the free Shercliff layer. In the large-M limit ($M \gtrsim 500$), $\langle\overline{u_\phi}\rangle \sim I$ and independent of M. For $M \lesssim 150$, the velocity appears to approach $\langle\overline{u_\phi}\rangle \sim (IB)^{2/3}$ with decreasing M.

at 300 A is roughly 1.4 m/s which translates to a Reynolds number of $Re = 2.23 \cdot 10^5$. In order to collapse the moderate-M data at different $M \lesssim 250$, it appears to be more useful to plot $\langle \overline{u_\phi} \rangle$ against the forcing IB (Fig. 4.12b) instead of the current alone. At our lowest magnetic field values ($M = 35$), the mean azimuthal velocity scales as $\langle \overline{u_\phi} \rangle \sim (IB)^\beta$ with $\beta = 2/3$. Boisson et al. [2012] found $\beta = 1/2$ in their narrow-gap geometry for moderate Hartmann numbers.

4.4.3.2 Free Shercliff layer thickness

From the profiles of mean azimuthal velocity $\overline{u_\phi}(r)$ (Fig. 4.11), we derive δ_S of the free Shercliff layer at the inner electrode. This is done by fitting a straight line to $\overline{u_\phi}(r)$ for $r \in [70, 85]$ mm and measuring the distance between its intersection points with zero and $\langle \overline{u_\phi} \rangle$. Figure 4.13 shows the resulting δ_S over Re/M^β with $\beta = 1$ and 1.2. For fixed M (colour curves) and increasing Re, δ_S exhibits a transition from $\delta_S \approx 10$ mm to roughly 40 mm which appears to be the large-Re limit at high M. The overshoot in δ_S above the transition is an artefact of the jet in this parameter regime and should not be interpreted on its own.

The theoretical prediction for a laminar shear layer parallel to the magnetic field is $\delta_S \sim M^{-1/2}$ which would lead to $\delta_S = 8.4$ mm and 1.1 mm for $M = 35$ and 2022 respectively in our experiment. For low M and moderate Re ($\delta_S \approx 10\ mm$), the observed Shercliff layer thickness has the same order of magnitude but does not scale with M as predicted. For large M and Re, the discrepancy in δ_S is more than an order of magnitude. Also the Shercliff layer in our experiment is different to the one found by Messadek and Moreau [2002] in a somewhat similar geometry which scaled as $\delta_S \sim (Re/M)^{1/2.3}$. In ZUCCHINI, the shear layer appears to be entirely hydrodynamically controlled with no dependence on M at large Re and M.

The transitional Reynolds number Re_t between a thin and the wide shear layer at moderate and large Re respectively scales with the Hartmann number M. We define it as $Re_t = Re(\delta_S = 40$ mm). For moderate $M \in [35, 200]$, we find a clear linear scaling $Re_t = 36M$, whereas it is $Re_t = 5.6M^{1.2}$ for large $M \gtrsim 200$ (Fig. 4.13). In the next sections, we will see that the δ_S-transition at Re_t coincides with a change in radial flow structure as well as spatial growth of the instabilities.

4.4.3.3 Radial and axial flow structure

Radial and axial velocities make up the secondary recirculation flow. Figure 4.14 shows mean radial velocity profiles $\overline{u_r}(r)$ for the same magnetic field strengths as Fig. 4.11. With increasing I, the velocity $\overline{u_r}$ increases; in the large-M case, it appears to approach saturation at 300 A. The structure of the profiles in both cases is largely self-similar at high currents I. However, a transition is observed between 1 and 2 A for $M = 35$,

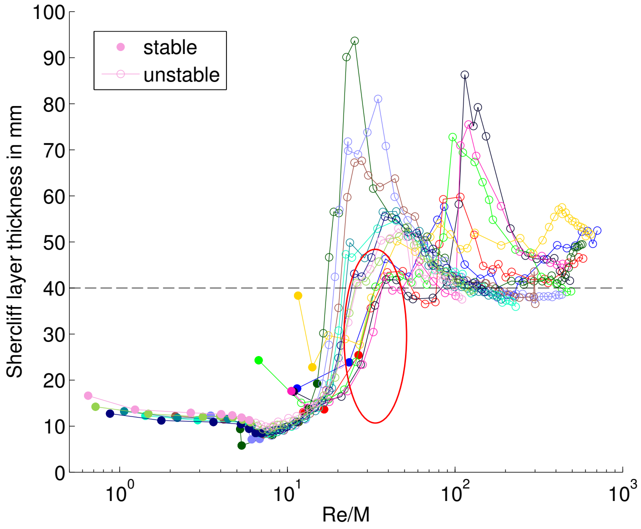

(a)

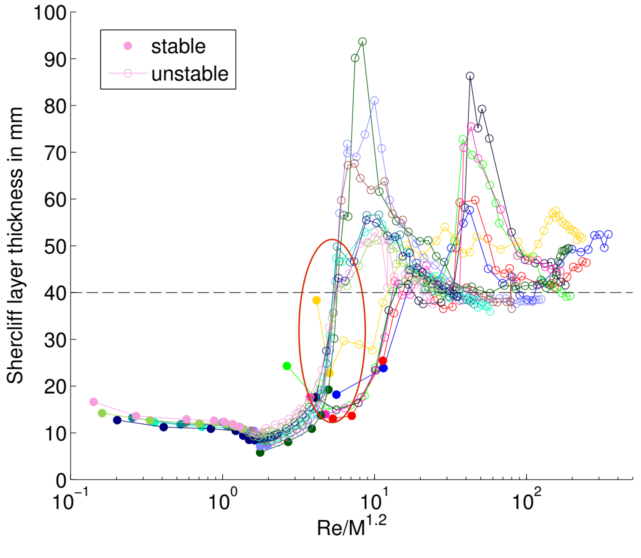

(b)

FIGURE 4.13: Free Shercliff layer thickness δ_S versus (a) Re/M and (b) $Re/M^{1.2}$. Colours as in Fig. 4.12. δ_S tends to 40 mm for large Re in the high-M limit. The transitional Reynolds number Re_t scales as $Re_t \sim M$ for moderate $M \in [35, 200]$, and as $Re_t \sim M^{1.2}$ for large M (red ellipses).

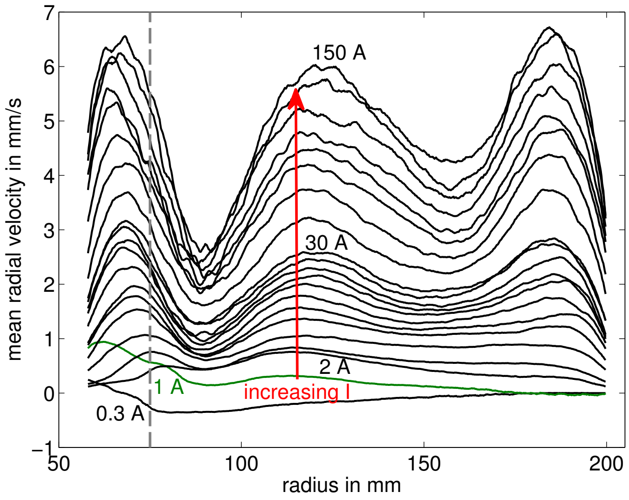

(a) $M = 35$ (17.5 mT)

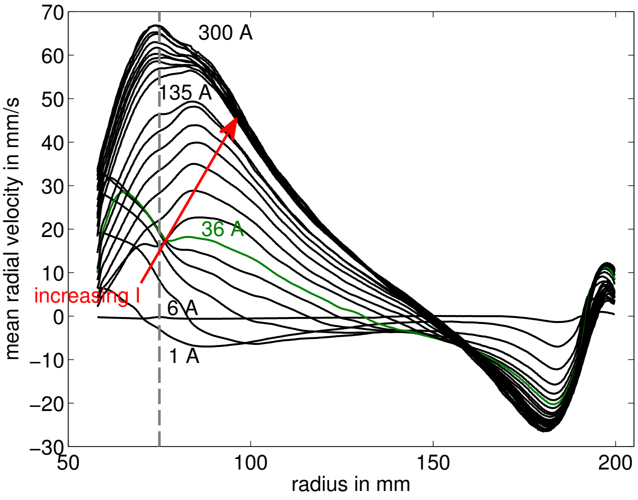

(b) $M = 1769$ (875 mT)

FIGURE 4.14: Mean radial velocity profiles $\overline{u_r}(r)$ at different magnetic fields. (a) $M = 35$: The structure of $\overline{u_r}(r)$ changes between 1 and 2 A. (b) $M = 1769$: The change in structure occurs between 36 and 45 A. Positive values of $\overline{u_r}$ indicate outward directed flow at the height of UDV probe 1.

and around 36 A for $M = 1769$. This transition occurs at Re_t, and is associated with the transition in the free Shercliff layer thickness δ_S. Mean radial velocities are almost exclusively directed outwards for $M = 35$ at the height of UDV probe 1. The profiles have several local minima and maxima which might indicate several recirculation cells. In contrast, $\overline{u_r}(r)$ exhibits only one sign change with inwards directed velocities near the outer wall for $M = 1769$, but otherwise shows only one clear local minimum and maximum.

The mean axial flow $\overline{u_z}(z)$ in the free Shercliff layer (UDV probe 3) is shown in Figure 4.15. For $M = 35$, it is symmetric around the center plane $z = 0$. The flow is

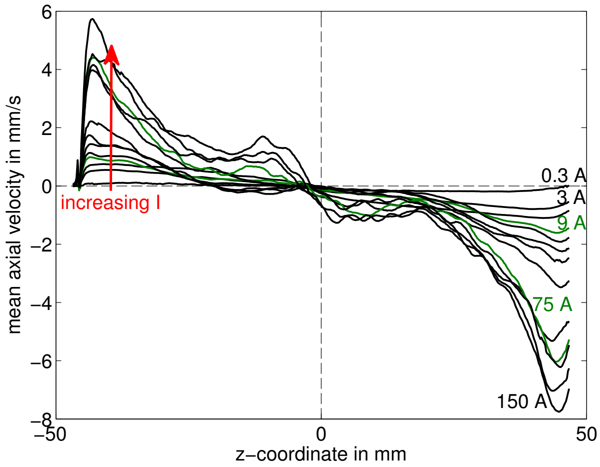

(a) $M = 35$ (17.5 mT)

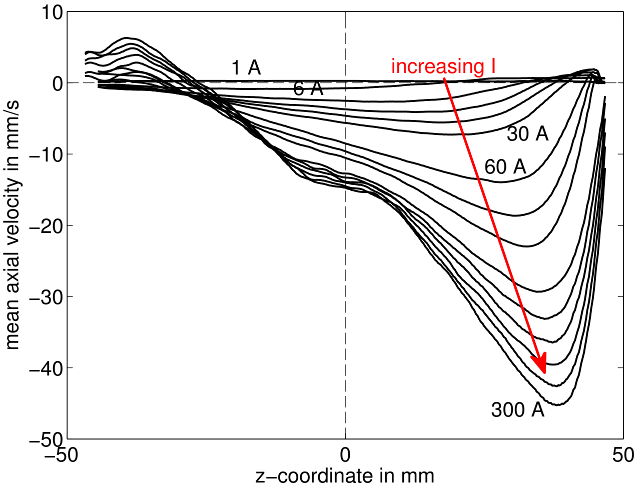

(b) $M = 1769$ (875 mT)

FIGURE 4.15: Mean axial velocity profiles $\overline{u_z}(z)$ at different magnetic fields. (a) $M = 35$: The structure of $\overline{u_z}(z)$ changes around 9 A and 75 A. (b) $M = 1769$: A slight change in structure occurs around 150 A. A negative (downward) u_z is superimposed onto the relatively symmetric structure.

directed towards the center plane with the highest velocities occurring near the top and bottom walls. The recirculation flow consists of two counter-rotating cells in the upper and lower half of the tank. This structure stays similar also above the transition in profile shape around 9 and 75 A. For large M, the axial velocity $\overline{u_z}$ is mainly directed downwards in the free Shercliff layer (Fig. 4.15b). The flow partially preserves the antisymmetry around the center plane $z = 0$, however, with a mean downwards velocity superimposed. In this case, the two vertically stacked cells exchange fluid.

Figure 4.16 shows the root-mean-square (rms) values $\langle\overline{u_r}\rangle_{rms}$ of the radial profile and $\langle\overline{u_z}\rangle_{rms}$ of the axial profile, as well as their ratio $\langle\overline{u_r}\rangle_{rms}/\langle\overline{u_z}\rangle_{rms}$ for the whole data set. Radial and axial velocities both grow with increasing current I, but they do not

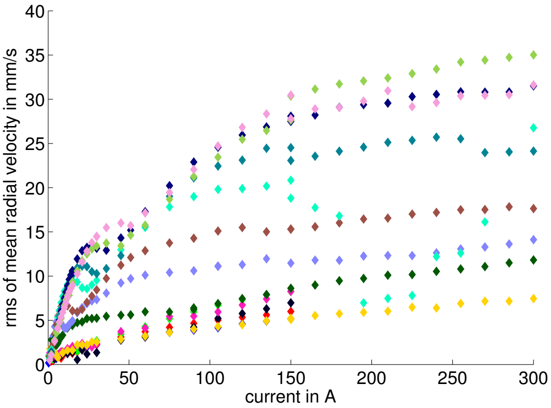

(a) $\langle\overline{u_r}\rangle_{rms}$

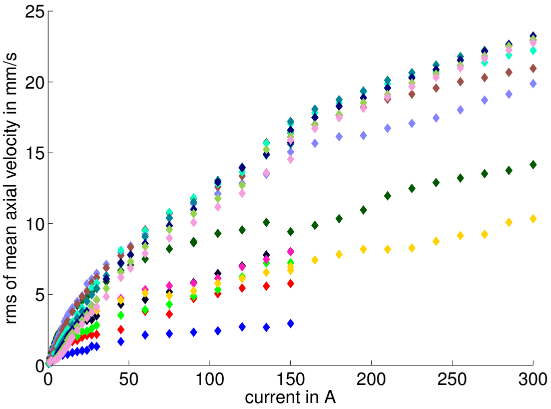

(b) $\langle\overline{u_z}\rangle_{rms}$

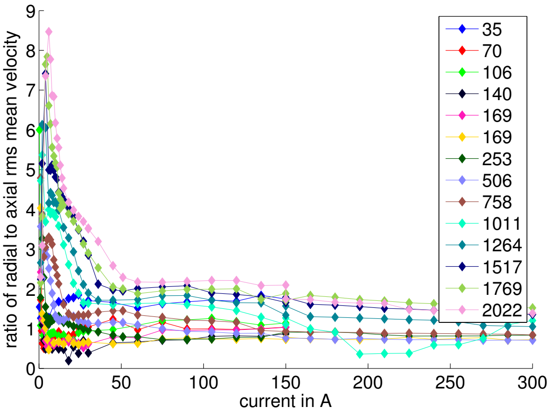

(c) $\langle\overline{u_r}\rangle_{rms}/\langle\overline{u_z}\rangle_{rms}$

FIGURE 4.16: Rms values along the UDV profiles of (a) mean radial and (b) axial velocity. In both cases, the data do not follow coherently simple power-law scalings. (c) Ratio of radial to axial rms values along the mean velocity profiles versus forcing current. For every M (colour), the ratio tends to become independent of I for high currents I. The transition to this behaviour occurs at Re_t when the structure of mean radial flow (Fig. 4.14) and also the free Shercliff layer thickness δ_S change.

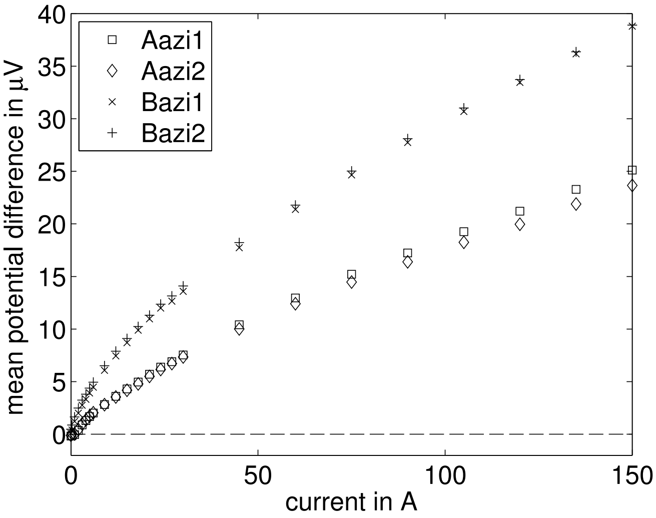

(a) $M = 35$ (17.5 mT)

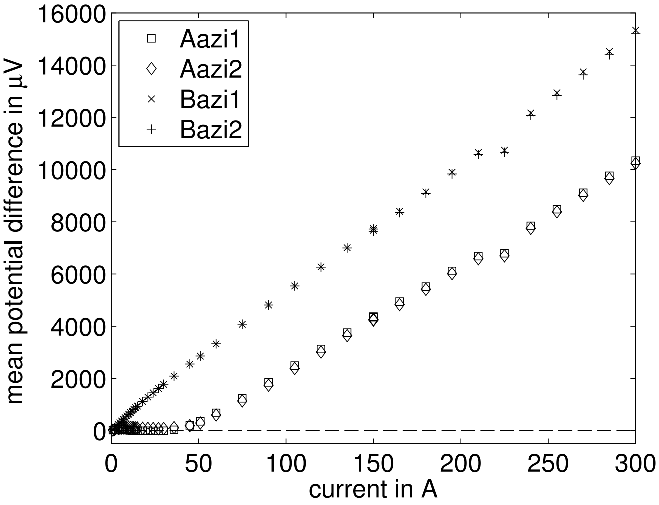

(b) $M = 1769$ (875 mT)

FIGURE 4.17: Mean of PDP measurements corresponding to azimuthal velocities. The scaling of the azimuthal velocity inferred by UDV is recovered (cf. Fig. 4.12). (a) $M = 35$: Power-law $\Delta\Phi \sim I^{\alpha}$ with $\alpha \approx 2/3$. (b) $M = 1769$: Linear scaling $\Delta\Phi \sim I$ over a large range of the current I.

consistently exhibit a clear power-law scaling. $\langle\overline{u_z}\rangle_{rms}$ appears to become independent of M at large $M \gtrsim 1000$ whereas $\langle\overline{u_r}\rangle_{rms}$ does not show this behaviour. For low I, radial velocities are up to an order of magnitude larger than axial velocities. With increasing I, the ratio $\langle\overline{u_r}\rangle_{rms}/\langle\overline{u_z}\rangle_{rms}$ drops and approaches a constant value. The transition to this constant ratio occurs at Re_t when the structure of the mean radial flow changes (Fig. 4.14) which is also connected to the transition in the Shercliff layer thickness δ_S.

4.4.3.4 PDP measurements

We use PDP recordings as a complementary measure of the flow inferred by UDV. Mean potential differences corresponding to azimuthal flow are shown in Figure 4.17 for the two cases $M = 35$ and 1769. In both cases, the UDV measurements (Fig. 4.12) are confirmed, i.e. a power-law scaling $\Delta\Phi \sim I^{\alpha}$ with $\alpha \approx 2/3$ for moderate M and a linear scaling with I for large M. A surprising feature is the behaviour of the potential differences at insert B remaining near zero until a forcing current of roughly 36 A is reached. This again occurs at Re_t where also the oscillations at the widened shear layer start to occupy the whole radial range as we will see in the next section.

4.4.3.5 Oscillations

For a given magnetic field strength B, the flow develops instabilities above a critical electric current $I_c(B)$. Figure 4.18 shows u_r measurements at $M = 1769$ with increasing current. At 6 A, we observe steady flow with some measurement noise. At 9 A, an instability with main frequency $f_1 = 2.05$ Hz develops around $r = 100$ mm, the outer edge of the free Shercliff layer. It is between these points that the slope of $\langle\overline{u_\phi}\rangle(I)$ decreases. The instability decreases the ratio of the input energy going to the mean azimuthal flow. Increasing I, $\langle\overline{u_\phi}\rangle$ grows as also does the frequency of the instability observed at the free Shercliff layer. At 45 A (corresponds to Re_t), another lower-frequency ($f_1 = 1.30$ Hz) instability appears, filling essentially the whole radial range of the duct. Above this threshold, $\langle\overline{u_\phi}\rangle(I)$ grows yet less with I.

Figure 4.19 shows the frequencies f_1 and f_2 of the two dominant spectral peaks in the UDV measurements of u_r and the PDP recordings 'Aazi1'. The two agree very well, mutually confirming their accuracy. For $M = 35$ and low I, we find frequencies $f < 0.2$ Hz. The second dominant frequency f_2 is the first harmonic of f_1. At 18 A, a jump to higher modes occurs. For $M = 1769$, the picture is more complex. At low I, the frequencies grow rapidly (cf. Fig. 4.18). At $I > 30$ A, the frequencies grow linearly with the current. The lower mode exhibits a frequency drop around 180 A.

The amplitudes A_1 and A_2 of the dominant modes in the UDV recordings of u_r are shown in Figure 4.20. Together with directly looking at $u_r(r,t)$, these plots are useful to define the threshold of instability. The critical current is $I_c \in [1, 2]$ A for $M = 35$, whereas it is $I_c \in [8, 9]$ A for $M = 1769$. By comparing A_1 with $\sqrt{2}\sigma_{u_r}$, it can also be seen how much of the temporal fluctuations in u_r are explained by the dominant mode alone. Note that a purely harmonic oscillation of amplitude $A_1 = \sqrt{2}\sigma_x$ has a standard deviation of σ_x. For $M = 35$ and low I, the instability consists of mainly one harmonic component.

From the UDV measurements of u_r and their FFT, we determine the critical current I_c of the first instability at all B (M) in our data set. Figure 4.21 shows the plots of I_c

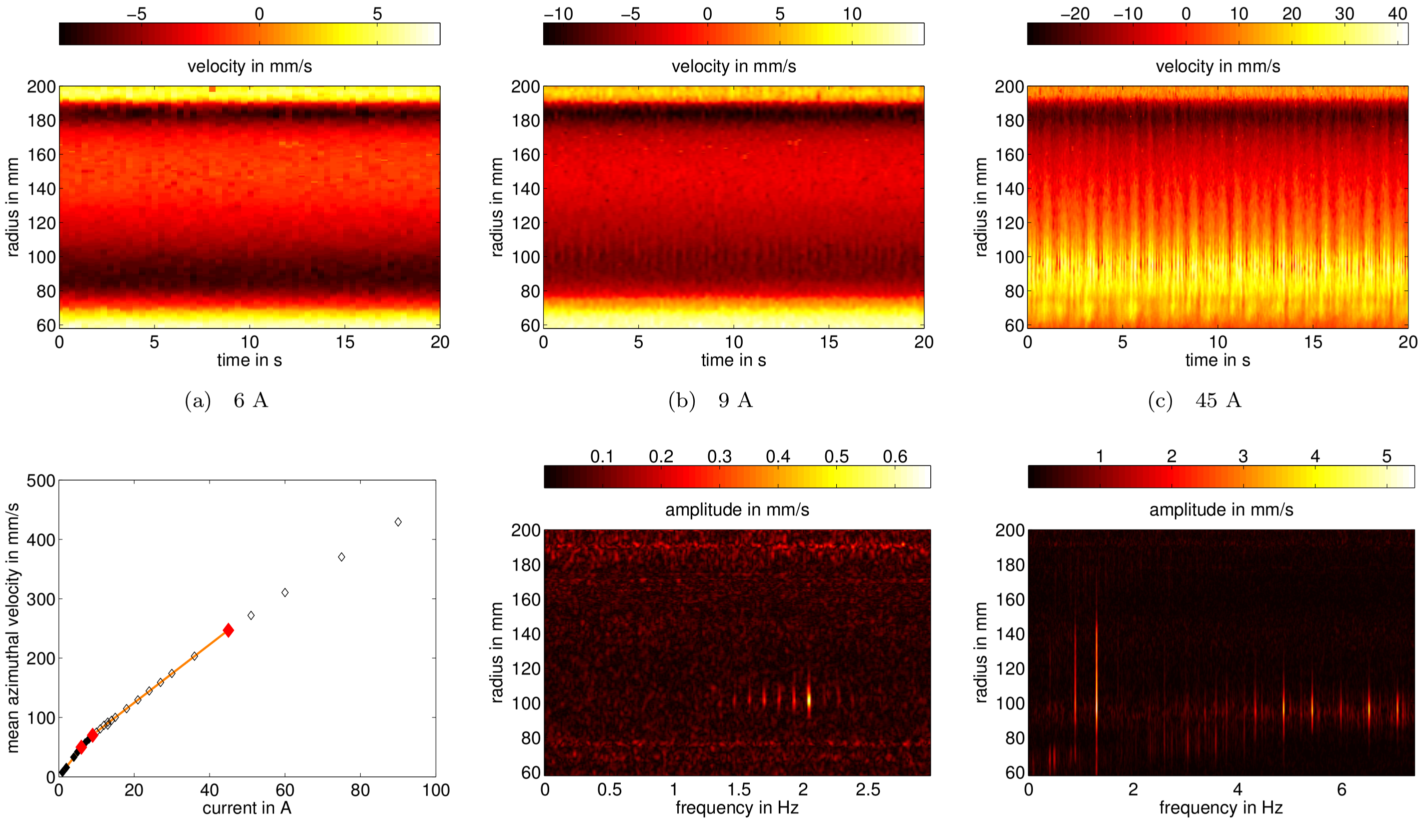

(a) 6 A (b) 9 A (c) 45 A

(d) $\langle\overline{u_\phi}\rangle$ (e) 9 A (f) 45 A

FIGURE 4.18: UDV measurements of u_r at 875 mT ($M = 1769$). (a-c) Space-time diagrams $u_r(r,t)$ of stable flow at 6 A ($Re = 8350$), slightly supercritical flow at 9 A ($Re = 1.17 \cdot 10^4$) and oscillations filling the entire radial range at 45 A ($Re = 4.14 \cdot 10^4$). (d) Radial mean of mean azimuthal velocity $\langle\overline{u_\phi}\rangle$ vs. current; stable flow is plotted as black filled symbols and the example cases (a-c) are indicated by large red symbols. (e,f) Space-frequency diagrams of (b,c) showing the location of the instabilities.

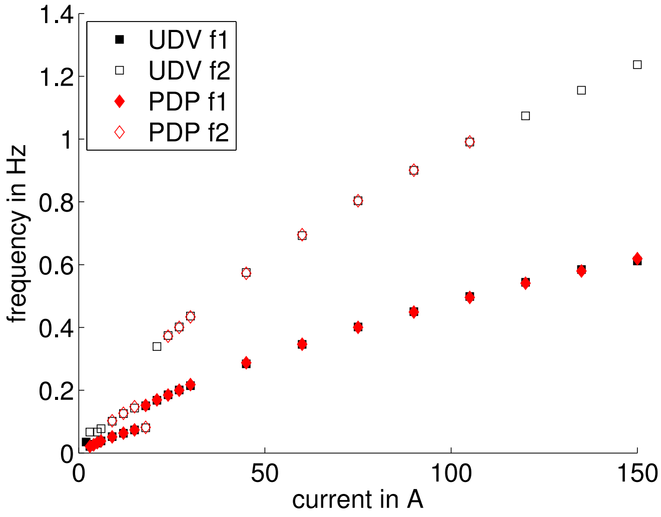

(a) $M = 35$ (17.5 mT)

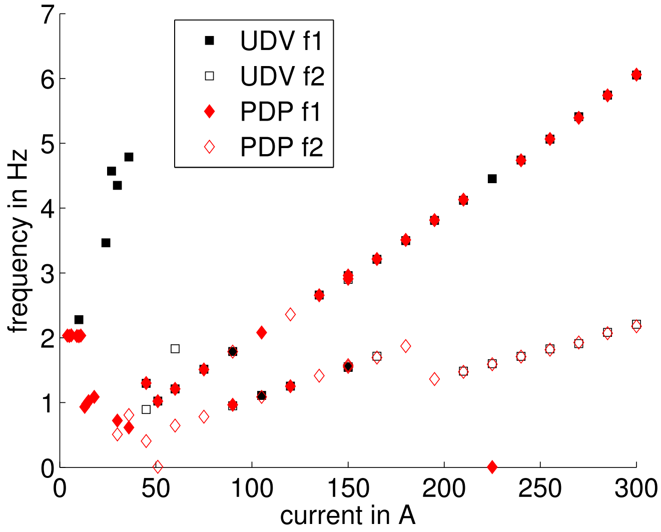

(b) $M = 1769$ (875 mT)

FIGURE 4.19: Frequencies f_1 (filled) and f_2 (open) of significant spectral peaks from UDV measurements of u_r (black squares) and PDP recordings of 'Aazi1' (red diamonds). All data shown fulfill $A_1 > 10\,\overline{A_i}$.

versus B and $R_c = Re_c/M$ versus M. For $B \lesssim 100$ mT ($M \lesssim 200$), the relative error in the threshold is large. The data show a minimum in I_c at 52.3 mT. In the limit of large $M \gtrsim 500$, the value of R_c becomes largely independent of M and approaches $R_c = 6$. This critical value for the threshold of the first instability is shown to play a role for the friction factor in the next section. From the data in Figure 4.21b, it is, however, not possible to extract whether the scaling for the threshold is in fact linear, $Re_c \sim M^{\alpha}$ with $\alpha = 1$, or rather a power law with $\alpha \in [0.7, 1]$.

What are the observed ZUCCHINI oscillations? A comparison of the dominant frequencies f (Fig. 4.19) with the mean azimuthal velocity $\langle\overline{u_\phi}\rangle$ (Figs. 4.12a and 4.17)

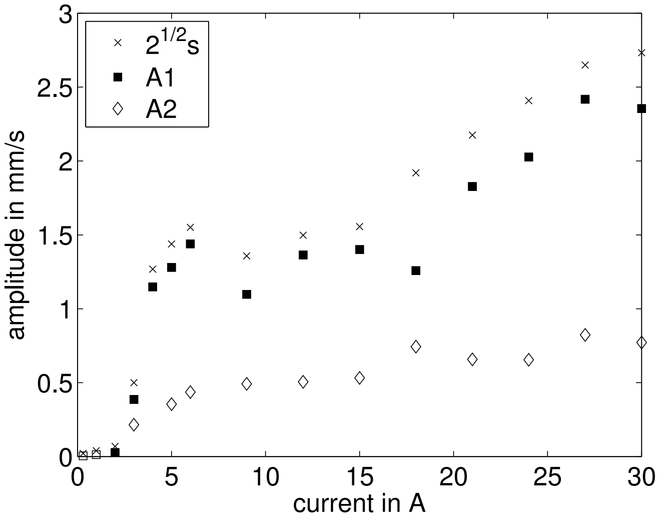

(a) $M = 35$ (17.5 mT)

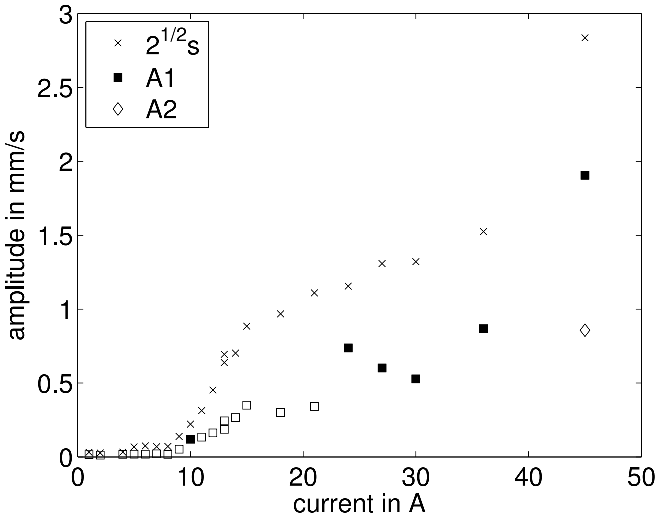

(b) $M = 1769$ (875 mT)

FIGURE 4.20: Amplitudes A_1 and A_2 of the dominant spectral peaks in UDV recordings of u_r compared with the renormalized standard deviation $\sqrt{2}\sigma_{u_r}$ of the signal. In (a), the critical current I_c for the threshold of instability is observed between 1 and 2 A; in (b), it is between 8 and 9 A. Open squares indicate maximum spectral peaks that do not fulfill the condition $A_1 > 10\,\overline{A_i}$.

suggests that the two scale similarly with the electric current I at the values of M studied. In fact, the plot of f versus $\langle\overline{u_\phi}\rangle$ in Figure 4.22 shows a clear correlation. Most of the data cluster on straight lines through the origin. The lines with different slope correspond to traveling modes with different azimuthal wave numbers m. In fact, the observed oscillations are consistent with vortices traveling in the direction of the mean flow as observed by Alboussiere et al. [1999] and investigated by Messadek and Moreau [2002]. These vortical structures are supposedly generated by a Kelvin-Helmholtz type instability of the free Shercliff layer [Roach et al., 2012, Spence et al., 2012].

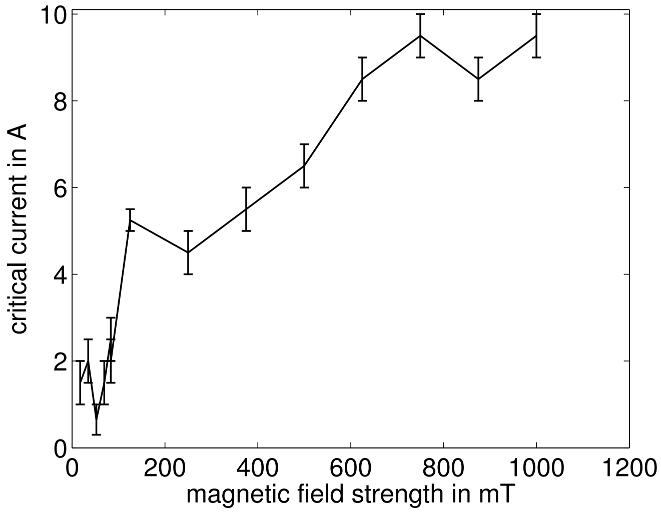

(a) I_c vs. B

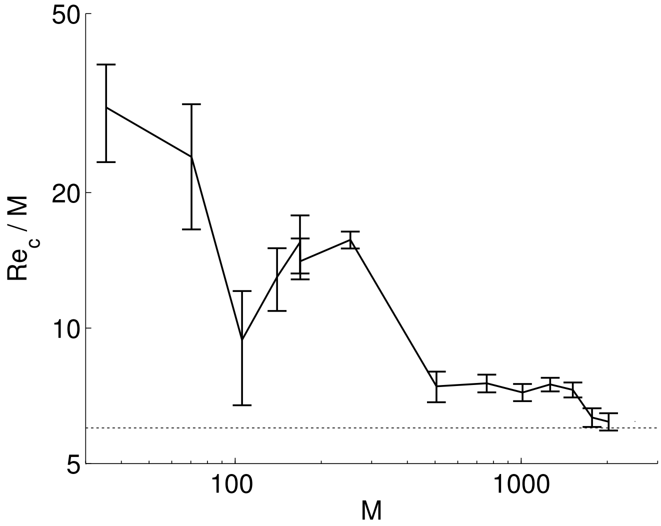

(b) Re_c/M vs. M

FIGURE 4.21: Threshold of the first instability as observed experimentally in UDV measurements of u_r. (a) Critical current I_c plotted versus magnetic field B. The error bars indicate the last stable and the first unstable flow respectively. (b) Same data in a loglog plot of Re_c/M versus M. The dotted line indicates $Re/M = 6$ (cf. Fig. 4.23).

Assuming that the recorded signal comes from disturbances traveling at transit velocity v_t, we derive the azimuthal wave number as

$$m = 2\pi r \frac{f}{v_t}. \tag{4.15}$$

We choose $r = 100$ mm which is where the instabilities occur (Fig. 4.18e-f). Taking the transit velocity v_t as slightly above $\overline{u_\phi}_{max}/2$ as found by Messadek and Moreau [2002], and $\overline{u_\phi}_{max} \approx 1.2 \langle \overline{u_\phi} \rangle$ in our data, we find $m \approx 2$ for the lowest mode. For the higher modes, it is not possible to recover unambiguous wave numbers. However, there is a clear tendency towards larger-scale (low-m) structures with higher forcing. This is attributed

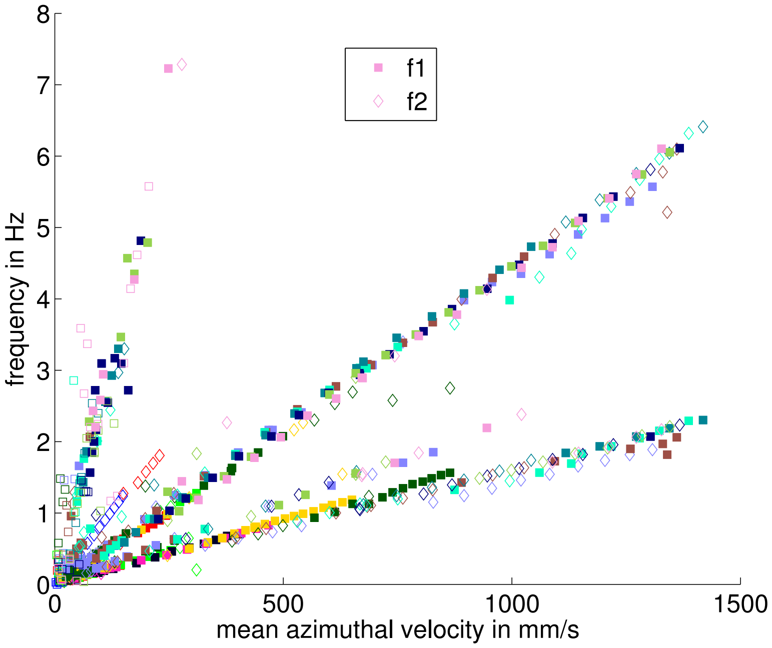

FIGURE 4.22: Plot of dominant frequencies f_1 (filled) and f_2 (open) in u_r versus the mean value of mean azimuthal velocity $\langle \overline{u_\phi} \rangle$. The data points cluster on straight lines through the origin. This suggests that the instabilities are traveling with the mean flow. Under this assumption, the lowermost line corresponds to an azimuthal wave number of $m = 2$. Colours as in Figs. 4.12 and 4.23.

to the inverse energy transfer leading to a merging of spatial structures in forced quasi-2D flows as also observed by [Alboussiere et al., 1999, Messadek and Moreau, 2002].

4.4.3.6 Friction factor

The friction factor F quantifies the dissipation in the system. Hence it is well suited to study processes that significantly affect the total amount of dissipation. In their study of the stability of the Hartmann layer, Moresco and Alboussiere [2004] (hereafter referred to as MA04) used friction factor measurements to determine the transition to turbulence in the Hartmann layer. They defined the friction factor as

$$F = \frac{IB}{u_m^2 \rho 2\pi r} \tag{4.16}$$

where they determined the mean azimuthal velocity u_m from measurements of the potential drop between inner and outer cylinder. We use $u_m = \langle \overline{u_\phi} \rangle$, the mean azimuthal velocity derived from UDV measurements. Figure 4.23 shows the relation between friction factor F and the parameter R for our data. The parameter $R = Re/M$ can be interpreted as the Reynolds number defined on the Hartmann layer thickness $\delta_H = a/M$. As in MA04, the data with different M are rather well collapsed in this plot. The dashed line shows the friction factor $F = 2/R$ for laminar flow. For $R < 6$, the data follow the laminar prediction. For large $M \gtrsim 250$, a transition occurs around $R_c = 6$, which shifts

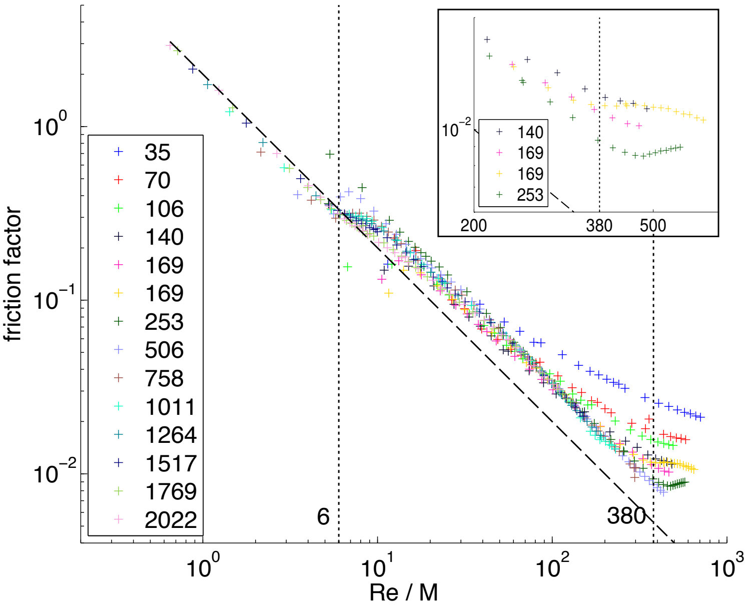

FIGURE 4.23: Friction factor F (Eq. 4.16) versus $R = Re/M$ which is the Reynolds number based on the Hartmann layer thickness. Colour indicates M. The dashed line gives the laminar value F_{lam}. Two transitions are observed at roughly $R_c = 6$ and $R_h = 380$ (dotted lines). The insert shows a zoom around $R_h = 380$ for the relevant data. The slow transition of F away from the straight line occuring at Re_f falls in between Re_c and Re_h.

the friction factor to a parallel line with values that are roughly 60% higher than the laminar case. $R_c = Re_c/M = 6$ is also the value where we found the threshold of the first instability for large M (cf. Fig. 4.21b). The occurrence of the first instability in the free Shercliff layer increases the friction factor but does not change the general scaling of $F \sim R^{-1}$.

For higher values of R, we observe another change in the behaviour of $F(R)$ away from the straight line. This transition at Re_f is not as clear as the previous one, and occurs at increasing Re_f with increasing M. It appears to scale roughly as $Re_f \sim M^2$ (cf. Fig. 4.24) but the error bars in its determination are significant. In contrast, the data with $M = 169$ and 253 exhibit another significant increase of F at $R_h = 370$ and 400 respectively. MA04 reported data with $R \in [10, 2000]$. They found a pronounced transition in F at $R_h \approx 380$ for all $M > 130$. Lower-M data were said not to be in the laminar regime. The change at $R_h \approx 380$ was attributed to the transition to turbulence in the Hartmann layer. Unfortunately we can neither follow Re_f nor Re_h to larger M due to limitations in the forcing current that do not allow sufficiently high Re at large M. The data at $M = 169$ and 253, however, appear to support the findings of MA04.

The transition in the free Shercliff layer around $R_c = 6$ was not observed by MA04 due to their different geometry lacking a free Shercliff layer. However, MA04 noticed that the experimental values of F for $R < 380$ were falling above the laminar line even though

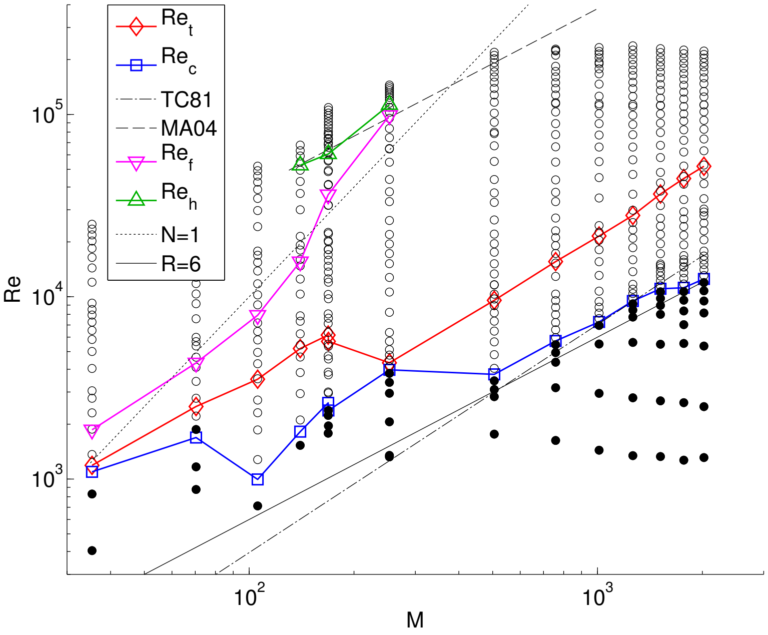

FIGURE 4.24: Stability diagram of the ZUCCHINI flow. Filled symbols denote stable flow. The blue line indicates Re_c, the threshold of the first observed instability which also changes the friction factor F. The red line is Re_t, the significant increase in the free Shercliff layer thickness δ_S. The dashed magenta line indicates Re_f, the second slight change in F. The green line is Re_h, the abrupt increase in F previously described by MA04. The following criteria are used to fit the observed transitions. The dashed black line gives $R_h = 380$, the transition in the Hartmann layer found in MA04 for $M > 130$. On the dotted line, the interaction parameter is $N = M^2/Re = 1$. The dash-dotted line indicates the transition below which inertial effects are negligible according to Tabeling and Chabrerie [1981]. The solid black line gives $R = Re/M = 6$.

by a much smaller fraction than in our experiment. Considering our observed instability in the free Shercliff layer around $R_c = 6$ and the picture of side wall-bounded turbulence in a duct drawn e.g. by Krasnov et al. [2012], it might be that an unstable side layer was responsible for the slightly increased friction factor in the MA04 experiment. The increase in F due to the side layer instability was, however, shown by Zhao and Zikanov [2012] to be noticeable in numerical simulations but not detectable in experiments as the one of MA04.

4.4.3.7 Stability diagram

From the UDV and PDP measurements reported in the preceding sections, we have a consistent picture of what is happening in the ZUCCHINI container. The stability diagram in Figure 4.24 summarizes the various observed transitions.

Re_c Onset of the first observed instability, determined from UDV measurements of u_r, also observed in friction factor F. It appears to approach $R_c = 6$ for large M. For $M \gtrsim 500$ and $Re_c < Re < Re_t$, the traveling vortices are restricted to the neighbourhood of the free Shercliff layer. For $M \lesssim 200$, they become container-filling already at Re_c.

Re_t Significant increase in the free Shercliff layer thickness δ_S from roughly 10 to 40 mm, associated with a change in radial flow structure and the ratio $\langle\overline{u_r}\rangle_{rms}/\langle\overline{u_z}\rangle_{rms}$ dropping towards a constant value of roughly unity. For moderate $M \in [35, 200]$, the scaling is $Re_t = 36M$. For large $M \gtrsim 500$, the vortices become space-filling above Re_t which in this parameter regime scales as $Re_t = 5.6M^{1.2}$. This scaling is similar to the criterion for the negligibility of inertial effects by Tabeling and Chabrerie [1981], $Re \sim M^{5/4}$.

Re_f Slight change in F, associated with a significant increase in the amplitude A of the oscillations, meaning that more energy is going into the vortices instead of the mean flow. The scaling is similar to $Re \sim M^2$ which is equivalent to a unity interaction parameter $N \sim 1$ and the criterion for the negligibility of inertial effects by Baylis and Hunt [1971].

Re_h Abrupt increase in F around $R_h = 380$ for $M \gtrsim 130$ as found by MA04 who interpreted it as the transition to turbulence in the Hartmann layer. This was confirmed by the numerical results of Krasnov et al. [2004].

4.4.4 Comparison with numerics

In Paper 1, we have shown that the qualitative structure and the magnitude of the experimental base flow are reasonably well recovered in the 2D3C FE simulations. The linear stability analysis for $M \in [10, 200]$ in the present paper builds on that base flow and makes predictions for the onset of the first instability, its frequency, azimuthal wave number and growth rate. Of those four, we can compare with experiments only the first two.

The critical current I_c for the onset of instability is in the range of 0.1 to 0.3 A in the numerics (Fig. 4.5) whereas it is between 0.5 and 2 A for comparable values of the magnetic field in the experiment. The numerics show a scaling of $I_c \sim B^{0.5}$ for $B > 15$ mT ($M > 30$); this parameter range would include aslo the lowest-M experimental data. However, a similar consistent scaling is reached in the experiment only for $M \gtrsim 500$. The frequencies observed due to the traveling vortices grow in both cases pretty much linearly for small currents I (Figs. 4.4b and 4.19). Their numerical and experimental values agree within the error bars.

The most striking agreement between experiment and numerics, however, are the location and the structure of the unstable modes. In the linear stability study (Fig. 4.7) as well as the actual ZUCCHINI container, the first instabilities originate at the free Shercliff layer in the form of counterrotating vortices traveling in the direction of the mean azimuthal velocity. In the numerics, the azimuthal wave number of the most unstable mode grows from $m = 3$ at $M = 10$ to $m = 8$ at $M = 200$. This agrees with the prediction of the theoretical stability analysis of Lieutaud and Neel [2001] for 2D instabilities in electrically-driven shear flow. In the experiment, it is not possible to determine the exact values of m especially at the onset of instability. There is, however, a trend towards larger m with increasing M at low forcing in agreement with the numerical prediction. The steepest cluster line which includes data with $M \gtrsim 500$ in Fig. 4.22 has a value of $m > 20$ which might be expected extrapolating the trend to higher m present in the numerics. Applying the theory of Lieutaud and Neel [2001], we would expect $m \approx 24$ for the onset of instability at $M = 2022$. Such large wave numbers are, however, only observed near the onset of instability. For stronger forcing, the vortical structures grow spatially, decreasing m. A clear difference is that in the numerics all values of m appear whereas in the experiment only a few distinct ones are observed. This is probably due to saturation and suppression of all other modes as described by Kaplan [2014]. Experimentally, we only observe the final saturated state.

In summary, the numerical study of the linear onset of instability agrees in many points with the experiment, e.g. the scaling of the onset, the frequencies, the location of the first instabilities at the free Shercliff layer and the trend towards higher m at onset with growing M. Most discrepancies are explained by the fact that the numerical study deals with the linearized problem whereas the experiment data are measured in the saturated and mostly strongly supercritical regime. It remains to be explained why I_c for the onset of instability differs by almost an order of magnitude, and why the experiment reaches the limit of large M only for $M \gtrsim 500$ which is also an order of magnitude larger than for the numerics.

4.5 Conclusions

We have performed an experimental and numerical study of electrically-driven shear flow in a modified cylindrical annulus. The focus of this work is the free Shercliff layer which develops at the prominent inner electrode and becomes unstable due to a Kelvin-Helmholtz type mechanism at a critical Reynolds number Re_c depending on the Hartmann number M. As found in both the numerical linear stability analysis and the experiment, the instability consists of counterrotating vortices traveling in the direction of the azimuthal flow. The critical current I_c for the onset of the first instability is an order of magnitude lower in the numerics. However, the azimuthal wave number m of the instability at low forcing grows with the M in both the linear stability analysis and the experiment. Experimentally we observe the saturated state containing only certain wave numbers reaching values $m > 20$ in agreement with theoretical predictions [Lieutaud and Neel, 2001]. The wave number of the vortices decreases with stronger forcing (larger

Re). The decrease in m with Re as well as the increase with M are features known from hydro- and magnetohydrodynamic spherical Couette flow [Hollerbach et al., 2004, Hollerbach, 2009]. For a follow-up study, it would be useful to determine more precisely the wave numbers.

The flow in the ZUCCHINI container has been probed by UDV and PDP. The two complementary methods mutually support their results. We were able to track the evolution of the flow structure and map the transitions as summarized in Figure 4.24. The onset of the first observed instability which is also observed in measurements of the friction factor F scales like $R_c = Re_c/M \approx 6$ for the limit of large $M \gtrsim 500$. In fact, an asymptotical behaviour is not reached below $M \approx 500$ also for other quantities like the mean azimuthal velocity which scales as $\langle \overline{u_\phi} \rangle \sim I$ and is independent of M in this regime, cf. [Baylis and Hunt, 1971]. For moderate $M \lesssim 150$, $\langle \overline{u_\phi} \rangle \sim (IB)^{2/3}$ rather depends on the Lorentz forcing (IB); this slightly differs from the $(IB)^{1/2}$-scaling found in [Boisson et al., 2012].

Increasing Re, the next observed transition occurs at Re_t where the free Shercliff layer thickness δ_S changes. It is remarkable that δ_S neither follows the laminar $M^{-1/2}$-scaling nor the $(Re/M)^{1/2.3}$ observed by [Messadek and Moreau, 2002]. Rather δ_S appears to approach a constant value of roughly 40 mm at large Re. The transition to this wide shear layer occurs at $Re_t \sim M$ for moderate M and at $Re_t \sim M^{1.2}$ for large M. Due to a criterion given by [Tabeling and Chabrerie, 1981], it might be interpreted as inertial effects becoming significant. Above Re_t, the vortices fill the whole radial range of the container which also affects the mean radial flow structure.

From measurements of the friction factor F, we interpret two further transitions in the flow. At $Re_f \sim M^2$, F shows a slight relative increase. This is accompanied by significantly more energy getting transferred to the vortices which leads to a growth in their velocity amplitude. A more pronounced increase in F at Re_h is only observed for $M \in [140, 250]$. It confirms the abrupt change at $R_h = Re_h/M \approx 380$ observed by [Moresco and Alboussiere, 2004, Krasnov et al., 2004] and attributed to the transition to turbulence in the Hartmann layer.

In conclusion, the ZUCCHINI experiment has been able to characterize different regimes of confined low-Rm MHD flow: stable flow, an unstable free Shercliff layer, unstable core flow and a turbulent Hartmann layer. The free Shercliff layer instability is of Kelvin-Helmholtz type while the action of the magnetic field is restricted to generating the Shercliff layer.

For the future, it would be interesting to study how the flow in ZUCCHINI is affected by a global rotation of the tank introducing a strong Coriolis force. Also it would be instructive to perform similar experiments in transparent electrolytes facilitating flow visualization. An intriguing question remains the role of the parameter R which is

Table 4.3: Comparison of kinetic energies in simulations of the base flow from the dedicated parameter study (superscript ^{o}, cf. Paper 1) with the ones from this study which have less degrees of freedom. The differences are marginal ($\lesssim 0.1\%$). This is also true for other quantities like local measurements of velocity and electrical current.

M	Re	$E^o_{kin,r}$	$E^o_{kin,\phi}$	$E^o_{kin,z}$	$E_{kin,r}$	$E_{kin,\phi}$	$E_{kin,z}$
20	1	1.01621e-7	2.77417	9.44823e-8	1.01612e-7	2.77412	9.44624e-8
20	100	7.97991e-4	2.73546	6.19458e-4	7.97921e-4	2.73539	6.19314e-4
50	100	7.35473e-4	19.87172	0.00176	7.35341e-4	19.87086	0.000176
200	10	5.14567e-6	350.76968	6.57648e-5	5.14776e-6	350.73361	6.56638e-5
200	100	4.77931e-4	351.05893	0.00574	4.78296e-4	351.02272	0.00573

theoretically only linked to the Hartmann layer. Why does R also govern the behaviour in the free Shercliff layer [Zikanov et al., 2014]?

It will be interesting to see how the experience from ZUCCHINI is applied to study the magnetostrophic regime, i.e. a balance between Lorentz and Coriolis forces, in the rapidly-rotating spherical SpiNaCH experiment which uses a similar electrical driving for a flow of liquid sodium.

Appendix

4.A Validation of the base flow

In the interest of computation time, we decrease the number of degrees of freedom in this study compared to the parameter study dedicated to the base flow (Paper 1). This is achieved by decreasing the order of discretization of the elements as well as coarsening the mesh. In order to ensure the validity of this proceeding, we compare kinetic energies (Table 4.3) as well as local measurements of velocity and electrical current density. The differences are negligible ($\lesssim 0.1\%$).

4.B PDP data example

PDP measurements are processed in a similar way as UDV recordings in Section 4.4.2.2. Figure 4.25 shows example recordings of the eight PDPs in inserts A and B at the same parameters as Figure 4.10; both inserts provide time series corresponding to radial and azimuthal flow. The largest potential differences are the ones measured at the outer azimuthal PDPs, Bazi1 and Bazi2. As Aazi1 and Aazi2 which show the largest-amplitude oscillations, they record the same signal. Potential differences connected to radial flow are oscillating around zero. Applying detrending, windowing and FFT as for the UDV data results in the spectrum of Fig. 4.25b which contains the same frequencies as the

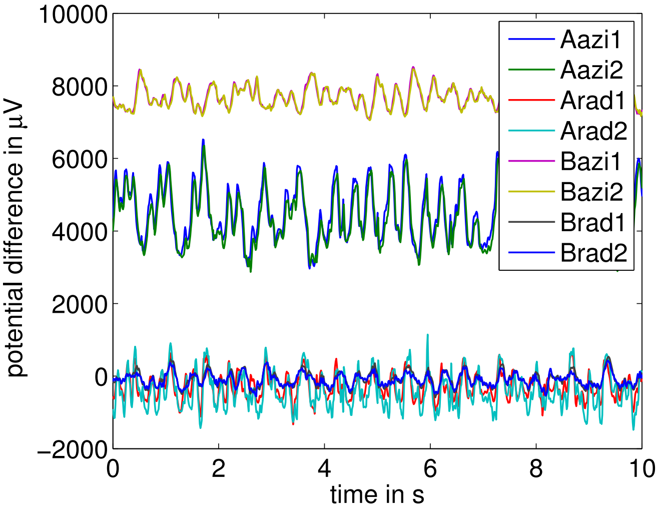

(a) Time series

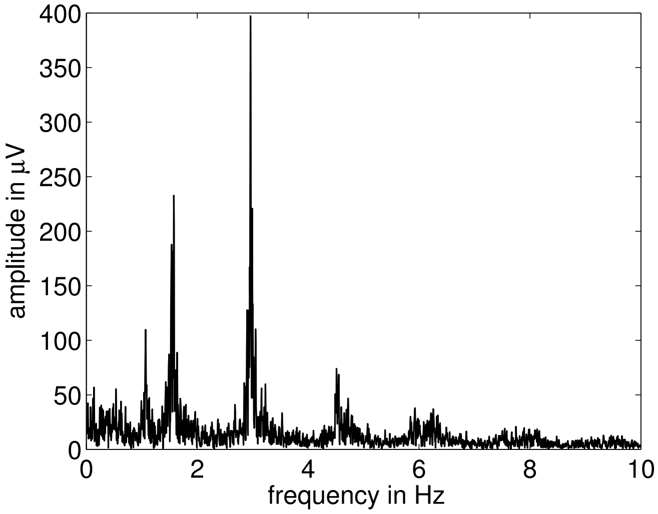

(b) Fourier transform of Aazi1

FIGURE 4.25: PDP example data: Potential differences $\Delta\Phi$ measured at the two inserts A and B indicating azimuthal and radial velocities for 875 mT and 150 A ($M = 1769$, $Re = 1.10 \cdot 10^5$). (a) Detail of the time series of all eight probes. (b) Detail of the FFT of Aazi1, measuring $\Delta\Phi_r$ at insert A and hence corresponding to the azimuthal velocity u_ϕ above the edge of the inner electrode (cf. Eq. 4.13). The spectra of the other PDPs look similar, as also does the one of u_r measured by UDV (Fig. 4.10d).

stacked UDV spectrum (Fig. 4.10d). Again we extract the two dominant frequencies f_1 and f_2, and their spectral amplitudes A_1 and A_2.

4.C First-order perturbation equations in cylindrical coordinates

We give here the first-order perturbation equations in cylindrical coordinates for the numerical study of the linear onset of instability. Quantities describing the base flow are written with a superscript ^{b}, first-order perturbations are denoted by a prime.

$$\begin{aligned}
&\frac{Re}{M^2}\left[\frac{\partial u_r'}{\partial t}+u_r'\frac{\partial u_r^b}{\partial r}+u_r^b\frac{\partial u_r'}{\partial r}+u_z'\frac{\partial u_r^b}{\partial z}+u_z^b\frac{\partial u_r'}{\partial z}-2\frac{u_\phi^b u_\phi'}{r}+\frac{u_\phi^b}{r}imu_r'\right]\\
&\quad=-\frac{\partial p'}{\partial r}+\frac{1}{M^2}\left[\frac{\partial^2 u_r'}{\partial r^2}+\frac{1}{r}\frac{\partial u_r'}{\partial r}-\frac{m^2}{r^2}u_r'+\frac{\partial^2 u_r'}{\partial z^2}-\frac{u_r'}{r^2}-\frac{2}{r^2}\mathrm{i}mu_\phi'\right]\\
&\qquad+B_\phi\frac{\partial\Phi'}{\partial z}-\frac{B_z}{r}\mathrm{i}m\Phi'+u_r'(B_r^2-1)+B_r(u_\phi'B_\phi+u_z'B_z)
\end{aligned}\tag{4.17}$$

$$\begin{aligned}
&\frac{Re}{M^2}\left[\frac{\partial u_\phi'}{\partial t}+u_r'\frac{\partial u_\phi^b}{\partial r}+u_r^b\frac{\partial u_\phi'}{\partial r}+\frac{u_\phi^b}{r}imu_\phi'+u_z'\frac{\partial u_\phi^b}{\partial z}+u_z^b\frac{\partial u_\phi'}{\partial z}+\frac{u_r'u_\phi^b}{r}+\frac{u_r^b u_\phi'}{r}\right]\\
&\quad=-\frac{1}{r}imp'+\frac{1}{M^2}\left[\frac{\partial^2 u_\phi'}{\partial r^2}+\frac{1}{r}\frac{\partial u_\phi'}{\partial r}-\frac{m^2}{r^2}u_\phi'+\frac{\partial^2 u_\phi'}{\partial z^2}-\frac{u_\phi'}{r^2}+\frac{2}{r^2}\mathrm{i}mu_r'\right]\\
&\qquad+B_z\frac{\partial\Phi'}{\partial r}-B_r\frac{\partial\Phi'}{\partial z}+u_\phi'(B_\phi^2-1)+B_\phi(u_r'B_r+u_z'B_z)
\end{aligned}\tag{4.18}$$

$$\begin{aligned}
&\frac{Re}{M^2}\left[\frac{\partial u_z'}{\partial t}+u_r'\frac{\partial u_z^b}{\partial r}+u_r^b\frac{\partial u_z'}{\partial r}+\frac{u_\phi^b}{r}\mathrm{i}mu_z'+u_z'\frac{\partial u_z^b}{\partial z}+u_z^b\frac{\partial u_z'}{\partial z}\right]\\
&\quad=-\frac{\partial p'}{\partial z}+\frac{1}{M^2}\left[\frac{\partial^2 u_z'}{\partial r^2}+\frac{1}{r}\frac{\partial u_z'}{\partial r}-\frac{m^2}{r^2}u_z'+\frac{\partial^2 u_z'}{\partial z^2}\right]\\
&\qquad+\frac{B_r}{r}\mathrm{i}m\Phi'-B_\phi\frac{\partial\Phi'}{\partial r}+u_z'(B_z^2-1)+B_z(u_r'B_r+u_\phi'B_\phi)
\end{aligned}\tag{4.19}$$

$$\frac{u_r'}{r}+\frac{\partial u_r'}{\partial r}+\frac{1}{r}\mathrm{i}mu_\phi'+\frac{\partial u_z'}{\partial z}=0\tag{4.20}$$

$$\begin{aligned}
&\frac{\partial^2\Phi'}{\partial r^2}+\frac{1}{r}\frac{\partial\Phi'}{\partial r}-\frac{m^2}{r^2}\Phi'+\frac{\partial^2\Phi'}{\partial z^2}\\
&\quad=-\frac{B_z}{r}\mathrm{i}mu_r'+B_\phi\frac{\partial u_r'}{\partial z}+\frac{B_z}{r}u_\phi'+B_z\frac{\partial u_\phi'}{\partial r}-B_r\frac{\partial u_\phi'}{\partial z}-\frac{B_\phi}{r}u_z'-B_\phi\frac{\partial u_z'}{\partial r}+\frac{B_r}{r}\mathrm{i}mu_z'.
\end{aligned}\tag{4.21}$$

Acknowledgments

We would like to thank P. Scarfe, R. Grimmer, F. Polli and T. Mörgeli for help with the design and manufacture of the experiment, as well as R. Hollerbach, T. Alboussière, A. Pothérat, F. Stefani, M. Seilmayer, T. Boeck and F. Samsami for fruitful discussions and advice on various topics within ZUCCHINI. Funding for this work by the ERC grant 247303 'MFECE' is gratefully acknowledged.

References

T. Alboussiere. A geostrophic-like model for large-hartmann-number flows. *Journal of Fluid Mechanics*, 521:125–154, 2004.

T. Alboussiere. Geostrophic versus mhd models. *Magnetohydrodynamics (book)*, 2007.

T. Alboussiere, V. Uspenski, and R. Moreau. Quasi-2D MHD turbulent shear layers. *Experimental Thermal and Fluid Science*, 20:19–24, 1999.

J. Baylis. Detection of the onset of instability in a cylindrical magnetohydrodynamic flow. *Nature*, page 563, 1964.

J. Baylis and J. Hunt. MHD flow in an annular channel; theory and experiment. *Journal of Fluid Mechanics*, 48(03):423–428, 1971.

J. Boisson, A. Klochko, F. Daviaud, V. Padilla, and S. Aumaitre. Travelling waves in a cylindrical magnetohydrodynamically forced flow. *Phys Fluids*, 24(4):044101, Jan 2012.

L. Bühler. Instabilities in quasi-two-dimensional magnetohydrodynamic flows. *Journal of Fluid Mechanics*, 326:125–150, 1996.

P. Davidson. *An Introduction to Magnetohydrodynamics.* Cambridge University Press, 2001.

P. Davidson and F. Siso-Nadal. On the structure of small-scale motion in the core of the earth. *Geophysical and Astrophysical Fluid Dynamics*, 96(1):49–76, 2002.

L. Davoust, M. Cowley, R. Moreau, and R. Bolcato. Buoyancy-driven convection with a uniform magnetic field. part 2. experimental investigation. *Journal of Fluid Mechanics*, 400:59–90, Jan 1999.

DOP3000 series User's manual. DOP Signal Processing S.A., www.signal-processing.com, software 4.01 edition.

S. Eckert, A. Cramer, and G. Gerbeth. *Magnetohydrodynamics - Historical Evolution and Trends*, chapter Velocity Measurement Techniques for Liquid Metal Flows, pages 275–294. Springer, 2007.

J. Hartmann and F. Lazarus. Hg-dynamics ii: Experimental investigations on the flow of mercury in a homogeneous magnetic field. *Mathematisk-fysiske Meddelelser, Det Kgl. Danske Videnskabernes Selskab*, XV(7):1–45, 1937.

R. Hollerbach. Non-axisymmetric instabilities in magnetic spherical couette flow. *Proceedings of the Royal Society A: Mathematical, Physical and Engineering Sciences*, 465 (2107):2003–2013, Jul 2009.

R. Hollerbach, B. Futterer, T. More, and C. Egbers. Instabilities of the stewartson layer part 2. supercritical mode transitions. *Theoret Comput Fluid Dynamics*, 18(2-4): 197–204, 2004.

E. Kaplan. On the saturation of non-axisymmetric instabilities of magnetized spherical couette flow. *submitted to PRE*, 2014.

A. Kljukin and A. Thess. Direct measurement of the stream-function in a quasi-two-dimensional liquid metal flow. *Exp Fluids*, 25:298–304, 1998.

D. Krasnov, E. Zienicke, O. Zikanov, T. Boeck, and A. Thess. Numerical study of the instability of the Hartmann layer. *Journal of Fluid Mechanics*, 504:183–211, 2004.

D. Krasnov, O. Zikanov, and T. Boeck. Numerical study of magnetohydrodynamic duct flow at high Reynolds and Hartmann numbers. *Journal of Fluid Mechanics*, 704: 421–446, 2012.

D. Krasnov, A. Thess, T. Boeck, Y. Zhao, and O. Zikanov. Patterned turbulence in liquid metal flow: Computational reconstruction of the Hartmann experiment. *Phys. Rev. Lett.*, 110(8):084501, Feb 2013.

P. Lieutaud and M. Neel. Instabilities of an electrically driven shear flow. *Comptes Rendus de l'Academie des Science - Series IIB - Mechanics*, 329(12):881–887, 2001.

K. Messadek and R. Moreau. An experimental investigation of MHD quasi-two-dimensional turbulent shear flows. *J. Fluid Mech.*, 456:137–159, Jan 2002.

C. Mistrangelo and L. Bühler. Perturbing effects of electric potential probes on mhd duct flows. *Exp Fluids*, 48, 2010.

P. Moresco and T. Alboussiere. Experimental study of the instability of the Hartmann layer. *J. Fluid Mech.*, 504:167–181, Jan 2004.

N. B. Morley, J. Burris, L. C. Cadwallader, and M. D. Nornberg. Gainsn usage in the research laboratory. *Review of Scientific Instruments*, 79(5), 2008.

H. C. Nataf, T. Alboussiere, D. Brito, P. Cardin, N. Gagniere, D. Jault, and D. Schmitt. Rapidly rotating spherical couette flow in a dipolar magnetic field: An experimental study of the mean axisymmetric flow. *Phys Earth Planet Int*, 170(1-2):60–72, 2008.

P. Olson. Overview of core dynamics. In G. Schubert, editor, *Treatise on Geophysics*, volume 8 on Core Dynamics. Elsevier Science Publishers, 2007.

A. Potherat, J. Sommeria, and R. Moreau. An effective two-dimensional model for mhd flows with transverse magnetic field. *Journal of Fluid Mechanics*, 424:75–100, 2000.

A. Potherat, J. Sommeria, and R. Moreau. Numerical simulations of an effective two-dimensional model for flows with a transverse magnetic field. *Journal of Fluid Mechanics*, 534:115–143, 2005.

W. Press, S. Teukolsky, W. Vetterling, and B. Flannery. *Numerical Recipes.* Cambridge University Press, 3rd edition edition, 2007.

A. Roach, E. Spence, C. Gissinger, E. Edlund, P. Sloboda, J. Goodman, and H. Ji. Observation of a free-Shercliff-layer instability in cylindrical geometry. *Phys. Rev. Lett.*, 108, 2012.

D. Schmitt, T. Alboussiere, D. Brito, P. Cardin, N. Gagniere, D. Jault, and H. C. Nataf. Rotating spherical Couette flow in a dipolar magnetic field: experimental study of magneto-inertial waves. *J. Fluid Mech.*, 604:175–197, 2008.

E. Spence, A. Roach, E. Edlund, P. Sloboda, and H. Ji. Free magnetohydrodynamic shear layers in the presence of rotation and magnetic field. *Phys Plasmas*, 19(056502), 2012.

B. Sreenivasan and T. Alboussière. Experimental study of a vortex in a magnetic field. *Journal of Fluid Mechanics*, 464:287–309, Jan 2002.

Z. Stelzer, D. Cebron, S. Miralles, J. Noir, S. Vantieghem, and A. Jackson. Experimental and numerical study of electrically-driven MHD flow in a modified cylindrical annulus: (1) Base flow. in prep.

P. Tabeling and J. Chabrerie. Magnetohydrodynamic secondary flows at high Hartmann numbers. *Journal of Fluid Mechanics*, 103:225–239, 1981.

S. Vantieghem and B. Knaepen. Numerical simulation of magnetohydrodynamic flow in a toroidal duct of square cross-section. *International Journal of Heat and Fluid Flow*, 32(6):1120–1128, 2011.

Y. Zhao and O. Zikanov. Instabilities and turbulence in magnetohydrodynamic flow in a toroidal duct prior to transition in Hartmann layers. *J. Fluid Mech.*, 692:288–316, 2012.

O. Zikanov, D. Krasnov, T. Boeck, A. Thess, and M. Rossi. Laminar-turbulent transition in magnetohydrodynamic duct, pipe and channel flows. *Applied Mechanics Reviews*, 66, 2014.

Chapter 5

Extracting scaling laws from numerical dynamo models

by **Zacharias Stelzer** and Andrew Jackson

Published in *Geophysical Journal International*, 193(3):1265-1276, March 2013.

Summary

Earth's magnetic field is generated by processes in the electrically conducting, liquid outer core, subsumed under the term 'geodynamo'. In the last decades, great effort has been put into the numerical simulation of core dynamics following from the magnetohydrodynamic (MHD) equations. However, the numerical simulations are far from Earth's core in terms of several control parameters. Different scaling analyses found simple scaling laws for quantities like heat transport, flow velocity, magnetic field strength and magnetic dissipation time.

We use an extensive dataset of 116 numerical dynamo models compiled by Christensen and co-workers to analyse these scalings from a rigorous model selection point of view. Our method of choice is leave-one-out cross-validation which rates models according to their predictive abilities. In contrast to earlier results, we find that diffusive processes are not negligible for the flow velocity and magnetic field strength in the numerical dynamos. Also the scaling of the magnetic dissipation time turns out to be more complex than previously suggested. Assuming that the processes relevant in the numerical models are the same as in Earth's core, we use this scaling to estimate an Ohmic dissipation of 3-8 TW for the core. This appears to be consistent with recent high CMB heat flux scenarios.

5.1 Introduction

The Earth's magnetic field is generated by motions of an electrically conducting fluid in the outer core, the bulk being liquid iron. The processes include magnetic induction and are subsumed under the term 'geodynamo'. It is generally accepted that the fluid motions in the outer core, which are most important for maintaining the geodynamo, are driven by convection, i.e. by thermal and compositional buoyancy forces [Olson, 2007]. There are in general three ways to study the dynamics of the outer core. The first builds on theoretical considerations like force balances and thermodynamics [e.g. Jones, 2011]. Secondly, it is possible to model the whole system numerically on the basis of the fundamental physical equations. Finally, laboratory experiments analogue to the processes proposed for the Earth's core can help to determine certain aspects of the dynamics. In this paper, we focus on the second approach.

An important part of the increase in knowledge about core dynamics in the last two decades came from numerical simulations of the dynamo process. Starting from the first successful 3D MHD self-sustained dynamo models of Glatzmaier and Roberts [1995] and Kageyama and Sato [1995], numerical dynamo simulations have been able to reproduce various features of the geomagnetic field such as field morphology, secular variations and polarity reversals. The problem, however, remains how to apply results from numerical simulations to the Earth.

A major challenge is the discrepancy between numerical models and the core in terms of the non-dimensional parameters defined in Table 5.1. Specifically, numerical dynamos have far too slow rotation (Ekman number too large), are less turbulent (Rayleigh number too small) and excessively viscous relative to their electrical conductivity (magnetic Prandtl number too large) compared to the core. This gap can not be bridged easily due to the enormous computational power required to resolve all relevant time and length scales.

One way of using present-day numerical dynamo simulations to estimate quantities that are relevant to Earth's core (e.g. heat flux, flow velocity, magnetic field strength) is to extract scaling laws between these quantities and other characteristic parameters from the data. Assuming that the relevant processes in the core are the same as in our simulations, we may extrapolate the results to the parameter regime of the core and in that way gain insight into the processes in Earth's core.

This has been done for various quantities. Important results were the diffusivity-free scalings of heat transport, flow velocity and magnetic field strength [Christensen and Aubert, 2006] and simple scalings for the magnetic dissipation time [Christensen and Tilgner, 2004, Christensen, 2010]. The question arises, however, how complex a model needs to be in order to do justice to the data.

We address the classical problem of model selection, where a model is defined in terms of a number of parameters. On the one hand, the paradigm of Occam prefers a model that is less complex over another that is more complex (when both fit the data equally well), generally meaning that the former model contains the fewest parameters of all models. But what is often not recognised, and is equally important, is that models with fewer parameters can have greater predictive power than more complicated models. Physical theories are not only validated by their fit to existing data, but even more by their performance in predicting new data. A few words are in order to motivate why this phenomenon is true.

We imagine a noisy dataset with n points and fit it with p parameters; we begin by taking $p = n$ to achieve a perfect fit to our data. Because of noise, this model is extremely complex, containing high frequency oscillations (in the case of a function $f(x)$ fitted to points distributed in x). Imagine now receiving a new datum. The n parameter model will have almost no predictive power for this new datum, since it has fitted all of the noise in the dataset from which it was derived. Indeed, a far simpler model, with $p \ll n$ will have far greater predictive power. We use this principle by implementing a procedure called 'leave-one-out cross validation', where we systematically omit one of the data points and hold it in reserve as a test point, against which different models can test their predictive power. In this way we evaluate the predictive power of models, and find models based on an optimal number of parameters that have the most predictive power.

The format of the paper is as follows: In Section 5.2, we present the database used in our analysis. In Section 5.3, we illustrate the method of cross-validation with a toy problem, before going on to apply it to the dynamo problem at hand. Subsequently, we analyse the scaling laws for heat transport, flow velocity and magnetic field strength using diffusivity-free parameters (Section 5.4) and traditional non-dimensional numbers (Section 5.5). Section 5.6 is concerned with the scaling of magnetic dissipation time as well as the application of the scalings to the core.

5.2 Dynamo dataset

5.2.1 Numerical dynamo simulations

In the numerical dynamo simulations used in this study, convection is driven by a fixed superadiabatic temperature contrast ΔT between inner and outer boundaries of a rotating spherical shell. Moreover the Boussinesq approximation is used, i.e. density variations enter the equations only through a buoyancy term in the momentum equation. The standard set of equations consists of five equations describing conservation of momentum (Navier-Stokes equation), magnetic induction, the transport of temperature and the solenoidal nature of the magnetic field $\mathbf{B}$ and the velocity field $\mathbf{u}$ (cf. Eq. 5.1-5.5).

TABLE 5.1: Non-dimensional parameters, their estimated values for Earth's core [following Olson, 2007] and values in the models studied here. The first four quantities are input parameters to the numerical simulations, the lower ones are output parameters. U is a characteristic velocity; ν is kinematic viscosity; k is thermal conductivity; κ is thermal diffusivity; α is thermal expansivity; $\eta = (\mu_0\sigma_e)^{-1}$ is magnetic diffusivity with σ_e, electrical conductivity; Q is heat flux; the remaining quantities are defined in the text.
Note that the thermal diffusivity κ and the electrical conductivity σ_e have recently been revised. These ab-initio calculations have increased the numerical values of κ and σ_e by roughly a factor of three [Pozzo et al., 2012, de Koker et al., 2012]. As a result, the non-dimensional parameters depending on those quantities have been revised with respect to those given in Olson [2007]. We give the updated numbers for Pr, Pm and Rm.

Quantity	Definition	Earth's core	This study
Ekman	$Ek = \nu/\Omega D^2$	$\sim 3 \cdot 10^{-14}$	$10^{-6} - 10^{-3}$
Rayleigh	$Ra = \alpha g_o \Delta T D^3/\nu\kappa$	$\sim 10^{20\pm?}$	$3 \cdot 10^5 - 2.2 \cdot 10^9$
Prandtl	$Pr = \nu/\kappa$	~ 0.1	$0.1 - 10$
Magnetic Prandtl	$Pm = \nu/\eta$	$\sim 3 \cdot 10^{-5}$	$0.06 - 33.3$
Nusselt	$Nu = QD/4\pi r_o r_i k \Delta T$	?	$2.02 - 29.8$
Magnetic Reynolds	$Rm = UD/\eta$	~ 2300	$39 - 5695$

These equations can be non-dimensionalised by introducing four independent control parameters. Their choice is not unique. We follow Christensen and Aubert [2006] and use the shell thickness $D = r_o - r_i$ of the outer core, the inverse rotation rate Ω^{-1} , the temperature difference ΔT, and the quantity $(\rho\mu_0)^{1/2}\Omega D$ as fundamental scales for length, time, temperature and magnetic field, respectively; r_o is the outer core radius, r_i the inner core radius, ρ density and μ_0 magnetic permeability. This leads to the following set of non-dimensional equations for magnetic field $\mathbf{B}$, fluid velocity $\mathbf{u}$ and temperature T:

$$\frac{\partial \mathbf{u}}{\partial t} + (\mathbf{u} \cdot \nabla)\mathbf{u} + 2(\hat{\mathbf{z}} \times \mathbf{u}) + \nabla\Pi = Ra Ek^2 Pr^{-1} \frac{\mathbf{r}}{r_o} T + (\nabla \times \mathbf{B}) \times \mathbf{B} + Ek \nabla^2 \mathbf{u} \quad (5.1)$$

$$\frac{\partial \mathbf{B}}{\partial t} = \nabla \times (\mathbf{u} \times \mathbf{B}) + Ek Pm^{-1} \nabla^2 \mathbf{B} \quad (5.2)$$

$$\frac{\partial T}{\partial t} + (\mathbf{u} \cdot \nabla) T = Ek Pr^{-1} \nabla^2 T \quad (5.3)$$

$$\nabla \cdot \mathbf{B} = 0 \quad (5.4)$$

$$\nabla \cdot \mathbf{u} = 0, \quad (5.5)$$

where $\hat{\mathbf{z}}$ is the unit vector in the direction of the rotation axis. In these equations, gravity is assumed to vary proportional to the radius, g_o being the value of gravity at the outer boundary; volumetric heating is neglected and Π is the non-hydrostatic pressure. The four non-dimensional parameters governing Equations 5.1-5.5 are defined in Table 5.1.

For our analysis of scaling laws, we use a database of 185 numerical dynamo models built over time by U. Christensen and co-workers. Most of the models were previously reported in Christensen and Aubert [2006] and Christensen et al. [2009], and studied in Christensen [2010] and King et al. [2010]. The mechanical boundary conditions are no-slip and the ratio between inner and outer core radius is 0.35 as in Earth's core. The inner core of the models is insulating in some simulations and conducting in others. The exterior of the shell is electrically insulating in all cases. We restrict our analysis to this database, which is homogeneous in terms of model setup and numerical method, in order to avoid unwanted effects of varying too many control parameters in the scaling law selection.

5.2.2 Scaling laws and model setup

We seek to extract scaling laws from numerical solutions of the MHD Equations 5.1-5.5 as explained in the introduction. Under certain conditions, these scaling laws may then be extrapolated to the more extreme parameter range of Earth's core. An example of a scaling law is the classical heat transport (Nu-Ra) scaling in non-rotating, plane-layer convection. The functional relationship between Nu and Ra can be expressed as $Nu \sim Ra^{\beta}$ with possibly different values of β for different convective regimes [e.g. Aurnou, 2007].

Similarly, we follow the ground-breaking work of Christensen and Aubert [2006] and others and restrict our scaling analysis to power laws of the from

$$\hat{y} = \alpha \prod_{j=1}^{p-1} x_j^{\beta_j}. \tag{5.6}$$

Observations are collected in y and are the output of the numerical simulations; predictions $\hat{y}$ in Equation 5.6 are calculated from x_j, the independent variables, which are mostly control parameters of the MHD equations. The number of data (numerical dynamo simulations) and thereby the size of $\hat{y}$ is n; the total number of free parameters is p consisting of the prefactor α and $(p-1)$ exponents β_j.

The task of fitting this functional form to given data can be transformed to a linear problem by taking the logarithm,

$$\log \hat{y} = \log \alpha + \sum_{j=1}^{p-1} \beta_j \log x_j. \tag{5.7}$$

Our linear model includes the coefficients $\log \alpha$ and β_j. These are fitted by multiple linear regression which minimizes the mean quadratic misfit,

$$\chi^2 = \frac{1}{n} \sum_{i=1}^{n} \left(\frac{\zeta_i - \hat{\zeta}_i}{\sigma_i} \right)^2, \tag{5.8}$$

where we have defined $\zeta = \log y$ for ease of notation. The contribution of the different data points to χ^2 can be weighted by their standard deviation σ_i.

As another measure of misfit between data and fitted values, we define the mean relative misfit to the original data y (not in log-domain),

$$\chi_{rel} = \sqrt{\frac{1}{n}\sum_{i=1}^{n}\left(\frac{y_i - \hat{y}_i}{y_i}\right)^2}, \tag{5.9}$$

for comparability with Christensen and Aubert [2006].

5.2.3 Errors in the dependent variable

We seek to fit the linear model to observed values ζ, but, in doing so, we face the question of what the appropriate attribution of errors for these observations is. In principle the numerical experiments are perfect, and it may be our parametrised theory that is an imperfect representation of the data. Obvious error sources are the limited resolution of the models and the limited time averaging of fluctuating properties; but equally there may be errors in the observations as a result of the simulations perhaps not achieving equilibrium, or perhaps as a result of bistability and/or hysteresis in the nonlinear system [see, for example, Simitev and Busse, 2009]. Two routes are available to us: following Christensen and Aubert [2006], we can assume that the errors are equal in $\zeta = \log y$, or we could alternatively assume that the errors are equal in the original measured variable y. The first hypothesis leads to the error $\sigma_\zeta = c$, where c is constant; one can see, from a consideration of the perturbation $\delta(\log y)$, that this leads to $\delta y/y = c$, namely that the *percentage* errors in the original observations y are constant. Whether this is a good model remains open. The second assumption, that there are constant errors σ_y in the original observations y, leads to

$$\sigma_\zeta = \sigma_y/y = \sigma_y/e^\zeta, \tag{5.10}$$

when the errors are small. In this model, the errors shrink drastically when ζ is large. In the absence of definitive knowledge concerning the errors, we choose to carry out fitting using both attributions of error. In the following sections, we assume equal errors in ζ. The results under the assumption of equal errors in the original variable y are given in Appendix 5.A. Considering the resulting error distributions, it is still not clear which error attribution is appropriate.

5.2.4 Parameter range

For the extraction of scaling laws from the dynamo database, we only use simulations that satisfy the following criteria [following Christensen and Aubert, 2006]:

1. The simulation must be fully convective as required by $Nu > 2$.
2. The generated magnetic field has to be dipole-dominated. As a measure of dipolarity, we use $f_{dip} = B_{dip}/B_{12}$, the time-averaged ratio of the mean dipole field strength to the field strength in harmonic degrees 1 to 12 on the outer boundary. The condition for a dipole-dominated field is taken as $f_{dip} > 0.35$.
3. The Prandtl number should not fall too far from the values estimated for Earth's core: $Pr \leq 10$. (Models in the dataset with $Pr > 10$ are rather new and have not been used by any other study.)

Applying these restrictions to the data, we are left with 116 numerical dynamo simulations. We also tested excluding the models with the highest Ekman numbers, $Ek = 10^{-3}$, as done in Christensen and Aubert [2006]. However, this hardly changed the result of our analysis. In Section 5.2.5, we will determine the effect of the requirements on Nu, f_{dip} and Pr.

The 116 numerical dynamo simulations contain 40 models with an imposed two- or four-fold symmetry. We tested the effect of discarding those and found the same scaling laws as for the full dataset (Section 5.4), with the exponents just slightly changed.

Figure 5.1 shows the distribution of the control parameters Ra, Ek, Pm and Pr as well as the output quantities Rm and Nu within the 116 models used in the scaling law analysis. In general, the distribution of the parameter values appears to be sufficiently uniform over some range to allow the extraction of scaling laws. Only in the case of Pr, the values cluster at $Pr = 1$ with very few differing values. Hence the database is not favourable to elicit a Pr-dependence. If we really were to apply the scaling laws to the Earth, Pr fortunately is the number that requires the least extrapolation (cf. Table 5.1).

5.2.5 Dynamical regime

Convective heat transfer can be separated into two regimes, the rapidly-rotating and the buoyancy-dominated regime [Aurnou, 2007]. In the rapidly-rotating regime, the flow is largely two-dimensionalised by the Taylor-Proudman theorem. For stronger forcing, buoyancy breaks the columnar structure leading to three-dimensional convective structures [King et al., 2009]. The two regimes are characterized by different heat transport efficiencies and different slopes in a plot of Nu versus Ra.

Figure 5.2 shows the quantities Nu versus Ra for the models in our database. Crossed-out models are rejected by the criteria in Section 5.2.4. Obviously, the majority of the 185 dynamo models falls into the rapidly-rotating regime. By applying the criteria on f_{dip} and Pr, we throw out the models that are slightly buoyancy-dominated or transitional.

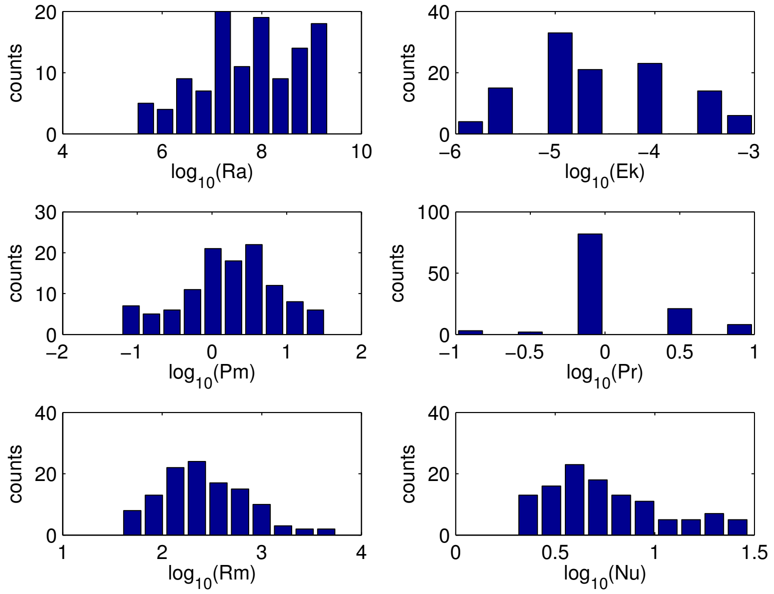

FIGURE 5.1: Histograms of the values of the non-dimensional parameters in the 116 simulations used in the scaling law analysis. All parameters apart from Pr show a distribution that allows the extraction of scaling laws.

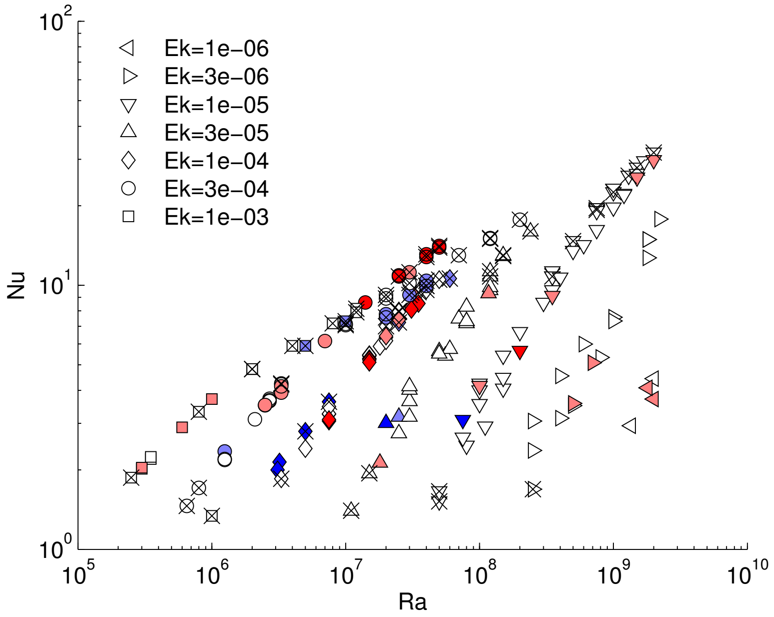

FIGURE 5.2: Plot of Nu vs. Ra for all 185 dynamo models of the database. Colour indicates the value of Pr: dark-blue $Pr \leq 0.1$, light-blue $0.1 < Pr < 1$, white $Pr = 1$, light-red $1 < Pr < 10$, dark-red $Pr \geq 10$. Crossed-out models do not fulfill the criteria of Section 5.2.4. Note that the remaining 116 models fall into the rapidly-rotating regime.

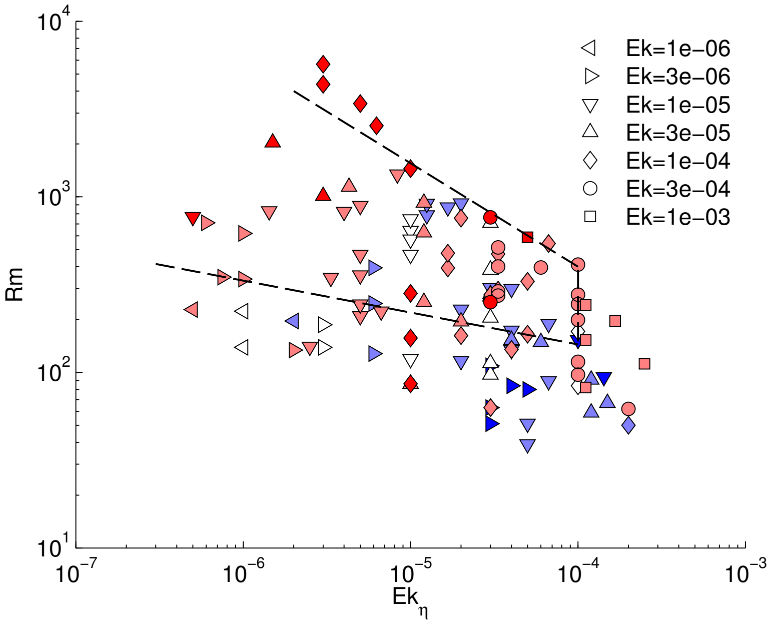

FIGURE 5.3: Earth-likeness of the 116 dynamo models used in this study according to the criteria of Christensen et al. [2010]. $Ek_\eta = Ek/Pm$ is the magnetic Ekman number. Models that exhibit an Earth-like magnetic field morphology plot inside the dashed line. Colour indicates the value of Pm: dark-blue $Pm \leq 0.1$, light-blue $0.1 < Pm < 1$, white $Pm = 1$, light-red $1 < Pm < 10$, dark-red $Pm \geq 10$.

The criterion $Nu > 2$ would appear not to make a great difference were it not applied. As a result, we are left with 116 rapidly-rotating models for our analysis.

There have been attempts to classify geodynamo models according to their Earth-likeness. Christensen et al. [2010] used four criteria based on magnetic field morphology, namely relative axial dipole power, equatorial symmetry, zonality and flux concentration. They found that Earth-like dynamo models fall into a certain area in the (Rm-Ek_η) domain, where $Ek_\eta = Ek/Pm$ is the magnetic Ekman number. Figure 5.3 shows where the 116 dynamo models of this study plot in terms of Ek_η and Rm. According to the criteria of Christensen et al. [2010], 61 of the models have a magnetic field morphology that is Earth-like. We applied our scaling law analysis also to this subset of the data. The resulting scaling laws are given in Appendix 5.B. They are very similar to the ones in Section 5.4 using all 116 dynamo models.

5.3 Cross-validation

5.3.1 Model selection

Extracting scaling laws from multivariate data is a model selection problem, or more specifically, a variable subset selection problem. In Section 5.2.2, we have defined the functional form of the scalings of interest (Eq. 5.6). The question now is which independent variables x_j, should be included in the linear model (Eq. 5.7) in order to explain the values of the dependent variable $\hat{y}$.

The solution to this problem is not trivial. Normally one wishes to examine the discrepancy between theory and observation through a quantity such as mean quadratic misfit χ^2 (Eq. 5.8). In a linear problem, however, it is always possible to reach $\chi^2 = 0$ with $p \leq n$, the number of free parameters less or equal to the number of data. Model selection ideally avoids over-fitting, so the model contains 'just the right' (number of) independent variables in the sense that the model accounts for the variability in the data but is not more complex than required (Occam's razor). In the introduction we explained how it is possible for simpler models to have more predictive power than complex ones, and this is the property we seek to exploit.

A variety of approaches exists in the areas of frequentist and Bayesian statistics to tackle the task of model selection. An elegant way of determining the required independent variables x_j for a model is cross-validation (CV). It is probably the simplest method for estimating prediction error [Hastie et al., 2009]. High predictive power, in turn, is certainly a desirable property for a scaling law.

5.3.2 Leave-one-out cross-validation

We use leave-one-out cross-validation (LOOCV) in our analysis. One observation of the n data is set aside as a validation sample. The parameters of the linear model, $\log \alpha$ and β_j, are estimated ('trained') from the remaining $(n-1)$ data (training sample) by minimizing mean quadratic misfit χ^2 (Eq. 5.8). Then the model is validated by applying it to the validation sample. This process is done consecutively, setting aside a different part of the data and predicting it from the remainder. The misfit between the validation data point and its prediction from the corresponding model is accumulated, leading to the cross-validation estimate of the prediction error,

$$P_{CV} = \frac{1}{n} \sum_{i=1}^{n} \left(\frac{y_i - \hat{y}_i^*}{\sigma_i} \right)^2, \tag{5.11}$$

where the prediction $\hat{y}_i^*$ has been obtained using the model that was trained on all but the i-th datum. The CV estimate of prediction error, P_{CV}, is calculated for models containing different combinations of independent variables, x_j. The favoured variable combination is the one with minimum P_{CV}. The parameters of the final scaling law are trained on all n data.

Various other model selection methods such as Akaike's information criterion (AIC), Mallows' C_p, the jackknife and the bootstrap, are asymptotically equivalent to LOOCV [Stone, 1977, Efron, 1983]. A generalization of LOOCV is k-fold CV with k instead of

n partitions. We experimented with different k. For the main purpose of this paper, however, the resulting differences are minor.

5.3.3 Example: Curve fitting

In order to illustrate the problem of model selection and how it can be solved by LOOCV, we give a synthetic example from the domain of curve fitting, which in this case also is a linear problem. Let us suppose we are given noisy data y and all we know is that the data come from a model in the form of a Chebyshev expansion

$$y = \sum_{i=0}^{m} \beta_i T_i(x) + \epsilon, \tag{5.12}$$

where T_i are Chebyshev polynomials and ϵ is the noise. Now, we want to retrieve the underlying functional form and especially determine the degree m of the underlying polynomial.

Figure 5.4(a) shows 51 noisy data points that were created from a Chebyshev polynomial of degree $m = 4$ by adding Gaussian noise with standard deviation $\sigma_{true} = 0.1$. The polynomial coefficients are listed in Table 5.2. As in the applications later in this study, the amplitudes of the contributions from different polynomial degrees differ significantly.

Figure 5.4(b) gives the mean quadratic misfit χ^2 (Eq. 5.8), assuming $\sigma = 1$ out of ignorance, for multiple linear regressions using polynomials of degrees 0 to 15; the corresponding numerical values are given in Table 5.3. The misfit χ^2 can, of course, be reduced successively by using polynomials of higher degrees and falls to 0 for a polynomial of degree 50, when $p = n$, the number of free parameters p equals the number of unknowns n.

Figure 5.4(c) shows the LOOCV estimate of prediction error P_{CV} (Eq. 5.11) for polynomials of degrees 0 to 15. The corresponding numerical values in Table 5.3 show that minimum P_{CV} is reached for polynomial degree 4. LOOCV is also able to correctly identify the noise in the data. For the correct degree 4 polynomial, the noise level is found to be $\sqrt{\chi^2} \approx 0.097$ (cf. Table 5.3). This value is better than for any other polynomial degree, the true answer being $\sigma_{true} = 0.1$.

The model selection procedure by LOOCV chooses the right degree m of polynomial by rating the different models according to their predictive abilities. Moreover, the subsequently estimated polynomial coefficients $\hat{\beta}$ and the estimated noise level are quite close to their true values β_{true} and σ_{true}, respectively.

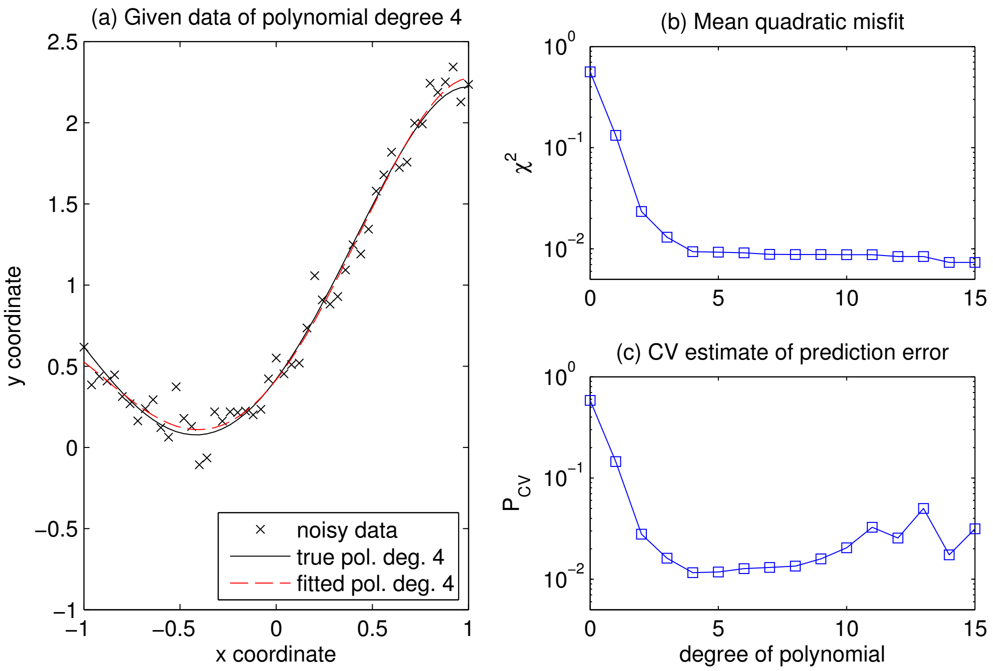

FIGURE 5.4: Curve fitting, synthetic example. (a) Black crosses are 51 noisy data that were created from a Chebyshev polynomial of degree $m = 4$ (black line) by adding Gaussian noise with standard deviation $\sigma = 0.1$. The dashed red curve is the final fitted polynomial. (b) Mean quadratic misfit χ^2 for polynomials of degrees 0 to 15. (c) LOOCV estimate of prediction error P_{CV} for the same polynomial degrees. χ^2 is successively reduced by increasing polynomial degree, whereas P_{CV} is minimum for the true polynomial degree. For numerical values see Table 5.3.

TABLE 5.2: Curve fitting, synthetic example. True polynomial coefficients β_{true} used in the synthetic example, and their multiple linear regression estimates $\hat{\beta}$.

Pol. degree	β_{true}	$\hat{\beta}$
0	1	1.0000
1	1	1.0335
2	0.5	0.4921
3	-0.2	-0.1590
4	-0.08	-0.0922

5.4 Diffusivity-free scalings

Following Christensen [2002], there have been several studies advocating diffusivity-free scaling laws for the application to Earth's core [Christensen and Aubert, 2006, Christensen et al., 2009, Christensen, 2010]. The underlying physical rationale is the hypothesis that diffusive processes do not play a primary role in Earth's core. Hence a modified Nusselt number,

$$\begin{aligned} Nu^* &= \frac{1}{4\pi r_o r_i} \frac{Q_{adv}}{\rho c \Delta T \Omega D} \\ &= (Nu - 1)\frac{Ek}{Pr}, \end{aligned} \tag{5.13}$$

TABLE 5.3: Curve fitting, synthetic example. Values of mean quadratic misfit χ^2 and LOOCV estimate of prediction error P_{CV} for polynomials of degrees m from 0 to 8 and 48 to 50, see also Figures 5.4(b) and 5.4(c). At polynomial degree $m = 50$, the number of free parameters equals the number of data, $p = n = 51$. Minimum values are bold.

Pol. degree	χ^2	P_{CV}
0	0.5624	0.5851
1	0.1324	0.1454
2	0.0234	0.0279
3	0.0131	0.0161
4	0.0094	**0.0116**
5	0.0093	0.0118
6	0.0091	0.0127
7	0.0088	0.0131
8	0.0088	0.0135
⋮	⋮	⋮
48	3.4620e-05	4.5578e+22
49	1.1865e-05	1.1348e+24
50	**0**	-

has been introduced, where Q_{adv} is advected heat flux and c is heat capacity; the remaining quantities were defined in Section 5.2.1. Moreover a modified Rayleigh number,

$$\begin{aligned} Ra^* &= \frac{Ra\,Ek^2}{Pr} \\ &= \frac{\alpha g_0 \Delta T}{\Omega^2 D}, \end{aligned} \tag{5.14}$$

and a modified flux-based Rayleigh number,

$$\begin{aligned} Ra^*_Q &= \frac{1}{4\pi r_o r_i} \frac{\alpha g_0 Q_{adv}}{\rho c \Omega^3 D^2} \\ &= Ra^* Nu^* \\ &= (Nu - 1)\frac{Ra\,Ek^3}{Pr^2}, \end{aligned} \tag{5.15}$$

are used, neither of them containing any diffusivity. On the basis of these diffusivity-free parameters, Christensen and Aubert [2006] studied the scaling of heat transport, flow velocity and magnetic field strength in numerical dynamo models. The preferred scalings for all three quantities were simple power laws only depending on Ra^*_Q. In this section, we use our model selection procedure by LOOCV in order to study whether a data-driven analysis yields the same result as the diffusivity-free hypothesis.

5.4.1 Heat transport

The heat transport in terms of diffusivity-free parameters is given by Nu^*. We test scaling laws of the form of Equation 5.6 and allow any combination of Ra^*_Q, Pm and

TABLE 5.4: Cross-validation estimates of prediction error P_{CV} for the best-fitting scaling laws for heat transport, flow velocity and magnetic field strength for all possible parameter combinations. Minimum values are again bold.

	(Ra^*_Q)	(Pm)	(Ek)	(Ra^*_Q, Pm)	(Ra^*_Q, Ek)	(Pm, Ek)	(Ra^*_Q, Pm, Ek)
Nu^*	0.0106	2.5772	1.0396	0.0100	**0.0095**	0.8412	0.0096
Ro	0.0438	1.8391	0.9118	**0.0116**	0.0315	0.6164	0.0118
$Lo/f_{ohm}^{1/2}$	0.0760	0.9238	0.3486	**0.0264**	0.0580	0.3466	0.0266

Ek as explanatory variables. The cross-validation estimates of the prediction error P_{CV} for the best-fitting laws with all different parameter combinations are given in Table 5.4. The scaling law with minimum P_{CV} includes the parameters Ra^*_Q and Ek:

$$Nu^* = 0.075\ Ra_Q^{*0.51} Ek^{0.03}. \tag{5.16}$$

Comparably low P_{CV} result from scaling laws including the parameter combinations (Ra^*_Q), (Ra^*_Q, Pm) and (Ra^*_Q, Pm, Ek). Table 5.5 shows the fitted values of Equation 5.16 together with their standard errors. The table also contains the mean relative misfit χ_{rel} defined in Equation 5.9.

Figure 5.5 shows the fit of the scaling law (Eq. 5.16) to the 116 data points. Disregarding the additional Ek-dependence, the scaling is very similar to $Nu^* = 0.076\ Ra_Q^{*0.53}$ [Christensen and Aubert, 2006]. Although the exponent of Ek is quite small, LOOCV, under the assumption of equal errors in $\zeta = \log(Nu^*)$, argues for this dependence, and the numerical value of the exponent is four times larger than its standard error in regression. One reason for the weak Ek-dependence could be that an asymptotic behavior has not yet been reached within the rapidly-rotating regime [cf. King et al., 2010]. Also, it should be mentioned that LOOCV under the assumption of equal errors in the original variable $y = Nu^*$ favours a simple Ra^*_Q-dependence devoid of any Ek-dependence (see Appendix 5.A).

We compare our heat flux scaling relation with others that have recently appeared in the literature. King et al. [2010] compare scaling relations developed for experiments in rotating cylinders (in which gravity is parallel to the rotation axis) with the same type of numerical results that are analysed herein, namely rotating convection with radial gravity. For the rapidly-rotating regime, they find a preferred fit to their experimental data that is also in reasonably good agreement with the numerical results of the form

$$Nu = A \left(\frac{Ra}{Ra_c} \right)^{6/5}, \tag{5.17}$$

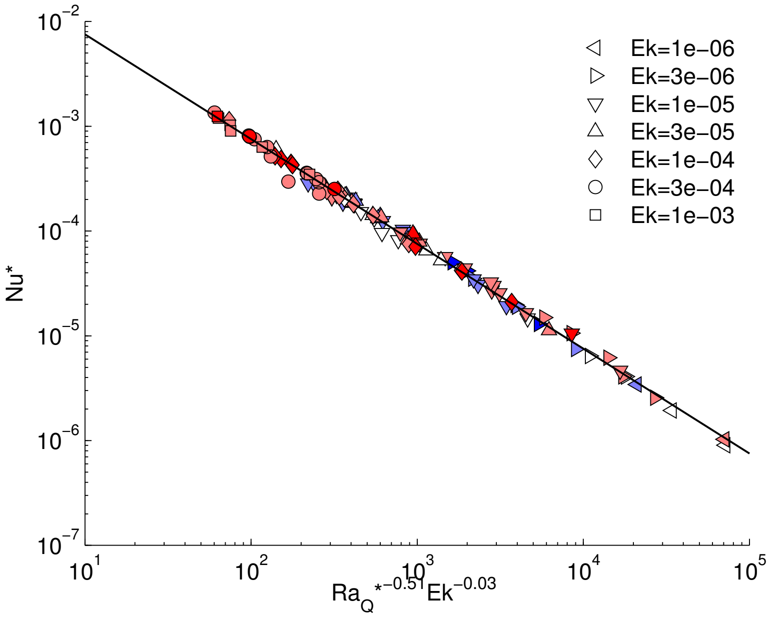

FIGURE 5.5: Heat transport scaling, preferred scaling law by LOOCV. Colour indicates the value of Pm: dark-blue $Pm \leq 0.1$, light-blue $0.1 < Pm < 1$, white $Pm = 1$, light-red $1 < Pm < 10$, dark-red $Pm \geq 10$.

where $Ra_c \propto Ek^{-4/3}$ is the critical Rayleigh number for the onset of convection. In terms of the flux-based quantities that we are considering here, this law becomes

$$Nu^* \propto (Ra_Q^*)^{6/11}(Ek\,Pr)^{1/11}. \tag{5.18}$$

The numerical values of these indices, 0.545 and 0.09, are not terribly different from the ones that we discovered here.

Conversely, a recent explanation of the same experimental data by King et al. [2012] proposes

$$Nu = A\left(\frac{Ra}{Ra_c}\right)^3 \propto Ra^3 Ek^4 \tag{5.19}$$

based on a physically-motivated boundary layer analysis. In terms of the flux-based parameters, this is equivalent to

$$Nu^* \propto (Ra_Q^*)^{3/4} Pr^{1/2} Ek^{-1/4}. \tag{5.20}$$

The Ekman dependence of this law is clearly much stronger than others that have been proposed (including our own), and has an opposite sign of exponent when converted to flux-based variables. The lack of experimental data in the strongly rotation-dominated regime contributes to this lack of understanding.

TABLE 5.5: Overview of the scaling laws preferred by LOOCV for the diffusivity-free parameters. The exponents of the non-dimensional parameters are shown together with their standard errors from the multiple linear regression. Covariances between the fitted values are minor. The mean relative misfit χ_{rel} of the different models is also displayed.

	prefactor	Ra_Q^*	Pm	Ek	χ_{rel}
Nu^*	0.075 ± 0.004	0.505 ± 0.005	-	0.033 ± 0.008	0.100
Ro	1.16 ± 0.05	0.436 ± 0.003	-0.126 ± 0.007	-	0.106
$Lo/f_{ohm}^{1/2}$	0.60 ± 0.04	0.306 ± 0.005	0.157 ± 0.011	-	0.161

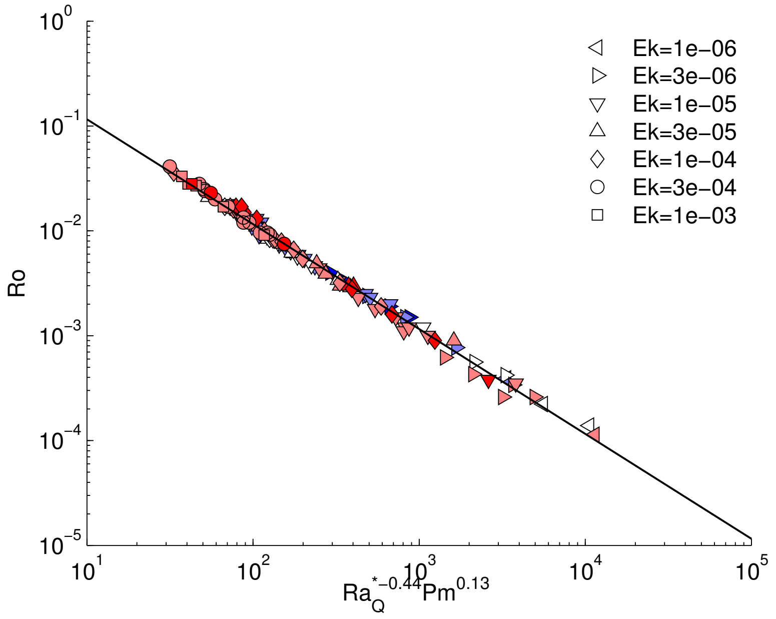

FIGURE 5.6: Flow velocity, favoured scaling law. Colours as in Figure 5.5.

5.4.2 Flow velocity

A measure for flow velocity in non-dimensional form is Ro as defined by

$$Ro = \left(\frac{2E_{kin}}{V}\right)^{1/2}, \tag{5.21}$$

where E_{kin} is kinetic energy and V is the volume of the shell [Christensen and Aubert, 2006]. Applying the same procedure as in Section 5.4.1 leads to a flow velocity scaling of

$$Ro = 1.16\, Ra_Q^{*0.44} Pm^{-0.13}. \tag{5.22}$$

This scaling law is shown in Figure 5.6. It is virtually identical to the $Ra_Q^{*0.43}Pm^{-0.13}$ law that could not firmly be established by Christensen and Aubert [2006] because the improvement in misfit compared to the one-parameter law $Ro = 0.85\, Ra_Q^{*0.41}$ did not seem to be sufficient. According to our analysis, however, Pm plays a role in the Ro-scaling with $P_{CV}(Ra_Q^*, Pm) = 0.0116$ compared to $P_{CV}(Ra_Q^*) = 0.0438$ arguing for the additional dependence (cf. Table 5.4). This becomes also evident in Figure 5.7 where the

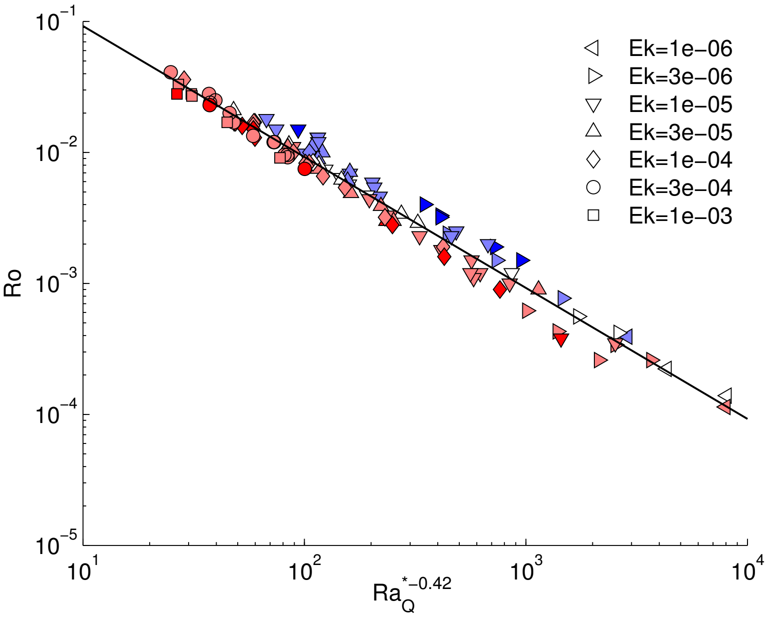

FIGURE 5.7: Flow velocity scaling only with Ra_Q^* (not preferred by LOOCV). Colours as in Figure 5.5. There is a clear division between blue ($Pm < 1$) and red ($Pm > 1$) above and below the fitting line.

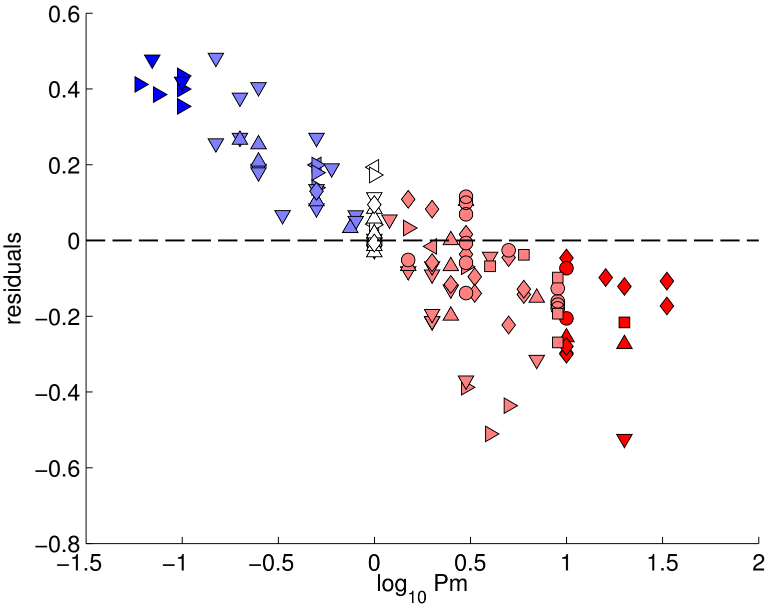

FIGURE 5.8: Residuals between Ro-data and model predictions from fig. 5.7 plotted vs. Pm. A clear unresolved Pm-dependence is visible. Colours as in Figure 5.5.

one-parameter fit (including only Ra_Q^*) to the velocity data is shown, and in Figure 5.8 where the corresponding residuals are plotted versus Pm. An unresolved Pm-dependence is visible.

5.4.3 Magnetic field strength

An adequate measure for magnetic field strength is given by $Lo/f_{ohm}^{1/2}$ according to Christensen and Aubert [2006]. The Lorentz number Lo is defined analogously to Ro (Eq. 5.21) as

$$Lo = \left(\frac{2E_{mag}}{V}\right)^{1/2}, \tag{5.23}$$

with magnetic energy replacing kinetic energy. The time-averaged fraction of Ohmic dissipation,

$$f_{ohm} = \frac{D_{ohm}}{P}, \tag{5.24}$$

is the ratio of Ohmic dissipation,

$$\begin{aligned} D_{ohm} &= \int \mathbf{j}^2/\sigma_e \, dV \\ &= \int (\eta/\mu_0)(\nabla \times \mathbf{B})^2 \, \mathrm{d}V, \end{aligned} \tag{5.25}$$

to the power P generated by buoyancy forces; $\mathbf{j}$ is the electrical current density.

Again, we look for a scaling of power law form that includes any combination of Ra_Q^*, Pm and Ek. The law favoured by our model selection analysis is

$$\frac{Lo}{f_{ohm}^{1/2}} = 0.60 \, Ra_Q^{*0.31} Pm^{0.16}. \tag{5.26}$$

It is shown in Figure 5.9. Also in this case, our analysis differs from Christensen and Aubert [2006] who preferred the one-parameter scaling $Lo/f_{ohm}^{1/2} = 0.92 \, Ra_Q^{*0.34}$ over the $Ra_Q^{*0.32} Pm^{0.11}$ law. (The exponent of Pm in a two-parameter law for $Lo/f_{ohm}^{1/2}$ has risen from 0.11 in the original study to 0.16 in Eq. 5.26, probably due to adding dynamo models with large Pm to the dataset.) The estimated prediction errors are $P_{CV}(Ra_Q^*, Pm) = 0.0264$ versus $P_{CV}(Ra_Q^*) = 0.0760$ favouring the additional dependence (cf. Table 5.4).

5.4.4 Discussion

The diffusivity-free scalings for heat transport, flow velocity and magnetic field strength contain only a dependence on Ra_Q^* [Christensen and Aubert, 2006]. Our model selection analysis by LOOCV, however, favours more complex scalings with an additional parameter. As mentioned in Section 5.4.1, the Ek-dependence in the Nu^*-scaling may be due to a non-asymptotical regime and disappears when a different error attribution is used (Appendix 5.A). The Pm-dependence in the scalings of Ro and $Lo/f_{ohm}^{1/2}$ is a significant feature which also persists when using different methods of model selection.

Summing up, we used diffusivity-free parameters in the first place. But the diffusivities come back into the scaling laws by additional dependencies complicating the simple

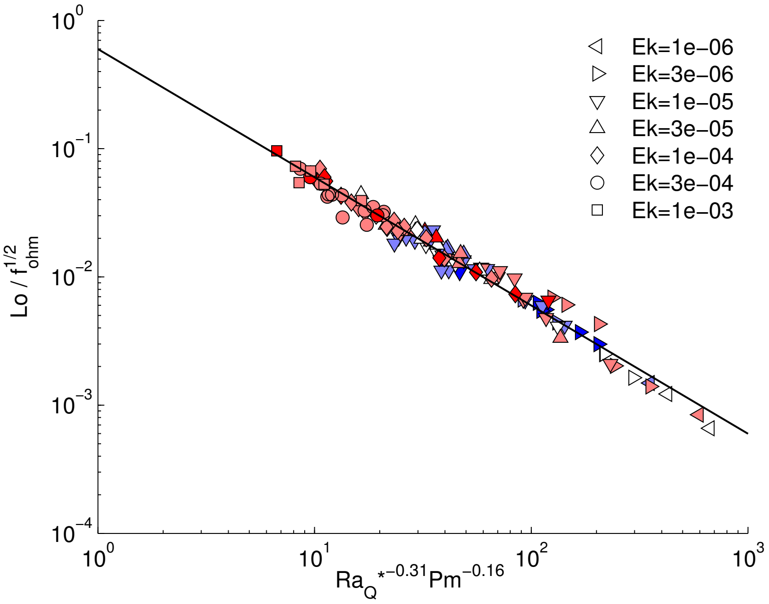

FIGURE 5.9: Magnetic field strength, favoured scaling law. Colours as in Figure 5.5.

laws. This means that diffusive processes may not be neglected in the regime of numerical dynamo models that we are looking at (cf. Section 5.2.5) An attempt to apply the scaling laws to Earth's core is undertaken in Section 5.6.4.

5.5 Scaling with traditional parameters

In the previous section, we have shown that the numerical dynamo simulations in general do not support diffusivity-free scalings of heat transport, flow velocity and magnetic field strength. The question is now about the scalings in terms of traditional parameters Ra, Pm, Ek and Pr (definitions in Table 5.1). In this case, it is necessary to allow a possible Pr-dependence in order to account for the variability in the data. (The diffusivity-free parameter Ra_Q^* in Equation 5.15 has an implicit Pr-dependence.)

Again, we look for exponential scaling laws of the form of Equation 5.6. LOOCV favours the following scaling laws for convective heat transport, flow velocity and magnetic field strength, respectively:

$$Nu - 1 = 0.009\, Ra^{0.93} Ek^{1.00} Pr^{-0.09}, \tag{5.27}$$

$$Ro = 0.15\, Ra^{0.84} Pm^{-0.13} Ek^{1.75} Pr^{-0.90}, \tag{5.28}$$

$$\frac{Lo}{f_{ohm}^{1/2}} = 0.18\, Ra^{0.54} Pm^{0.17} Ek^{1.15} Pr^{-0.71}. \tag{5.29}$$

(We choose $(Nu - 1)$ as measure of convective heat transport and stay with $Lo/f_{ohm}^{1/2}$ as measure of magnetic field strength in order to get laws that are comparable with the scalings of Section 5.4. In the case of the magnetic field scaling, it should be noted that

Table 5.6: Overview of the scaling laws preferred by LOOCV for the traditional parameters. The exponents of the non-dimensional parameters are shown together with their standard errors from the multiple linear regression. χ_{rel} is the mean relative misfit between fitted and observed values (Eq. 5.9).

	prefactor	Ra	Pm	Ek	Pr	χ_{rel}
$Nu-1$	0.009 ± 0.001	0.93 ± 0.02	-	1.00 ± 0.02	-0.09 ± 0.02	0.165
Ro	0.15 ± 0.02	0.84 ± 0.01	-0.13 ± 0.01	1.75 ± 0.02	-0.90 ± 0.02	0.100
$Lo/f_{ohm}^{1/2}$	0.18 ± 0.03	0.54 ± 0.02	0.17 ± 0.02	1.15 ± 0.03	-0.71 ± 0.02	0.173

even the simplest law, $Lo/f_{ohm}^{1/2} \sim Ra_Q^{*\beta}$, is actually not diffusivity-free in general, since f_{ohm} contains the magnetic diffusivity η via the Ohmic dissipation D_{ohm}, cf. Eqs. 5.24 and 5.25. The scaling is only diffusivity-free when $f_{ohm} \approx 1$ as assumed for Earth's core.)

The dependencies in Equations 5.27-5.29 are complex enough to require all parameters in the scaling laws. Only in the $(Nu-1)$-scaling, Pm is not included as it is the case in Section 5.4.1. It is, however, clear that these scalings are pure linear regression results on the data lacking any physical rationale. Table 5.6 shows that the scalings are quite complex. Creating diffusivity-less parameters (Eq. 5.13-5.15) with inbuilt Ek- and Pr-dependencies has been an attempt to simplify the relations.

We can actually find a parameter similar to the modified Rayleigh number, $Ra^* = RaEk^2Pr^{-1}$ (Eq. 5.14), in the scalings for flow velocity and magnetic field strength (Eqs. 5.28 and 5.29), when we look at the exponents of Ra, Ek and Pr that form a ratio of approximately 1 : 2 : -1 in the Ro- and $Lo/f_{ohm}^{1/2}$-scalings. This parameter combination is also known as the convective Rossby number, $Ro_c = (Ra^*)^{1/2}$ [e.g. Liu and Ecke, 1997, Aurnou et al., 2007]. The convective Rossby number describes the ratio of buoyancy over Coriolis forces when using the convective free-fall velocity, $u_{conv} \sim \sqrt{\alpha g_o \Delta T D}$, which results from a balance between inertia and buoyancy, as velocity scale. Hence, it is not surprising to find Ra^* in the velocity scaling. It is slightly more surprising to see it in the magnetic field scaling, although induction scales with the velocity field. On top of the Ra^*-dependence, there is certainly a Pm-dependence present in both scalings. The heat transport scaling (Eq. 5.27), however, is not at all reminiscent of Ra^* and does not contain a Pm-dependence either.

5.6 Magnetic dissipation in Earth's core

5.6.1 Magnetic dissipation time

The magnetic dissipation time τ_{diss} is defined as the ratio of magnetic energy over Ohmic dissipation (Eq. 5.25),

$$\tau_{diss} = \frac{E_{mag}}{D_{ohm}}. \tag{5.30}$$

With knowledge about τ_{diss} and an estimate of E_{mag}, we are able to put numbers on the Ohmic dissipation D_{ohm} in Earth's core.

Christensen and Tilgner [2004] found an inverse dependence of τ_{diss} on the magnetic Reynolds number Rm. The same study rejects an additional dependence on $Re = Rm/Pm$ (which is equivalent to an additional dependence on Pm) because of results of the Karlsruhe laboratory dynamo. Later, Christensen [2010] revisited the τ_{diss}-scaling favouring an additional dependence on the magnetic Ekman number $Ek_\eta = Ek/Pm$.

Using the magnetic diffusion time $\tau_\eta = D^2/\eta$ to normalise the magnetic dissipation time,

$$\tau^*_{diss} = \frac{\tau_{diss}}{\tau_\eta}, \tag{5.31}$$

the 2004 and the 2010 laws are given as

$$\begin{aligned}\tau^*_{diss,04} &= 0.27\, Rm^{-1}, && (5.32)\\ \tau^*_{diss,10} &= 0.59\, Rm^{-5/6} Ek_\eta^{1/6} \\ &= 0.59\, Rm^{-5/6} Pm^{-1/6} Ek^{1/6}. && (5.33)\end{aligned}$$

5.6.2 LOOCV analysis for τ_{diss}

According to the scaling laws of Equations 5.32 and 5.33, it seems reasonable to test scaling laws for τ^*_{diss} that have power law form including the parameters Rm, Pm, Ek (and possibly Pr). Our model selection analysis by LOOCV on the basis of the 116 numerical dynamo models favours the full model,

$$\tau^*_{diss} = 0.33\, Rm^{-0.89} Pm^{0.10} Ek^{0.09}, \tag{5.34}$$

shown in Figure 5.10. $P_{CV}(Rm, Pm, Ek) = 0.0777$ compared to $P_{CV}(Rm) = 0.1400$ and $P_{CV}(Rm, Ek_\eta) = 0.1321$. The standard errors on the prefactor and on the exponents in Equation 5.34 are 0.08, 0.03, 0.03 and 0.02, respectively. The mean relative misfit χ_{rel} of this scaling law is 0.289, significantly larger than for the previous scalings. (Allowing a Pr-dependence in the model selection procedure again leads to the full model including Pr and reduces the mean relative misfit to 0.205. However, see the remarks on the distribution of Pr in our dataset in Section 5.2.4.)

A scaling law with only Rm as independent variable on the basis of the 116 dynamo models would be $\tau^*_{diss} = 0.083\, Rm^{-0.80}$, displayed in Figure 5.11. While the numerical dynamo database of Christensen and co-workers has grown over the years, the exponent of Rm in a simple one-parameter law for τ^*_{diss} has decreased in absolute magnitude from -1 [Christensen and Tilgner, 2004] via -0.93 Christensen [2010] to -0.8 in this study. The first thing to notice in the plot is the clear unresolved Pm-dependence in the data plotted according to this law. The subsets of data with equal Ek (and similar Pm) appear to

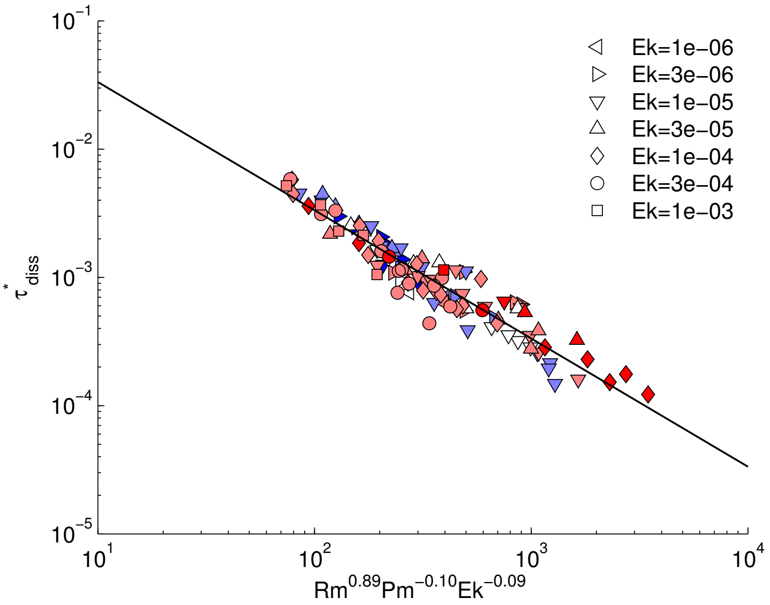

FIGURE 5.10: Magnetic dissipation time. Favoured scaling law. Colours as in Figure 5.5.

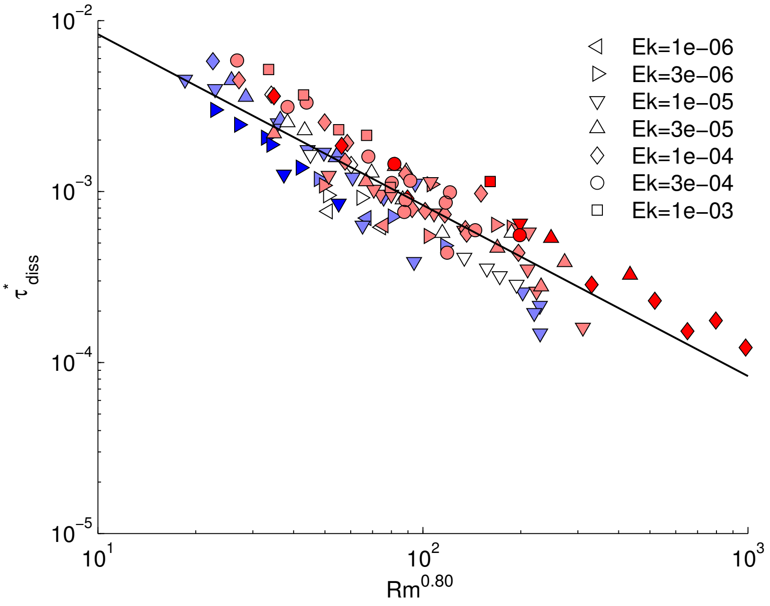

FIGURE 5.11: Magnetic dissipation time. Simple *Rm*-law with unresolved further dependencies. Colours as in Figure 5.5.

follow slopes that are similar to -0.8 with different y-axis intercepts. This would mean that Ek and Pm mainly determine the prefactor in the exponential scaling law. The favoured scaling law for τ^*_{diss} (Eq. 5.34) implies that this quantity grows with increasing Pm. This dependence is contrary to the scaling including the magnetic Ekman number (Eq. 5.33).

5.6.3 Application to Earth's core

One quantity that is of interest for the study of the Earth's deep interior is the amount of Ohmic dissipation in the core. Christensen and Tilgner [2004] used their scaling law for the magnetic dissipation time (Eq. 5.32) to derive 42 years for the magnetic dissipation time and an estimate of 0.2-0.5 TW for the Ohmic dissipation, which was a rather small value compared to other estimates. These calculations are based on $Rm = 800$ (note the differing parameter definition in the original paper) and $E_{mag} = (2.8 - 6.2) \cdot 10^{20}$ Joules. Christensen [2010] found an Ohmic dissipation time that is five times shorter and hence a five times higher value for the Ohmic dissipation using the revised scaling law (Eq. 5.33).

We base our calculations on the current estimates for the non-dimensional parameters given in Table 5.1. A major revision of these numbers has resulted from studies by de Koker et al. [2012] and Pozzo et al. [2012] that have increased the numerical values of the thermal and the electrical conductivities, κ and σ_e, for Earth's core by roughly a factor of three. Together with flow velocities of $\sim$ 15 km/year inferred from secular variation studies [Bloxham and Jackson, 1991, Holme, 2007], this yields $Rm \approx 2300$. Note, however, that large uncertainties are associated with this estimate that is based on the large-scale flow only.

The value for the magnetic energy in Christensen and Tilgner [2004] was derived from an assumed magnetic field strength of 2-3 mT in the core that comes from considerations about the field strength at the core-mantle boundary (CMB). More recent studies of the magnetic field strength in the core found similar values. Aubert et al. [2009] used two end-member scenarios, high and low power, to study the evolution of heat flow in the core. The high-power model gives a present-day r.m.s. core magnetic field of 2.3 mT, whereas the low-power model leads to a magnetic field of 1.1 mT. Buffett [2010] studied tidal dissipation in the Earth's core. In this context, nutation observations can be explained by a core-averaged field strength of 2.5 mT. Gillet et al. [2010] studied variations of length-of-day (LOD) in the context of torsional waves. They estimated an r.m.s. field strength of $\sim$ 4 mT inside the Earth's core. Concluding, the value of 2-3 mT for the r.m.s. field strength in the Earth's core still lies in the range of recent estimates, although the value could also be slightly higher. Hence, we use the same estimate of $(2.8 - 6.2) \cdot 10^{20}$ J for the magnetic energy as Christensen and Tilgner [2004].

Finally, we have to assume that the processes in the numerical simulations are relevant to the dynamics of Earth's core in order to be able to extrapolate using scaling laws.

This is by no means certain. But we may try since Earth's core appears to reside in the rapidly-rotating regime [King et al., 2010] as do the numerical dynamo models of this study (cf. Section 5.2.5).

Under these assumptions, the scaling in Equation 5.34 yields a magnetic dissipation time of 2.3 years. Using Equations 5.30 and 5.31, this leads to an Ohmic dissipation of 3.4-8.4 TW in Earth's core. (Using a τ^*_{diss}-scaling that additionally includes Pr leads to a slightly higher Ohmic dissipation.) If we include the uncertainties of the non-dimensional parameters Rm, Pm and Ek, the error bars will increase further. Due to the size of the exponents, however, a change in the value of Rm would alter the result most as would a change in the estimate of E_{mag}.

The Ohmic dissipation contributes to the total heat flux at the CMB. For the conductive heat flux at the top of the core, de Koker et al. [2012] find 14-20 TW using their new estimate for the thermal conductivity. Also Pozzo et al. [2012] suggest high adiabatic heat flux at the CMB with 15-16 TW on the basis of the increased thermal conductivity. These estimates are higher than the 5-15 TW found from independent considerations of core temperature, geodynamo energetics and buoyancy flux of lower-mantle thermal plumes [Lay et al., 2008], which at that time were already large compared to the previously estimated 3-4 TW. Since the dissipation should be a fraction of the total heat flux through the system, the lower range of the values 3.4-8.4 TW for Ohmic dissipation in Earth's core appears to be consistent with the recent high CMB heat flux scenarios.

5.6.4 Implications

The scaling laws for flow velocity (Eq. 5.22), magnetic field strength (Eq. 5.26) and Ohmic dissipation time (Eq. 5.34), as defined here, are not independent (U. Christensen, pers. comm.). The parameter definitions lead to $E_{mag} \sim Lo^2$ (Eq. 5.23), $\tau_{diss} = E_{mag}/D_{ohm}$ (Eq. 5.30) and $D_{ohm} = f_{ohm}P \sim f_{ohm}Ra^*_Q$ (Eq. 5.24); the latter scaling is not exact, but for large enough Nu almost perfectly satisfied [Appendix A of Christensen and Aubert, 2006]. The interdependence of the three laws enables us to predict the τ_{diss}-scaling from the Ro- and the $Lo/f^{1/2}_{ohm}$-scalings yielding $\tau^*_{diss} \sim Rm^{-0.89}Pm^{0.09}Ek^{0.11}$. The compliance with the LOOCV-preferred scaling law (Eq. 5.34) shows the internal consistency.

Using the scaling laws for flow velocity (Eq. 5.22) and magnetic field strength (Eq. 5.26) as well as the parameter values from Table 5.1, we can also extrapolate these quantities from the numerical models to Earth's core. Combining Equations 5.22 and 5.26 and eliminating Ra^*_Q yields

$$Lo/f^{1/2}_{ohm} = 0.54\, Ro^{0.70}Pm^{0.25}. \tag{5.35}$$

Two ways are viable here: either (a) we use an estimate for the velocity in the core to derive a magnetic field strength, or (b) we do the calculation vice versa. In case (a), assuming a velocity of $\sim$ 15 km/year at the core surface (see Section 5.6.3) and $f_{ohm} \approx 1$ in the core as in Christensen and Aubert [2006], we find a magnetic field strength

$$\begin{aligned} B_{rms} &= \sqrt{\Lambda \rho \mu_0 \eta \Omega} \\ &= Lo \, (\rho \mu_0)^{1/2} \, \Omega D \end{aligned} \tag{5.36}$$

of $\sim$ 0.1 mT, where $\Lambda = Lo^2 Pm Ek^{-1}$ is the Elsasser number. This number is lower compared to the estimates in Section 5.6.3 by a factor 10 to 40. In case (b), using an estimate of $\sim$ 3 mT for the magnetic field strength in the core, we find $\sim$ 5.6 cm/s for the velocity, which is by a factor of 100 larger than the usual estimates. So using the scaling laws for Ro (Eq. 5.22) and $Lo/f_{ohm}^{1/2}$ (Eq. 5.26), either (a) the magnetic field strength is too low, or (b) the velocity is too high. The Pm-dependence in Equations 5.22, 5.26 and hence also 5.35 is at variance with the scalings found by Christensen and Aubert [2006], whose laws lead to much better agreement between magnetic field strengths and flow velocities thought to occur in the Earth.

It should, however, be noted that the usual velocity estimate of $\sim$ 15 km/year is only valid for the large-scale motions on the surface of the core since it is derived from secular variation data. Small-scale velocities in the core's interior might well be significantly higher. Besides, the resolution of this discrepancy might be a modification of the scaling laws in the low-Pm limit. In any case, the application of the scalings of flow velocity and magnetic field strength to Earth's core remains to be addressed.

5.7 Conclusions

Numerical dynamo simulations can complement theoretical considerations and laboratory experiments in the goal to gain insight into Earth's core. The derivation of scaling laws has been one important way. This approach, however, involves two major difficulties. The first is that we have to make sure that the numerical models are in the same dynamical regime as Earth's core. Although numerical models can produce Earth-like magnetic fields [e.g. Christensen et al., 2010], this point is by no means certain. The second task is extracting scaling laws from the data that capture all relevant parameters.

We have studied approaches to the second task on the basis of 116 numerical dynamo models from the database of Christensen and co-workers. Model selection deals with the question of how many independent variables have to be included in a model (scaling law) in order to account for the variability in the data, while avoiding over-fitting. Our method of choice is leave-one-out cross-validation (LOOCV). It rates models according to their predictive abilities and ideally prevents over-fitting.

Using LOOCV, we have studied the diffusivity-free scalings of heat transport (Nu^*), flow velocity (Ro) and magnetic field strength ($Lo/f_{ohm}^{1/2}$) proposed by Christensen and

Aubert [2006] as well as the scaling of the magnetic diffusion time [Christensen and Tilgner, 2004, Christensen, 2010]. The physical rationale leading to diffusivity-free scalings is the idea that diffusive processes do not play a major role in Earth's core. However, it turns out that in velocity and magnetic field strength scaling, an additional dependence on Pm is required by the numerical dynamo data (Table 5.5). (The small Ek-dependence in the heat transport scaling disappears under a different error attribution to the data and might be blamed on the non-asymptotical regime of the data.) The additional dependencies mean that diffusivities come back into the scalings. Hence we find that diffusive processes are relevant in the numerical dynamos.

Similarly, Soderlund et al. [2012] find that transitions in dynamo behaviour from dipolar to multipolar are controlled by a competition of inertial and viscous forces. This means that also in this fundamental change in the systematics of present-day numerical dynamos, (viscous) diffusivity matters.

The relevance of diffusive processes is also apparent from our study of scalings with traditional parameters (Section 5.5). The favoured scaling laws are complex and require almost all possible parameters. Interestingly, it is possible to find something similar to a modified Rayleigh number Ra^* with an additional Pm-dependence in the scalings for velocity and magnetic field strength. This is not at all true for the heat transport scaling.

The magnetic dissipation time τ^*_{diss} is a quantity relevant to the study of Earth's core since it allows us to estimate the Ohmic dissipation. However, also the preferred τ^*_{diss}-scaling is more complex than suggested in previous studies. This leads to large error bars in the estimated quantities.

Using the τ^*_{diss}-scaling and an estimate for the magnetic energy, we derived a range of 3-8 TW for the Ohmic dissipation in Earth's core. The lower range, 3-4 TW, of these values appears to be consistent with recent high CMB heat flux scenarios [Lay et al., 2008, de Koker et al., 2012, Pozzo et al., 2012]. An unresolved issue is the application of velocity and magnetic field strength scaling to the core.

Acknowledgments

We are grateful to U. Christensen for providing the data of the numerical dynamo simulations used in this study and for providing some arguments given in Section 5.6.4. We would also like to thank F. Takahashi and K.M. Soderlund for providing data, as well as J.M. Aurnou and E.M. King for discussion. Constructive reviews by U. Christensen and an anonymous reviewer have helped to improve the manuscript. Funding for ZS by the ERC grant 247303 'MFECE' is gratefully acknowledged.

Table 5.7: Overview of the scaling laws preferred by LOOCV assuming equal errors in y. The corresponding laws assuming equal errors in $\zeta = \log(y)$ are given in Table 5.5. The exponents of the non-dimensional parameters are shown together with their standard errors from the multiple linear regression. χ_{rel} is the mean relative misfit between fitted and observed values (Eq. 5.9).

	prefactor	Ra_Q^*	Pm	Ek	χ_{rel}
Nu^*	0.083 ± 0.004	0.545 ± 0.005	-	-	0.137
Ro	1.20 ± 0.07	0.471 ± 0.006	-0.098 ± 0.006	-0.034 ± 0.007	0.123
$Lo/f_{ohm}^{1/2}$	0.59 ± 0.05	0.302 ± 0.008	0.147 ± 0.010	-	0.174

Table 5.8: Earth-like dynamo models: Overview of the scaling laws preferred by LOOCV for the diffusivity-free parameters assuming equal errors in $\zeta = \log(y)$. The exponents of the non-dimensional parameters are shown together with their standard errors from the multiple linear regression. χ_{rel} is the mean relative misfit between fitted and observed values (Eq. 5.9).

	prefactor	Ra_Q^*	Pm	Ek	χ_{rel}
Nu^*	0.069 ± 0.007	0.479 ± 0.009	-	0.054 ± 0.013	0.114
Ro	1.49 ± 0.08	0.460 ± 0.004	-0.126 ± 0.008	-	0.075
$Lo/f_{ohm}^{1/2}$	0.38 ± 0.04	0.268 ± 0.008	0.179 ± 0.016	-	0.155

Appendix

5.A Equal errors in the original variable

In Section 5.2.3, we discuss two possibilities of attributing errors to the data. Either we assume equal errors in $\zeta = \log(y)$ as above, or equal errors in the original measured variable y. Table 5.7 lists the scaling laws that are preferred by LOOCV under the second assumption when we allow the parameters Ra_Q^*, Pm and Ek to enter the laws as in Section 5.4.

There are two major differences between the scaling laws derived under the assumption of equal errors in ζ (Table 5.5) and the ones with equal errors in y (Table 5.7). In the first case, the Nu^*-law exhibits an Ek-dependence, whereas in the second case it does not. However, in the second case, the Ro-law additionally depends on Ek. In order to check the validity of the assumption of Gaussian errors either in ζ or in y, we looked at the histograms of the residuals resulting from the two Nu^*-laws. In both cases, the assumption of Gaussian errors seems to be justified.

5.B Reduced dataset: Earth-like dynamo models

Only considering models that lie in the 'Earth-like triangle' for magnetic field morphology in Figure 5.3 [criteria of Christensen et al., 2010], the dynamo dataset is reduced from 116 to 61 models. Table 5.8 shows the scaling laws that in this case are preferred by LOOCV under the assumption of equal errors in $\zeta = \log(y)$. Although the dataset is reduced by almost half, the resulting laws only differ in their exponents (up to ±0.04), but not in the parameters included (cf. Table 5.5).

Recent developments

Our study of scaling laws from numerical dynamo models as presented so far has been published in the Geophysical Journal International as Stelzer and Jackson [2013]. Due to its implications for our understanding of Earth's core, the topic has received sustained interest since then. This is reflected in eight citations of our study in the course of one year. In the following wrap-up section, we present some of the recent findings.

Davidson [2013] theoretically derived scaling laws for planetary dynamos based on Christensen's hypothesis that the saturated magnetic energy density should not depend on the rotation rate. This assumption was justified by the observation that small-scale vorticity in rotating convection is independent of the rotation rate. In contrast to other studies, the inertial term was omitted due to the smallness of Ro in planetary settings. From a dimensional analysis, the magnetic field was concluded to scale as $B \sim l^{1/3} P^{1/3}$ where l is the integral length scale of motions and P the power generated by buoyancy. In a second step, a balance between Coriolis, buoyancy and Lorentz forces (MAC balance) was exploited to derive scaling laws for the velocity Ro and the magnetic dissipation time τ_{diss}. The resulting scaling $Ro \sim P^{4/9}$ agrees well with our Equation 5.22 since $Ra_Q^* \sim P$ [Christensen and Aubert, 2006]. Pm-dependences were not part of the scaling analysis since they were supposed to disappear in the low-Pm limit relevant for planetary cores. Applying the resulting slightly different power-based scaling laws to the numerical data set of Christensen as well as to the planets yielded reasonable agreement.

Most previous studies, including our own in this chapter, studied convection-driven incompressible spherical shell dynamo models with constant material properties. While this setup might be an appropriate model for the Earth's and similar cores, it is certainly not a good representation of the gas giants and low-mass stars. In order to study those bodies, Yadav et al. [2013] analyzed 273 numerical models using the anelastic approximation, which allows the density $\rho(r)$ to vary with the radius, and radius-dependent diffusivities $\eta(r)$, $\kappa(r)$ and $\nu(r)$. They found largely the same scaling laws for flow velocity, magnetic field strength and magnetic dissipation time as the ones discussed before for the Boussinesq case. Also in the anelastic cases, a Pm-dependence is required for an optimal data fit on top of the fundamental power-based scaling.

Similar studies of anelastic dynamos by Schrinner et al. [2014] and Raynaud et al. [2014] lead to comparable results. The scaling laws for heat flux, flow velocity, magnetic field strength and dissipation time with the flux-based Rayleigh number Ra_Q^* are not significantly changed by compressible effects compared to the Boussinesq case. However, the authors could not resolve the secondary Pm-dependence due to the studied parameter range.

Dynamo simulations of yet another setup were performed by Tilgner [2014] recently. This study of rotating plane layer convection at first glance yields similar scalings for magnetic energy and dissipation as the spherical shell case. However, the data are not fit well without taking into account an additional Ek-dependence which is not present in Equation 5.26. Regardless of which change in the model is responsible for the difference, this result suggests that the purely power-based scaling might not be as universal as previously believed.

An interesting contribution to the topic of planetary and numerical dynamo simulations was recently published by Oruba and Dormy [2014]. Based on Christensen's data base, they showed that previous scaling laws for the magnetic field strength mainly reflect a simple balance between energy production and dissipation which is necessarily valid for any statistically steady dynamo. This also explains the applicability of power-based scaling laws regardless of driving mechanism, geometry and boundary conditions. However, power-based scaling laws merely relate output quantities and hence do not have any power to a priori predict the output of a dynamo. Following a similar path as our Section 5.5, Oruba and Dormy [2014] constructed 'predictive' scaling laws, i.e. laws that only contain true input parameters on the right-hand side. It turned out that a suitable input parameter related to Ra is the relative distance to either the onset of convection or of dynamo action, $(Ra - Ra_c)/Ra_c$ or $(Ra - Ra_d)/Ra_c$ respectively. Employing a Viscous-Archimedean-Coriolis (VAC) balance as King and Buffett [2013], leads to the predictive flow scaling

$$Rm \sim \frac{Ra - Ra_c}{Ra_c} Ek^{-1/3} Pm\, Pr^{-1} \left(\frac{Pr}{1 + Pr} \right)^{2/3} \tag{5.37}$$

where the functional form of the Pr-dependence comes from the scaling of the onset of convection Ra_c. The magnetic field strength as given by the Elsasser number $\Lambda = Lo^2 Pm/Ek$ is predicted to scale as

$$\Lambda \sim \frac{Ra - Ra_d}{Ra_c} Pm\, Pr^{-1} \left(\frac{Pr}{1 + Pr} \right)^{2/3} . \tag{5.38}$$

This scaling implies a dependence of the magnetic field on the rotation rate. It fits the numerical dynamos comparably well as the power-based scalings. As in King and Buffett [2013], Oruba and Dormy [2014] showed that viscosity plays an important role in the current numerical dynamos. Hence all scaling laws extracted from numerical dynamos are probably not relevant to planetary settings where the governing force balances are different.

In conclusion, we have observed a great success of theoretical and empirical power-based scaling laws in fitting e.g. flow velocities and magnetic field strengths of numerical and planetary dynamos regardless of parameter values, driving mechanisms and model setup. This is explained by the fact that they are based on a balance between energy production and dissipation which should in principle be valid for any steady dynamo. However, their use is limited by the fact that they merely relate output quantities. The construction of predictive scaling laws based on true input parameters circumvents this limitation.

Due to the recent recognition that current numerical dynamos are viscously dominated and hence do not operate in the same regime as their planetary couterparts, scaling laws extracted from simulations might not be useful to infer properties of planetary cores. This might explain the observed discrepancies when extrapolating velocities and field strength to the parameters of the Earth's core. In any case, dynamo scaling laws from simulations are an interesting area of research. Currently the catalogue suffers from strong correlations in the input parameters, e.g. Pm and Ek. More topics for future study include the secondary dependence of flow velocity and magnetic field strength on diffusivities, e.g. on Pm, which is required by the data in our study, and predicted to vanish when approaching planetary parameters, as well as the recently predicted dependence of the magnetic field amplitude on the rotation rate.

References

J. Aubert, S. Labrosse, and C. Poitou. Modelling the palaeo-evolution of the geodynamo. *Geophysical Journal International*, 179(3):1414–1428, Jan 2009.

J. Aurnou, M. Heimpel, and J. Wicht. The effects of vigorous mixing in a convective model of zonal flow on the ice giants. *Icarus*, 190(1):110 – 126, 2007.

J. M. Aurnou. Planetary core dynamics and convective heat transfer scaling. *Geophysical & Astrophysical Fluid Dynamics*, 101(5-6):327–345, Oct 2007.

J. Bloxham and A. Jackson. Fluid-flow near the surface of Earth's outer core. *Rev Geophys*, 29(1):97–120, Jan 1991.

B. A. Buffett. Tidal dissipation and the strength of the Earth's internal magnetic field. *Nature*, 468(7326):952–955, Jan 2010.

U. Christensen. Zonal flow driven by strongly supercritical convection in rotating spherical shells. *J. Fluid Mech.*, 470:115–133, Jan 2002.

U. Christensen and A. Tilgner. Power requirement of the geodynamo from ohmic losses in numerical and laboratory dynamos. *Nature*, 429(6988):169–171, Jan 2004.

U. R. Christensen. Dynamo scaling laws and applications to the planets. *Space Sci Rev*, 152(1-4):565–590, May 2010.

U. R. Christensen and J. Aubert. Scaling properties of convection-driven dynamos in rotating spherical shells and application to planetary magnetic fields. *Geophysical Journal International*, 166(1):97–114, Jul 2006.

U. R. Christensen, V. Holzwarth, and A. Reiners. Energy flux determines magnetic field strength of planets and stars. *Nature*, 457(7226):167–169, Jan 2009.

U. R. Christensen, J. Aubert, and G. Hulot. Conditions for Earth-like geodynamo models. *Earth Planet Sc Lett*, 296(3-4):487–496, Jan 2010.

P. Davidson. Scaling laws for planetary dynamos. *GJI*, 195(1):67–74, 2013.

N. de Koker, G. Steinle-Neumann, and V. Vlcek. Electrical resistivity and thermal conductivity of liquid Fe alloys at high P and T, and heat flux in Earth's core. *P Natl Acad Sci Usa*, 109(11):4070–4073, Jan 2012.

B. Efron. Estimating the Error Rate of a Prediction Rule - Improvement on Cross-Validation. *J Am Stat Assoc*, 78(382):316–331, Jan 1983.

N. Gillet, D. Jault, E. Canet, and A. Fournier. Fast torsional waves and strong magnetic field within the Earth's core. *Nature*, 465(7294):74–77, Jan 2010.

G. Glatzmaier and P. Roberts. A 3-dimensional self-consistent computer-simulation of a geomagnetic-field reversal. *Nature*, 377(6546):203–209, Jan 1995.

T. Hastie, R. Tibshirani, and J. Friedman. *The Elements of Statistical Learning*. Springer, 2009.

R. Holme. Large-scale flow in the core. In *Treatise on Geophysics*, volume 8 Core Dynamics, pages 107–130, 2007.

C. A. Jones. Planetary magnetic fields and fluid dynamos. *Annu. Rev. Fluid Mech.*, 43 (1):583–614, Jan 2011.

A. Kageyama and T. Sato. Computer-simulation of a magnetohydrodynamic dynamo .2. *Phys Plasmas*, 2(5):1421–1431, Jan 1995.

E. King and B. Buffett. Flow speeds and length scales in geodynamo models: The role of viscosity. *Earth Planet Sc Lett*, 371-372:156–162, 2013.

E. M. King, S. Stellmach, J. Noir, U. Hansen, and J. M. Aurnou. Boundary layer control of rotating convection systems. *Nature*, 457(7227):301–304, Jan 2009.

E. M. King, K. M. Soderlund, U. R. Christensen, J. Wicht, and J. M. Aurnou. Convective heat transfer in planetary dynamo models. *Geochem. Geophys. Geosyst.*, 11(6), Jun 2010.

E. M. King, S. Stellmach, and J. M. Aurnou. Heat transfer by rapidly rotating Rayleigh–Bénard convection. *J. Fluid Mech.*, 691:568–582, 2012.

T. Lay, J. Hernlund, and B. A. Buffett. Core-mantle boundary heat flow. *Nat Geosci*, 1 (1):25–32, Jan 2008.

Y. Liu and R. Ecke. Heat transport scaling in turbulent Rayleigh-Benard convection: Effects of rotation and Prandtl number. *Phys Rev Lett*, 79(12):2257–2260, Jan 1997.

P. Olson. Overview of core dynamics. In G. Schubert, editor, *Treatise on Geophysics*, volume 8 on Core Dynamics. Elsevier Science Publishers, 2007.

L. Oruba and E. Dormy. Predictive scaling laws for spherical rotating dynamos. *Geophysical Journal International*, 198(2):828–847, 2014.

M. Pozzo, C. Davies, D. Gubbins, and D. Alfe. Thermal and electrical conductivity of iron at Earth's core conditions. *Nature*, 485(7398):355–358, Jan 2012.

R. Raynaud, L. Petitdemange, and E. Dormy. Influence of the mass distribution on the magnetic field topology. *A&A*, 567(A107), 2014.

M. Schrinner, L. Petitdemange, R. Raynaud, and E. Dormy. Topology and field strength in spherical, anelastic dynamo simulations. *A&A*, 564(A78), 2014.

R. Simitev and F. H. Busse. Bistability and hysteresis of dipolar dynamos generated by turbulent convection in rotating spherical shells. *Epl-Europhys Lett*, 85:19001, 2009.

K. M. Soderlund, E. M. King, and J. M. Aurnou. The influence of magnetic fields in planetary dynamo models. *Earth Planet Sc Lett*, 333–334(0):9 – 20, 2012.

Z. Stelzer and A. Jackson. Extracting scaling laws from numerial dynamo models. *Geophysical Journal International*, 193(3):1265–1276, 2013.

M. Stone. An Asymptotic Equivalence of Choice of Model by Cross-Validation and Akaike's Criterion. *Journal of the Royal Statistical Society. Series B (Methodological)*, 39(1):pp. 44–47, 1977.

A. Tilgner. Magnetic energy dissipation and mean magnetic field generation in planar convection-driven dynamos. *Phys Rev E*, 90, 2014.

R. K. Yadav, T. Gastine, U. R. Christensen, and L. D. V. Duarte. Consistent scaling laws in anelastic spherical shell dynamos. *The Astrophysical Journal*, 774(6), 2013.

Chapter 6

Conclusions and perspectives

6.1 ZUCCHINI

This dissertation is concerned with two topics from the area of magnetohydrodynamic (MHD) flows. In the first part (Chapters 3-4), we studied electrically-driven MHD flow in a cylindrical geometry both experimentally and numerically. This topic blends into the history of liquid metal MHD studies which were started by Hartmann [1937] and operate in the low-magnetic-Reynolds number regime. The setup of our ZUCCHINI experiment contains a prominent inner electrode which gives rise to a free Shercliff layer. It was chosen as a prelude to our upcoming rapidly rotating spherical shell experiment SpiNaCH. We were able to acquire high-quality velocity information about the flow of liquid GaInSn using ultrasound Doppler velocimetry (UDV) and potential difference probes (PDP) with their measurements mutually confirming each other. Moreover we gained experience in handling liquid metals and driving a flow by current injection which is valuable for our future experiment.

Chapter 3 dealt with the steady base flow, and Chapter 4 with the observed instabilities in ZUCCHINI. The base flow occurring at low forcing current was found to have a weakly moving inner part. Above and below the edge of the inner electrode, the Lorentz-forcing generates a free Shercliff layer. Going to greater radii, the dominant azimuthal velocity drops roughly as predicted by the theory of Baylis and Hunt [1971]. The magnitude of the base flow in the experiment is approximately recovered in the 2D3C simulations using the finite element software COMSOL Multiphysics. Differences exist in the thickness of the free shear layer, which does not exhibit the expected dependence on the magnetic field in the experiment, and the threshold of the large-Hartmann-number regime. The latter appears to be reached in the base flow simulations for $M \gtrsim 50$, whereas in the experiment it needs $M \gtrsim 500$. An interesting observation of a jet near the outer wall was attributed to the deviation of the real magnetic field from a uniform axial field supported by numerical models.

At higher forcing, the flow was observed to become unstable first at the free Shercliff layer. The instability consisted of vortices moving in the direction of the azimuthal flow, and was attributed to a Kelvin-Helmholtz-type mechanism where the action of the magnetic field is restricted to setting up the base flow profile. In the limit of large M, the critical Reynolds number scales as $Re_c/M \approx 6$. A similar scaling was found by a linear stability analysis based on our previous numerical simulations. This analysis also showed that azimuthal wave number m of the linearly most unstable mode grows with M. In the experiment, the vortices grow for larger Re, decreasing m. This process is accompanied by further transitions in the mean structure and the friction factor. The transitions were attributed to various criteria known from the literature. A remarkable finding is that the free Shercliff layer thickness approaches a constant value at large Re. Also the transition to turbulence in the Hartmann layer at $Re/M \approx 380$ was observed [Moresco and Alboussiere, 2004] which underlines the importance of $R = Re/M$ as a universal control parameter of the system. In general, we were able to characterize different regimes of confined low-Rm flow: stable flow, an unstable free Shercliff layer, unstable core flow and a turbulent Hartmann layer.

6.2 Perspectives for future experiments

Future perspectives for the topic of low-Rm MHD flow in general include the apparent universal role of the parameter R. To date it is not understood why R plays such an important role even if the Hartmann layer thickness is not a characteristic length scale of the system, e.g. in the case of the free Shercliff layer and side layer instabilities [Zikanov et al., 2014]. For ZUCCHINI in particular, it would be interesting to determine the azimuthal wave number m of the vortical structures more rigorously. This requires measurements at several azimuthal positions, and could be achieved by installing stripes of PDPs in the azimuthal direction. In the large-M limit, this would allow for a mapping of the horizontal velocity components. Another upgrade of the experiment would be a UDV probe located in the outer cylinder measuring along a chord. This would help to constrain the azimuthal velocity by avoiding the assumption of axisymmetry that we had to employ in this work.

Certainly an area for future study are MHD experiments in ducts or annuli using transparent electrolytes. In comparison to liquid metals, their electrical conductivity is very low (e.g. $\sigma_e = 39(\Omega\text{m})^{-1}$ for hydrochloric acid). Hence such experiments do not reach as high M, typically up to $\mathcal{O}(1-10)$. The forcing current through the electrolyte in a continuous experiment is limited by the voltage of electrolysis. But even at low currents, the velocities are significant as proven by a small demo experiment that we performed in salt water at $B = 0.1$ T. The big advantage of experiments with electrolytes is that the flow can be visualized optically. This would allow for a closer study of instability mechanisms and a comparison with high-resolution numerical simulations.

In the astrophysical context, an area of research is concerned with the magnetorotational instability (MRI, cf. Sec. 1.3.9). Khalzov et al. [2010] explored the possibility of an electrically-driven MRI experiment. The theoretical profile $u_\phi \sim r^{-1}$ in our experiment would be marginally stable when removing the free shear layer, any side layer effects. Moreover the recirculation flow (or inertial effects respectively) should be negligible. For an experiment in the parameter range of ZUCCHINI, this severely limits the reachable velocities and hence Re and Rm. Instead of the standard MRI which requires significant induced fields, only the observation of the helical MRI (HMRI) with an additionally imposed azimuthal field seems feasible [Hollerbach and Rüdiger, 2005]. This would require an axial current rod with a current of several thousand Amperes along the center line similar to the first experimental evidence for HMRI by Stefani et al. [2006].

Finally it will be interesting to study how the effect of global rotation changes the flow and the stability criteria. This will be possible in a spherical geometry in our upcoming SpiNaCH experiment. The presence of an inner sphere together with strong rotation and magnetic fields leads to a shear layer on the tangent cylinder [Hollerbach et al., 2013]. Due to the higher electrical conductivity and the lower density of sodium compared to GaInSn, SpiNaCH will also reach larger M than ZUCCHINI. Already the first tests even without global rotation will certainly bring new insights.

6.3 Scaling laws from numerical dynamos

The second part of the dissertation (Chapter 5) addressed the extraction of scaling laws from numerical dynamo models. These simulations in the high-Rm regime were used to infer quantities like heat flux, flow velocities and magnetic field strength for the Earth's core due to their ability to reproduce some features of the geomagnetic field. In the past, particularly power-based scaling laws without dependencies on diffusivities have been successfully applied not only to the Earth but also other planets, e.g. by Christensen and Aubert [2006]. However, since numerical dynamo models and the Earth's core live in completely separate parameter regimes, we have to make sure that the same dynamics occurs in both and that we consider all relevant parameters.

When extracting scaling laws from a numerical data base, the problem of variable selection occurs which we tackled by leave-one-out cross-validation (LOOCV). It turned out that flow velocity and magnetic field strength in the numerical dynamos are not actually independent of diffusivities. In these cases, the scaling law that accounts for the variability in the data but is not more complex than required (Occam's razor) includes the magnetic Prandtl number Pm. Applying the extended scaling laws to the core, we found an Ohmic dissipation of 3 to 8 TW. However, either the flow velocity or the magnetic field strength do not agree with our estimates gained by other methods. This might be due to the fact that viscous effects play an important role in current numerical dynamo models while they are negligible in Earth's core [King and Buffett, 2013].

Hence it seems inevitable in numerical dynamo modeling either to reach smaller Ek which also puts requirements on Pm or to use physics-based approximations. Also the efforts in building 'predictive scaling laws' relating output quantities to pure input quantities Oruba and Dormy [2014] are worth to be continued. The secondary dependence on diffusivities which might disappear at core parameters stays an interesting topic. Potentially experiments are able to advance this area of research.

References

J. Baylis and J. Hunt. MHD flow in an annular channel; theory and experiment. *Journal of Fluid Mechanics*, 48(03):423–428, 1971.

U. R. Christensen and J. Aubert. Scaling properties of convection-driven dynamos in rotating spherical shells and application to planetary magnetic fields. *Geophysical Journal International*, 166(1):97–114, Jul 2006.

J. Hartmann. Hg-dynamics i: Theory of the laminar flow of an electrically conductive liquid in a homogeneous magnetic field. *Mathematisk-fysiske Meddelelser, Det Kgl. Danske Videnskabernes Selskab*, XV(6):1–28, 1937.

R. Hollerbach and G. Rüdiger. New type of magnetorotational instability in cylindrical taylor-couette flow. *Phys Rev Lett*, 95:124501, 2005. URL `http://journals.aps.org/prl/abstract/10.1103/PhysRevLett.95.124501`.

R. Hollerbach, X. Wei, J. Noir, and A. Jackson. Electromagnetically driven zonal flows in a rapidly rotating spherical shell. *Journal of Fluid Mechanics*, 725:428–445, 2013.

I. Khalzov, A. Smolyakov, and V. Ilgisonis. Equilibrium magnetohydrodynamic flows of liquid metals in magnetorotational instability experiments. *Journal of Fluid Mechanics*, 644:257–280, 2010.

E. King and B. Buffett. Flow speeds and length scales in geodynamo models: The role of viscosity. *Earth Planet Sc Lett*, 371-372:156–162, 2013.

P. Moresco and T. Alboussiere. Experimental study of the instability of the Hartmann layer. *J. Fluid Mech.*, 504:167–181, Jan 2004.

L. Oruba and E. Dormy. Predictive scaling laws for spherical rotating dynamos. *Geophysical Journal International*, 198(2):828–847, 2014.

F. Stefani, T. Gundrum, G. Gerbeth, G. Rüdiger, M. Schultz, J. Szklarski, and R. Hollerbach. Experimental evidence for magnetorotational instability in a taylor-couette flow under the influence of a helical magnetic field. *Phys Rev Lett*, 97:184502, 2006.

O. Zikanov, D. Krasnov, T. Boeck, A. Thess, and M. Rossi. Laminar-turbulent transition in magnetohydrodynamic duct, pipe and channel flows. *Applied Mechanics Reviews*, 66, 2014.

When you finish reading this book,
tie a stone to it and cast it into the midst of the Euphrates.

Jeremiah 51,63